An Instrumental Evaluation of Selected Metal Functionalised Semiconductors in the Facilitation of Photo-Organic Transformations.

Thesis submitted to:

The University of
KwaZulu-Natal
Pietermaritzburg
South Africa

For the Title of

Doctor of Science
(Chemistry)

Read By

Timothy Michael Underwood

March 2019

UNIVERSITY OF
KWAZULU-NATAL

Thesis Declaration

The project described herein (experimental research and compilation of this thesis) was conducted and completed at the School of Chemistry and Physics, University of KwaZulu-Natal (Pietermaritzburg campus) under the supervision of Professor Ross S. Robinson.

All research findings presented in this thesis by Timothy Michael Underwood are of an original nature that has not been presented elsewhere for the application of an academic degree.

Signed:……………………………………………………......

T. M. Underwood (Candidate)

Signed:………………………………………………………..

Professor R. S. Robinson (Supervisor)

The University of KwaZulu-Natal

(Pietermaritzburg campus)

School of Chemistry and Physics

South Africa

March 2019

My thesis has taught me know to think, interpret and logically reason the art of science.

My corrections have taught me how to believe in myself again, and possibly more importantly, made me realise just how many amazingly kind people there are in this world.

Acknowledgements

A doctoral title may only be awarded to the individual, of whose name is on the cover of this dissertation, yet the project's success was undoubtedly due to the countless hours so kindly given by the staff from The School of Chemistry and Physics at The University of KwaZulu-Natal, Pietermaritzburg, South Africa.

Professor Ross Robinson, of whom has been my postgraduate research supervisor since 2012, has guided me with generosity, kindness and respect to this milestone in my life.

And now for the bullet points:

> ➢ His continued motivation and allowing for a wide cross-disciplinary research leash have illuminated numerous excitonic pathways in science that have been fascinating (yet, sometimes inexplicably painful when most of them never succeeded) to explore.
> ➢ The weekend devotions to completing National Research Foundation applications at the 12th hour and the countless attempts at submitting publications for review on a Sunday evening cannot go unrecognised.
> ➢ Neither can the exciting expeditions to the University of Bristol in the United Kingdom to study chemical vapour deposition diamonds.
> ➢ His patience while waiting for my two MacBook Pro's to load Windows, that's always made for a good chuckle.
> ➢ I know have a good understanding of the difference between a hyphen, minus sigh, en dash and em dash.

His mentoring over these past seven years has allowed me to grow as a person, by becoming more confident in the laboratory, towards others and especially in myself. Especially, whilst working on my corrections, it was a challenging time and I can't be more grateful for all that you've done for me! *Thanks* Prof!

Besides Professor Robinson, two particular technicians have *always* gone the extra mile. Caryl Janse Van Rensburg's comprehension and knowledge of chromatography and mass spectrometry has without a doubt facilitated the full success of my doctoral thesis. What seemingly appeared impossible to quantify through an isolation process, Caryl was able to demonstrate how internal standards, calibration curves, peak deconvolutions, and response factors could easily determine the conversion of my 10 µL reaction products. There was also the recent explanation of knowing when to introduce a semicolon, stop for a sip of tea ';' and then continue. Besides chemistry, many lunch-time discussions of the weather, rabbits, and where my next outrageous trail running marathon will be, whilst enjoying the friendly gesture of a cup of tea and a cookie has been a thoroughly enjoyable highlight of the period. Caryl's husband, Quintus, who has been my Apple Macintosh saviour, is someone I can't thank enough. He single-handily saved two Apple laptops with the contents of my research.

Craig Grimmer, of whom has seemingly endless patience, is a person (and a very clever NMR technician) I will always acknowledge with the utmost respect and thank for all he has done to help me. Despite not utilising NMR spectroscopy to its full potential during my postgraduate research, he went out of his way and developed a quantitative method for me to accurately determine the conversion of those stubborn 10 µL reaction products during my masters/doctoral research. He has also been an extremely kind individual who has taken an interest in my research and on numerous occasions provided plausible solutions to semiconductor-mediated photocatalysis problems, where I thought none existed. Our discussions of science in general, motorcars and how not to injure one's self while running, has always sparked for fascinating conversations. Craig has always been 'the go-to person' for I.T. troubles, chemistry related software programmes, spanners and screwdrivers, and despite none of these duties being a part of his job to fulfil, his continued kind-heartedness and compassion is what makes him such a unique individual.

It cannot go unsaid to thank Mbuso, Guy, Paul, Laurence, Sabelo, Clarence, Fayzil and Bheki for their technical expertise in designing exotic radiation sources, intricate glassware items and potentially explosive glass reactors. Their smiles have also always made for a friendly place to visit after a long week of chemistry. Kevin Wickee from Shimadzu has also gone out of his way on numerous occasions to find and operate

Table of Contents

List of Abbreviations

^{1}H NMR	Proton nuclear magnetic resonance spectroscopy
Ag-CdS	Silver functionalised cadmium sulfide
Ag-CdS on Cu/Pd-N-TiO$_2$	Silver functionalised cadmium sulfide and copper/ palladium on nitrogen functionalised titanium dioxide
AR	Alizarin red
atm	Atmosphere
B.E.	Binding energy (eV)
B.E.T.	Brunauer-Emmett-Teller theory
BTF	Benzotrifluoride
C$_2$D$_2$Cl$_4$	Deuterated 1,1,2,2-tetrachloroethane
CDCl$_3$	Deuterated chloroform
Cd(NO$_3$)$_2$·4H$_2$O	Cadmium (II) nitrate tetrahydrate
CdS	Cadmium sulfide
CeO$_2$	Cerium dioxide
CH$_3$CN	Acetonitrile
CNL	Charge neutrality level
CBO	Conduction band offset
Cu(NO$_3$)$_2$·3H$_2$O	Copper (II) nitrate trihydrate
Cu|Pd	Copper and palladium alloy
Cu$_3$TiO$_5$	Copper doped titanium dioxide
Cu/Pd-N-TiO$_2$	Copper/Palladium and nitrogen three-component doped titanium dioxide.
DFT	Density functional theory
DMPO	5,5-Dimethyl-1-pyrroline N-oxide
E$_{EA}$	Electron affinity$_{semiconductor}$ [E$_{EA}$]
EIS	Electrochemical impedance spectroscopy
EPR	Electron paramagnetic resonance spectroscopy
EDX	Energy-dispersive X-ray spectroscopy
EtOH	Ethanol
EY	Eosin Y

FESEM	Field emission scanning electron microscopy
FEGSEM	Field emission gun scanning electron microscope
FET	Field effect transistors
FFT	Fast-Fourier transform
FRPCP	Free-radical-decorated porous coordination polymer
FTIR	Fourier Transform Infrared Spectroscopy
GC-MS	Gas chromatography-mass spectrometry
h^+	Positive hole
^1H NMR	Proton nuclear magnetic resonance spectroscopy
H_2	Molecular hydrogen
H_2O	Water
HOMO	Highest occupied molecular orbital
IBX	o-Iodobenzoic acid
ICP-MS	Inductively coupled plasma-mass spectrometry
IUPAC	International Union of Pure and Applied Chemistry
JCPDS	Joint committee of Powder Diffraction Standards
K_2CO_3	Potassium carbonate
LED	Light emitting diode
LUMO	Lowest occupied molecular orbital
MB	Methylene blue
MLCT	Metal-to-ligand charge transfer
Mn_3TiO_5	Manganese doped titanium dioxide
MOSFET	Metal oxide semiconductor field effect transistor
M_xO_y	Metal oxide
$M\text{-}TiO_2$	Metal-doped titanium dioxide
Na_2S	Sodium sulfide
NHE	Normal Hydrogen Electrode
$MnCl_2 \cdot 4H_2O$	Manganese (II) chloride tetrahydrate
$Ni(OAc)_2 \cdot 4H_2O$	Nickel(II) acetate tetrahydrate
NMR	Nuclear magnetic resonance spectroscopy
N/P	Non-photocatalytic reaction
N/S	Not specified

N-TiO$_2$	Nitrogen doped titanium dioxide
PCC	Pyridinium chlorochromate
Pd	Metallic palladium
Pd(OAc)$_2$	Palladium(II) acetate
PDC	Pyridinium dichromate
Pd-TiO$_2$-OV	Palladium functionalised titanium dioxide
PDF	Powder Diffraction File
RhB	Rhodamine B
SC	Semiconductor
SEM	Scanning electron microscopy
STEM	Scanning transition electron microscopy
TBHP	*t*-Butyl hydroperoxide
TBN	TEMPO/*tert*-butyl nitrate
TEM	Transmission electron microscopy
TEMPO	2,2,6,6-tetramethylpiperidinyloxyl radical
TCPP	*meso*-Tetra(4-carboxyphenyl)porphyrinato cobalt (II)
TiO$_2$	Titanium dioxide
TON	Turn over number
TTIP	Titanium tetraisopropoxide
UV	Ultraviolet
UV-Vis	Ultraviolet-visible light spectrophotometry
V$_2$O$_5$	Vanadium pentoxide
VAS	Visible-light activated semiconductors
wt%	Weight percent
W$_{metal}$	Work function$_{metal}$
XPS	X-ray photoelectron spectroscopy
XRD	Powder X-ray diffraction
Φ_B	Schottky Barrier
ζ	Zeta potential

Abstract

Throughout this research study, various strategies to design, synthesise and test the photo-reactivity of attenuated wide band gap semiconductors in alcohol oxidation studies have been explored. An alizarin red-sensitised zinc oxide photocatalyst which was stabilised in a silver-sodium electrolyte effectively facilitated a broad aromatic and aliphatic alcohol oxidation table with reported conversions ranging from 10 to ≥ 99 %. A systematic characterisation of the alizarin red-sensitised zinc oxide investigated the photoelectronic migrations across the alizarin red–zinc oxide interface and detected the transfer of electrons from the highest occupied molecular orbital of alizarin to the defect site of zinc oxide at 507 nm.

Further studies were directed towards the development of a novel titanium dioxide semiconductor that was activated by visible light. Three attempted strategies (pseudo perovskites [Cu_3TiO_5, Ni_3TiO_5, and Mn_3TiO_5], silver functionalised cadmium sulfide and a heterojunction between cadmium sulfide and titanium dioxide) explored the possibility of lowering the band gap potential of wide band gap semiconductors through metal ion functionalisation (Cu, Ni, Mn, and Ag) and heterojunction principles for the purpose of finding applications in mediating alcohol oxidations.

Whilst the three strategies were unable to demonstrate viable photocatalytic properties, the instrumental insight obtained during the process identified a suitable three-component semiconductor system ($Cu/Pd-N-TiO_2$). $Cu/Pd-N-TiO_2$ was extensively characterised with an array of instrumental techniques, thus developing an in-depth understanding of the photophysical properties that governed the photo-oxidative transformation of a range of cyclic alcohols and in the remediation of two dyestuffs typically associated with environmental contamination.

1. Introduction

1.1. Background Theory to Wide Band Gap Semiconductors

For semiconductors (for example, titanium dioxide) to operate effectively in a photocatalytic environment, an intensive knowledge of band gap energies underpins their success of photoactivation.

Large band gap energies greater than 2.0 eV (619.9 nm) categorise semiconductors as 'wide-band gap' photocatalysts that typically require irradiation sources at or below ultraviolet wavelengths ($\lambda < 400$ nm) for the necessary energy to photo-activate the semiconductor (**Figure 1**).
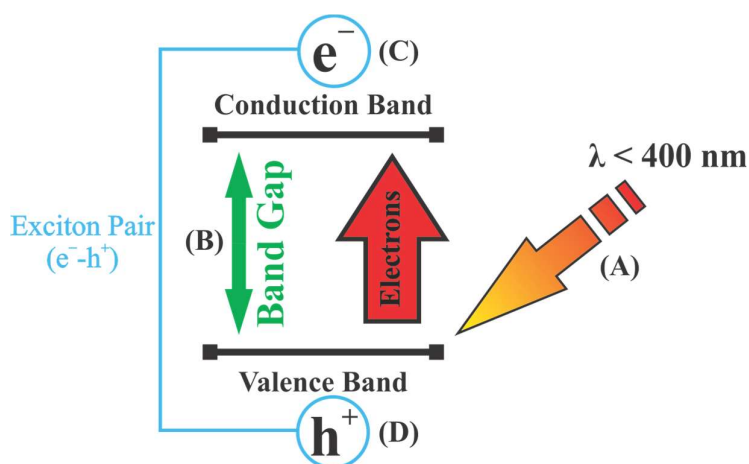
Figure 1: An illustration to represent the band gap excitation at specific energy inputs. When the incoming radiation (A) matches or exceeds the wide band gap energy (B), exciton pairs are generated. Thus electrons (C), and holes (D) migrate to the surface of the semiconductor.

After supplying the required energy, an electron is promoted from the valence to conduction band, and an exciton pair is generated. The charges (a free electron and

positive hole) migrate to the semiconductor's surface where redox processes occur.[1],[2],[3] The energy of a semiconductor's band gap (E) can be related to the respective wavelength (λ) through the following relationship:

$$E = h\nu, \text{where } \nu = \frac{c}{\lambda},$$

$$E = \frac{hc}{\lambda}$$

The band gap energy (E) of semiconductors is commonly reported in units of electron volts (eV), therefore; for wavelength (λ) in nm,

$$E \text{ (eV)} = \frac{1240 \text{ eV nm}}{\lambda},$$

where the coefficient, **1240** has been calculated from $\frac{hc}{10^{-9}\,e}$ and **1 nm = 10^{-9} m**.

In the above expressions, $\boldsymbol{h}$ is the (Planks Constant = 6.626×10^{-34} Js), $\boldsymbol{c}$ (speed of light in free space $= 2.998 \times 10^8$ ms^{-1}), and $\boldsymbol{e}$ (electron's elementary charge $= 1.602 \times 10^{-19}$ C).

With surface or lattice additions of metal, non-metal or organic dyes, wide band gap species such as titanium dioxide (**anatase**) can have their wide band gap (*e.g.* 3.2 eV for anatase[4]) attenuated away from ultraviolet and towards visible wavelengths for photocatalytic reactions. For approximately forty years, pure and engineered forms of titanium dioxide have been found in gas sensing,[5] inorganic and organic substrate oxidations and reductions,[6],[7] dye degradations,[8] dye-sensitised systems[9] and volatile pollutant remediation studies.[10]

1.2. Modes of Functionalising Semiconductors

An important consideration when studying 'doped' semiconductors is the nature of extrinsic species incorporated into or on the semiconductor's lattice. The vast majority of incorporation studies into a semiconductor are beyond the scope of this study (the current research will only reflect on the instrumental insight into the interpretation of heterogeneous semiconductors). However, the text below shall highlight their theory.

Despite the term *'doping'* of semiconductors being commonly used in the literature, it is more accurate to characterise as *'functionalising'* by one of the three methods listed in **Scheme 1**.

> ➢ Metal or non-metal ion exchange (substitution).
>
> ➢ Metal ion doping into interstitial sites.
>
> ➢ Surface loading of metals, non-metals or organic dyes.

Scheme 1: The three modes of functionalising heterogeneous semiconductors.[11],[12]

Functionalising a semiconductor can proceed *via* three routes, namely, ion implantation into the semiconductor's lattice through metal and or non-metal ion exchange (substitution), interstitial ion incorporation or, surface loading (of either metal, non-metal or organic dye particles). Methods of functionalising the surface of semiconductors using metals, non-metals and organic dyes are discussed in the proceeding texts.

1.2.1 Metal and Non-Metal Functionalisation Strategies of Semiconductors.

In this chapter, metal and non-metal functionalised semiconductors are discussed. The characteristics (enhanced visible light reactivity, reduced band gap and improved charge separation) imparted to metal chalcogens by extrinsic metal incorporation and

the instrumental methods used to characterise the metal loading techniques of numerous case studies are reported.

Both metal and non-metal ions are commonly reported in the literature as 'doping agents', which are shown to attenuate the light activating properties of semiconductor materials through either surface or bulk loading scenarios. This project, however, will explore (with reference to **Scheme 1**), the 'how' and 'why' functionalised semiconductors accomplish higher photocatalytic activities. This has been addressed by studying the instrumental techniques used to probe the 'functionalised' semiconductor species.

Noble metals offer the unique contribution to semiconductor-mediated photocatalysis through absorption of itinerant electrons *via* harnessing of the metal's electronic cloud, known as surface plasmon resonance.[13]

Over the past decade, silver, gold, and platinum (Ag, Au, and Pt) have received in-depth photocatalytic investigations due to their ability to enhance photocatalysis reactions through intrinsic surface plasmon resonance properties.[14],[15],[16]

The surfaces' of adsorbed species (metallic Ag, Au or Pt) experience an enhanced photo-response in the electromagnetic field, which arises from the contact between the metal nanoparticle and the adsorbent's surface (*i.e.* titanium dioxide).[17] Furthermore, when the nanoparticles are within close proximity to the adsorbent's surface, they induce a plasmonic resonance to the surrounding particles with a synergistic effect of a dipole-dipole relationship existing between nanoparticles.[18] During the irradiation period, the synergy between a dielectric medium and metallic nanoparticles (which function as radiating antennae) mounted on the support is capable of creating a photoelectrical excitation in response to wavelength energies that match the unique radius of the nanoparticle.[19]

Coupling metallic nanoparticles and an electromagnetically activated metal oxide produce a solid-state material capable of 'visible-light-driven' photocatalytic functions (oxidation and reduction reactions). The selection of metal nanoparticle (silver or gold)

either favours ultraviolet (UV) or visible light activation, respectively, and are highly dependent on the size and shape of the nanoparticles.[20]

Studies have shown that controlled morphological growth of noble metal nanomaterials (size and shape [prisms, rods, spheres]) and monitoring preparation temperatures greatly affect the plasmonic wavelength's absorbance response.[17],[21],[22]

Non-metal species also offer the possibility to alter the band structure of semiconductors. In the process, extending exciton lifetimes, reducing electron-hole recombinations and attenuating away from ultraviolet light activation are all possible.[23],[24] As an example, nitrogen has demonstrated the ability to alter the valence band position of titanium dioxide and therefore enhance the visible light absorption capacity of the semiconductor.[25],[26]

In a co-doped titanium dioxide study (**Figure 2**), Kuvarega *et al.*[25] investigated the effects of nitrogen and palladium co-doped titanium dioxide (N/Pd doped TiO_2) towards the degradation of eosin yellow (eosin Y) dye under visible light irradiation. They observed significant shifts in the absorption profiles from the diffuse reflectance data (**Figure 2**). Nitrogen caused a slight blue shift at the cut-off wavelength of titanium dioxide's intrinsic band gap. However, electronic excitation from a mixed nitrogen/oxygen *2p* orbital state to Ti^{4+} and enhanced exciton charge separation from palladium (Pd:Ti 0.6 %) promoted an overall improved absorbance of incoming radiation compared to bare TiO_2 for eosin Y degradation.
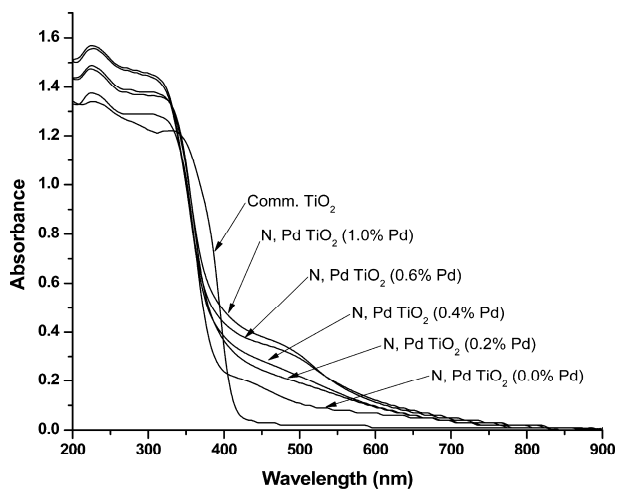
Figure 2: Co-doping TiO_2 with nitrogen and palladium. The graph demonstrates the red shifting wavelength effect of introducing extrinsic dopants (N and Pd) into TiO_2. Reprinted with permission from A. T. Kuvarega, R. W. M. Krause, B. B. Mamba, *J. Phys. Chem. C*, 2011, *115* (45), pp 22110–22120. Copyright (2011) American Chemical Society.

Subsequently, Kuvarega *et al.*[25] undertook powder diffuse X-ray studies and revealed that anatase was present as the dominant TiO_2 polymorph (**Figure 3**).

Comparable results have been reported elsewhere. Choudhury *et al.*[27] identified that titanium dioxide nanoparticles with numerous surface defects and amorphous grain boundaries induce stress fields that subsequently hindered anatase phase transformation to rutile. **Figure 3** depicts a uniform anatase presence (A) throughout each sample except N/Pd TiO_2 (0% Pd) where a small rutile (R) peak existed at 2θ of 26.2.
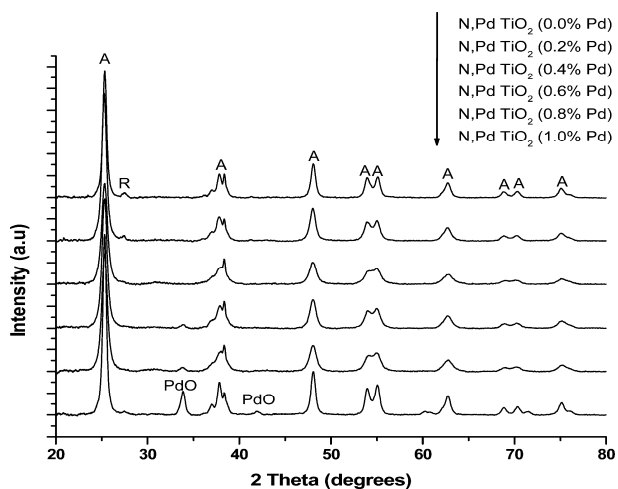
Figure 3: Powder X-ray diffraction spectra of anatase doped with nitrogen and palladium inhibiting rutile formation at higher palladium percentages (1.0% Pd). Reprinted with permission from A. T. Kuvarega, R. W. M. Krause, B. B. Mamba, *J. Phys. Chem. C*, 2011, *115* (45), pp 22110–22120. Copyright (2011) American Chemical Society.

The authors suggested that palladium was incorporated as palladium oxide (PdO) into TiO_2 interstitial lattice sites (**Scheme 1**, point 2) due to the large difference in atomic radii between Ti^{4+}(0.86 Å) and Pd^{2+} (0.68 Å).

Raman spectroscopic data (**Figure 4**) of N/Pd doped TiO_2 further suggested that palladium was interstitially doped into TiO_2 due to minimal molecular bond vibrational distortions within the TiO_2 lattice. Raman spectroscopy is a highly sensitive technique to detect molecular bond vibrations whereas powder X-ray diffraction is only suitable to probe lattice planes of crystalline materials at a structural order significantly higher than molecular bonds.[28]
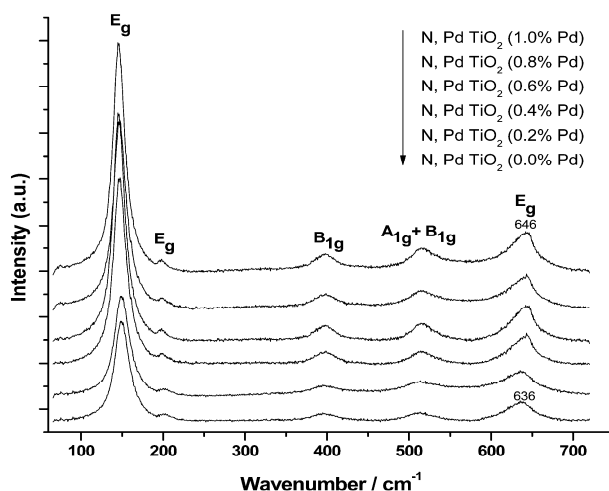
Figure 4: Spectroscopic Raman data of N/Pd-TiO$_2$ depicting the Eg, B$_1$g, A$_1$g+B$_1$g, and E$_g$ of TiO$_2$. Reprinted with permission from A. T. Kuvarega, R. W. M. Krause, B. B. Mamba, *J. Phys. Chem. C*, 2011, *115* (45), pp 22110-22120. Copyright (2011) American Chemical Society.

In further studies, Zhou *et al.*[29] also reported diffuse reflectance UV/Vis spectroscopic data of palladium doped TiO$_2$ (**Figure 5**). Both Pd and PdO doped TiO$_2$ from **Figure 5** image (a) and (b) revealed an extrinsic absorption tail after the 380 nm intrinsic band gap of TiO$_2$. However, **Figure 5** image (b) illustrates the absence of an extrinsic absorption tail on TiO$_2$ and rather an improved overall absorption profile extending into the infra-red region, which arises from the surface plasmonic effect of metallic palladium and not PdO. Zhou *et al.*[29] further reported the synthesis of Pd-and PdO-doped TiO$_2$ *via* a co-precipitation method to favour the production of surface-bound PdO and Pd species, instead of interstitially bound palladium.
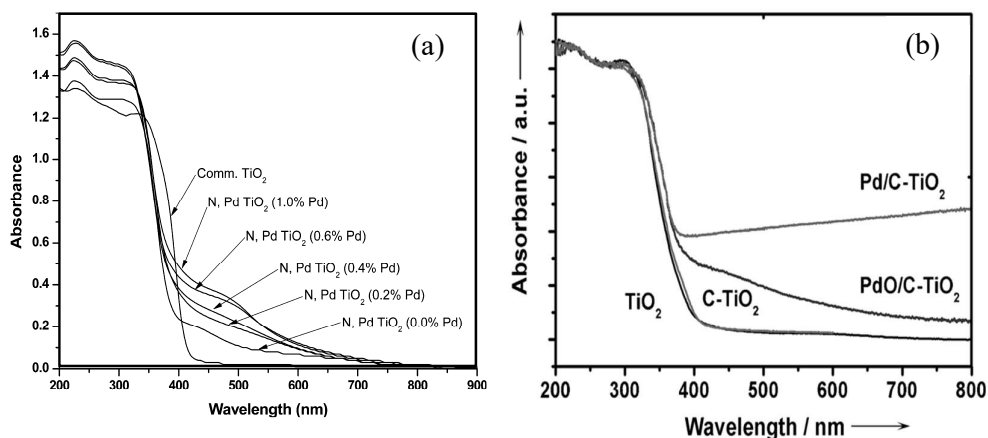
Figure 5: Diffuse reflectance data provided by *Kuvarega et al.* (image a) and *Zhou et al.* (image b).[25],[29] The inclusion of dopants (N and Pd) in image (a), and dopants (PdO and Pd/C) in image (b) demonstrate the absorbance shift of TiO_2 towards longer wavelengths. Reprinted with permission from A. T. Kuvarega, R. W. M. Krause, B. B. Mamba, *J. Phys. Chem. C*, 2011, *115* (45), pp 22110−22120 Copyright (2011) American Chemical Society. Reprinted with permission from W. Zhou, Y. Guan, D. Wang, X. Zhang, D. Liu, H. Jiang, J. Wang, X. Liu, H. Liu, S. Chen, *Chemistry, an Asian journal* 2014, *9*, pp 1648−1654. Copyright (1999−2018) John Wiley & Sons, Inc. All rights reserved.

The comparative texts by *Kuvarega et al.*[25] and *Zhou*[29] demonstrate whether the '*dopant*' is '*inserted*' into the crystal lattice of the semiconductor or whether surface metal oxides (PdO) are produced during the synthetic process and whether they are '*interstitially*' or '*surface*' bound to the metal oxide semiconductor.

Related studies on neodymium doped TiO_2 by *Nassoko et al.*,[30] which investigated the degradation of rhodamine-B dye using simulated solar radiation further demonstrates the concept of '*interstitial lattice*' doping. Powder X-ray diffraction data and Raman spectroscopic data identified the major vibrational modes belonging to anatase: 144.86, 398.17, 515.33 and 637.86 cm^{-1} with minor brookite signatures (24.22, 317.01, and 360.44 cm^{-1}) (see Raman spectrum in **Figure 6** below).

It was further disclosed that the first vibrational mode (E_g) of anatase (144.86 cm^{-1}) presented as a well-defined and sharp peak. This suggested that anatase had been prepared *in-situ* during the sol-gel synthetic process. However, after neodymium doping, the 144.86 cm^{-1} vibrational mode of titanium dioxide (anatase) had shifted to higher wavelengths (**Figure 6** image [B], curves [b] and [c]). The authors[30] proposed

that the small shifts in the E*g* mode (144.86 cm^{-1}) was an indication that titanium dioxide was functionalised with neodymium, either interstitially or substituted for titanium cations. A higher concentration of neodymium (**Figure 6** image [B], the red curve (b) depicts a Ti:Nd ratio of 23:1) also induced a higher wavenumber shift of the 144.86 cm^{-1} peak, which indicated a further extent to which, titanium dioxide was functionalised with neodymium compared to **Figure 6** image [B], green curve (c) with a Ti:Nd ratio of 11:1.
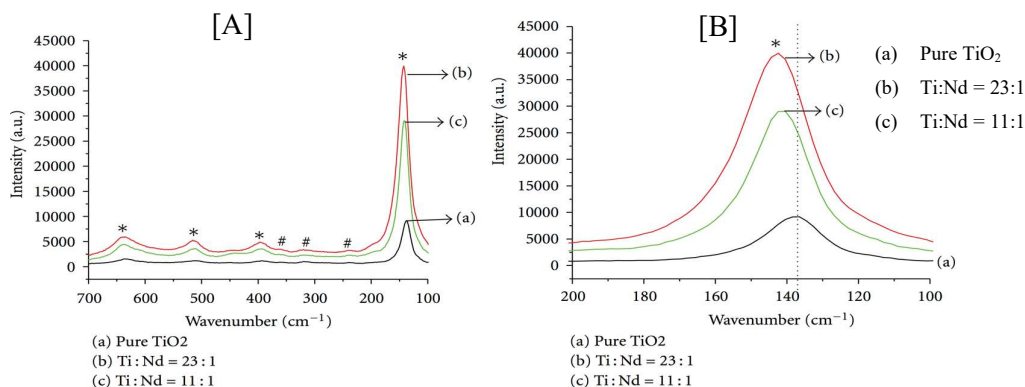
Figure 6: Raman spectroscopic data of Nd doped TiO$_2$ prepared from *sol-gel* methods ([image A]). The inset of the 100−200 cm^{-1} region ([image B]) depicts the small shifts in the E$_g$ mode of TiO$_2$. Reprinted with permission from D. Nassoko *et al.*[30] Copyright 2012.

Diffraction peak data for (101) [anatase] and (121) [brookite] (Joint Committee of Powder Diffraction Standards [JCPDS] card no. 21−1272) presented a slight small-angle shift after functionalising titanium dioxide with neodymium during initial preparations (**Figure 7**).
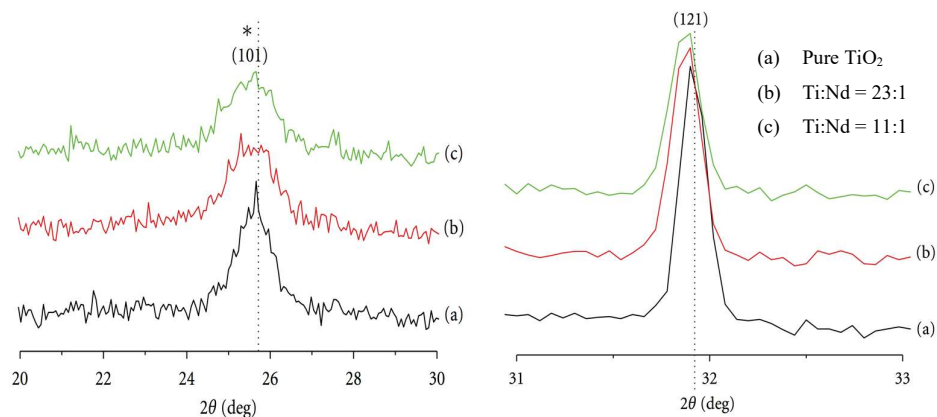
Figure 7: Diffraction data of Nd doped TiO_2 illustrating the small angle shift within intrinsic TiO_2 anatase (left image) and brookite (right image) for the (101) and (121) peaks, respectively. Reprinted with permission from D. Nassoko *et al.*[30] Copyright 2012.

The authors stated that neodymium incorporation was believed to occur interstitially, or lattice bound. However, the ionic radius of Nd^{3+} (0.11 nm) is appreciably larger than Ti^{4+} (0.064 nm). Significant lattice distortions from ionic radii mismatch between Nd^{3+} with Ti^{4+} species would suggest the preferentially interstitial incorporation of neodymium into titanium dioxide's lattice (**Scheme 1**, point 2) as Nd-O-Ti species.[31]

Recent studies have shown that intrinsic defects within semiconductor lattices greatly enhance the photo-redox abilities of the semiconductor. Fan *et al.*[32] have reviewed reduced Ti^{3+} on TiO_2 as a capable species of enhancing methylene blue decomposition while hindering the photo-driven production of gaseous hydrogen. Pan *et al.*,[33] also discussed the photo-oxidation of alcohol derivatives using metal (Ag, Pt, or Pd) functionalised titanium dioxide (Degussa P25). The metallic nanoparticles were loaded onto titanium dioxide through a pre-irradiative cycle of titanium dioxide with benzyl alcohol. The presence of benzyl alcohol produced oxygen vacancies, which in turn initiated the reduction and precipitation of metal salts onto the surface of titanium dioxide. A 'yellow powder' was reported after the oxidative cycle was complete. The authors studied the oxygen vacancies in yellow P25 TiO_2 using powder X-ray diffraction and identified the anatase 2θ peak values and crystal planes of 25.3 (101), 37.8 (004), 48.0 (200), 53.9 (105), 55.1 (211), 62.7 (204), 68.8 (116), 70.3 (220), and 75.0 (215), with a small contribution from rutile 27.4 (110). They[33] also disclosed that X-ray photoelectron spectroscopy data revealed no change in oxidation state to Ti^{4+}

cations, while X-ray diffractograms supported the predictions of Ag, Pt or Pd's absence from titanium dioxide's lattice. However, with the sensitivity of Raman spectroscopy to detect symmetrical bending and stretching vibrations (O-Ti-O) in TiO$_2$, a statement supporting the lattice state of TiO$_2$ with oxygen vacancies would have greatly elevated their research.[34]

Another useful technique to qualify the morphological structure of a semiconductor (scanning electron microscopy [SEM]) and provide information pertaining to the specific lattice spacings of the desired material (transmission electron microscopy [TEM]) is electron microscopy. Yu *et al.*[35] monitored the photo-catalytic decomposition of methyl orange, rhodamine B, and eosin B under a simulated solar spectrum after the development and application of dendritic cadmium sulfide assemblies (**Figure 8**).
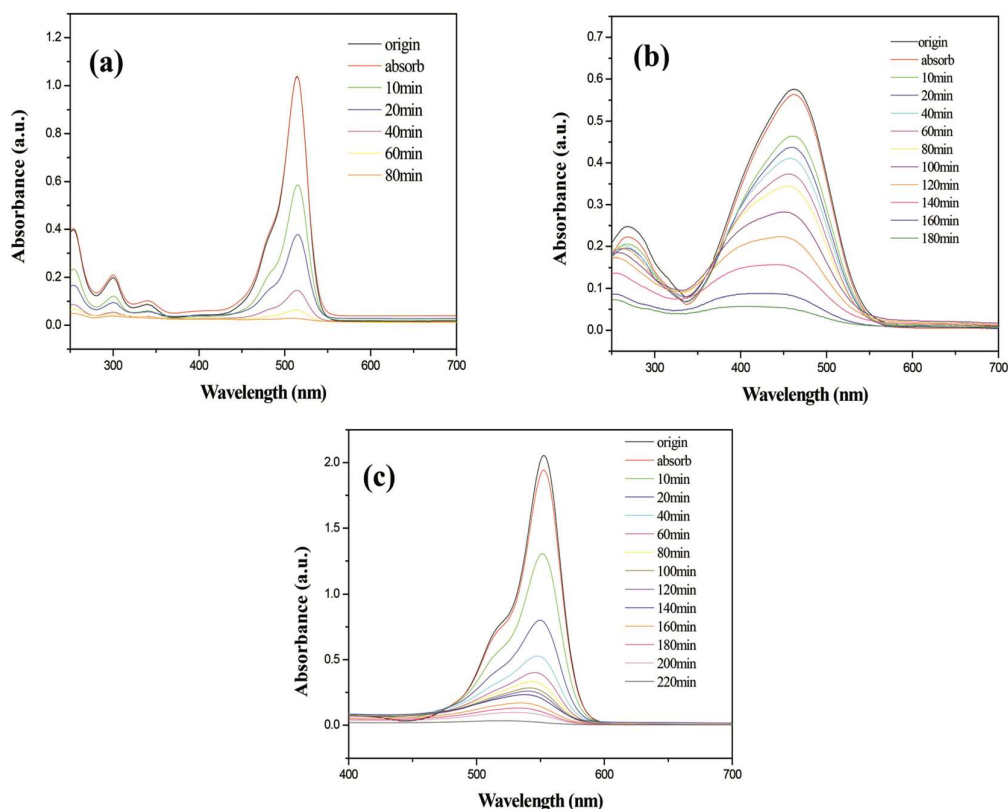
Figure 8: The photo-degradation timelines of (image a) eosin B, (image b) methyl orange and (image c) rhodamine B in the presence of dendritic cadmium sulfide assemblies under visible light irradiation. Adapted from Z. Yu, F. Qu, X. Wu, Dalton Trans., Copyright (2014), 43, 4847−4853, with permission of The Royal Society of Chemistry.

Figure 8 presents the photocatalytic decomposition of eosin B (99 % after 80 minutes, image a), methyl orange (92 % after 180 minutes, image b) and rhodamine B (> 97 % after 220 minutes, image c) while using dendritic cadmium sulfide under visible light irradiation. When fabricating novel photocatalysts, researchers focus on size and shape to ensure the highest photo-catalytic response of their newly formulated semiconductors.[36] The efficiency and compatibility of the cadmium sulfide towards the photo-degradation of three organic dyestuffs were subsequently explored using SEM analyses to probe the morphology of the cadmium sulfide surface (**Figure 9**).
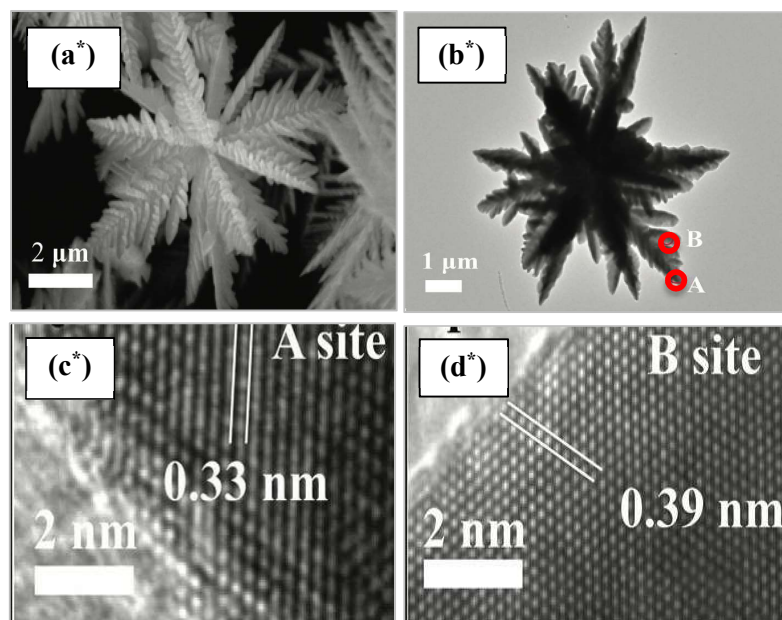
Figure 9: Dendritic structure of CdS (SEM images a*, b*). HRTEM micrographs with lattice *d*-spacings (images c* and d*) were taken at sites A and B on image b*. Adapted from Z. Yu, F. Qu, X. Wu, Dalton Trans., Copyright (2014), 43, 4847−4853, with permission of The Royal Society of Chemistry.

Figure 9 demonstrates the potential of high-resolution transmission electron microscopy (HRTEM) to differentiate the various crystallographic planes of a solid-state material in heterogeneous photocatalysis. **Figure 9** (image c*) and (image d*) represents the circled regions in **Figure 9** (image b*) for the cadmium sulfide trunk and dendrite respectively. The recorded lattice values of 0.39 and 0.33 nm correlate to the crystal plane data and furthermore characterise the spacing between two {1010} and two [0001] crystal planes, respectively. High-resolution transmission

electron microscopy has been well reported in the literature as a reliable technique to aid in identifying the crystallographic phases of TiO_2,[37],[38],[39] ZnO,[40] and ZnO_2[41] through the identification of unique lattice *d-spacings* for each polymorph, respectively.

While semiconductor nanoparticles have exemplified promise in organic dyestuff decomposition studies, they also offer the unique ability for the photo-oxidation of alcohols under visible light activation. When a semiconductor is functionalised with either Ag, Au, or Pt and exposed to a visible light source ($\lambda \geq 420$ nm), intraband electron excitations occur (Ag: *4d −> 5sp*; Au: *6sp −> sp* conduction band (CB) (principal quantum number was not defined) and Pt: *5d −> 6sp* conduction band).[42],[43] Preceding the photo-activation of the nanoparticle, electron transfer into the conduction band of the metal oxide support resolves two redox processes simultaneously. The freely available positive holes (h^+) in the metal nanoparticles are capable of performing alcohol oxidations, as graphically summarised below (direct photocatalysis, **Figure 10**, route a); meanwhile the electrons transferred to the metal oxide's conduction band are captured by a terminal electron acceptor (molecular oxygen for example), whereby the production of superoxide radicals act as secondary oxidising agents for alcohol oxidations (indirect photocatalysis, **Figure 10**, route b).[44]
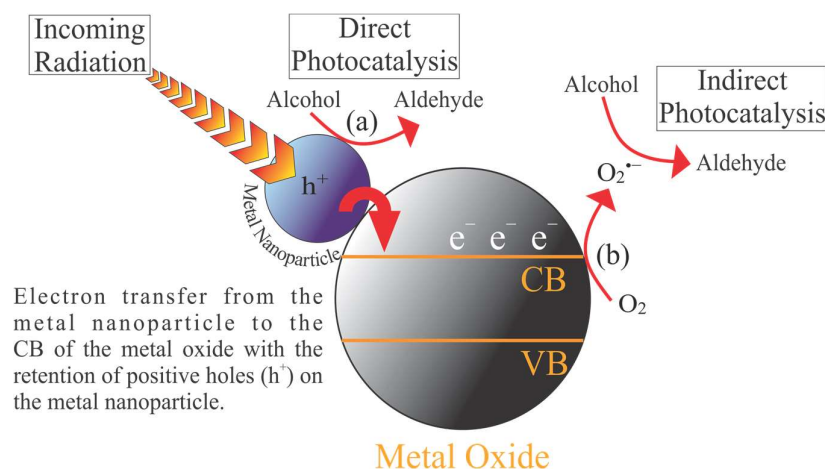
Figure 10: Representation of the dual component action of photoredox chemistry on semiconductor surfaces *via* direct (a) or indirect (b) photocatalytic routes.

However, to ensure an efficient synergy between metal nanoparticle and metal oxide support, the 'Schottky Barrier' (denoted as Φ_B in **Figure 11**) formed between the metal/semiconductor heterojunction needs to be assessed (**Figure 11**).[43]
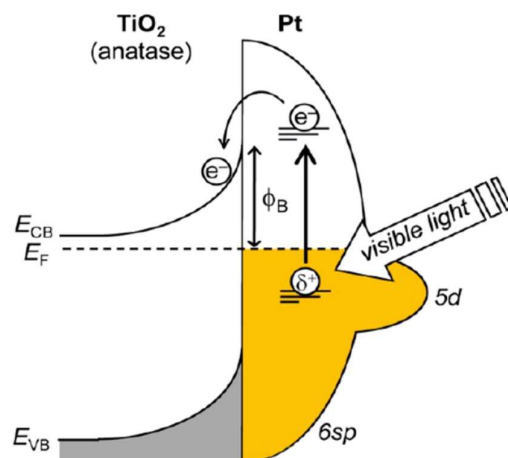
Figure 11: Schottky Barrier existence across platinum and titanium dioxide's surface. Once the Schottky barrier is overcome, electrons (e$^-$) from platinum relax into the conduction band (E$_{CB}$) of TiO$_2$. Reprinted with permission from Y. Shiraishi, H. Sakamoto, Y. Sugano, S. Ichikawa, T. Hirai, *ACS Nano* 2013, *7*, 9287−9297. Copyright (2013) American Chemical Society.

Sufficient energy to overcome the Schottky Barrier is required for electron ejection from the metal (dopant species) into the conduction band of the chosen semiconductor (here titanium dioxide as mentioned above). After the Schottky Barrier has been surpassed, electron ejection and hence exciton recombination quenching occurs due to the limited back electron transfer.

Three physical parameters (Schottky Barrier [Φ_B], work function$_{metal}$ [W$_{metal}$] and electron affinity$_{semiconductor}$ [E$_{EA}$]) govern how successful a metal functionalised semiconductor system proceeds. After creating an interface between a semiconductor and a metal ion (refer to **Scheme 1**), orbital band bending between the semiconductor and metal occurs due to a compulsory dipole field effect at the semiconductor-metal boundary. In order for an electron to be subsequently transferred from the metal to the semiconductor, the height of the Schottky Barrier (Φ_B) has to be overcome. The Schottky Barrier is defined as the difference of the metal's work function (W$_{metal}$, energy requirement to remove an electron from the metal's surface to vacuum) and the electron affinity of the semiconductor (E$_{EA}$, the accumulated energy gathered after an electron positioned within the vacuum level of the semiconductor moves to the

conduction band). In-depth knowledge of Schottky Barriers has been well reported in the physics domain.[45],[46],[47]

The area of field effect transistors (FET) is beyond the scope of this review. However, in 2016, Kim *et al.*[48] published details of a metal oxide semiconductor field effect transistor (MOSFET) with n-channel germanium. Relevant information within their research was noted to pertain to this review on heterogeneous semiconductor mediated photocatalysis. They noted while attempting to construct a titanium-germanium contact that Fermi level pinning and a large Schottky Barrier were formed. In an effort to overcome the restriction induced by the Schottky Barrier, which was impeding electron flow between the metal contact and germanium surface, a metal-interface-semiconductor film was introduced to remediate this limitation. The metal-interface-semiconductor was tested after the introduction of an optimal 2 nm TiO$_2$ film between the Ti and Ge surfaces (**Figure 12**).
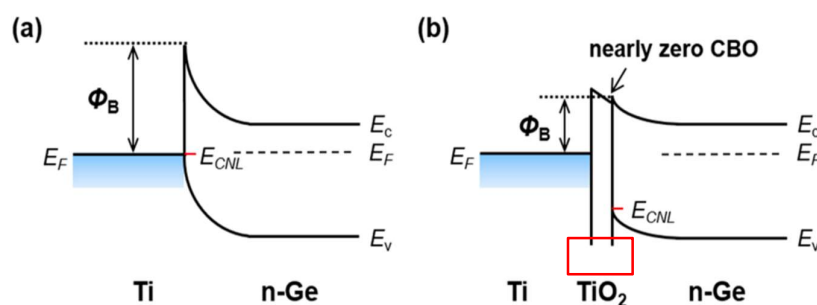
Figure 12: Insertion of TiO$_2$ film in-between the Ti/Ge films to lower the Schottky Barrier. Reprinted with permission from G.-S. Kim, S.-W. Kim, S.-H. Kim, J. Park, Y. Seo, B. J. Cho, C. Shin, J. H. Shim, H.-Y. Yu, *ACS Applied Materials & Interfaces* 2016, *8*, 35419−35425. Copyright (2016) American Chemical Society. (Note, CBO above: 'Conduction band offset').

The TiO$_2$ semiconductor thin film was noted to drastically reduce the Schottky Barrier height (**Figure 12** [image b]) due to the relaxation of the Fermi level of titanium towards the charge neutrality level (Note E$_{CNL}$ in **Figure 12**) that arose from the near proximity to its conduction band edge. Furthermore, the authors identified that the addition of a 1 nm thick GeO$_2$ layer introduced a perfect ohmic contact between the Ti and *n*-Ge layers.

In 2013, Shiraishi and co-workers[43] attempted to determine the optimised Schottky Barrier conditions of a two-component metal nanoparticle system (copper [Cu] and platinum [Pt]) loaded on anatase for the oxidation of alcohols to aldehydes. Copper and platinum with known work functions of the bulk material (4.65 and 5.65 eV respectively)[49] are capable of alloying to create a lowered binding energy of the Cu/Pt dopant species hence lowering the Schottky Barrier for electron ejection into the conduction band of titanium dioxide.

After inspecting the TEM results, the Cu/Pt alloy particles of the (111) diffraction plane with lattice spacing (0.223 nm) were reported by the authors[43] to exist between those of platinum (111, Joint Committee of Powder Diffraction Standards [JCPDS] card no. 04−0802, 0.226 nm) and copper (111, JCPDS no. 04−0836, 0.209 nm) nanoparticles. The microscopic analysis concluded the formation of a solid-state homogeneous alloy of Cu/Pt nanoparticles (**Figure 13**).
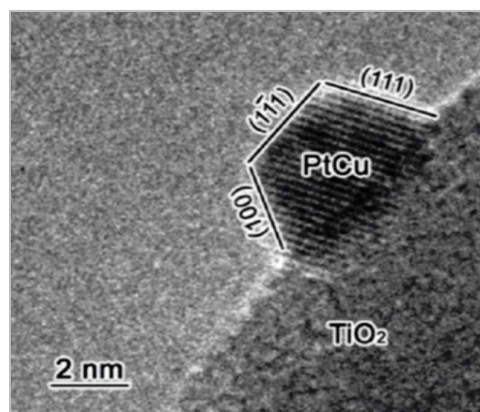
Figure 13: Observable (111) Cu/Pt alloy nanoparticles surface bound to TiO_2 under TEM imagery. Reprinted with permission from Y. Shiraishi, H. Sakamoto, Y. Sugano, S. Ichikawa, T. Hirai, *ACS Nano* 2013, *7*, pp 9287−9297. Copyright (2013) American Chemical Society.

The result of alloying a $Pt_{0.8}/Cu_{0.2}$ mixture onto the surface of anatase favoured a 200 % increase in benzaldehyde production (18 μmol) compared to Pt/TiO_2 (9 μmol) and Cu/TiO_2 (no detectable benzaldehyde) after 4 hours visible light irradiation. The authors' justification for enhanced photocatalytic reactivity was the effect of a decreased work function of platinum from copper alloying. Similar findings have been reported elsewhere on work function lowering from metal alloying.[50] The outcome

was an inhibited electron ejection and improved alcohol oxidation efficiency. The authors noted that the alloying system ($Pt_{0.8}/Cu_{0.2}$) produced the highest concentration of superoxide anion ($O_2^{\bullet-}$) on the surface of anatase and was the primary oxidant of benzyl alcohol to benzaldehyde in the photocatalysed mechanism. $O_2^{\bullet-}$ was later confirmed with electron paramagnetic resonance (EPR) spectroscopy (**Figure 14**).

Electron paramagnetic resonance spectroscopy is useful to detect unpaired electrons in paramagnetic species, especially in semiconductor-mediated systems that produce superoxide ($O_2^{\bullet-}$) and hydroxyl radicals ($^{\bullet}OH$) (singly un-paired electrons) as terminal oxidants for dye degradations and redox transformation studies. The detection of the transient paramagnetic species usually requires the use of a radical trap, *i.e.* 5,5-Dimethyl-1-pyrroline *N*-oxide (DMPO). The radical trap captures the free electron species as (DMPO-$^{\bullet}OH$ and DMPO-$O_2^{\bullet-}$), which makes the detection viable.

Shiraishi *et al.*[43] studied superoxide radical production on the surface of $Pt_xCu_yTiO_2$ in the presence of oxygen gas and xenon light irradiation (**Figure 14**). The existence of electromagnetic resonance signatures was detected on a Bruker EMX-10.12 spectrometer. Black background peaks (at g-factor value [g] = 2.001 and 2.029) on each curve represent singlet oxygen species ([O^-], produced under dark conditions in the presence of $Pt_xCu_yTiO_2$).
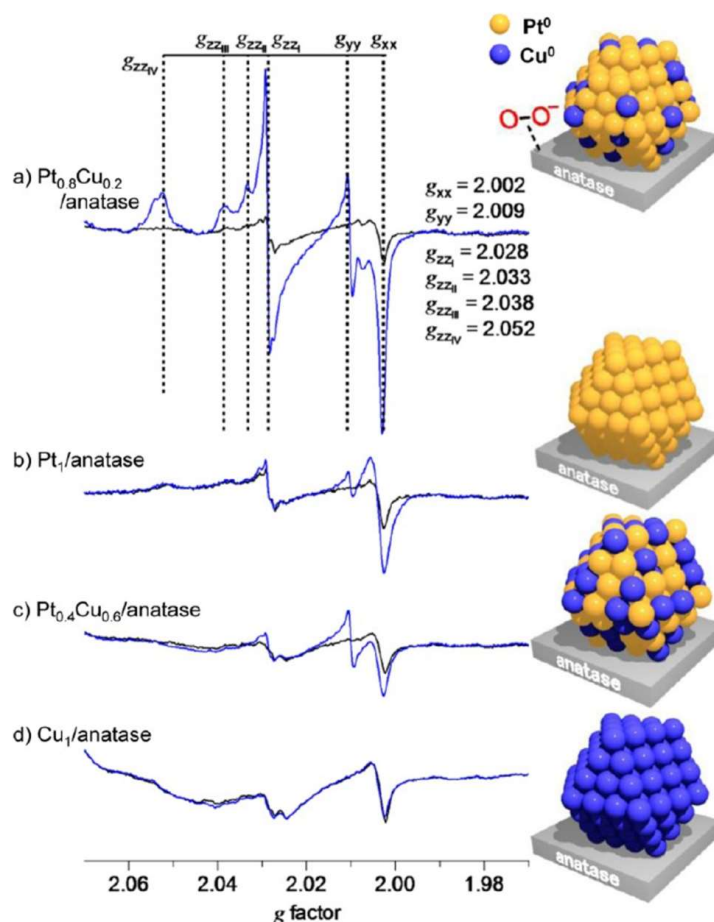
Figure 14: Electron paramagnetic resonance study for the detection of peroxide radical production on Cu/Pt-TiO$_2$. Reprinted with permission from Y. Shiraishi, H. Sakamoto, Y. Sugano, S. Ichikawa, T. Hirai, *ACS Nano* 2013, *7*, pp 9287−9297. Copyright (2013) American Chemical Society.

Meanwhile the blue forefront peaks (g_{xx} = 2.002, g_{yy} = 2.009, g_{zzI} = 2.028, g_{zzII} = 2.033, g_{zzIII} = 2.038, and g_{zzIV} = 2.052) were indicative of superoxide ion formation. It was evident that the platinum and copper ratio greatly influenced the superoxide ion production. Pt$_{0.8}$Cu$_{0.2}$TiO$_2$ (**Figure 14**, curve a) produced the highest superoxide ion response whereas Pt/TiO$_2$, Pt$_{0.4}$Cu$_{0.6}$TiO$_2$ and Cu/TiO$_2$ were significantly lower (**Figure 14**, curves b, c and d).

DMPO-·OH and DMPO- O$_2$·⁻ production has also been reported in the literature from tin (Sn) and nitrogen (N) doped TiO$_2$ (SNT) during investigations to degrade rhodamine

B and photocatalytically produce molecular hydrogen.[51] Various Sn/N doped TiO_2 samples were prepared at different calcination temperatures (400, 500, and 550 ˚C). Studying the evolution of terminal oxidants ($^{\bullet}OH$ and $O_2^{\bullet-}$) produced from the SNT under irradiative conditions revealed that $O_2^{\bullet-}$ was preferentially formed on SNT when calcinated at 500 ˚C. Notice SNT-500 in **Figure 15** below.
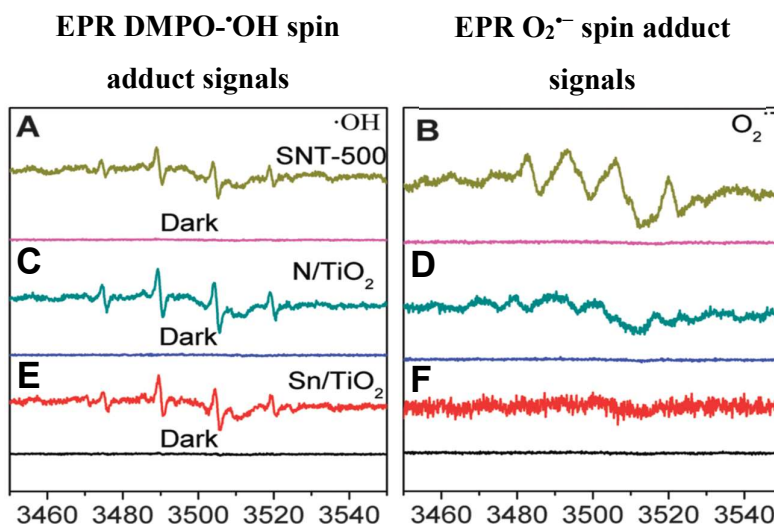
Figure 15: Controlled DMPO-hydroxyl (DMPO-$^{\bullet}OH$, left) and DMPO-superoxide (DMPO- $O_2^{\bullet-}$, right) radical production with visible light irradiation on SNT-500 (calcinated at 500 ˚C) (A and B), N/TiO_2 (C and D), and Sn/TiO_2 (E and F). The radicals were detected using EPR spectroscopy. Reproduced from H. Zhuang, Y. Zhang, Z. Chu, J. Long, X. An, H. Zhang, H. Lin, Z. Zhang, X. Wang, *Physical Chemistry Chemical Physics* 2016, *18*, 9636−9644 with permission from the PCCP Owner Societies.

Obata *et al.*[52] took advantage of paramagnetic Fe^{3+} to detect substitutional-bound iron and iron surface loaded species in TiO_2. Their studies investigated the effects of platinum- and iron-doped TiO_2 for the photocatalytic decomposition of ammonia (NH_3) into hydrogen (H_2) and nitrogen (N_2) gases. Due to the mid band gap incorporation of Fe^{3+} into TiO_2, visible light sensitivity was possible for ammonia decomposition. A *g*-value (2.08) corresponding to surface-bound Fe^{3+} spin ($S = 5/2$) on anatase TiO_2 was detected *via* electron paramagnetic studies, *albeit* very weak. However, the method of calcinating Fe_2O_3 with TiO_2 afforded Fe^{3+} that was substituted for Ti^{4+} and bound within the rutile lattice; corresponding g = values (2.63, 3.37, 5.63, and 8.31). Additional studies (Cu^{2+} and Ag^{2+}) have also demonstrated favourable substitutional

functionalisations of titanium dioxide together with Fe^{3+} due to similar atomic radii. However europium's (Eu^{3+}) incompatible atomic radius *vs* Ti^{4+} (0.6 Å *vs* 0.95 Å) hinders the process due to excessive compressive strains.[53]

Sakamoto *et al.*[54] have demonstrated the significance of coupling two d-block metals (platinum and palladium) to form an alloy with the potential to overcome Fermi level restrictions of platinum alone, for the dehalogenation of aromatic halides using hydride ions on the surface of Pt-Pd/Ta_2O_5 nanoparticles.

During Sakamoto and co-workers[54] study of Pt-Pd/Ta_2O_5, platinum and palladium formed an alloyed synergy on Ta_2O_5 that facilitated the decomposition of aromatic halides. In the absence of the coupling platinum and palladium, platinum's *d*-band centre was located below the Fermi level of the H-Pt transient state (σ^*) on Ta_2O_5 (alcoholic solutions were used as a source of hydride ions). Consequently, platinum supported unfavourably molecular hydrogen (H_2) generation. However, palladium was identified to possess an electrochemical overpotential above H-Pt, thereby alloying platinum and palladium preserved the surface-bound hydride ions for the dehydrogenation of aryl halides (**Figure 16**).
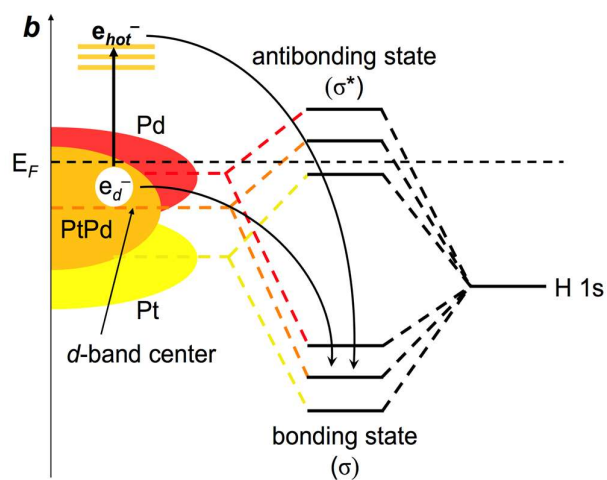
Figure 16: Molecular orbital energy states of hydrogen-metal bonding on the Pt-Pd/Ta_2O_5 surface with subsequent hot electron migration into the bonding state of hydrogen. Reprinted with permission from Y. Shiraishi, H. Sakamoto, Y. Sugano, S. Ichikawa, T. Hirai, *ACS Nano* 2013, *7*, pp 9287−9297. Copyright (2013) American Chemical Society.

Despite the Schottky Barrier enhancing the wide band gap semiconductor's response to absorbing visible light through metal functionalisation, an improved visible-light activated photocatalytic material is vulnerable to lowered photocatalytic efficiencies if metal deactivation processes occur. This can happen after deterioration (*i.e.* oxidation) of the metallic species, thus altering the bonding synergy between the semiconductor and metal. However, the stability of the Schottky Barrier can be preserved when metal/semiconductor barrier methods are considered. Metal nanoparticle encapsulation offers the approach to safeguard metal species from surface bleaching and leaching during catalytic recycling.[55] Zhang *et al.*[56] reported an environmentally friendly route to encapsulate platinum nanoparticles within cerium dioxide (Pt-CeO$_2$) in both yolk and core-shell structures (**Figure 17**).
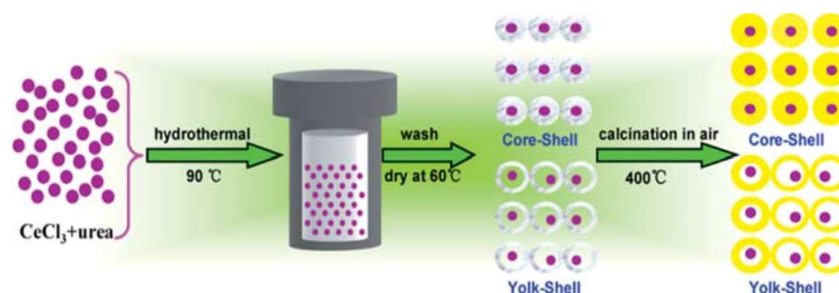
Figure 17: Synthesis of platinum nanoparticles (purple circles) encapsulated within core-shell or yolk-shell CeO$_2$ (yellow rings). Reprinted with permission from N. Zhang, X. Fu and Yi-J. Xu, *J. Mater. Chem.*, 2011,21, pp. 8152−8158. Copyright (2011) Royal Society of Chemistry.

Zhang *et al.*[56] investigated platinum's encapsulation within CeO$_2$ using electron microscopy (SEM and HRTEM, **Figure 18**) and X-ray photoelectron spectroscopy (XPS). The purpose of the encapsulation was to contrast the effect of housing platinum nanoparticles within cerium dioxide in either a core-shell or yolk-shell configuration (**Figure 17**) for the selective oxidation of benzyl alcohol to benzaldehyde. Zhang and co-workers[56] discovered that the core-shell configuration offers superior selective oxidation of benzyl alcohol to benzaldehyde when compared to yolk-shell Pt@CeO$_2$. The enhanced photocatalytic properties of core-shell Pt@CeO$_2$ are attributed to greater interfacial charge transfer kinetics of the material to transport photogenerated electrons and furthermore store the electrons more effectively in the core-shell configuration opposed to the yolk-shell.
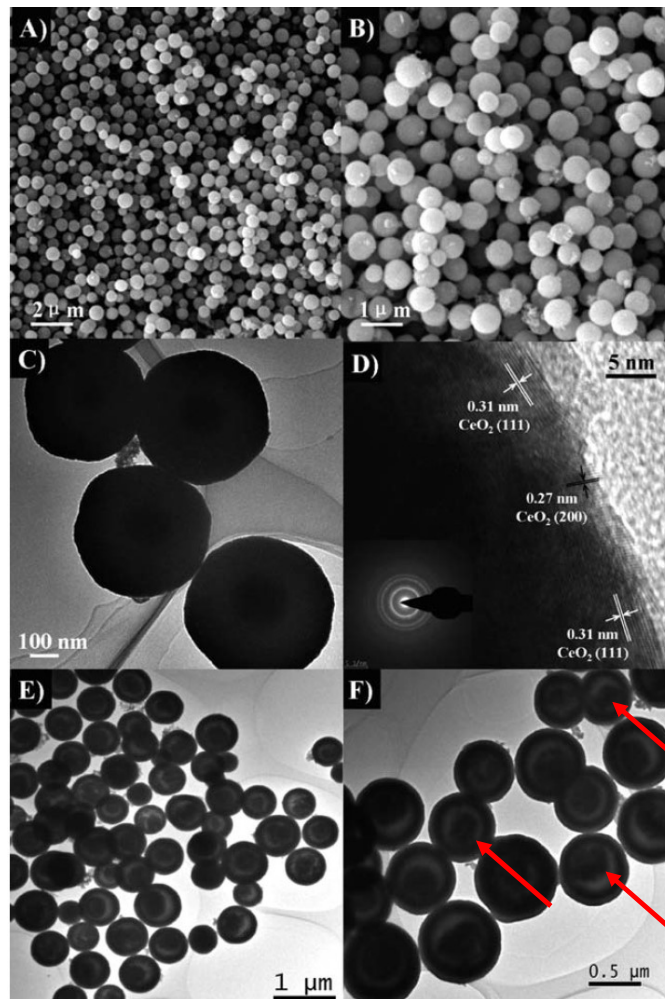
Figure 18: Microscopic analysis of platinum encapsulated cerium dioxide. Note the red arrows point to platinum nanoparticles encapsulated within cerium dioxide spheres. Reprinted with permission from N. Zhang, X.Fu and Yi-J. Xu, *J. Mater. Chem.*, 2011,21, pp. 8152−8158. Copyright (2011) Royal Society of Chemistry.

As depicted in **Figure 18**, images A) and B), spherical ball-like micron materials were observed using scanning electron microscopy (SEM). However, it was only from the application of HRTEM in **Figure 18**, images E) and F) that the authors[56] were able to observe platinum encapsulated within CeO_2 as illustrated by the red arrows in **Figure 18**, image F).

With the application of X-ray photoelectron spectroscopy (XPS), Zhang *et al.*[56] attempted to detect encapsulated platinum within CeO_2. XPS analyses are typically studied with either an Al K_α (1486.6 eV) or Mg K_α (1253.6 eV) X-ray monochromator source. The nature of

surface detection using XPS permits the applicator to detect photoelectron emissions from individual species that possess unique signatures based upon their kinetic energies when leaving the sample surface. XPS has the potential to detect and identify surface characteristics and chemical states (oxidation number) of surface species.[57] However, due to the nature of solid substances, free electrons only exist within the top few surface atomic layers. The authors[56] claimed that platinum would enhance the photocatalytic efficiency of CeO_2 towards selectively oxidising alcohols. However, as the encapsulated shell exceeded the detection depth-limit of 10 nm, no such data were obtainable.[56]

The significance of identifying surface components for the characterisation of complex mixed metal oxide systems can be highly advantageous to validate the expected outcomes from the chosen synthetic procedure for the desired semiconductor and required photo-reactivity. In a text by Balachandran *et al.,*[58] an attempt to synthesise Ag-ZnO-CdO for the photocatalytic decomposition of acid violet and acid black was investigated. In their synthetic method, Ag-ZnO-CdO was prepared from an oxalic acid precipitation-hydrothermal/calcination technique to prepare nanomaterials (clusters, and hexagonal sheets).

The collection of X-ray photoelectron spectroscopic binding energies confirmed the presence of four compounds in the Ag-ZnO-CdO system. Two different binding energies for oxygen (α-531.1 eV and β-533.2 eV) were identified to exist as ZnO/CdO lattice oxygen species (α-phase) and hydroxyl groups as chemisorbed surface oxygen.[57] Furthermore, reported binding energies for the oxidation states of Zn^{2+} and Cd^{2+} confirmed the formation of ZnO and CdO (Zn $2p_{1/2}$ [1045.2 eV], Zn $2p_{3/2}$ [1022.2 eV], Cd $3d_{3/2}$ [412.1 eV] and Cd $3d_{5/2}$ [405.3 eV]).[57] Lastly, X-ray photoelectron spectroscopy identified signature binding energies assigned to metallic silver at Ag $3d_{3/2}$ and Ag $3d_{5/2}$ (374.5 and 368.4 eV respectively). Silver oxides were reportedly absent due to the lack of binding energies above 374 eV.[58]

In efforts to enhance the visible light absorption efficiency of titanium dioxide and achieve alcohol oxidations, Pan and Xu[33] prepared Degussa P25 TiO_2 with oxygen vacancies through pre-irradiating a mixed suspension of benzyl alcohol and Degussa P25 TiO_2 in trifluorotoluene. The purpose of pre-irradiating Degussa P25 TiO_2 was to create surface oxygen vacancies *via* the action of benzyl alcohol oxidation from the

presence of surface lattice oxygen atoms on TiO_2. The surface oxygen vacancies were subsequently used to reduce metallic ions onto the surface of TiO_2.

To ensure that the postulated mechanism of deposited metal ions onto TiO_2 was correct, XPS was utilised to detect and quantify the various oxidation states of the elemental species bound to the doped TiO_2 surfaces. Characteristic peaks for Ag *3d*, Pt *4f*, and Pd *3d* were evident from the respective spectra. However, it was unclear whether the dopants loaded onto the TiO_2 were metallic or ionic. Therefore, using high resolution X-ray photoelectron spectroscopy (HR XPS), the authors identified the oxidation state of the three metals. Silver, platinum and palladium spectra revealed Ag, Pt, and Pd peaks: Ag *3d$_{5/2}$* and Ag *3d$_{3/2}$*, Pt *4f$_{7/2}$* and Pt *4f$_{5/2}$*, and Pd *3d$_{5/2}$* and Pd *3d$_{3/2}$* with their respective binding energies (368.0 & 374.0 eV), (70.5 & 73.9 eV) and (334.6 & 339.9 eV). These results confirmed that the metal ions that had been implanted onto the surface of TiO_2 were reduced during initial preparations.

After loading the noble metals (Ag/Pt/Pd) onto the surface of TiO_2 with oxygen vacancies (TiO_2-OV), benzyl alcohol was further introduced as a test substrate to assess the oxidative potential of the metal-doped TiO_2 under visible light irradiation. Pd-TiO_2-OV produced the highest alcohol to aldehyde conversion efficiency (fourteen times greater than TiO_2-OV), Pt-TiO_2-OV (six times higher greater than TiO_2-OV) and Ag-TiO_2-OV (two times greater than TiO_2-OV).

In an attempt to understand why Pd-TiO_2-OV was superior, Pan and Xu[33] investigated Ag, Pt, and Pd doped TiO_2 with photoluminescence spectroscopy (**Figure 19**). Photoluminescence studies of Ag, Pt, and Pd functionalised TiO_2 were conducted on an Edinburgh FL/FS 900 spectrophotometer to detect peak height variation of pure and functionalised titanium dioxide.
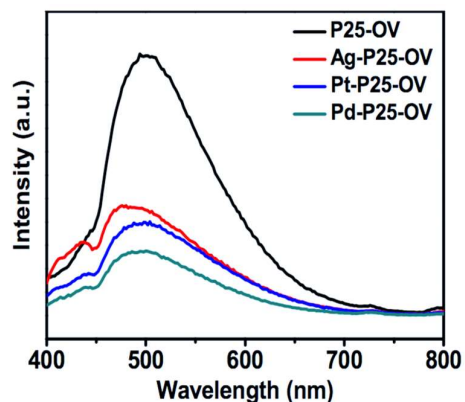
Figure 19: The reported photoluminescence spectra of Ag, Pt, and Pd doped TiO_2 with oxygen vacancies, which demonstrate the enhanced charge separation (lower peak intensities) within titanium dioxide after metal ion incorporation. Reprinted with permission from X. Pan and Yi-J. Xu, *J. Phys. Chem. C*, 2013, *117* (35), pp 17996–18005 Copyright (2013) American Chemical Society.

Figure 19 has illustrated the peak responses of photo-excited Pd-TiO_2-OV, Pt-TiO_2-OV, and Ag-TiO_2-OV to a 365 nm excitation wavelength. The intensities of the respective peaks provided an indication of the overall charge separation efficiency within the M-TiO_2-OV samples (M = Pd, Pt and Ag).[33] The lower the peak intensity, the greater the charge separation within the semiconductor and hence an improved photocatalytic activity. Larger peak intensities demonstrated increased photon emission, which arose from electron-hole (exciton) recombination. Pd-TiO_2-OV produced the lowest peak intensity signal of the three M-TiO_2-OV (M = Ag, Pt or Pd) species. The lowest peak intensity confirmed that Pd-TiO_2-OV had the largest exciton separation and greatest visible light absorption efficiency, thus the highest overall photo-redox potential for benzyl alcohol oxidation.

1.2.2. Surface Loading of Semiconductors using Organic Dyes.

Fine-tuning a multi-component semiconductor system towards visible light sensitivity is of great interest to materials scientists and chemists. Furthermore, applying dye-sensitised semiconductors towards alcohol oxidation studies offers an environmentally friendly approach for the synthesis of valuable feedstock aldehydes and ketones.

In 2008, Zhang *et al.*[9] investigated alcohol oxidations using alizarin red-sensitised titanium dioxide. The synergetic band alignment between alizarin red and titanium dioxide facilitated the reaction's oxidant, 2,2,6,6-tetramethylpiperidinyloxyl radical (TEMPO), to complete the oxidative cycle of alcohols to aldehydes (**Figure 20**).
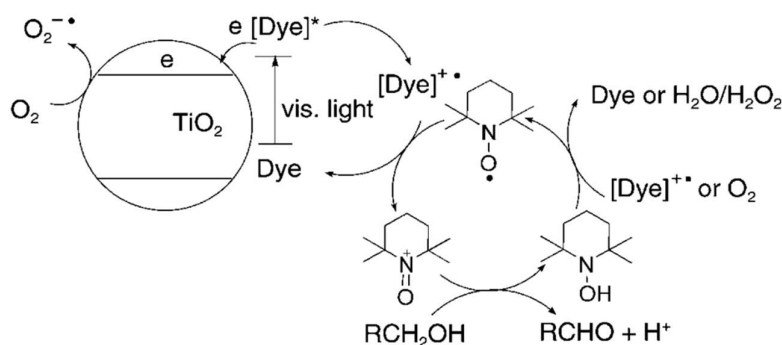
Figure 20: The proposed mechanistic route for alcohol oxidations which used alizarin red-sensitised titanium dioxide. Reprinted with permission from M. Zhang, C. Chen, W. Ma, J. Zhao, *Angewandte Chemie International Edition* 2008, *47*, pp 9730−9733. Copyright (1999−2018) John Wiley & Sons, Inc. All rights reserved.

In later research, Jeena *et al.*[59],[60] published a silver-alizarin-sensitised zinc oxide photocatalytic system for the photo-oxidation of alcohols to aldehydes with high selectivity. Both articles followed the photo-electronic pathways through electron paramagnetic resonance spectroscopy (**Figure 21**).
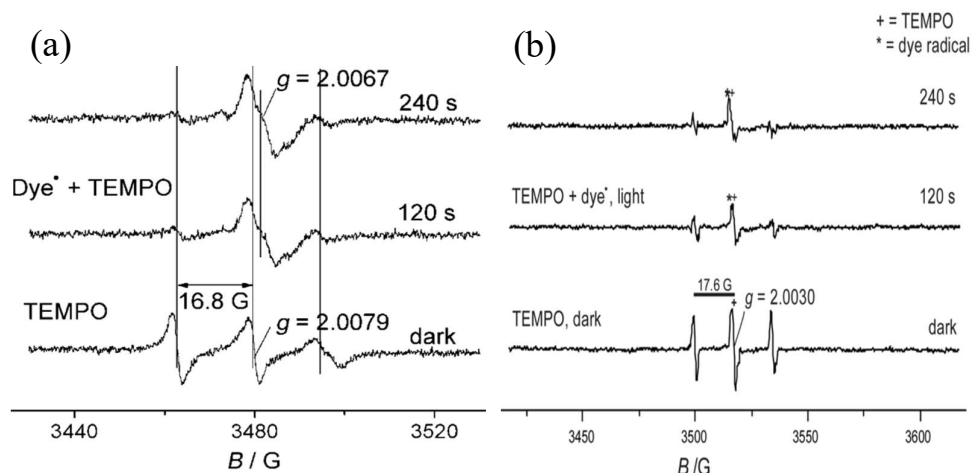
Figure 21: Monitoring TEMPO radical adducts using electron paramagnetic resonance spectroscopy as reported by Zhang *et al.*,[9] image (a) and Jeena and Robinson,[59] image (b). Reprinted with permission from M. Zhang, C. Chen, W. Ma, J. Zhao, *Angewandte Chemie International Edition* 2008, *47*, pp 9730−9733. Copyright (1999−2018) John Wiley & Sons, Inc. All rights reserved. Reproduced from V. Jeena, R. S. Robinson, *Dalton transactions* 2012, *41*, pp. 3134−3137 with permission from The Royal Society of Chemistry.

Both **Figure 21** (image a) and (image b) depict stabilised triplet TEMPO signals in addition to singlet peaks arising from photo-excited alizarin red. **Figure 21** (image a) and (image b) also presented with TEMPO splitting constants (a_N = 16.8 and 17.6 G respectively), confirming the catalytic participation of the TEMPO free radical in the oxidation of alcohols to aldehydes.

Typical organic dye-sensitised semiconductors have an organic dye (*i.e.* alizarin red) supported on a wide band gap metal oxide (*i.e.* TiO_2, ZnO or WO_3). During the irradiation period with visible light, the organic dye is excited, and an electron is transferred to the conduction band of the metal oxide support. Since the dye is photo-excited, opposed to the metal oxide (that can only be photo-activated with UV light, in which strong positive holes are produced), a mild and selective oxidation reaction can be harnessed for oxidative purposes (as described above).[9]

In analogous research to the literature which was conducted by Zhang *et al.*,[9] and, Jeena and Robinson,[60] Kar *et al.*[61] illustrated the potential application of functionalised

mesoporous titanium dioxide with a catecholate scaffold to produce a visible light sensitive tetracyanato ruthenium (III) polypyridyl cocatalyst.

During their investigation,[61] several pertinent observations were noted. UV-Vis spectrophotometry identified a red shift absorbance in the dye molecule (tetracyanato ruthenium (III) polypyridyl) after the addition of a colloidal suspension of TiO_2 nanoparticles (**Figure 22**).
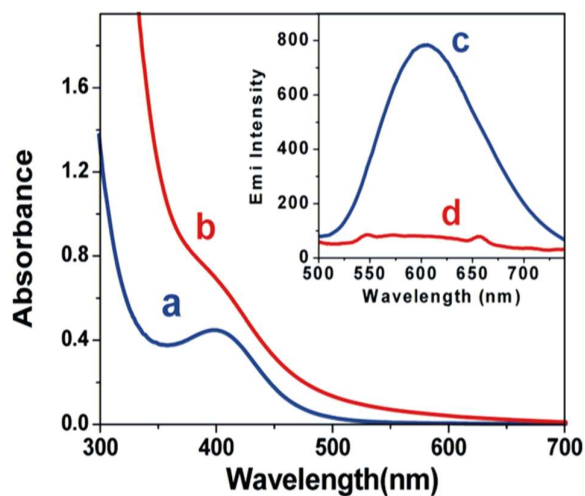
Figure 22: UV-Vis monitoring of red shifted absorbance for tetracyanato ruthenium (III) polypyridyl after the addition of TiO_2. (Note: Spectrum 'a' depicts the absorbance before the addition of TiO_2 to the catecholate scaffold; spectrum 'b', after TiO_2 addition in water. Spectra 'c' and 'd' represent emission spectra of tetracyanato ruthenium (III) polypyridyl before and after coordination binding to TiO_2 in water, respectively). Reprinted with permission from P. Kar, S. Verma, A. Sen, A. Das, B. Ganguly, H. N. Ghosh, *Inorganic Chemistry* 2010, *49*, pp. 4167−4174. Copyright 2010 American Chemical Society.

The red shift was suspected to arise from a strong catecholate dye/metal oxide interaction.[61] Further studies revealed a convincing emission maximum from the luminescence spectrum. This was reported to be the effect of a $Ru_{d\pi} > L_{\pi*}$ transition. In comparison, upon further addition of TiO_2 nanoparticles, the signal diminished drastically, thus indicating strong electron ejection from the dye into the conduction band of TiO_2 (see **Figure 22**, Spectra 'c' and 'd'). Computational studies were investigated for both the free dye complex (tetracyanato ruthenium (III) polypyridyl) and dye bound TiO_2 (**Figure 23**).
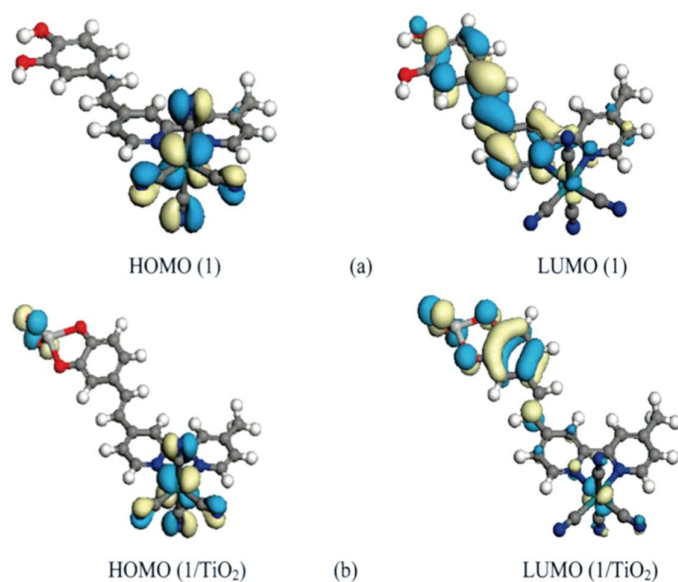
Figure 23: HOMO/LUMO from DFT calculations of the free dye complex (tetracyanato ruthenium (III) polypyridyl and dye bound TiO_2. The figure depicts the electron migration pathways from the Ru(II) centre and into the conduction band of titanium dioxide. Reprinted with permission from P. Kar, S. Verma, A. Sen, A. Das, B. Ganguly, H. N. Ghosh, *Inorganic Chemistry* 2010, *49*, 4167−4174. Copyright 2010 American Chemical Society.

The data collected from the electronic charge distribution identified that tetracyanato ruthenium (III) polypyridyl orbital's coefficient of the highest occupied molecular orbital (HOMO) was predominately located over the Ru (II) centre and neighbouring nitrile (CN) ligands whereas, the lowest unoccupied molecular orbital (LUMO) was located on the 4-[2-(4'-methyl-2,2'-bipyridinyl-4-yl)vinyl]benzene-1,2-diol) ligand component of the tetracyanato ruthenium (III) polypyridyl dye. In comparison, for the dye bound-TiO_2, the HOMO was present on the same Ru (II) centre and neighbouring nitrile (CN) ligand sites but the LUMO had shifted towards the catechol ring. This computational data would further corroborate electron ejection from the photo-excited Ru (II) centre, across the catecholate/TiO_2 bridge and into titanium dioxide's conduction band.

1.3. Photocatalytic Reports of Semiconductor Heterojunctions

1.3.1. Straddling, Staggered, and Broken Heterojunction Band Gaps

As described in the literature, an interface which forms between two different band structures of two dissimilar semiconductors that can lead to the alignment of the band structure pair, is known as a 'heterojunction'.[62]

Heterojunction research between two semiconductors continues to expand with novel methods to synthesise, characterise and understand the light absorptivity, photo excitations (excitons) and physical mechanics of the solid-state materials. Instrumental methodologies that have evaluated the three aspects of photonics; correct heterojunction pairing, band edge alignments, and photoelectron transfers (**Figure 24**) between semiconductors are discussed. Furthermore, the application of semiconductor heterojunctions in alcohol photo-oxidation and organic dye degradation studies are reviewed.
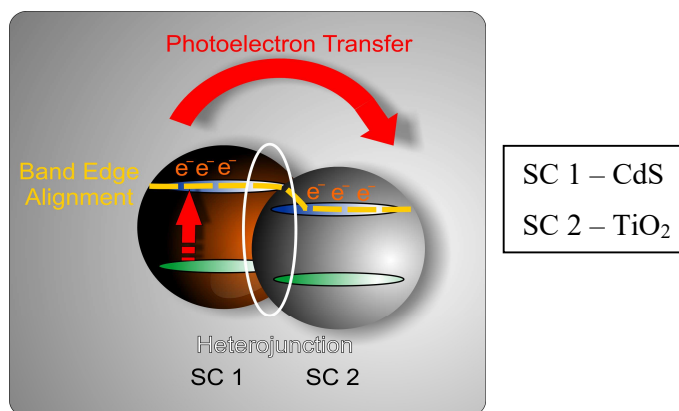
Figure 24: Illustration depicting the CdS/TiO$_2$ heterojunction between SC 1 and SC 2, with photoelectron ejection from the higher energy conduction band of CdS and into the lower energy conduction band of TiO$_2$.

As previously shown in **Scheme 1** (*viz* metal or non-metal ion exchange [substitution], metal ion doping into interstitial sites, or surface loading of metals, non-metals or organic dyes), the methods to functionalise semiconductors are much alike with the technique of forming a heterojunction between two semiconductors. The objective of the heterojunction utilises the redox positions of two semiconductors to optimise band edge alignment for an array of synthetic-organic transformations under visible light conditions.[63],[64],[65],[66]

A well-known heterojunction exists between cadmium sulfide and titanium dioxide (CdS/TiO_2).[67],[68] The efficiency of CdS/TiO_2 to transfer photoelectrons from the visible-light-activated cadmium sulfide (2.4 eV, 517 nm) to ultraviolet-light-activated titanium dioxide (3.2 eV, 387 nm[4]) is accomplished through close contact of the CdS/TiO_2 heterojunction.

Literature has reported four photoelectron migration mechanisms that occur between two semiconductors. The first three are described in **Figure 25**.

Straddling band gap (Type 1)

Conduction bands

Valence bands

SC 1 SC 2

Note:
SC 1 = semiconductor 1
SC 2 = semiconductor 2

Staggered band gap (Type 2)

Conduction bands

Valence bands

SC 1 SC 2

Broken band gap (Type 3)

Conduction bands

Valence bands

SC 1 SC 2
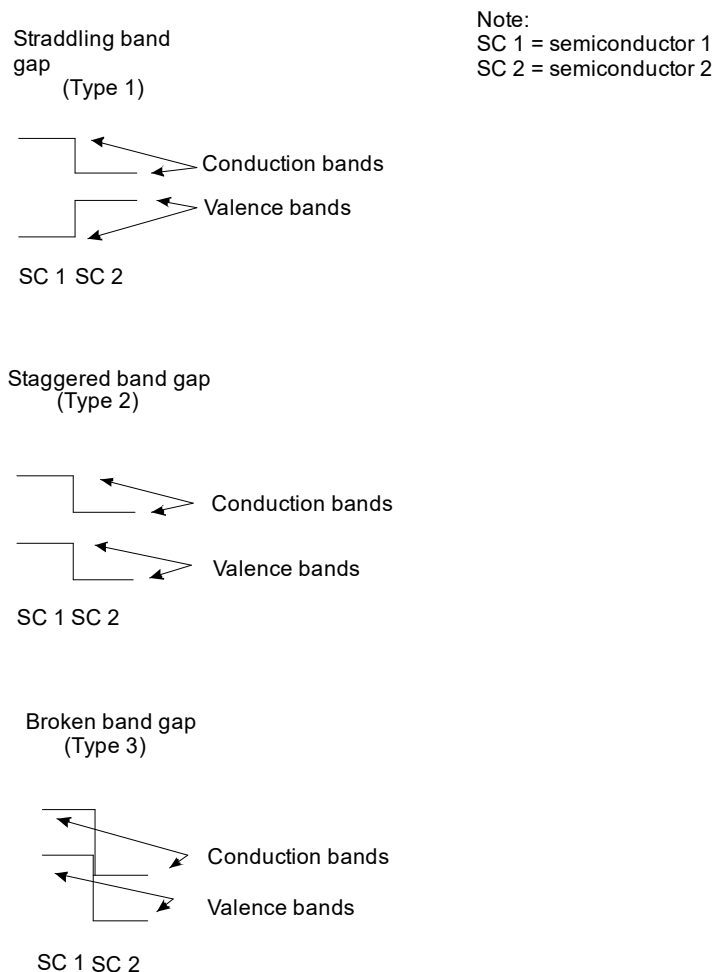
Figure 25: The three possible band gap schemes for valence and conduction band pairs of two heterojunctioned semiconductors: straddling (Type 1), staggered (Type 2), and broken (Type 3).

According to literature,[69] one of three potential heterojunction systems can exist between two different (*p*- and *n*-Type) semiconductors, namely; straddled (Type 1), staggered (Type 2) and broken (Type 3) (**Figure 25**). Type 2 systems have been well reported in the chemical domain.[70] However, two significant drawbacks arise from conventional heterojunctions (Types 1,2, and 3). Firstly, due to the electron migration from the higher conduction band of semiconductor A to the lower conduction band of semiconductor B, the redox potential of the conduction band electron is significantly reduced. The same conditions apply to the reduced oxidation potential of semiconductor B, after hole migration from semiconductor A. Furthermore, due to the influx of photoelectron migration from the conduction band of semiconductor A and

into the conduction band of semiconductor B (which is already electron rich), electrostatic repulsion forces arise (**Figure 26**).
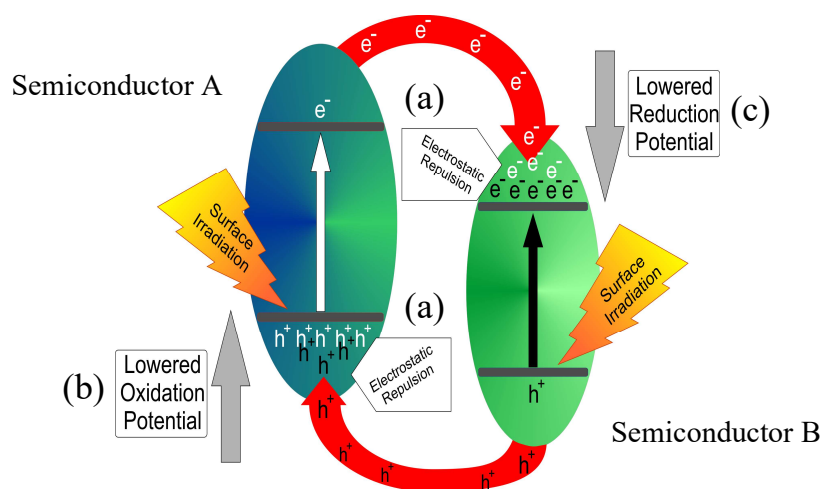
Figure 26: Inherent limitations of heterojunctions (Type 1, 2 and 3). Electrostatic repulsion from the accumulation of either e^- and/ or h^+ in separate band states (a), and lowered oxidation and reduction potentials (b and c, respectively).

However, the forth heterojunction system which forms a unique band alignment and is known as the ***Z-scheme*** has received considerable attention due to its superior photoelectronic properties to minimise exciton recombination and inhibit weak photo-redox positive hole and photoelectron production. Further details of the *Z*-scheme mechanism have been discussed in greater detail in **Chapter 1.3.2**, *vide infra*.

 Two well-known polymorphs of titanium dioxide, which have received considerable attention in the literature are anatase and rutile.[71] Despite rutile having a lower band gap making it more favourable for photocatalytic studies, its counterpart, anatase, has received considerably more attention as an attractive semiconductor material. The heightened efficiency of anatase is still open to debate; yet band positioning, crystal orientations, indirect *vs* direct band gap alignment and exciton mobilities of anatase are believed to contribute to the higher photocatalytic activity of anatase over rutile.[71]

Scanlon *et al.*[72] exemplified the need to further understand semiconductor mechanics through the application of theoretical and instrumental studies towards titanium dioxide's two polymorphs (anatase and rutile). Madelung Potentials that were

calculated from the polarisable shell model were used for anatase and rutile.[72] The electrostatic potential of -45.025 V for titanium in the anatase polymorph was determined to be 0.17 eV higher than rutile (-45.199 V). In addition, anatase's oxygen ($+26.232$ V) was placed 0.47 eV higher than rutile ($+25.767$ V). These findings demonstrate that a higher electrostatic potential exists for titanium in the anatase phase and therefore contributes to a larger band gap value (3.2 eV for anatase *vs* 3.03 eV for rutile), hence valence band (VB) positioning of rutile was placed 0.47 eV above anatase.

In similar studies to the text by Scanlon *et al.*[72] various semiconductor articles have described the fundamental photo-physics of semiconductor mediated photocatalysis of fine chemicals and pharmaceutical-based photocatalysis, which have received heightened interest in past years.[69],[73] Prior to semiconductor-mediated photocatalysis, pharmaceutical feedstock materials were synthesised from chlorinated agents (Cl_2, ClO^-), high oxidation state metal ions (Cr^{6+} and Mn^{7+}), harsh reaction temperatures and pressures, in addition to reducing agents including carbon monoxide and gaseous hydrogen.[74] Since the advent of semiconductor-mediated photocatalysis, a movement toward environmentally friendly catalysis for the production of feedstock material is rapidly developing. Binary and tertiary photocatalytic systems are of particular interest amongst synthetic chemists.

Hamrouni and co-workers[75] explored the possibility of attenuating the properties of zinc oxide after ternary SnO_2-ZnO-$ZnWO_4$ systems were discovered to enhance the charge separation effect of ZnO and the impact on benzylic alcohol oxidation studies. 4-Methoxybenzyl alcohol was oxidised in the presence of zinc oxide with various tin and tungsten dopings. The authors provided a synopsis of the binary and tertiary systems and reported a 100 % improvement in 4-methoxybenzyl alcohol conversion with a 10 % increase in selectivity compared to zinc oxide alone. Various instrumental techniques were utilised to identify why the ternary (SnO_2-ZnO-$ZnWO_4$) system had an apparent heightened visible light response through photoluminescence spectroscopy, powder X-ray diffraction and powder UV/Vis spectroscopic studies.

Photoluminescence spectroscopy identified that all three complex ternary derivatives of SnO_2-ZnO-$ZnWO_4$ showed lower peak intensities (at red shifted values greater than 450 nm, **Figure 27**, Spectra b, c, and d) than ZnO (**Figure 27**, Spectrum a) and were

reported to originate from a reduction in radiative recombination of photogenerated electrons, and holes on the surface of zinc oxide. However, in order to optimise and thereby reduce exciton recombinations near the band gap of zinc oxide (380−440 nm), the SnO_2-ZnO-WO_4 ratios needed careful consideration as $Sn_{0.025}$-Zn-$ZW_{0.025}$, (**Figure 27**, Spectrum d) demonstrated poor band-edge exciton quenching characteristics compared to ZnO (**Figure 27**, Spectrum a).
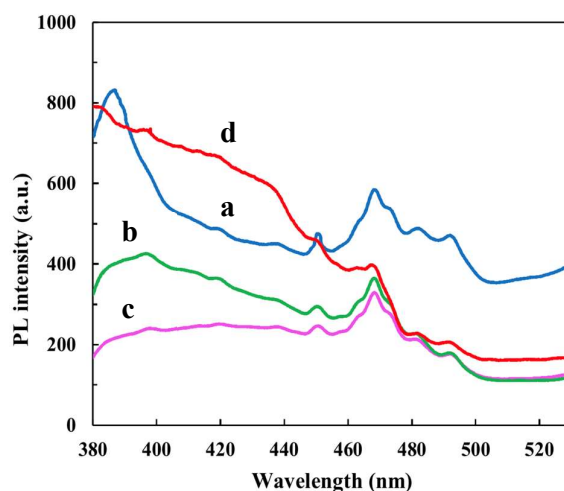
Figure 27: Photoluminescence spectra of intrinsic ZnO (blue, spectrum a), Zn-$ZW_{0.05}$ (green, spectrum b), Zn-$Sn_{0.05}$ (pink, spectrum c) and $Sn_{0.025}$-Zn-$ZW_{0.025}$ (red, spectrum d). The lowered peak intensities of the ZnO complexes (Spectra b, c, and d at $\lambda > 450$ nm) originated from reduced radiative recombinations compared to intrinsic ZnO. Reprinted from Journal of Photochemistry and Photobiology A: Chemistry, Vol 309, A. Hamrouni, *et al.*, Photocatalytic activity of binary and ternary SnO2-ZnO–ZnWO4 nanocomposites, pages No. 47−54, Copyright (2015), with permission from Elsevier.

Powder X-ray diffractograms identified the major crystalline phases in the compound SnO_2-ZnO-$ZnWO_4$ system as tetragonal SnO_2 (JCPDS card number: 41−1445), monoclinic $ZnWO_4$ (JCPDS card number: 15−0774), and hexagonal ZnO (JCPDS card number: 36−1451). However, after collecting complementary powder UV/Vis diffuse reflectance spectra on a Shimadzu UV-2401 PC spectrophotometer, (**Figure 28**), the Zn-$Sn_{0.05}$ (spectrum d), Zn-$ZW_{0.05}$ (Spectrum e) and $Sn_{0.025}$-Zn-$ZW_{0.025}$ (spectrum f) species produced poor absorbance characteristics compared to ZnO (spectrum a) and SnO_2 (spectrum b), which were suspected to arise from poor crystallinity of the ternary SnO_2-ZnO-$ZnWO_4$ systems. Furthermore, the undoped ZnO (**Figure 28**, spectrum a)

49

and SnO_2 (**Figure 28**, spectrum b) were observed to retain higher optical absorbance values and lower cut-off wavelengths compared to the functionalised species. The spectra cut-off wavelength variations showed that doping ZnO and SnO_2 red shifted the optical band gap and hence, improved visible light activities were detected.
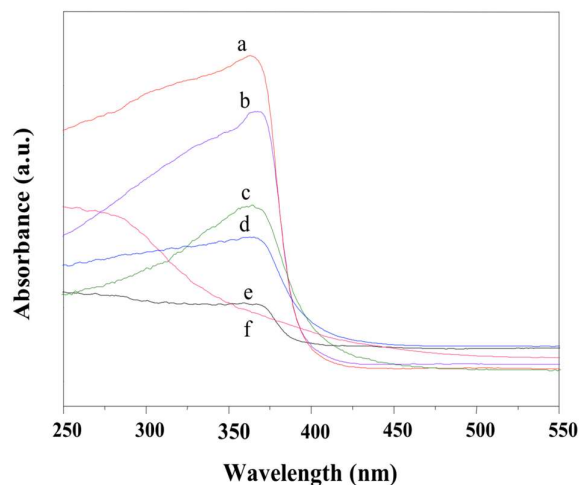
Figure 28: Powder UV/Vis diffuse reflectance spectra from the SnO_2-ZnO-$ZnWO_4$ mixed metal oxides. Spectra 'a' and 'b' represent ZnO and SnO_2, while spectra 'c' and 'd' depict $ZnWO_4$, Zn-$Sn_{0.05}$, Zn-$ZW_{0.05}$ and $Sn_{0.025}$-Zn-$ZW_{0.025}$, respectively. Reprinted from Journal of Photochemistry and Photobiology A: Chemistry, Vol 309, A. Hamrouni, *et al.*, Photocatalytic activity of binary and ternary SnO2–ZnO–ZnWO4 nanocomposites, pages No. 47−54, Copyright (2015), with permission from Elsevier.

This observation was subsequently corroborated by using scanning and transmission electron microscopy to identify nanoparticles of 20−150 nm in size (**Figure 29**, image d), which consisted of aggregated clusters (**Figure 29**, images a, b, and c).
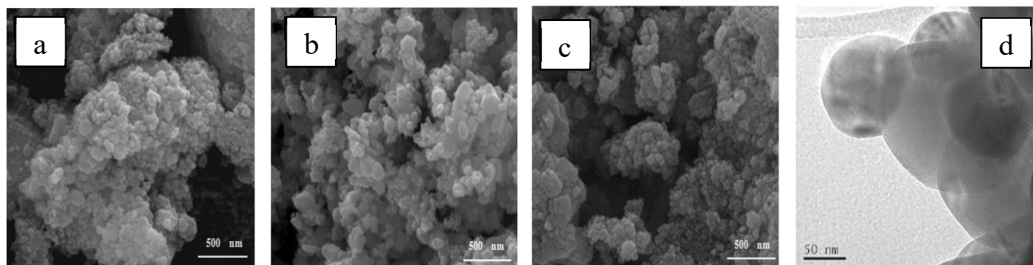
Figure 29: Nano-aggregates of SnO_2-ZnO-$ZnWO_4$ spheres (SEM images a-c), HRTEM (image d). Reprinted from Journal of Photochemistry and Photobiology A: Chemistry, Vol 309, A. Hamrouni, *et al.*, Photocatalytic activity of binary and ternary SnO_2-ZnO-$ZnWO_4$ nanocomposites, pages No. 47−54, Copyright (2015), with permission from Elsevier.

In similar texts that also investigated complex semiconductors for oxidising organic substrates, Yang *et. al.,*[76] published a dual redox functioning silver nanoparticle mediated metal-organic framework (MOF) photocatalyst, 'MIL-125/Ag/C_3N_4' compound semiconductor (MIL-125 = $Ti_8O_8[O_2C-C_6H_5-CO_2]_6$) that operated as both an oxidant of alcohols to aldehydes and reductant of nitrobenzene to aniline in alcoholic solvents.

An interesting observation regarding the adhesion of silver nanoparticles to MIL-125 and graphitic carbon nitride (*g*-C_3N_4) semiconductors was reported. X-ray diffraction data revealed that (111) silver nanoparticles were unable to adsorb onto the surface and formed a part of the lattice structure of the MIL-125 surface. However, after incorporating *g*-C_3N_4 with MIL-125, silver adhered to the surface of MIL-125 in the multicomponent semiconductor system. The authors[76] never postulated why silver was only adsorbed in the presence of *g*-C_3N_4 which posed an interesting question to resolve. There was evidence reported in their FT-IR findings for *g*-C_3N_4 that revealed the presence of C-N heterocycles. This suggests possible Ag-N coordination and hence postulates the adhesion of MIL-125/Ag/*g*-C_3N_4 and not MIL-125/Ag. Further omitted evidence in the authors'[76] X-ray photoelectron spectroscopic data were amino groups at 401.3 eV that augmented the possibility of free nitrogen coordination sites.

Besides studying exciton lifetimes with photoluminescence spectroscopy and powder UV/Vis spectroscopy, Yang *et al.*[77] explored the fast interfacial charge transfer dynamics of MIL-125/Ag/*g*-C_3N_4 using a three-component electrodic system using an AC impedance-potential model (saturated calomel reference electrode, platinum foil

counter electrode and MIL-125/Ag/g-C$_3$N$_4$ as the working electrode). The electrode's reaction rate of a given study can be monitored from the arc radius of the electrochemical impedance Nyquist plot (**Figure 30**). A decrease in the arc radius indicates a fast-interfacial charge transfer and separation of the photogenerated exciton pairs occurring on the semiconductor's surface.[*]
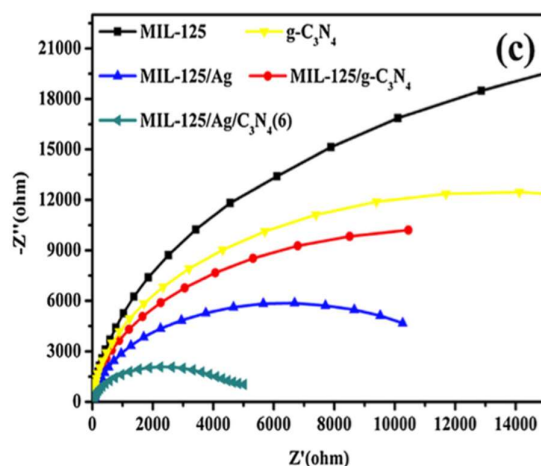
Figure 30: The observed arc radii for the electrochemical impedance of the investigated semiconductors (MIL-125, g-C$_3$N$_4$, MIL-125/Ag, MIL-125/g-C$_3$N$_4$, and MIL-125/Ag/C$_3$N$_4$), demonstrating the superior photo-efficiency of the MIL-125/Ag/C$_3$N$_4$ material. Reprinted from Journal of Applied Catalysis B: Environmental, Vol 205, Z. Yang, X. Xu, X. Liang, C. Lei, Y. Cui, W. Wu, Y. Yang, Z. Zhang and Z. Lei., Construction of heterostructured MIL-125/Ag/g-C$_3$N$_4$ nanocomposite as an efficient bifunctional visible light photocatalyst for the organic oxidation and reduction reactions, Pages 42−54, Copyright (2017), with permission from Elsevier.

The application of electrochemical impedance spectroscopy characterised the positive photocatalytic effect arising from silver in the case of MIL-125/Ag/C$_3$N$_4$. Silver was incorporated into the MIL-125/C$_3$N$_4$ matrix to enhance the interfacial charge transfer between MIL-125 and C$_3$N$_4$ through the action of a bridging electron transfer agent (Ag).

---

[*] Within a semiconductor's lattice, excitons are generated after photo-excitation with an appropriate electromagnetic radiation source (**Figure 30**). The exciton pairs that do not participate in redox reactions decay *via* non-radiative routes (exothermic emission) or radiative pathways.

Yang *et al.*[78] have also demonstrated the potential of electrochemical impedance spectroscopy to access the photo-reactivity of complex semiconductors after studying a MIL-53(Fe) metal-organic framework (consisting of continuous $FeO_4[OH]_2$ units) doped with graphene (**Figure 31**). In the presence of graphene doping (**Figure 31**), the electrochemical impedance data demonstrated an improved exciton lifetime extension through electron migration across the MIL-53(Fe)-GR heterojunction.
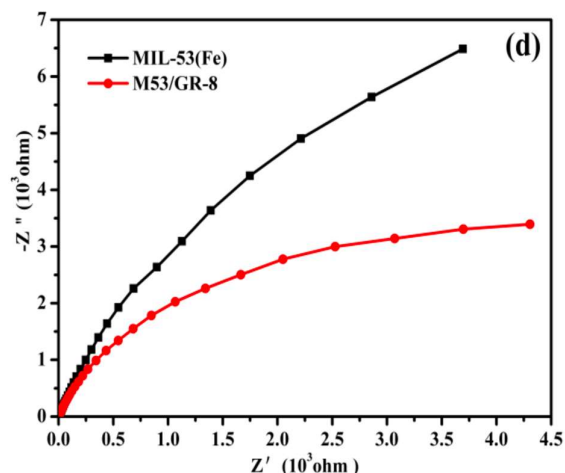
Figure 31: Nyquist plot of fast charge separation from MIL-53(Fe)/graphene (M53/Gr-8) opposed to MIL-53(Fe) alone. Reprinted from Applied Catalysis B: Environmental, Vol 198, Z. Yang, *et al.*, MIL-53(Fe)-graphene nanocomposites: Efficient visible-light photocatalysts for the selective oxidation of alcohols, pages No. 112−123, Copyright (2016), with permission from Elsevier.

While semiconductor heterojunctions have demonstrated to be excellent platforms for fine chemical synthesis, numerous studies have also been directed towards the remediation of dyes from wastewater streams and the decomposition of volatile organics, as graphically summarised in **Figure 32**.[66]
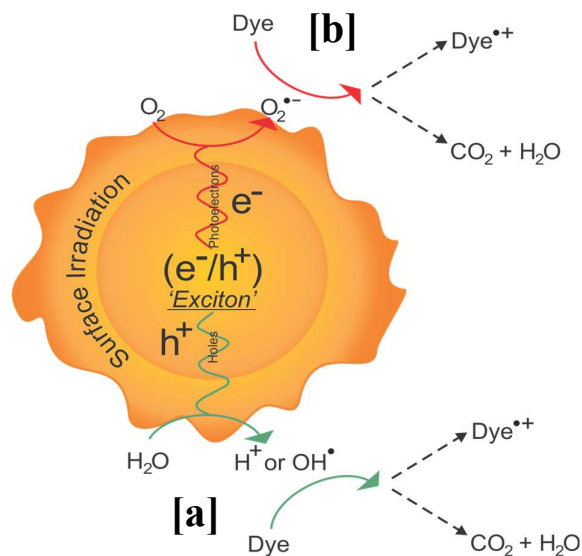
Figure 32: An illustration summarising the two possible visible-light driven photocatalytic pathways (hydroxyl [a] and superoxide [b] radicals) of semiconductors for dyestuff remediation studies.

In an organic dyestuff degradation of Rhodamine B published by Fagan *et al.*,[79] an attempt to elucidate the doping mechanics of g-C_3N_4 onto TiO_2 was investigated. After studying g-C_3N_4/TiO_2 using Fourier Transform Infrared spectroscopy (FTIR), they identified the major stretching ($2900-3600$ cm^{-1} as terminal NH_2 /NH) and breathing (807 cm^{-1}) modes of g-C_3N_4. However, in g-C_3N_4/TiO_2, the authors could neither qualitatively confirm surface loading nor doping of g-C_3N_4 into TiO_2 (**Figure 33**). FTIR spectroscopy has further demonstrated applications elsewhere for phase compositions in WO_3/$CdWO_4$ materials for methylene blue, methyl orange, and rhodamine B degradation.[63]
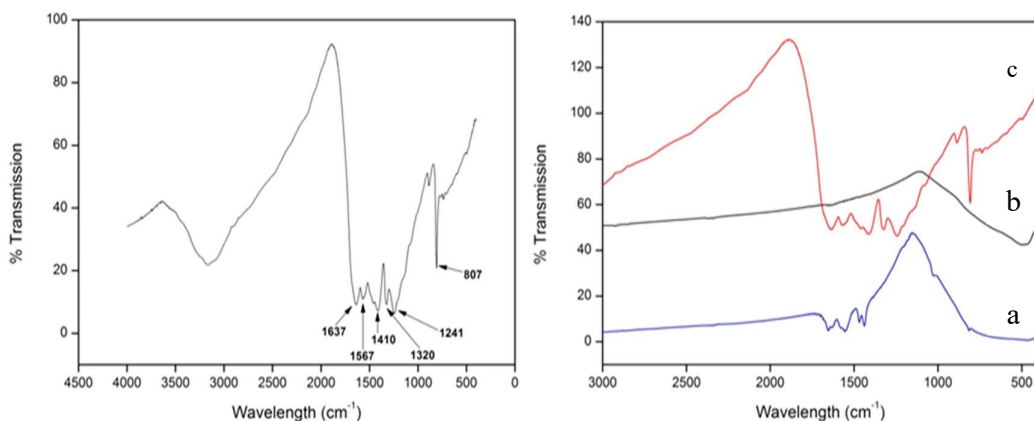
Figure 33: FTIR studies of g-C_3N_4 (left) and g-C_3N_4/TiO_2 (right) revealing the co-doping effect of coupling g-C_3N_4 and TiO_2. Note on g-C_3N_4/TiO_2 (right): a = 4% g-C_3N_4-TiO_2, b = undoped TiO_2 and c = g-C_3N_4. Reprinted with permission from R. Fagan, D. E. McCormack, S. J. Hinder, S. C. Pillai, *Materials* 2016, *9* (4), pg. 286, © (2016) MDPI AG, Basel, Switzerland.

The uncertainty was later addressed after studying g-C_3N_4/TiO_2 with X-ray photoelectron spectroscopy. XPS confirmed the functionalisation of g-C_3N_4 onto TiO_2 after detecting N-lattice bound (399.7 eV) O–Ti–N species. Furthermore, titanium dioxide's oxygen (O *1s*) peak shifted from 534.0 to 529.8 eV when loaded with g-C_3N_4, indicating metal-singlet-oxygen bonding (as Ti–O).

Anandan and Miyauchi[80] studied the surface doping sites of lead oxide (PbO_2) when Cu-WO_3/TiO_2 was irradiated with visible light (**Figure 34**) for the oxidation of Pb^{2+} and acetaldehyde decomposition to carbon dioxide. This has been summarised in **Figure 34**, in which the photo-excited WO_3 transferred positive holes to the 'more positive' valence band of TiO_2, which undertook the oxidation and subsequent decomposition of acetaldehyde to carbon dioxide and Pb^{2+} oxidation to PbO_2.
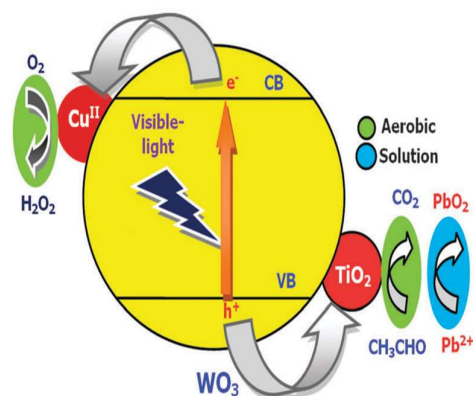
Figure 34: Schematic representation of the electronic migration pathways across irradiated Cu-WO$_3$/TiO$_2$. Reproduced from S. Anandan, M. Miyauchi, *Chemical Communications* 2012, *48*, pp 4323−4325 with permission from The Royal Society of Chemistry.

Arising from a favourable band alignment under the visible light conditions, hole promotion from WO$_3$ to TiO$_2$ took place. Furthermore, to test for the existence of hole transfer from WO$_3$ to TiO$_2$ and possibly confirm their theory, photo-oxidising Pb(NO$_3$)$_2$ on the surface of the Cu-WO$_3$/TiO$_2$ photocatalyst was studied using an Auger electron microscope (**Figure 35**).
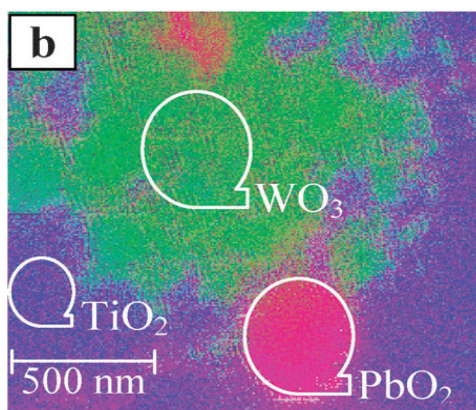
Figure 35: The detection of WO$_3$, PbO$_2$ and TiO$_2$ in Cu-WO$_3$/TiO$_2$ using Auger elemental mapping as indicated by the circled regions. The pink circled region indicated that PbO$_2$ preferentially precipitated over TiO$_2$ (purple circled region). Adapted from S. Anandan, M. Miyauchi, *Chemical Communications* 2012, *48*, pp 4323−4325 with permission from The Royal Society of Chemistry.

Anandan and Miyauchi[80] noted that PbO_2 mainly precipitated over TiO_2 (as seen by the pink circled region [PbO_2] on top of the purple circled region [TiO_2]) at the WO_3/TiO_2 interface (**Figure 35**) due to hole transfer from WO_3 to TiO_2 during photo-irradiation. The reported photo-activity of Cu-WO_3/TiO_2 was considerably higher than Cu(II)-WO_3, which arose from the efficient charge separation of photo-generated electrons and holes across the WO_3/TiO_2 interface. The extent of the excitons' lifetimes across the WO_3/TiO_2 was measured experimentally using time-resolved fluorescence spectroscopy (**Figure 36**).
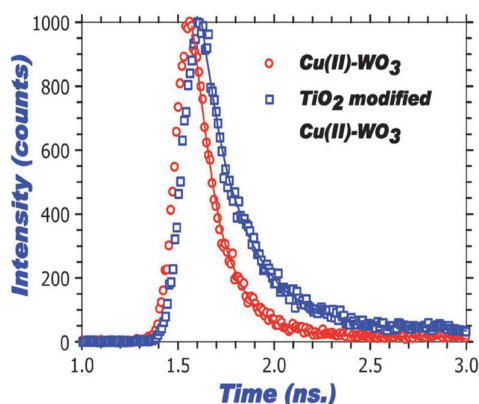
Figure 36: Time-resolved exciton measurements of modified (Cu and WO_3) TiO_2. The extension period of TiO_2 modified Cu(II)-WO_3 indicated an approximate 0.5 ns longer exciton lifetime than Cu(II)-WO_3 alone. Reproduced from S. Anandan, M. Miyauchi, *Chemical Communications* 2012, *48*, pp 4323−4325 with permission from The Royal Society of Chemistry.

Figure 36 demonstrates an extension of the Cu-WO_3/TiO_2 excitons' lifetime generated under irradiation compared to Cu(II)-WO_3 alone. The migration of photo-generated holes from the valence band of WO_3 to TiO_2 and the transfer of excited electrons from the conduction band of WO_3 to Cu(II) or Ag(I) revealed a fluorescence time decay for Cu-WO_3/TiO_2 compared to Cu(II)-WO_3.

1.3.2. *Z*-scheme heterojunctions in photocatalysis

While Anandan and Miyauchi[80] established electron migration across the WO_3/TiO_2 interface proceeding through favourable band alignment and electron transfer between the respective valence bands of tungsten trioxide and titanium dioxide, it is important to emphasise the significance of the fourth heterojunction, the *Z*-scheme.

The first noted study of a hybrid *Z*-scheme couple (using *g*-C_3N_4 and TiO_2 [*g*-C_3N_4|TiO_2] heterojunction) *without* an electron mediator has been reported by Yu *et al*.[81] in 2013 on the photo-decomposition of gaseous formaldehyde. Similar *Z*-scheme research has been subsequently published on the reduction of carbon dioxide to methanol over Si/TiO_2,[82] formaldehyde decomposition on platinum ceramics,[83] hydrogen gas evolution over $NiS/C_3N_4/CNT$ nanoparticles,[84] enrofloxacin photo-decomposition with carbon dot decorated TiO_2/C_3N_4 and the selective detection of Cu^{2+} while using a direct *Z*-scheme BiOI-CdS semiconductor.[85],[86]

The '***direct Z-scheme mechanism***' affords a significantly improved mechanism over conventional heterojunctions (**Figure 25**) because a highly oxidative positive hole is retained on semiconductor **A**, meanwhile, photoelectron ejection into the electrostatically attracted valence band of semiconductor **B** enhances strongly reductive electron production (**Figure 37**).
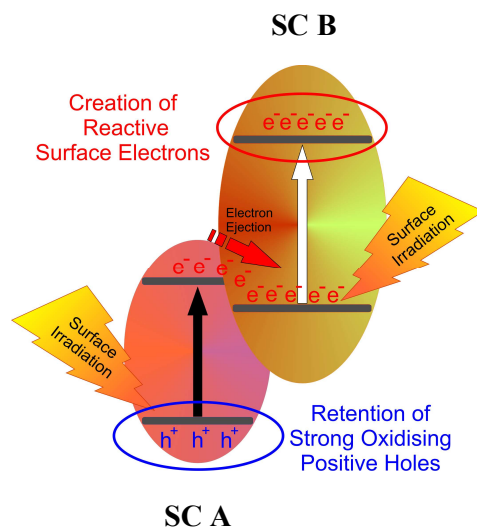
Figure 37: Exciton migration across the *Z*-scheme heterojunction. The positive hole (**blue h$^+$**) remain in SC A, meanwhile photogenerated electrons (**red e$^-$**) are injected into the valence band of SC B.

Literature has also reported that *Z*-scheme heterojunctions with a staggered (Type 2) heterostructure are an effective photocatalytic means for hydrogen production from the semiconductors' heterojunction formation.[87],[88]

Wang and co-workers[66] attempted to photocatalytically reduce carbon dioxide after constructing a direct *Z*-scheme heterojunction from Fe_2O_3 and Cu_2O (α-Fe_2O_3/Cu_2O). X-ray diffraction data verified that α-Fe_2O_3/Cu_2O consisted of cubic Cu_2O (Powder Diffraction File^{TM} [PDF] No: 01−078−2076), α-hematite (Fe_2O_3, PDF No: 01−086−2368) and no amalgam of Fe_2O_3 and Cu_2O was detected. Fast-Fourier transform (FFT) diffraction patterns did, however, reveal that Fe_2O_3 and Cu_2O were fused at the interface of both oxides. The enhanced photocatalytic activity arose from the α-Fe_2O_3/Cu_2O heterojunction, which ensured a high reduction potential. After irradiating for three hours using a 300 W xenon arc source, an optimal 50 mol % Cu_2O-Fe_2O_3 (50Cu-Fe) nanocomposite was capable of producing 5 μmol g_{cat}^{-1} $CO_{(g)}$ at an H_2O/CO_2 ratio of 0.025 at 313 K.

During their study, the authors postulated an additional mechanism for carbon dioxide photo-reduction. This was later confirmed after deducing the relative valence and conduction band positions in the Cu_2O-Fe_2O_3 heterojunction. A method to determine

band position and hence a possible means to evaluate the carbon dioxide photo-reduction was proposed from ultraviolet photoelectron spectroscopic measurements recorded on a Perkin Elmer PHI 5300 X-ray photoelectron spectrometer equipped with a HeI (21.2 eV) monochromatic light source. Wang and co-workers[66] interpreted the ultraviolet photoelectron data using a linear intersection method (which estimated band edge positioning) and determined the valence band of Cu_2O to reside at –5.32 eV (*vs* vacuum) and a calculated Fermi level at –5.17 eV (*vs* vacuum).

Furthermore, with a knowledge of the relationship (**Equation 1**):

$$E_{abs} = E^{\theta} - 4.44, \text{ where: } \quad E_{abs} = \text{vacuum energy}$$
$$E^{\theta} = \text{normal electrode potential}$$

Equation 1

The corresponding valence and conduction band positions could be determined (for Cu_2O, valence band [0.88 eV] and conduction band [–1.17 eV] *vs* normal hydrogen electrode) (**Figure 38**).
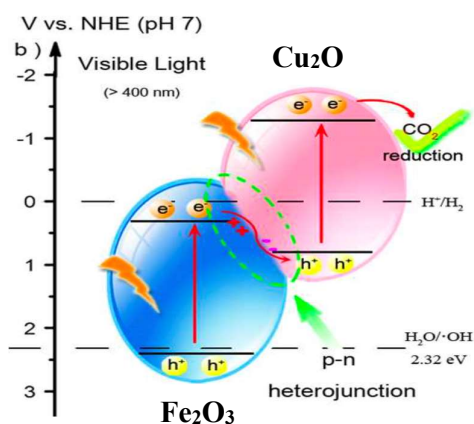
Figure 38: A schematic of the heterojunction formed between the band edge positions of Fe_2O_3 and Cu_2O. The 'heterojunctioned zone' (dashed green sphere) demonstrates the ejection of electrons from the conduction band of Fe_2O_3 and into the valence band of Cu_2O for CO_2 reduction. Adapted with permission from J.-C. Wang, L. Zhang, W.-X. Fang, J. Ren, Y.-Y. Li, H.-C. Yao, J.-S. Wang, Z.-J. Li, *ACS Applied Materials & Interfaces* 2015, *7*, 8631−8639. Copyright (2015) American Chemical Society.

Previously reported in 2013 by Miyauchi *et al.,*[89] a *Z*-scheme photocatalytic system ($CaFe_2O_4/WO_3$) was prepared for the photocatalytic decomposition of acetaldehyde to

carbon dioxide. Two methods (hydrothermal and mechanical mixing) were utilised to obtain 10% ($CaFe_2O_4/WO_3$). The hydrothermally prepared $CaFe_2O_4/WO_3$ (H) exhibited a superior carbon dioxide yield compared to the mechanically mixed ($CaFe_2O_4/WO_3$) (M).

The improved photocatalytic activity arising from $CaFe_2O_4/WO_3$ (H) was unknown at the time because the instrumental analysis using Brunauer-Emmett-Teller (B.E.T.) surface area measurements, powder X-ray diffraction (XRD) and ultraviolet-visible light spectrophotometry (UV-Vis) yielded identical physical characterisation between $CaFe_2O_4/WO_3$(H) and $CaFe_2O_4/WO_3$ (M).

Calculated BET measurements for $CaFe_2O_4/WO_3$ (H) and $CaFe_2O_4/WO_3$ (M) determined both species to have similar surface areas (12.9 m^2/g and 14.8 m^2/g respectively), thus concluding surface morphology was not the cause of $CaFe_2O_4/WO_3$ (H) having enhanced photocatalytic activity. The powder X-ray diffraction results depicted identical single phased and well-crystallised $CaFe_2O_4$ peaks with monoclinic WO_3 in both samples. Neither $CaFe_2O_4/WO_3$ (H) nor $CaFe_2O_4/WO_3$ (W) exhibited any peak shifting in the powder X-ray diffraction results, thus indicating no solid-state formation between $CaFe_2O_4$ and WO_3 in either sample. In addition, both $CaFe_2O_4/WO_3$ (H) and $CaFe_2O_4/WO_3$ (W) presented identical broad UV-Vis absorption profiles. However, scanning electron microscopy (SEM) results indicated that the $CaFe_2O_4/WO_3$ (H) preparation method yielded equally dispersed WO_3 particles in high concentrations on $CaFe_2O_4$. Meanwhile, WO_3 had aggregated significantly on the surface of $CaFe_2O_4/WO_3$ (W).

An important parameter to consider when synthesising heterostructured semiconductors is the zeta (ζ) potential. Zeta potentials measure electrostatic attraction/repulsion forces existing between particles within close proximity. Mis-matched electrostatic charges affect solid stability and hence photocatalytic activity. Miyauchi and co-workers reported that zeta potential measurements for an isoelectric point of $CaFe_2O_4$ occurred at a *ca.* pH of 1.5. However, at this pH, WO_3 was reported to remain as a homogeneous colloidal suspension.

Therefore, the pH was adjusted to approximately neutral conditions, which promoted a negative $CaFe_2O_4$ surface charge and therefore encouraged the electrostatic attraction of

W^{6+} cations. This lends reason to support the enhanced photocatalytic activity of $CaFe_2O_4/WO_3$ (H) over $CaFe_2O_4/WO_3$ (W), which arose from the electrostatically bound heterojunction of $CaFe_2O_4/WO_3$ (H) compared to the mechanically fixed $CaFe_2O_4/WO_3$ (W) composite. The electrostatically synthesised heterojunction of $CaFe_2O_4/WO_3$ (H) was identified to favour charge separation across the *Z*-scheme heterostructure.

2. Aims of the Project

2.1. Problem Statement

The research project has been structured to design and synthesise a selection of metal chalcogenides (zinc oxide, vanadium pentoxide supported on silica gel beads, cadmium sulfide and titanium dioxide semiconductors). The objective of lowering the optical band gaps after introducing organic dyes (alizarin red) and a selection of appropriate period three and or four transition metal ions will be explored.

The semiconductor systems will be carefully characterised to understand the nature and composition of the materials, which are likely to include an array spectroscopic, microscopic and X-ray diffraction techniques. The information gathered from these studies is anticipated to identify band gap potentials, phase identities, potential defect centres, ion speciation, and the respective quantitative compositions.

The first aim of the project will attempt to refine an alizarin red-sensitised zinc oxide study by lowering the number of silver equivalents (18) while still achieving high alcohol conversions. In addition, a better understanding of the mechanistic processes between AR and ZnO needs further clarification. Therefore, additional photoluminescence spectroscopic, powder diffuse reflectance UV/Vis spectroscopic data, and a computational density functional theory have been identified as suitable characterisation techniques to investigate the photoelectronic migration pathways between alizarin red and zinc oxide.

After enhancing the alizarin red-sensitised zinc oxide photocatalytic system, the research scope will be expanded to develop an approach of photo-activating the titanium dioxide semiconductor with only visible light. Proposed strategies include the functionalisation of titanium dioxide with vanadium, iron, cobalt, copper, palladium, and silver metallic species. Potential heterojunction strategies, Fe_2O_3 with TiO_2 and CdS with TiO_2 may also be investigated.

The semiconductors which are identified as being able to oxidise alcohols in preliminary studies will be fully characterised using various spectroscopic, microscopic, and X-ray diffraction techniques to postulate a mechanism for their photo-activation. Further testing of the target semiconductors in an array of alcohol oxidations will assess the potential viability of the materials as contemporary oxidants.

Within the industrial context, environmental pollutants are of significant concern to the water quality in hydrological systems. If a novel metal functionalised titanium dioxide semiconductor establishes the conversion of alcohols to aldehydes, a brief study to monitor the photo-decomposition of a typical organic dyestuff will be undertaken.

3. Results and Discussion

3.1. Research Overview

In this project, four semiconductor systems have been designed with the objective of identifying photocatalytic materials that are capable of oxidising alcohols to aldehydes.

The four semiconductor systems, which are discussed, include:

- ➢ Alizarin red-sensitised zinc oxide in a silver-sodium aqueous solution
- ➢ Three titanium dioxide derivatives with transition three period metals, *viz*. TMT-Cu, TMT-Ni and TMT-Mn.
- ➢ Silver functionalised cadmium sulfide
- ➢ A three-component (Cu, Pd, and N) titanium dioxide system, $Cu/Pd-N-TiO_2$

After fabricating viable target photocatalysts, broad alcohol oxidation surveys have assessed the suitability of the materials against contemporary literature.

Lastly, instrumental techniques were utilised to characterise the visible-light activated photocatalysts and obtain an understanding of the photo-physical and mechanistic properties of the newly fabricated materials.

3.2. Alizarin Red-Sensitised Zinc Oxide in an Aqueous Silver-Sodium Solution.

3.2.1. Background to the Theory

Jeena and Robinson[59] designed an approach to physi-adsorb and therefore sensitise zinc oxide with alizarin red in a solution saturated with silver (Ag^+), while 2,2,6,6-tetramethylpiperidinyloxyl radical (TEMPO) acted as the terminal oxidant. The photocatalytic system was demonstrated to be an effective mediator for the oxidation of benzylic alcohols to benzaldehyde derivatives with high conversion and selectivity (**Figure 39**).[59]
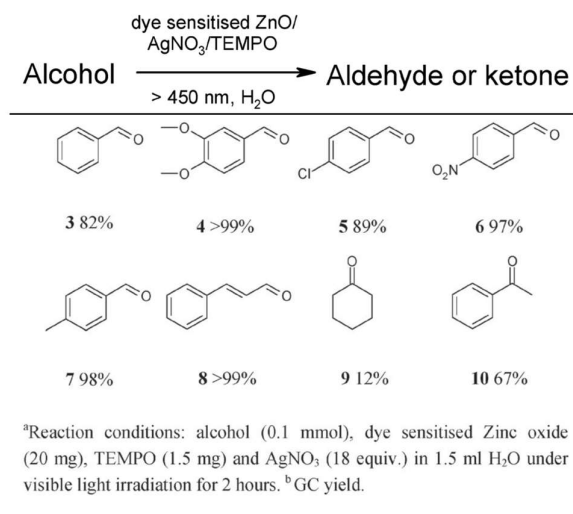
Figure 39: Alcohol photo-oxidations with the use of alizarin red/ZnO/Ag/TEMPO.[59] Adapted from V. Jeena, R. S. Robinson, Chemical Communications 2012, 48, 299−301 with permission of The Royal Society of Chemistry.

An observed limitation of the photocatalytic system was determined after Jeena and Robinson[59] confirmed that a minimum of 18 equivalents (!) of silver nitrate was necessary to inhibit the desorption of alizarin red dye off the surface of the zinc oxide. In the absence of the sensitiser-metal oxide interface, a disruption in the photocatalytic system would inhibit the alcohol oxidation.

The authors[59] used silver nitrate for its favourable redox potential that matched well with zinc oxide's conduction band edge. During the photocatalytic reaction, alizarin red was photo-excited, and electron ejection from alizarin red into the conduction band of zinc oxide facilitated electron quenching by silver ions (Ag^+) forming metallic silver (Ag^0). Silver (I) has a more positive redox potential ($+0.8$ V)[90] against zinc oxide's conduction band (-0.2 V)[91] and electrons were therefore preferentially quenched by silver (Ag^+) as opposed to residing in the conduction band of zinc oxide.

After careful consideration of the quantum processes in the photocatalytic mechanism (**Figure 40**),[59] five distinct electronic transfer steps were observed to facilitate the photo-oxidation of a single alcohol molecule:

Step I: After *one* dye molecule was photo-excited, *one* electron was promoted to the conduction band in alizarin red.

Step II: The electron was then transferred to the conduction band of zinc oxide.

Step III: *One* silver ion (Ag^+) quenched the electron.

Step IV: *One* dye molecule from **Step I** oxidised *one* TEMPO radical.

Step V: The oxidised TEMPO (*N*-oxoammonium salt) oxidised *one* alcohol molecule.

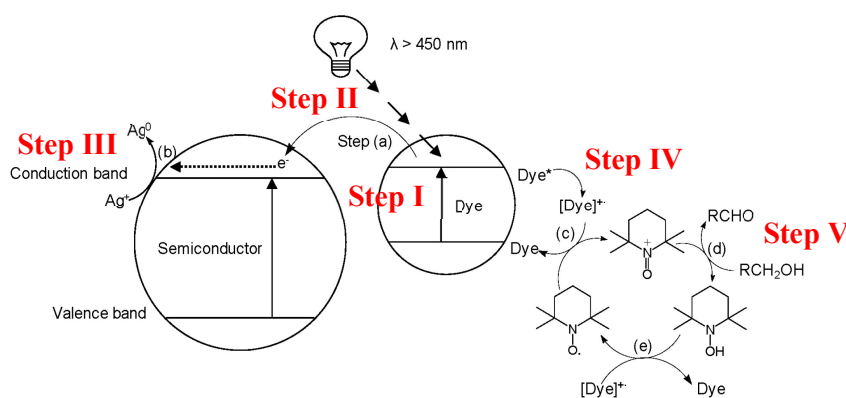**Figure 40:** Alizarin red-sensitised zinc oxide proposed by Jeena and Robinson[59] Adapted from V. Jeena, R. S. Robinson, Chemical Communications 2012, 48, 299−301 with permission of The Royal Society of Chemistry.

As noted by Jeena and Robinson,[59] eighteen equivalents of silver nitrate were needed to stabilise the photocatalytic system that would mediate the photo-oxidation of one

alcohol molecule. However, from Steps I-V of **Figure 40**, the intention of this study was to investigate an alternative method to alleviate eighteen equivalents of silver nitrate with the aim of mitigating excessive silver waste and developing a more environmentally friendly semiconductor.

3.3. Enhancing Alizarin Red-Sensitised Zinc Oxide

The alizarin red-sensitised zinc oxide photocatalytic material was prepared in accordance with the literature, after which, sodium nitrate was introduced as a complementary ionic salt to reduce the eighteen equivalents of silver nitrate (a detailed outline for the synthesis of alizarin red-sensitised ZnO is available in the Experimental).[59] Sodium nitrate was chosen for two reasons. Firstly, both salts (NaNO$_3$ and AgNO$_3$) had the same counter anion (NO$_3^-$). Furthermore, its highly negative redox potential (-2.7 V) exceeded zinc oxide's conduction band potential and therefore had a significantly lower electron affinity. Sodium ions were therefore incapable of accepting the in-flux of photo-generated electrons on the zinc oxide surface and only functioned as ionic electrolytes to stabilise alizarin red adsorbed onto the surface of zinc oxide.

A preliminary *proof-of-concept* study was conducted to establish the required ionic electrolyte (sodium) concentration to stabilise the alizarin red-zinc oxide interface and facilitate a quantitative oxidation of 3,4-dimethoxybenzyl alcohol using alizarin red-sensitised zinc oxide (**Table 1**).

Table 1: Refined photo-reaction conditions for 3,4-dimethoxybenzyl alcohol oxidation.[a]

Entry	Ag equivalents	Na equivalents	Conversion (%)[b]
1	0	18	18
2	1	15	> 99
3	1	10	> 99
4	1	5	> 99
5	**1**	**3**	**99**
6	1	1	97

[a]Reaction conditions: 0.2 mmol 3,4-dimethoxybenzyl alcohol, 20 mg dye-ZnO, 1.24 M Ag-Na solution electrolyte, 0.096 mmol TEMPO, 0.5 mL de-ionised H_2O, 7 hours visible light irradiation. [b]Conversions determined using GC-MS peak areas.[†]

The results from **Table 1** (entry 5), confirmed the early predictions that only one equivalent of silver nitrate was necessary to facilitate the alcohol oxidation *albeit* the reaction times were extended from three (as reported by Jeena and Robinson[59]) to seven hours for a quantitative alcohol conversion. The time extension arose from a reduced silver ion concentration and therefore the rapid electron quenching effect from a concentrated silver contact had been reduced.

However, in the absence of silver nitrate (**Table 1**, entry 1), the conversion of 3,4-dimethoxybenzaldehyde was considerably lower (18 %). Further attempts to lower the sodium equivalents below three (**Table 1**, entry 6) resulted in sub-quantitative conversions of 3,4-dimethoxybenzaldehyde. It was deemed necessary to retain the reaction conditions listed in **Table 1**, entry 5 and hence a quantitative means to photo-oxidise 3,4-dimethoxybenzyl alcohol to 3,4-dimethoxybenzaldehyde.

After identifying the refined reaction conditions (**Table 1**, entry 5), the oxidative scope of alizarin red/ZnO/Ag-Na/TEMPO was evaluated by attempting to oxidise various cyclic (**Table 2**) and aliphatic alcohol (**Table 3**) derivatives. In addition to evaluating the oxidative potential of the alizarin red/ZnO/Ag-Na/TEMPO photocatalyst, an analytical system was required to accurately determine the conversion, yield, and

---

[†] **Chapter 6.2: Experimental** has detailed the ionic strength calculations to refine the electrolyte concentrations.

selectivity of the desired aldehyde products. The quantitative detection of conversion, yield and selectivity for each aldehyde product were determined using the three established equations noted below.[92]

$$\text{Conversion (\%)} = \frac{c_{OH}^0 - c_{OH}^t}{c_{OH}^0} \times 100$$

$$\text{Yield (\%)} = \frac{c_{CHO}^t}{c_{OH}^0} \times 100$$

$$\text{Selectivity (\%)} = \frac{c_{CHO}^t}{c_{OH}^0 - c_{OH}^t} \times 100$$

In the adjacent equations:
- C^0_{OH} = Molar alcohol concentration before the start of the reaction.
- C^t_{OH} = Molar alcohol concentration at the end of the reaction.
- C^t_{CHO} = Molar aldehyde concentration at the end of the reaction.

It should also be noted that the alcohol oxidations were accurately quantified from relative response factors and peak area integrals using an established method with an internal standard.[93],[94]

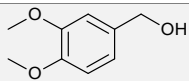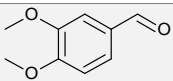**Table 2:** Cyclic alcohol oxidations with the alizarin red/Ag-Na/ZnO/TEMPO photocatalyst system.[a]
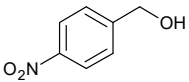
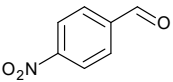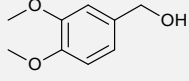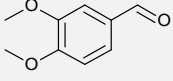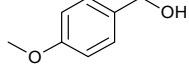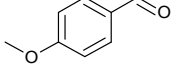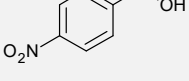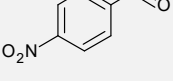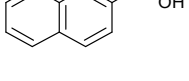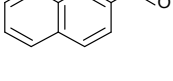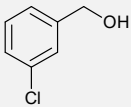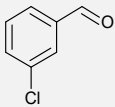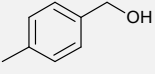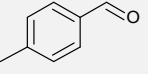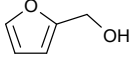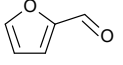| Entry	Alcohol	Aldehyde	Conv. (%)	Yield (%)	TON (AR)
1			≥ 99	11	132
2			97	7	129
3			69	69	92
4			59	59	79
5			74	65	99
6			70	74	93
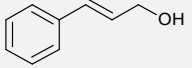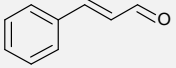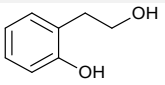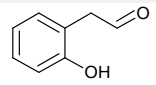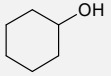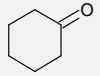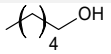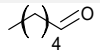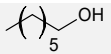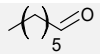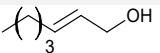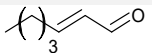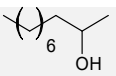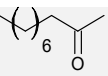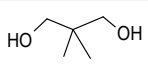
Table continued overleaf

7			66	65	88
8			72	25	96
9[b]			70	N/D	93
10			73	22	97

[a]Refined reaction conditions: 0.2 mmol alcohol, 20 mg dye-ZnO, 1.24 M Ag-Na solution electrolyte, 0.096 mmol TEMPO, 0.5 mL de-ionised H_2O, 7 hours visible light irradiation. [b]N/D (Not determined), the corresponding aldehyde was not available to determine the relative response factor. Note: TON (AR) was the turn over number (TON) of alizarin (AR) = $n_{product}/n_{alizarin\ red}$.

Electron donating substituted aromatic alcohols (**Table 2**, entries 1, 3, 4, 6, and 9) and electron withdrawing substituted species (**Table 2**, entries 2, 5, and 7) were oxidised in moderate to excellent conversions. Cyclohexanol oxidation (**Table 2**, entry 8) proceeded far better than expected using the alizarin red/ZnO/Ag-Na/TEMPO photocatalytic system (cyclohexanol conversion to cyclohexanone at 72 %) because literature has reported that attempting to oxidising aliphatic alcohols using mild reaction conditions is a challenging task.[95] After identifying that alizarin red/ZnO/Ag-Na/TEMPO had the potential to mediate the oxidation of aromatic alcohols, the scope of the photocatalytic system was expanded to include a broad aliphatic alcohol oxidation study (**Table 3**).

Table 3: Aliphatic alcohol oxidation using alizarin red/ZnO/Ag-Na/TEMPO.[a]

Entry	Alcohol	Aldehyde	Conv. (%)	Yield (%)	TON (AR)
1			69	65	92
2[b]			50	(N/D)	67
3			82	11	96
4[c]			66	(A/D)	88
5			75	28	100
6[c]			60	(A/D)	80
7[b]			10	(N/D)	13
8[b]			88	(N/D)	117

[a]Refined reaction conditions: 0.2 mmol alcohol, 20 mg dye-ZnO, 1.24 M Ag-Na solution electrolyte, 0.096 mmol TEMPO, 0.5 mL de-ionised H_2O, 7 hours visible light irradiation. [b]N/D (Not determined), the corresponding aldehyde was not available to determine the relative response factor. [c]A/D (Aldehyde decomposed), the aldehyde used to determine the relative response factor decomposed upon short-path distillation. Note: TON (AR) was the turn over number (TON) of alizarin (AR) = $n_{product}/n_{alizarin\ red}$.

The tabulated data (**Table 3**) confirmed that alizarin red/ZnO/Ag-Na/TEMPO was a capable oxidant to mediate the selective conversion of aliphatic alcohols to aldehydes. Notably was the oxidation of 3-Phenyl-2-propen-1-ol with a high conversion, (**Table 3**, entry 1, 69 %). The oxidative conversion of 2-(2-hydroxyphenyl) ethanol was lower (**Table 3**, entry 2, 50 %), which was speculated to arise from the hydroxy moiety at the ortho-position on the benzyl ring that induced a strong electron withdrawing character and further destabilised the aliphatic chain during photo-oxidation. The oxidative success of the alizarin red/ZnO/Ag-Na/TEMPO photocatalytic system was accentuated after reviewing the results from **Table 3**, entries 4−8. Despite decan-2-ol

(**Table 3**, entry 7) only affording a 10 % conversion of decan-2-one, the oxidations of hexan-1-ol (**Table 3**, entry 4, 66 %), heptan-1-ol (**Table 3**, entry 5, 75 %), trans-2-hexen-1-ol (**Table 3**, entry 6, 60 %) and 2,2-dimethyl-1,3-propanediol (**Table 3**, entry 8, 88 %) were highly satisfactory results. However, the regioselective oxidation of 2,2-dimethyl-1,3-propanediol to 2,2-dimethyl-3-hydroxypropionaldehyde (and not the di-carbonyl- 'dimethylmalonaldehyde' alternative) (**Table 3**, entry 8, 88 %) further demonstrated the suitability of alizarin red/ZnO/Ag-Na/TEMPO as a contemporary oxidant of alcohols to aldehydes.

In comparison to the original study conducted by Jeena and Robinson using alizarin red/ZnO/Ag/TEMPO (**Figure 39**) that utilised eighteen equivalents of silver nitrate, the alcohol conversions reported in **Table 2** and **Table 3** were slightly lower.[59] Although, the significant reduction in silver loading (18 to 1 equivalent) was highly favourable in the alizarin red/ZnO/Ag-Na/TEMPO photocatalytic system.

Despite the fair to excellent conversions of both aromatic and aliphatic alcohols using the alizarin red/ZnO/Ag-Na/TEMPO photocatalytic system, the reported aldehyde yields were lower than expected (**Table 2**, entries 1 and 2). The low values were of slight concern as the chromatographic data depicted that alizarin red/ZnO/Ag-Na/TEMPO was chemoselective for the oxidation of alcohols to aldehydes.

Six reactions listed in **Table 2** (entries 3−7) and **Table 3** (entry 1) were rerun in different reaction vials (sealed GC vials) to ensure minimal loss of the crude reaction mixture. After five extractions of the crude alcohol and aldehyde organic phase into chloroform (opposed the previous triplicate extraction), the reaction flask was washed with deuterated methanol and the remaining water phase was studied using proton nuclear magnetic resonance (^{1}H NMR) spectroscopy, which detected the presence of aldehyde product material.‡ The process of five extractions for each reaction also demonstrated a vast improvement in the observed yields of 59−74 % (**Table 2**, entries 3−7 and **Table 3**, entry 1) opposed to 7−11 % (**Table 2**, entry 1 and 2).

---

‡ The supporting ^{1}H NMR spectra confirming the presence of aldehydes remaining in the aqueous phase are available in the **Appendix**.

Conventional oxidation techniques employing toxic chromium salts such as chromium trioxide, chromic acid, pyridinium chlorochromate (PCC), pyridinium dichromate (PDC), Jones Reagent (requires sulfuric acid), and *o*-iodoxybenzoic acid in dimethyl sulfoxide (potentially explosive) do facilitate quantitative alcohol conversions, yet due to their toxicity have limited contemporary usage. For comparative purposes, the oxidative potential of alizarin red/ZnO/Ag-Na/TEMPO has been compared against similar oxidation systems (**Table 4**).

Table 4: Contemporary oxidising agents used to convert primary alcohols to aldehydes in the literature.
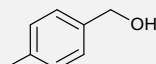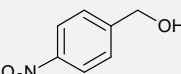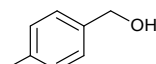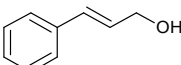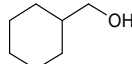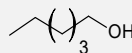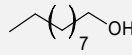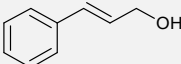
	Author	Catalyst	Alcohol	Conv. (%)	Comments
1	Yang et al.[76]	MIL-125/ Ag/g-C$_3$N$_4$		72 / 12	➢ 0.2 mmol alcohol ➢ Ethanol (solvent) ➢ O$_2$ atm ➢ 6-hour reactions ➢ 500 W xenon lamp ➢ 8 mg catalyst ➢ 97−100 % aldehyde selectivity
2	Zhang et al.[9]	Alizarin red/ TiO$_2$/TEMPO		87 / 66 / 7	➢ 0.1 mmol alcohol ➢ BTF (solvent) ➢ O$_2$ atm ➢ 10−100-hour reactions ➢ 93−99 % aldehyde selectivity
3	Sifani et al.[96]	V$_6$O$_{13}$-γ-Al$_2$O$_3$		78 / 93 / 70	➢ 0.2 mmol alcohol ➢ BTF solvent ➢ O$_2$ atm ➢ 16−24-hour reactions ➢ LED lamp ➢ 50 mg catalyst
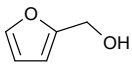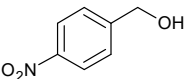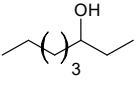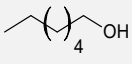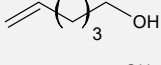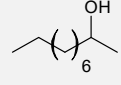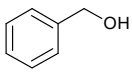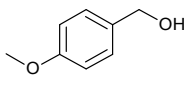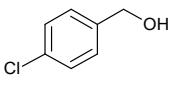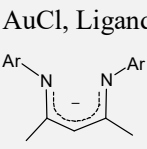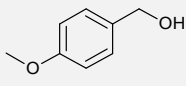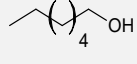
#	Author	Catalyst		Yield	Conditions
					➤ 35−100 % aldehyde selectivity
4	Corey et al.[97]	CrO$_3$-3,5-dimethyl Pyrazole complex		47	➤ 2 mmol alcohol
				98	➤ DCM (solvent)
				93	➤ O$_2$ atm
					➤ 40-minute reactions
					➤ N/P
					➤ 55 mmol catalyst
					➤ Aldehyde selectivity N/S
5	Delina et al.[98]	Pd(II) polyoxometalate		92	➤ 0.1 mmol alcohol
				44	➤ BTF (solvent)
				27	➤ O$_2$ atm
					➤ 30-minute reactions
					➤ N/P
					➤ 5 $u$mol catalyst
					➤ 56 −>99 % aldehyde selectivity
6	Lin et al.[99]	o-Iodoxybenzoic acid (IBX)		94	➤ 1.0 mmol alcohol
				95	➤ CH$_3$CN (solvent)
				97	➤ O$_2$ atm
					➤ 2.5–11-hour reactions
					➤ N/P
					➤ 1.2 mmol catalyst and 1.2 mmol acetic acid
					➤ Aldehyde selectivity N/S
7	Guan et al.[100]	AuCl, Ligand		99	➤ 1.0 mmol alcohol
				68	➤ Toluene (solvent)
					➤ O$_2$ atm
					➤ 10–48-hour reactions
					➤ N/P
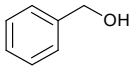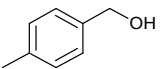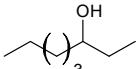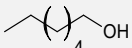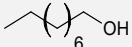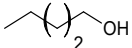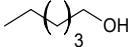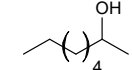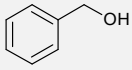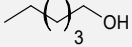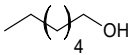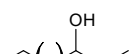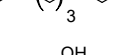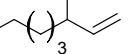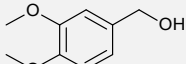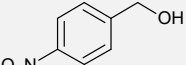
					➢ 5.0 mol % AuCl catalyst and 5.0 mol % ligand
					➢ Aldehyde selectivity N/S
8	Hunsen *et al.*[101]	Pyridinium chlorochromate (PCC)/ H_5IO_6		72 96 93	➢ 5.0 mmol alcohol ➢ CH_3CN (solvent) ➢ O_2 atm N/S ➢ 2.25-hour reactions ➢ N/P ➢ 1.19 g H_5IO_6 and 20 mg PCC catalyst ➢ Aldehyde selectivity N/S
9	Xiao *et al.*[102]	Au-Pd@HT-PO$_4$$^{3-}$		40 13	➢ 0.2 mmol alcohol ➢ BTF solvent ➢ O_2 atm ➢ 24-hour reactions ➢ 500 W tungsten lamp ➢ 100 mg catalyst ➢ 3−92 % aldehyde selectivity
10	Lu *et al.*[103]	Pt/Bi$_3$O$_3$-200		(94% acid) (90% acid) 100	➢ 2.5 mmol alcohol ➢ Water (solvent) ➢ O_2 atm ➢ 5-hour reactions ➢ N/P 200 mg catalyst 78−94 % acid selectivity
11	Li *et al.*[104]	FRPCP, TBN		94 27	➢ 0.016 mmol alcohol ➢ $C_2D_2Cl_4$ (solvent) ➢ O_2 atm ➢ 3–96-hour reactions ➢ N/P

					➤ FRPCP (3.5 mol %) and TBN (20 mol %)
					➤ Aldehyde selectivity N/S
12	Raji *et al.*[105]	(001) faceted TiO$_2$	(structure)	86	➤ 0.5 mmol alcohol
					➤ BTF (solvent)
					➤ O$_2$ atm
			(structure)	75	➤ 24-hour reactions
					➤ 40 WCFL lamp
			(structure)	70	➤ 15 mg catalyst
					➤ Aldehyde selectivity N/S
13	**This Work**	**Alizarin red/ZnO/Ag-Na/TEMPO**	(structure)	**≥ 99**	➤ **0.2 mmol alcohol**
					➤ **Water (solvent)**
					➤ **Air atm**
			(structure)	**97**	➤ **7-hour reactions**
					➤ **High-pressure sodium lamp**
			(structure)	**88**	➤ **20 mg catalyst**

After an exhaustive comparison with literature (**Table 4**), alizarin red/ZnO/Ag-Na/TEMPO has compared favourably for aromatic alcohol conversions, utilising water as the reaction solvent and photo-activated using environmentally friendly visible light. The broad substrate result when using alizarin red/ZnO/Ag-Na/TEMPO has suggested that comparable alcohol oxidations can be achieved without the need for toxic chromium salts and potentially explosive iodine reagents mentioned above (**Table 4**, entries 4, 6, and 8). Eight aliphatic alcohols were also partially oxidised using alizarin red/ZnO/Ag-Na/TEMPO (**Table 3**), which has proven the photocatalytic system to be a viable oxidant of un-activated alcohols. The results from **Table 2** and **Table 3** are currently being drafted for publication.

3.3.1. Spectroscopic and Computational Investigations of Alizarin red/ ZnO/Ag-Na/TEMPO

With reference to the original alizarin red/ZnO/Ag/TEMPO photocatalytic report,[59] Jeena and Robinson confirmed the presence of TEMPO and alizarin red dye radical production (during the irradiation period) using electron paramagnetic resonance spectroscopy (EPR, **Figure 41**).[60]
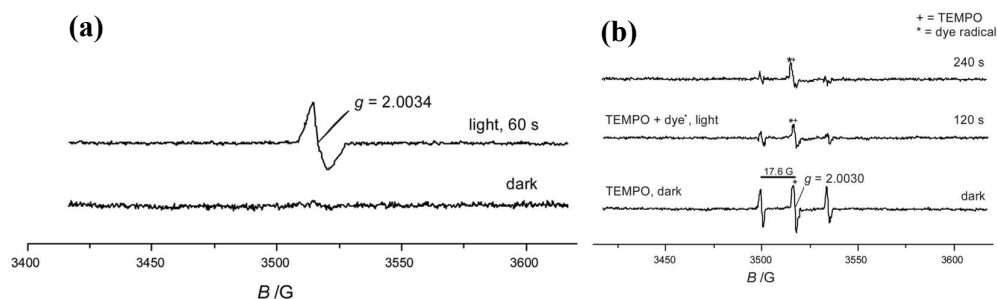
Figure 41: Electron paramagnetic resonance spectra of alizarin red (a) and TEMPO (b) radicals. Adapted from V. Jeena, R. S. Robinson, Chemical Communications 2012, 48, 299−301 with permission of The Royal Society of Chemistry.

The singlet peak (g = 2.0034) in **Figure 41** (a) demonstrated the generation of an alizarin red dye radical after its photo-excitation and electron capture by the TEMPO radical, which was later reduced to the *N*-oxoammonium salt of TEMPO as depicted in **Figure 41** (b). **Figure 41** (b) has depicted the time-diminishing TEMPO radical (g = 2.0030) until equilibrium (note 240 seconds) with the *N*-oxoammonium salt (the active oxidant of the photocatalytic system).

Despite Jeena and Robinson[60] utilising EPR spectroscopy to confirm the dynamic electron transfer between the alizarin red sensitiser and the TEMPO radical, no spectroscopic data was presented to verify the electron migration from the conduction band of alizarin red and into the conduction band of zinc oxide. Studying the literature[64],[106] identified pertinent research information, from which relevant instrumental techniques (photoluminescence and UV/Vis spectroscopy) and a density functional theory (DFT) study were identified to possibly confirm the electron migration across the alizarin red-zinc oxide interface.

3.3.1.1. Tracing Electron Migrations across the Alizarin Red-Zinc Oxide Bridge via Photoluminescence Spectroscopy.

Shifu *et al.*[64] developed a *Z*-scheme NaNbO$_3$/WO$_3$ photocatalyst to photo-degrade chromium (VI, Cr$_2$O$_7{}^{2-}$), methylene blue, and rhodamine B; during the photocatalytic cycle, hydroxyl radicals were produced, and the authors detected them using a terephthalic acid-photoluminescence spectroscopy technique. Terephthalic acid was reported to quench any localised hydroxyl radicals in solution and form 2-hydroxy-terephthalic acid, which produced a sharp photoluminescence emission signal (425 nm). This literature finding was of great significance as it suggested a plausible approach to detect transient species.

In the alizarin red/ZnO/Ag/TEMPO photocatalytic system previously proposed by Jeena and Robinson,[59] photo-generated electrons on the surface of alizarin red were transferred to the conduction band of zinc oxide after the powder was irradiated ($\lambda > 450$ nm) at which point electrons were quenched by silver (I) ions in solution. This was believed to be a sequential process as graphically summarised in **Figure 42**.
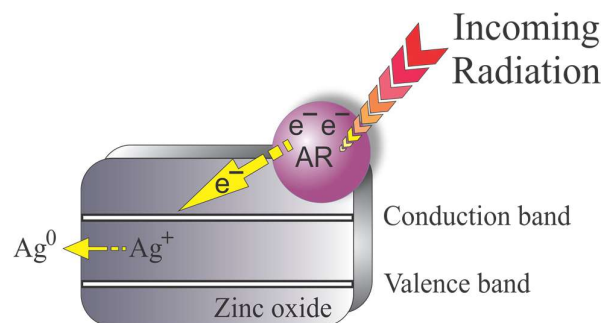
Figure 42: The proposed electron migration from alizarin red (AR) to the conduction band of zinc oxide and lastly to silver ions (Ag$^+$) that are reduced to metallic silver (Ag).

In an article published by Han *et al.*[106] zinc oxide was reported to possess a defect, which produced strong emission signatures at 500 nm (2.48 eV) whilst being irradiated with a 325 nm He-Cd laser (**Figure 43**).
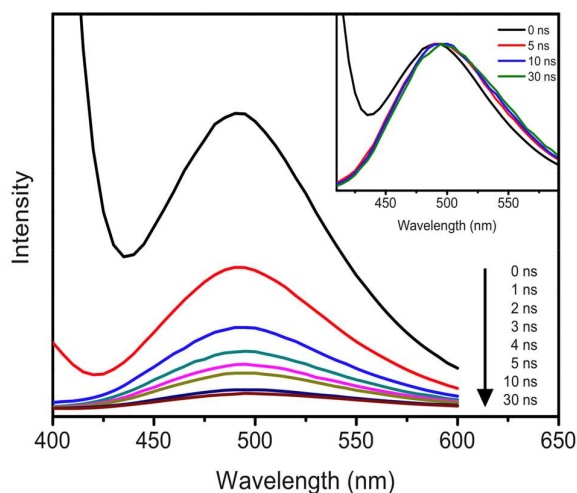
Figure 43: 500 nm emission signature from defect sits of hexagonal cone-like ZnO as proposed by Han *et al.* using time-resolved photoluminescence spectroscopy. The intensities of the emission spectra decrease as the detection time is increased. The insert depicts a minor red shift of the UV emission peak from 0 ns to 30 ns. Reprinted from Han *et al.*, Journal of Applied Physics 107, 084306 (2010), Copyright 2010 American Institute of Physics.

Arising from the observation by Han and co-workers,[106] a secondary electronic transfer protocol may have existed between the surfaces of alizarin red and zinc oxide. When electrons in the HOMO energy level of alizarin red were photo-excited, they could potentially relax into the lower-energy conduction band state of zinc oxide. Previous assumptions as outlined in **Figure 42** suggested that the electron was solely quenched by silver (I) ions. However, the possibility for electrons to fall into the conduction band of zinc oxide and further relax into defect sites of the metal oxide seemed plausible.

In order to evaluate the possibility of electrons (from alizarin red) relaxing into the defect sites of zinc oxide, the following instrumental procedures were followed using photoluminescence spectroscopy:

1) Excite non-sensitised zinc oxide in a fluorescence spectrometer equipped with a 325 nm He-Cd laser. This process would excite electrons from the valence band of zinc oxide and into its conduction band. Monitoring the emission responses once the exciton pair re-combined would determine the

major recombination centres *i.e.* the photoelectron returning to the valence band *or* relaxing into a defect site.

2) Repeat the procedure as outlined in point 1) above using alizarin red-sensitised zinc oxide and a 325 nm He-Cd laser. In this case, the electrons of alizarin red would be ejected into the conduction band of zinc oxide after photo-excitation (**Figure 44**).
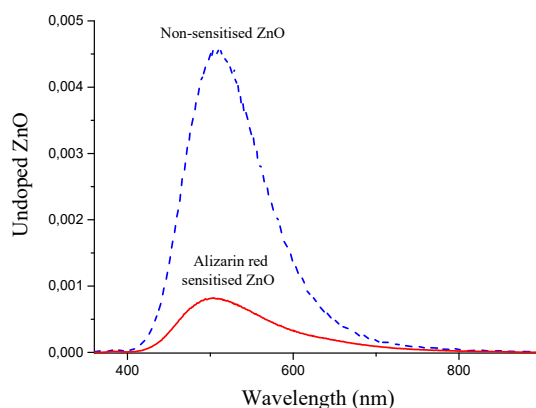
Figure 44: Photoluminescence spectra of alizarin red-sensitised (solid red) and non-sensitised ZnO (dashed blue).

Without alizarin red adsorbed onto the surface of zinc oxide, zinc oxide exciton pairs were free to recombine at the defect site (**Figure 44**, dashed blue curve, 507 nm). Han *et al.*[106] reported that zinc oxide nanoparticles have a known defect site at 500 nm, which corresponded well with the findings recorded in **Figure 44**. After zinc oxide was sensitised with alizarin red, a significant decrease in the peak intensity was observed (**Figure 44**, solid red curve).

It is acknowledged in the literature that various mechanisms for zinc oxide's defect emission (507 nm, as indicated in **Figure 44**) have been proposed.[107],[108],[109],[110] One possible scenario has been discussed in this work, with planned future studies to quantify it further.

At this point, a potential electron relaxation mechanism was postulated to exist between alizarin red and zinc oxide during a photo-excitation period. This has been graphically represented in **Figure 45** and will be described in detail below.
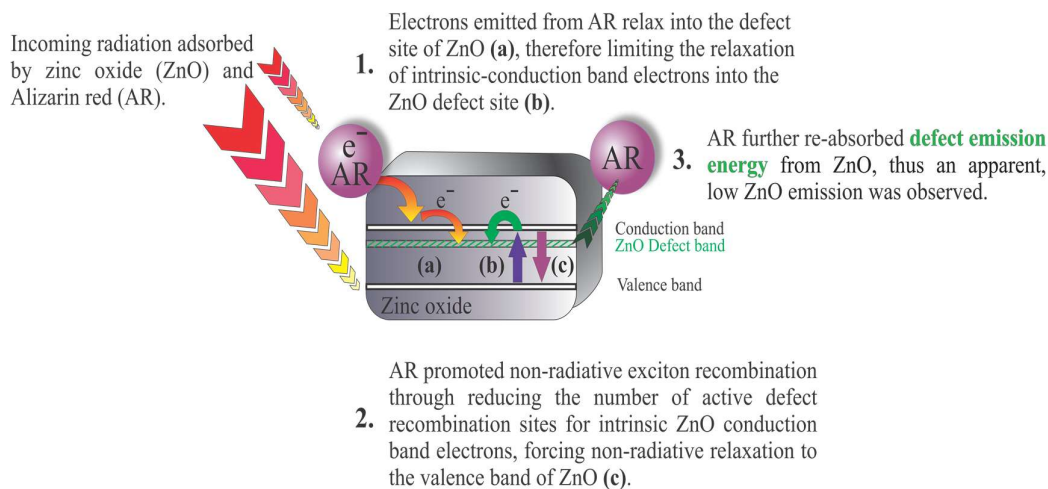
Figure 45: A three-stage graphical representation for the suggested mechanism of exciton recombination on the surface of alizarin red (AR) sensitised zinc oxide. Due to the visible light absorbing properties of alizarin red, emitted green light from ZnO was expected to be re-absorbed by alizarin red.

In order to lend additional support to the proposed mechanism (**Figure 45**), additional spectroscopic evidence was required.

From the information that was collected during the photoluminescence spectroscopy study (**Figure 44**), the existence of the 507 nm emission signature for alizarin red-sensitised zinc oxide (**Figure 44**) had almost masked the intrinsic exciton emission of zinc oxide's band gap (literature band gap of 3.26 eV, 383 nm[111]). However, after careful inspection of the raw photoluminescence data, an emission peak at 383 nm was observed as illustrated in **Figure 46**.
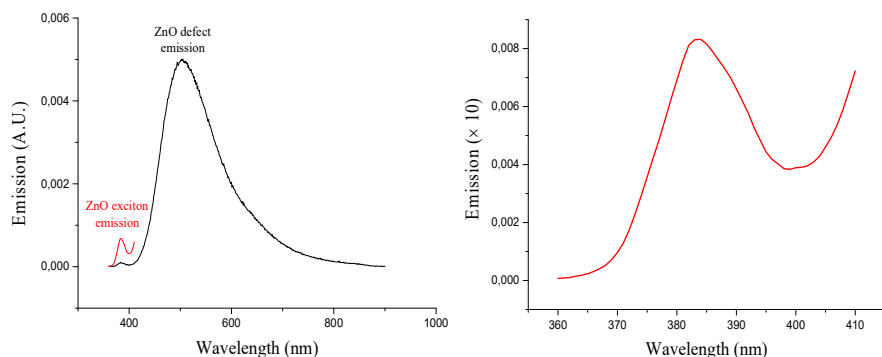
Figure 46: Intrinsic band gap exciton of alizarin red-sensitised zinc oxide (left) and magnified (×10, right).

This result confirmed that a very weak exciton band emission had been recorded for zinc oxide's intrinsic band gap during the irradiation process but the emission profile (**Figure 44**) emphasised that the defect site on zinc oxide was the major contributing factor towards accepting relaxing electrons from the excited state of alizarin red.

In an attempt to further clarify the migration pathway of excited electrons from the valence band to the conduction band of zinc oxide, photoluminescence spectra of the excitonic peaks for non-sensitised and alizarin red-sensitised zinc oxide were obtained (**Figure 47**).
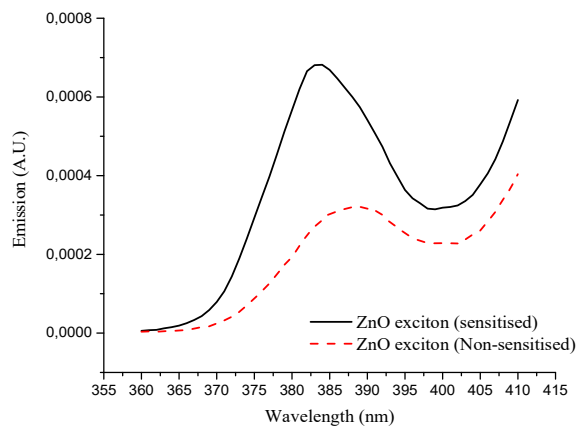
Figure 47: Excitonic peaks for non-sensitised (solid black curve) and alizarin red-sensitised zinc oxide (dashed red curve). The larger peak intensity of the alizarin red-sensitised zinc oxide was an indication of more excitonic recombinations occurring upon irradiation.

The excitonic (383 nm) emission for non-sensitised zinc oxide was observed at a lower emission intensity compared to alizarin red-sensitised zinc oxide (*i.e.* zinc oxide's excitonic recombinations were more active when alizarin red was adsorbed onto the surface). This result lent support to further motivate that alizarin red was interacting with the defect sites of zinc oxide. The alizarin red suppressed the availability of zinc oxide's photogenerated electrons to relax into the defect site, thus forcing them to fall back into the valence band.

The photoluminescence spectra in **Figure 44** depicted an approximate five-fold decrease in emission intensity after zinc oxide was sensitised with alizarin red. This was understood to originate from the alizarin red absorbing the energy (507 nm) emitted from zinc oxide's defect site (**Figure 45**). The five-fold decrease in zinc oxide's emission at 507 nm was subsequently explored using powder diffuse reflectance UV/Vis spectroscopy in absorbance mode on a Shimadzu UV-2600 UV/Vis spectrophotometer to identify if a five-fold absorbance increase between alizarin red-sensitised zinc oxide and non-sensitised zinc oxide was observed. The spectrophotometer was equipped with an integrating sphere attachment.

3.3.1.2. Monitoring the Absorption Bands of Alizarin Red-Sensitised Zinc Oxide using Powder Diffuse UV/Vis Spectroscopy.

The absorbance spectra of alizarin red-sensitised zinc oxide and non-sensitised zinc oxide were collected on a Shimadzu UV-2600 equipped with an integrating sphere attachment (**Figure 48**).
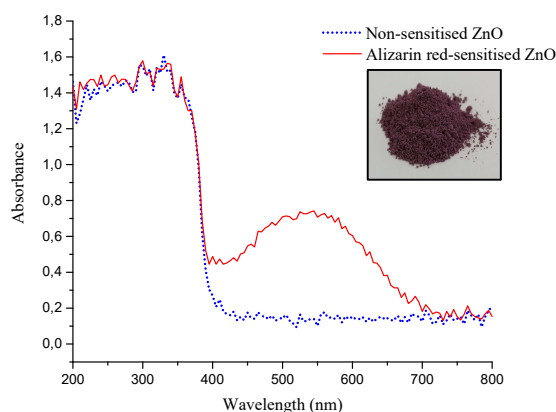
Figure 48: Powder UV/Vis absorption spectra of alizarin red-sensitised zinc oxide (solid red line) and non sensitised zinc oxide (dotted blue line). Inset figure of alizarin red-sensitised ZnO.

Alizarin red-sensitised zinc oxide possessed an absorption peak centralised at 535 nm, which was ascribed to the absorption of alizarin red in the visible region. However, in consideration of the relative absorption values for alizarin red-sensitised zinc oxide and non-sensitised zinc oxide at 535 nm, the intensity of the absorbance difference (0.15 to 0.71) corresponded well with the five-fold emission decrease as previously observed in the photoluminescence studies (**Figure 44**).

3.3.1.3. DFT Simulations Across the Alizarin Red-Sensitised Zinc Oxide Interface.

After collecting emission and absorption spectra of alizarin red-sensitised zinc oxide and non-sensitised zinc oxide, density functional theory (DFT) simulations were performed to further probe the electron migration patterns between alizarin red and alizarin red-sensitised zinc oxide using singlet excited states of the respective molecules (**Figure 49**). Gaussian (09W at the CAM-B3LYP/6-31G[d,p])[112],[113],[114],[115],[116],[117] level of theory was used for all the simulations.
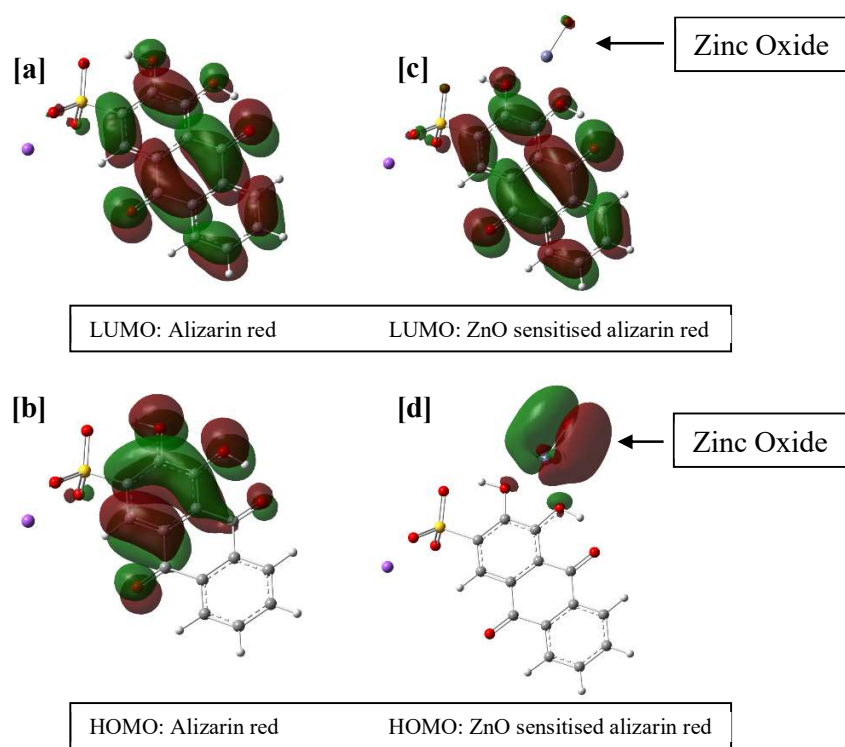
Figure 49: Singlet excited states of alizarin red and alizarin red-sensitised zinc oxide.

An electron density shift was observed within alizarin red after modelling the coordination of alizarin red onto zinc oxide from the binding of two hydroxy groups on alizarin red (notice the LUMO state of alizarin red in **Figure 49** [a]). Once alizarin red was photo-excited with $\lambda > 450$ nm, the electron density shifted to the catecholate moiety of the alizarin red molecule (**Figure 49**, [b]). After alizarin red was physi-adsorbed onto the surface of zinc oxide, a uniform electron density was observed across the entirety of the alizarin red/ zinc oxide complex (**Figure 49**, [c]). However, when alizarin red-sensitised zinc oxide was photo-excited ($\lambda > 450$ nm), the HOMO state proceeded to reside over the alizarin red-zinc oxide coordination site (**Figure 49**, [d]).

3.3.2. Concluding Remarks to Alizarin Red-Sensitised Zinc Oxide

A refined Alizarin red/ZnO/Ag-Na/TEMPO photocatalytic system was developed that mediated an array of aromatic, cyclic, and traditionally unreactive aliphatic alcohol oxidations. The summation of the research has concluded five pertinent findings for the photocatalytic system governing the alcohol oxidations:

> The silver loadings have been drastically reduced from 18 to 1 equivalent of Ag from the previous literature.[59]
>
> Alizarin red/ZnO/Ag-Na/TEMPO has demonstrated a wide alcohol substrate scope oxidation.
>
> Alizarin red/ZnO/Ag-Na/TEMPO was also capable of mediating the oxidation of challenging aliphatic alcohol conversions.
>
> The controlled regioselective oxidation of 2,2-dimethyl-1,3-propanediol to 2,2-dimethyl-3-hydroxypropionaldehyde was also noteworthy.
>
> Relatively inexpensive and biologically non-toxic catalytic materials in earth abundant water were utilised in the photo-oxidative scheme.

It has been noted that extracting the aldehyde product requires further improvement, and future studies to recycle the alizarin red-sensitised zinc oxide components are being considered.

In conclusion to the instrumental studies for the photoelectronic pathways between alizarin red and zinc oxide, the proposed literature mechanisms for the 507 nm defect emission in ZnO could not be ignored.[107],[108],[109],[110] Although, the photoluminescence, powder diffuse reflectance UV/Vis spectroscopy, and density functional theory results have all lent support for the mechanism described in **Figure 45**. The two key observations from the studies were:

1) A five-fold emission decay and a corresponding absorption at 535 nm after alizarin red was adsorbed onto the surface of zinc oxide, substantiated a re-absorption of emitted radiation by alizarin red from zinc oxide's defect site.

2) Computational studies further identified an electronic migration pathway from the catecholate moiety of alizarin red, across to the alizarin red/ zinc oxide complex, and subsequently over the alizarin red-zinc oxide coordination site after visible-light irradiation was introduced.

Future studies with additional photoluminescence, Raman and X-ray photoelectron spectroscopy, and different organic dye sensitisers may be considered to provide further evidence towards a refined model.

3.4. Sensitising Titanium Dioxide with Transition Metals.

After completing the alizarin red/ZnO/Ag-Na/TEMPO study, the attention was focused towards synthesising a small library of novel, visible light-sensitive titanium dioxide materials based on period three transition metals (Cu, Ni, and Mn). In Chapter 3.4 discussed below, five main research objectives were explored:

➢ Background to the development of the copper, nickel and manganese titanium dioxide derivatives.

➢ An attempted synthesis of three titanium dioxide derivatives, namely TMT-Cu (copper functionalised TiO_2), TMT-Ni (nickel functionalised TiO_2) and TMT-Mn (manganese functionalised TiO_2). *

➢ Evaluating the red shifted character of TMT-Cu, TMT-Ni and TMT-Mn, followed by assessing the oxidative potentials of TMT-Cu, TMT-Ni and TMT-Mn as photo-organic oxidants in proof-of-concept alcohol oxidation studies.

➢ Should a target be identified, various alcohols would be tested using the chosen photocatalyst.

➢ The photocatalytic materials would be instrumentally characterised in order to interpret the photo-physical properties of the materials.

3.4.1. Background to Metal Functionalised Titanium Dioxide in Photo-oxidation Studies

Titanium dioxide has continued to be well researched in the literature as a highly active, chemically stable, chemically selective and easy-to-synthesise metal oxide.[118],[119] Yet its large band gap (3.20−3.23 eV)[74] has restricted the metal oxide's scope to ultraviolet light for photo-excitation.

---

* The methodology used to synthesise TMT-Cu, TMT-Ni, and TMT-Mn has been reported in **chapter 6.5.1**.

Numerous articles have reported the functionalisation of titanium dioxide with period three transition metals; Fe-TiO$_2$,[120],[121],[122] Mn-TiO$_2$,[123],[124],[125] Ni-TiO$_2$,[126],[127],[128] Cu-TiO$_2$,[129],[130],[131] Zn-TiO$_2$[132],[133],[134] (as shown below in **Figure 50**), and have demonstrated shifting of titanium dioxide's photo-reactivity into the visible region with various degrees of success. In 2014, Wang *et al.*[135] reported that attenuating titanium dioxide's crystal structure with metal dopants afforded photocatalysts with narrowed band gaps (**Figure 50**).
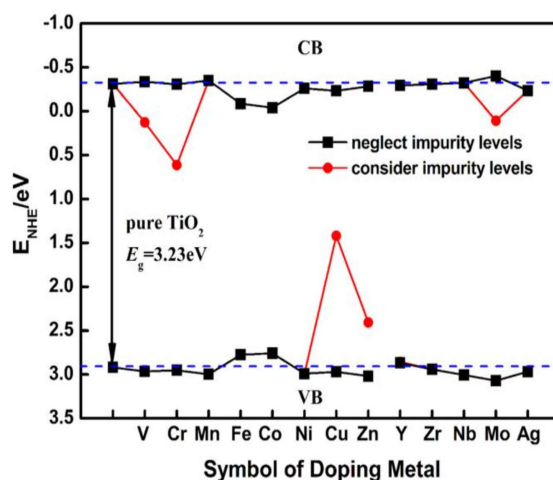
Figure 50: Band gaps of various metal functionalised titanium dioxide species. The figure has depicted the impurity level positionings of period 4 and 5 metal ion species (V to Ag) relative to the valence and conduction band edges of titanium dioxide after doping. Reprinted from Wang *et al.*[135] Copyright 2014 licensee Springer.

As noted above, information was available on metal-doped titanium dioxide (M-TiO$_2$). The objective of the proposed research was not however, to re-engineer a metal-doped titanium dioxide species but rather develop a compounded titanium dioxide material of the general molecular formula 'A$_3$TiO$_5$–a pseudo perovskite material' with three transition metals (A); Cu (TMT-Cu), Ni (TMT-Ni) and Mn (TMT-Mn), respectively. It was observed in the literature that very little information was published on the three A$_3$TiO$_5$ type derivatives.[136],[137],[138] However, there was no literature on the A$_3$TiO$_5$ concept that was observably reported to mediate alcohol oxidations in photocatalytic environments.

A second option was to explore $ATiO_3$ type materials (where A = a period three transition metal). However, Kanhere and Chen,[139] published an article entitled '*A Review on Visible Light Active Perovskite-Based Photocatalysts.*' The text described methods to functionalise titanium dioxide with Pb, Co, Fe, Ni, Mn and Sr and form $PbTiO_3$, $CoTiO_3$, $FeTiO_3$, $NiTiO_3$, $MnTiO_3$, and $SrTiO_3$ materials. Therefore, A_3TiO_5 materials were studied due to their limited reported applications.

Numerous synthetic methodologies are reported in the literature; sol-gel, microwave, hydrothermal, spray pyrolysis, co-precipitation and combustion synthesis as suitable techniques to develop mixed metal oxides.[140],[141],[142],[143] However, effectively reproducing sample preparations without the need for sophisticated laboratory techniques or equipment, has made the *sol-gel* approach highly desirable.

The three prospective transition metal functionalised titanium dioxide semiconductors (Cu_3TiO_5, Ni_3TiO_5, and Mn_3TiO_5, hereafter listed as TMT-Cu, TMT-Ni and TMT-Mn, respectively) were therefore synthesised using a facile sol-gel approach. In a typical reaction, organic titanium precursors were dissolved in ethanol and aged overnight. After forming a mixture with a gel-like consistency, the precipitates were filtered, oven dried, and calcinated.

3.4.2. Optical Measurements and Photoactivating the Band Gap Energies of TMT-Cu, TMT-Ni, and TMT-Mn.

TMT-Cu, TMT-Ni and TMT-Mn were initially screened with powder diffuse reflectance UV/Vis spectroscopy, operating in absorbance mode to assess if red shifted absorbances were observed after incorporating transition metals into titanium dioxide (**Figure 51**). If TMT-Cu, TMT-Ni or TMT-Mn presented with red shifted absorbance values, the viable photocatalyst(s) would be tested in proof-of-concept alcohol oxidation studies. Subsequent band gap values would also be determined by the method described by PerkinElmer, *vide infra*.

An applicate note published by PerkinElmer describes a method to easily measure titanium dioxide's band gap using a UV/Vis spectrometer equipped with an integrating sphere.[144] The process of determining the 'cut-off' point where the absorbance

wavelength of titanium dioxide was at a minimum from extrapolating the straight line of the absorption curve to the *x*-axis (wavelength) was discussed. From the equation: $E = hc/\lambda$, the band gap energy (E in eV) could be determined.
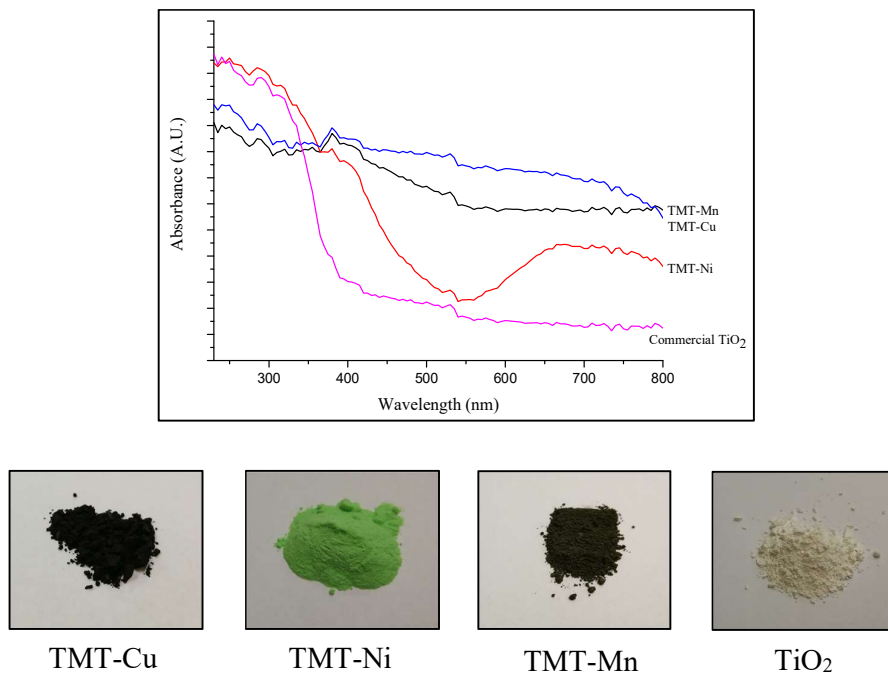
Figure 51: Powder diffuse reflectance UV/Vis spectra of TMT-Cu, TMT-Ni, and TMT-Mn. The spectra depict higher absorbances for TMT-Cu, TMT-Ni, and TMT-Mn than commercial TiO_2 at wavelengths greater than 343 nm

After collecting the powder diffuse reflectance UV/Vis spectroscopic data (**Figure 51**) for TMT-Cu, TMT-Ni, and TMT-Mn, several pertinent findings were evident. TMT-Cu, TMT-Ni, and TMT-Mn all presented with optical absorbances above commercial TiO_2 from wavelengths of 343 nm up to 800 nm.

Absorbances above 800 nm suggested that the titanium dioxide derivatives were absorbing light within the visible spectrum, far exceeding the limited capacity of non-functionalised titanium dioxide to absorb wavelengths higher than 400 nm.

TMT-Cu and TMT-Mn also depicted no band cut-off wavelength between 300−600 nm. The disadvantage of having no band cut-off wavelength within this region was an

indication that the band gap structures of TMT-Cu and TMT-Mn were capable of being photo-excited by visible-light wavelengths greater than 650 nm.

The ability of these materials to absorb visible red-infrared light would suggest that TMT-Cu and TMT-Mn would not possess the ability to grasp incoming radiation of high enough energy (low wavelengths) to support photoredox transformations. However, photons were also observed to absorbed at shorter frequencies (wavelengths < 400 nm), which were postulated to originate from a potential TiO_2 phase that was not expected during the synthesis of the TMT-Cu and TMT-Mn materials.

At which point, a proof-of-concept alcohol oxidation study was explored using TMT-Cu, TMT-Ni and TMT-Mn (**Table 5**). An OSRAM® Ultramed UH High-Pressure lamp was chosen as the appropriate irradiation source (**Figure 52**).
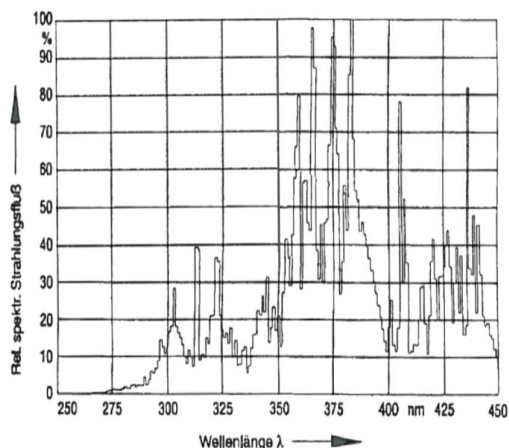
Figure 52: Emission spectrum recorded from OSRAM® Ultramed UH-High Pressure Lamp.Sourced from product brochure.

The OSRAM® UH-High Pressure lamp was chosen for its broad emission signature across the ultraviolet-deep visible region (300−450 nm). Titanium dioxide (anatase) has a known band gap of 3.20 eV (387.4 nm).[74] Therefore to ensure the excitation of the unknown band gaps of the metal (Cu, Ni, and Mn) functionalised titanium dioxide materials, an ultraviolet source was utilised in the preliminary alcohol oxidation investigations (**Table 5**).

Table 5: Benzyl alcohol oxidation attempts using TMT-Cu, TMT-Ni and TMT-Mn.[a]

Entry	Catalyst	Aldehyde Yield (%)[b]
1	TMT-Cu	Trace
2	TMT-Ni	Trace
3	TMT-Mn	Trace

[a]Reaction conditions: 1 mmol benzyl alcohol, 40 mg each of metal (Cu, Ni, and Mn) functionalised titanium dioxide, acetonitrile solvent (3 mL) and ultraviolet light irradiation (6 hours). [b]Yields determined using ^{1}H NMR peak integrations. NMR spectra are available in the **Appendix**.

The results from **Table 5** demonstrated that TMT-Cu, TMT-Ni, and TMT-Mn were incapable of mediating the oxidation of benzyl alcohol and only trace yields of benzaldehyde were detected using ^{1}H nuclear magnetic resonance (NMR) spectroscopy.

Despite the promising red shifted wavelengths of TMT-Cu, TMT-Ni and TMT-Mn compared to commercial TiO_2 (**Figure 51**), the proof-of-concept alcohol oxidations did not substantiate any viable photocatalyst. As previously noted with regards to **Figure 51**, photons were being absorbed at short frequencies (wavelengths < 400 nm), which were postulated to originate from an un-expected TiO_2 phase in TMT-Cu, TMT-Ni, and TMT-Mn. The unknown compositions of TMT-Cu, TMT-Ni, and TMT-Mn were subsequently examined using powder X-ray diffraction and phase mapping analyses.

3.4.3. Detecting and identifying the crystalline components in the Proposed 'Cu_3TiO_5, Ni_3TiO_5, and Mn_3TiO_5' materials.

The absorbance profiles for TMT-Cu, TMT-Ni and TMT-Mn from the powder diffuse reflectance UV/Vis spectroscopic study lent support to suggest that a potential TiO_2 phase was unexpectedly present. To assess the composition of TMT-Cu, TMT-Ni and TMT-Mn, the three materials were studied using powder X-ray diffraction to detect crystalline materials besides the desired 'A_3TiO_5' (**Figure 53**).
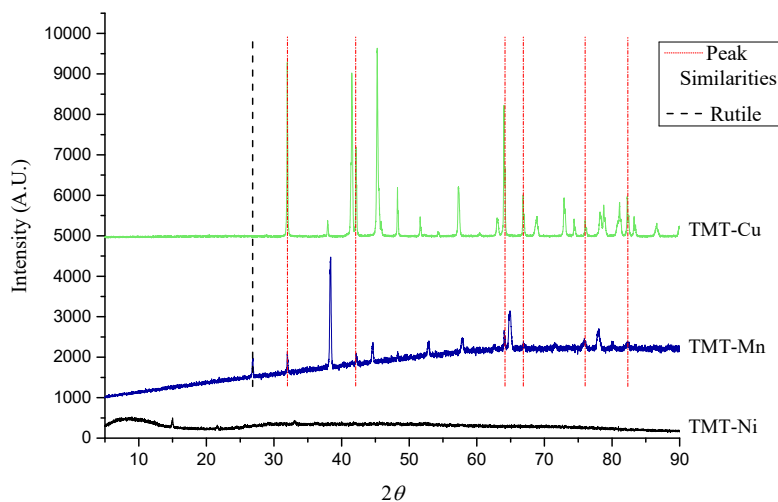
Figure 53: Powder X-ray diffractograms of Cu_3TiO_5 Ni_3TiO_5, and Mn_3TiO_5.

After collecting powder X-ray diffractograms of TMT-Cu, TMT-Ni, and TMT-Mn, the 2θ peaks in **Figure 53** confirmed that TMT-Ni had no crystalline form after studying the material between 2θ values of 5−90. Amorphous titanium dioxide analogues have been reported in the literature to partially assist alcohol oxidation studies; however, when solely used as the chosen photocatalytic material, the amorphous powder hampered the alcohol oxidation reaction.[145] Due to poor crystallinity, TMT-Ni was identified as an unsuitable, amorphous solid-state material to facilitate alcohol oxidation studies. No further instrumental characterisation of TMT-Ni was therefore conducted. The nature of the TMT-Cu and TMT-Mn powders needed further characterisation since no correlating literature evidence could assign the materials to the desired 'A_3TiO_5' crystalline phase. Powder X-ray diffraction phase matching was investigated to relate the peak lines of the unknown 'Cu_xTiO_y' and 'Mn_xTiO_y' with potentially known phases (**Figure 54**).
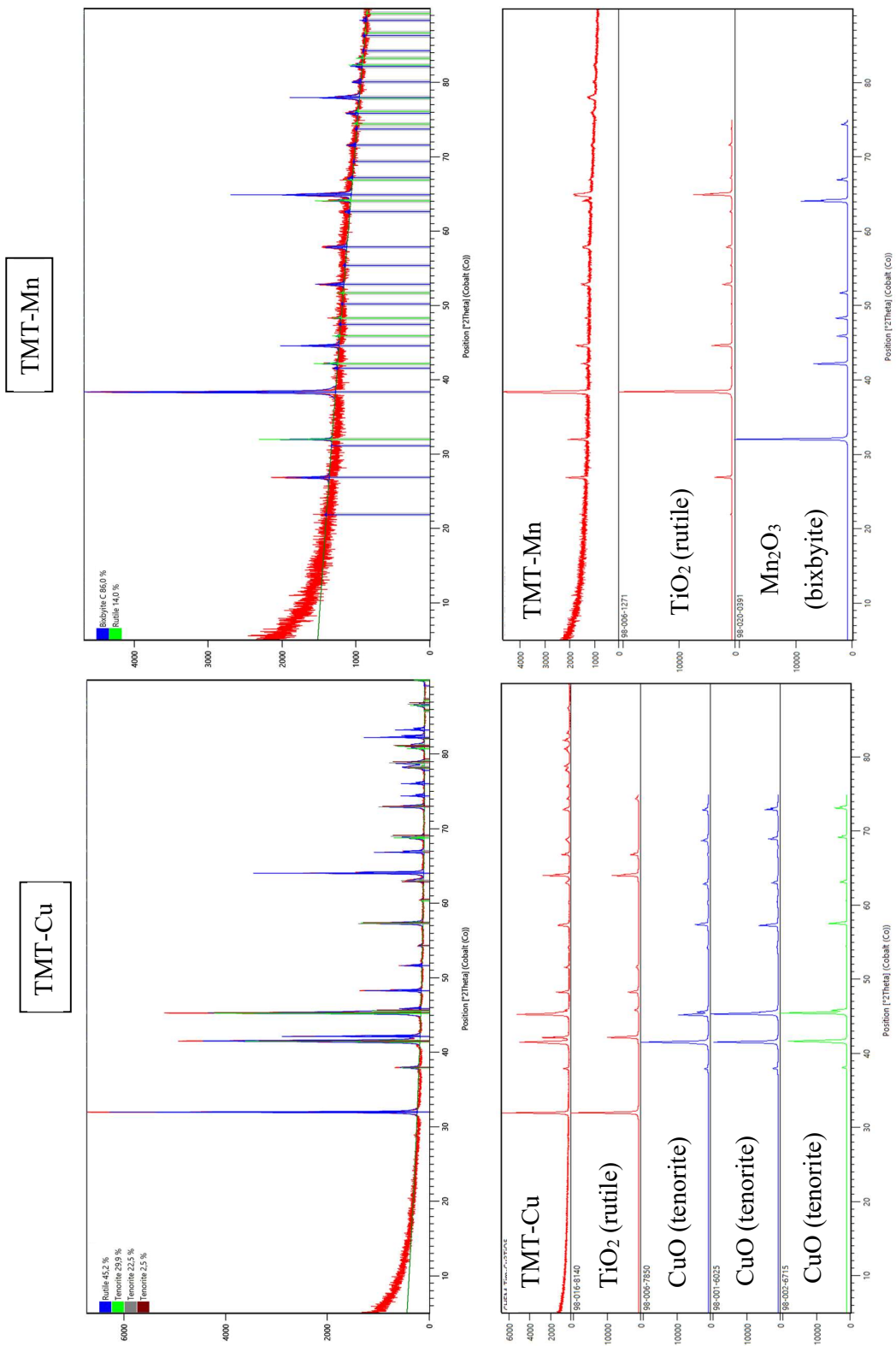
Figure 54: Phase mapping of TMT-Cu and TMT-Mn to TiO_2, CuO, and Mn_2O_3, respectively (top) and individual phases (bottom).

TMT-Cu and TMT-Mn were identified on HighScore Plus (version 3.0.4) software using mineral phase identifications and the crystal structures were subsequently optimised using the Rietveld refinement process. The results from **Figure 54** led to conclude that the TMT-Cu and TMT-Mn were not the desired A_3TiO_5 titanium dioxide derivatives but rather mixtures of CuO, TiO_2 (rutile) and Mn_2O_3, TiO_2 (rutile), respectively. Referenced data used by HighScore Plus to compare the phases of CuO, TiO_2 (rutile), and Mn_2O_3 were obtained from the literature.[146],[147],[148],[149],[150],[151]

3.4.4. Concluding Remarks to the A_3TiO_5 Chapter on Mixed-Metal Oxides.

Various literature information was identified that supported the powder diffuse reflectance UV/Vis spectroscopic and powder X-ray diffraction data of TMT-Cu, TMT-Ni and TMT-Mn. Deng *et al.*[123] reported similar observations after titanium dioxide was functionalised with various elements (Eu, W, La, Nd, C, N and Co).[152],[153],[154],[155],[156] Comparable red shifted absorption profiles of metal functionalised titanium dioxide were observed, yet (as noted in the present research, **Figure 51**) the photocatalysts were unable to demonstrate an improved visible-light photocatalytic activity. The data obtained from the literature [152],[153],[154],[155],[156] led the authors to conclude that the poor visible light photo-response of the functionalised titanium dioxide arose from defect sites. The defect sites may have initiated the auto recombination of excitons at the surfaces' of the titanium dioxide materials and hence the poor visible-light photo-response. Yan *et al.*[157] further substantiated the disadvantage of functionalising titanium dioxide with only a single transition metal as the metallic species was reported to hinder charge mobility and hence the photo-current generation on the semiconductor's surface.

Based on the information obtained from the powder diffuse reflectance UV/Vis spectroscopy study, the UV-component of the OSRAM® UH-High Pressure lamp was not required to photo-activate the band gaps of TMT-Cu, TMT-Ni, and TMT-Mn, as all three materials were absorbing visible light wavelengths. In addition, the powder X-ray diffraction phase mapping analyses confirmed that the desired A_3TiO_5 type structure was not obtained in either of the three examples (TMT-Cu, TMT-Ni, and TMT-Mn).

In further consideration of the literature reports by Deng *et al.*,[123] and Yan *et al.*,[157] a replacement semiconductor was required that was photo-activated by visible light through appropriate metal functionalising agents.[*]

3.5. Sourcing an Appropriate Visible-Light Irradiation Source

Whilst attempting to further understand the photo-inefficiencies of the TMT-Cu, TMT-Ni and TMT-Mn materials, a pertinent oversight of the ultraviolet irradiation setup used in **Table 5** was identified after accessing a literature article published by Pavan *et al.*[158] The authors[158] described the auto-oxidation effect of ultraviolet radiation to over-oxidise benzyl alcohol (without the addition of a semiconductor). On reflection of the literature, numerous researchers have disregarded the potential contribution from ultraviolet light assisted auto-oxidations. RuO_2/TiO_2 and g-C_3N_4/TiO_2 compounded semiconductors have been developed for benzyl alcohol photo-oxidation reactions, and methylene blue, rhodamine B, acridine orange, and 2,4-dichlorophenol photo-degradation studies using both ultraviolet and visible light irradiation, respectively.[159],[160] Superior yields were observed while using ultraviolet irradiation conditions and were reported to occur from enhanced photo-activity at the semiconductor surface but the auto-oxidation contribution from ultraviolet irradiation was not considered.

As noted in **Table 5**, ^{1}H NMR spectroscopy was utilised to quantify the desired product of the photocatalytic reactions, *viz.* benzaldehyde. Despite the spectral data excluding the presence of benzoic acid, hydrogen ions are known to exchange with water molecules in the analytical solvent (deuterated chloroform was used in all experiments, $CDCl_3$), thus potentially masking the benzoic acid 'OH' signal.

---

[*] At the time of the photoluminescence analyses, the powder X-ray diffractometer was non-operational as such. Considering the current phase mapping results, the photoluminescence data has been made available in the **Appendix**.

Therefore, gas chromatography-mass spectrometry (GC-MS) was utilised to identify all the oxidised content from the ultraviolet light-facilitated reactions conducted in **Table 5**. In a test reaction, benzyl alcohol was irradiated (using identical conditions listed in **Table 5**) with and without a photocatalyst, and a startling 72% yield of benzoic acid was detected chromatographically without a photocatalytic material. Despite the photocatalytic reactions The findings from the un-catalysed photo-oxidation of benzyl alcohol confirmed the research suggested by Pavan *et al.*[158] and also validated that a new irradiation source was required before continuing with the photo-oxidation studies. Despite TMT-Cu, TMT-Ni, and TMT-Mn not facilitating the oxidation of alcohols to aldehydes, the ultraviolet photo-oxidation process inadvertently identified one unforeseen consideration. The fact that the OSRAM® Ultramed UH High-Pressure lamp caused benzyl alcohol to auto-oxidise to the overly oxidised derivative (benzoic acid, with no selectivity) confirmed that the ultraviolet lamp was not suitable for the proposed investigations. Since wide band gap semiconductors (band gap > 2.0 eV) require ultraviolet irradiation to excite the intrinsic band gap, literature has overlooked the possibility of ultraviolet light to initiate unwanted photo-oxidation processes. Therefore, an appropriate irradiation source that could photo-excite the band gap of semiconductors without causing an independent photo-oxidation of the alcoholic reactants was of primary concern. A visible-light irradiation source that was cheap to construct, non-carcinogenic (no UV-A or UV-B emissions) and easy to access would also prove noteworthy for further photocatalytic studies.

Numerous potential irradiation sources were identified within the literature; tungsten halide, light emitting dioxides (LEDs), sodium lamps and simulated solar xenon sources (**Figure 55)**.
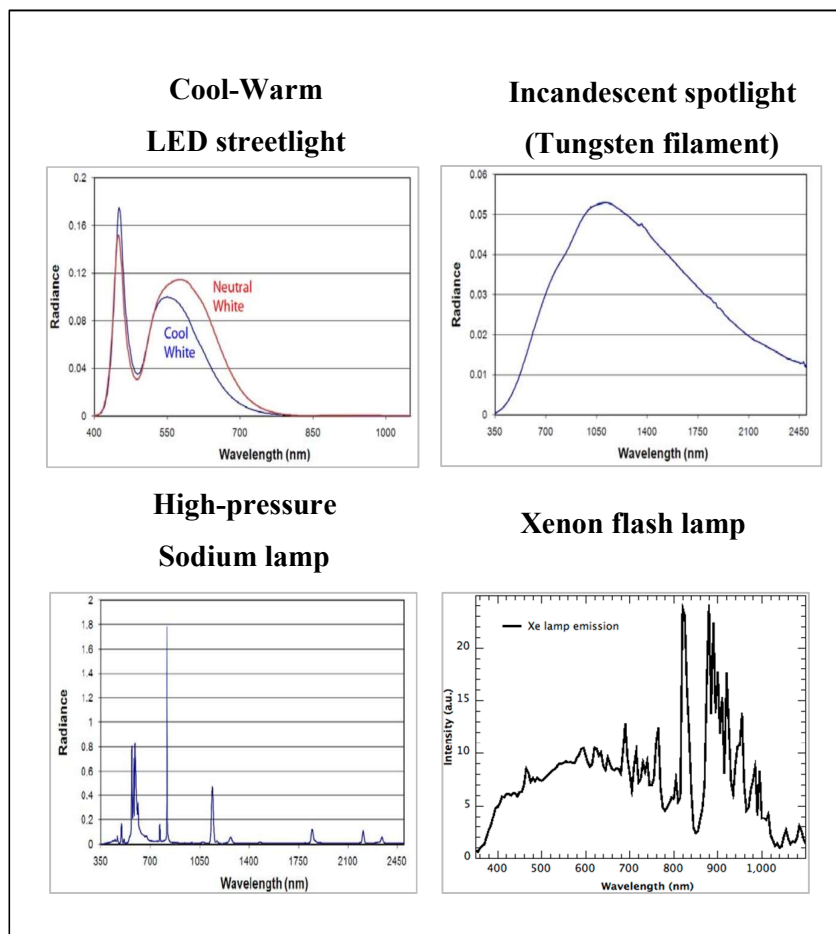
Figure 55: The emission spectra of LED, tungsten-halide, high-pressure sodium, and xenon irradiation sources.[161],[162]

Each irradiation source produced a unique emission spectrum (**Figure 55**). The xenon irradiation source produced a broad emission spectrum (400−1000 nm), which favourably replicated visible light. Light emitting diodes (LEDs) only produced two emission maxima at approximately 450 and 560 nm, respectively. High-pressure sodium and incandescent irradiation sources had low-energy far red shifted wavelengths. However, after inspecting the curves shown in **Figure 55**, only one irradiation source (*xenon*) was deemed appropriate for the photo-investigation of titanium dioxide analogues. Therefore, an in-house solar-simulation xenon irradiation source was built from 4 × 35W xenon lamps (**Figure 56**).
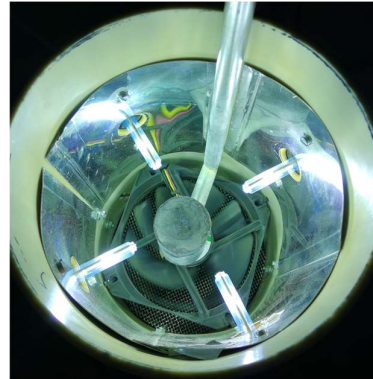
Figure 56: The constructed solar-simulated xenon irradiation source.

After constructing the solar-simulation xenon irradiation source, the emission spectrum was obtained using a Newport Oriel Instruments minispectrometer (model-number: 78356), which was calibrated against visible laser lines and is depicted below (**Figure 57**).
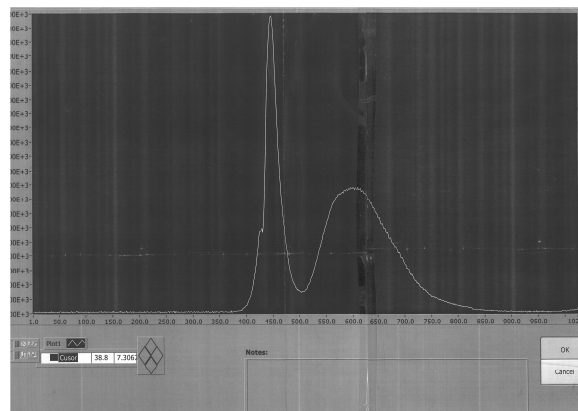
Figure 57: Emission spectrum of solar-simulation xenon irradiation source.

The emission spectrum depicted in **Figure 57** presented a favourable electromagnetic peak response starting at 400 nm, which corresponded well to the intrinsic band gap of titanium dioxide (387−413 nm).[74] In addition, a broad emission peak over the 500−750 nm region would aptly accommodate any functionalised titanium dioxide derivatives with red shifted band gaps.

3.6. Re-Assessing the Photocatalytic Study

The A_3TiO_5 concept warranted a re-assessment of the strategy towards the development of a novel visible-light sensitive titanium dioxide material. After instrumentally studying TMT-Cu, TMT-Ni, and TMT-Mn, it was clear that activating a visible-light-activated semiconductor such as cadmium sulfide would provide valuable insight to later synthesising a titanium dioxide material that could be attenuated away from UV-irradiation to function in visible light. The objective was to optimise the photo-reactivity of cadmium sulfide whilst being irradiated with the new solar simulated xenon irradiation source. The knowledge gained during the proceeding chapter was envisaged to later support the development and application of a novel titanium dioxide material.

3.7. Plans of Functionalising Cadmium Sulfide with Silver for Photocatalytic Studies under Visible Light Irradiation

3.7.1. Context Behind Functionalising Cadmium Sulfide for Applications in Visible Light-Activated Photocatalysis

As previously discussed in **Chapter 1.2.** (**Scheme 1**), the theory of semiconductor functionalising has been reported to proceed by one of three distinctive mechanisms. Introducing foreign materials into a semiconductor's crystal lattice by any of the three-functionalising methods would alter the band structure alignment and hence modify the photocatalytic activity.

The next attempt to develop a visible-light-active photocatalyst included silver nanoparticles that were used to functionalise calcinated cadmium sulfide (CdS). The concept was adapted from a method developed by Zhang *et al.*[56] who encapsulated platinum nanoparticles within cerium dioxide to facilitate the selective conversion of benzyl alcohol to benzaldehyde using visible light irradiation.

In this study, silver atoms were precipitated using tri-sodium citrate that formed a colloidal suspension. Subsequently, cadmium sulfide was prepared from cadmium nitrate tetrahydrate ($Cd[NO_3]_2 \cdot 4H_2O$), sodium sulfide (Na_2S) and urea in a sol-gel synthesis approach.* Silver was chosen as a functionalising agent due to its inherent surface plasmonic resonance effect.[13]

The choice of utilising cadmium sulfide as a visible-light activated semiconductor was based on the literature, which has described the visible-light-activated properties of cadmium sulfide, coupled graphene or *g*-C_3N_4-cadmium sulfide, titanium dioxide-cadmium sulfide nanomaterials, to photocatalyse organic transformations (alcohol oxidations, nitrobenzene reductions, molecular hydrogen production).[163],[164],[165],[166],[167],[168]

---

* see the **Experimental Chapter 6** for the synthetic procedure.

3.7.2. Assessing the Photocatalytic Potential of Cadmium Sulfide in Alcohol Oxidation Studies

The newly assembled solar simulated xenon irradiation source was ready for use and to test the photo-oxidative capability of the silver functionalised cadmium sulfide, 3,4-dimethoxybenzyl alcohol was oxidised to 3,4-dimethoxybenzaldehyde in a proof-of-concept study (**Scheme 2**).
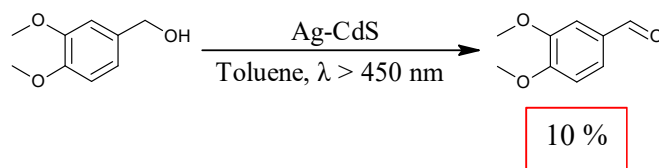
Scheme 2: Photo-oxidation of 3,4-dimethoxybenzyl alcohol using silver functionalised cadmium sulfide.

A low 10 % yield of 3,4-dimethoxybenzaldehyde was surprising as cadmium sulfide was a visible light-activated photocatalyst with a reported band gap of 2.50−2.55 eV (486−496 nm).[169] Furthermore, the acquisition of the new solar simulated xenon irradiation source met the requirements to photo-activate the band gap of cadmium sulfide, which subsequently should have facilitated the oxidation of 3,4-dimethoxybenzyl alcohol. Control reactions (without the photocatalyst, with and without xenon irradiation, and oxygen) also only yielded trace quantities of 3,4-dimethoxybenzaldehyde.*

Therefore, to establish why the silver functionalised cadmium sulfide was incapable of oxidising 3,4-dimethoxybenzyl alcohol, the only reasonable deliberation was to address the photo-physical properties of the semiconductor. Throughout the semiconductor mediated photocatalysis study, semiconductor band gaps, band edge alignments, redox potentials, appropriate irradiation wavelengths and synthetic methodologies to fabricate semiconductors were all considered in great detail through intensive literature research. However, instrumentally obtaining experimental data for the fabricated semiconductors

---

* Chromatograms have been listed in the **Appendix**.

was key to finally resolving the poor photocatalytic activities of the various fabricated semiconductors.

3.7.3. Utilising Instrumental Techniques to Characterise Silver Functionalised Cadmium Sulfide.

An instrumental study was undertaken using electron microscopy, and numerous spectroscopic techniques in support of characterising the silver functionalised cadmium sulfide to obtain an understanding behind the low photocatalytic activity of the semiconductor.

3.7.3.1. A Morphological Study of Silver and Cadmium Sulfide.

Whilst a similar approach was adapted from Zhang *et al.*[56] who encapsulated platinum within cerium dioxide, it was uncertain in this research whether silver was successfully incorporated with cadmium sulfide during the synthetic procedure to manufacture the semiconductor.

The size and morphology of the silver nanoparticles were first studied using field emission scanning electron microscopy (FESEM) after evaporating the colloidal silver suspension to dryness and mounting on carbon tape before the analysis (**Figure 58**).
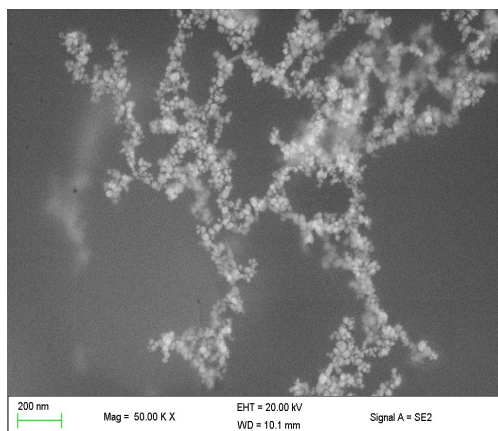
Figure 58: 50,000 times magnification of silver nanoparticles (scale bar = 200 nm).

After inspecting **Figure 58**, the silver nanoparticles were an approximate size of less than 20 nm and appeared to be irregularly sized spheres.

Silver's inclusion with cadmium sulfide was subsequently explored using field emission scanning electron microscopy (**Figure 59**), high-resolution transmission electron microscopy and line scanning with scanning transition electron microscopy (STEM). A quantitative inductively coupled plasma-mass spectrometry (ICP-MS) compositional analysis was also performed on the calcinated cadmium sulfide nanomaterials. The results determined that the concentration of silver nanoparticles within the cadmium sulfide material was limited to 0.1%.*
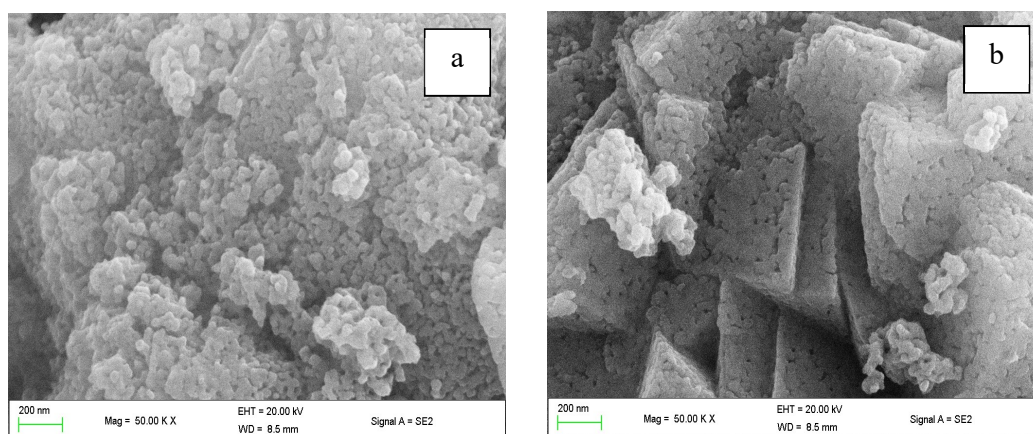
Figure 59: FESEM images of calcinated silver functionalised cadmium sulfide (scale bar = 200 nm).

Figure 59 has depicted as-prepared cadmium sulfide consisting of irregular spheres (**Figure 59**, image a) that aggregated into semi-packed triangular structures (**Figure 59**, image b). However, due to the small particle size of the silver nanoparticles, HRTEM imagery was explored to elucidate the location of silver nanoparticles (**Figure 60**).

---

* The full ICP-MS compositional analysis is available in the **Appendix**.
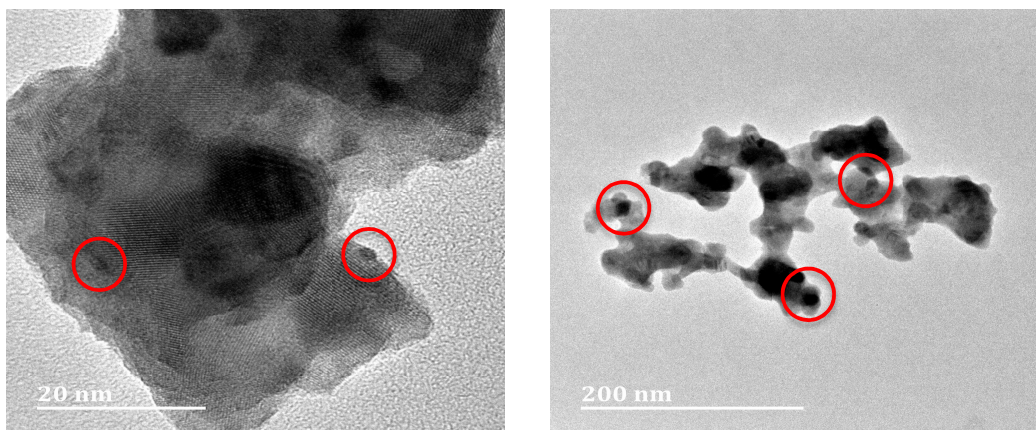
Figure 60: HRTEM images of calcinated silver functionalised cadmium sulfide. The red circled regions indicated potential silver nanoparticles.

As observed by the red-circled regions of the dark spots in **Figure 60**, silver was potentially identified as being located on cadmium sulfide as individual nanoparticles that were surface loaded onto larger cadmium sulfide clusters. **Figure 60** further depicted that cadmium sulfide had aggregated during the synthetic procedure and no uniform morphology was observed.

An additional technique to determine the relative atomic distribution of silver within the cadmium sulfide material was investigated using EDX line scanning with the application of two STEM analyses (**Figure 61**).

Figure continued overleaf

Cadmium La1

Cadmium La1

Sulfur Ka1

Sulfur Ka1

Silver La1

Silver La1

Figure continued overleaf

108
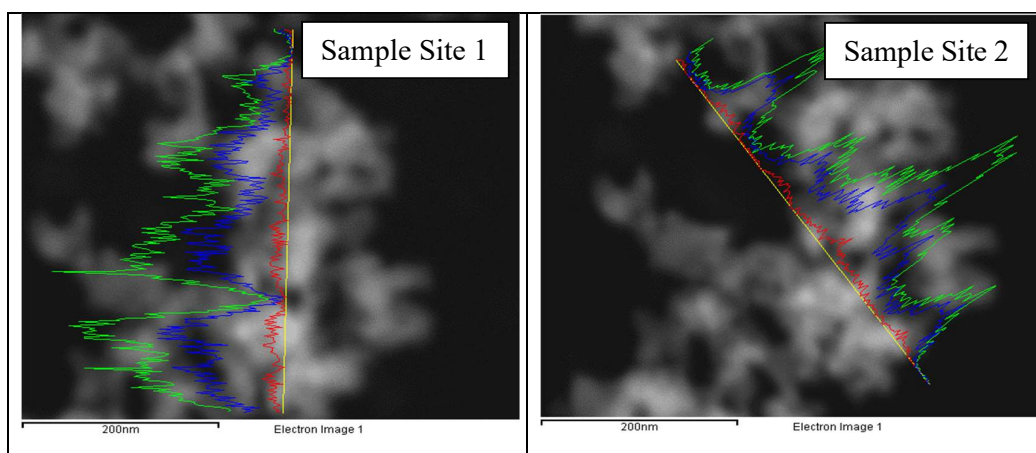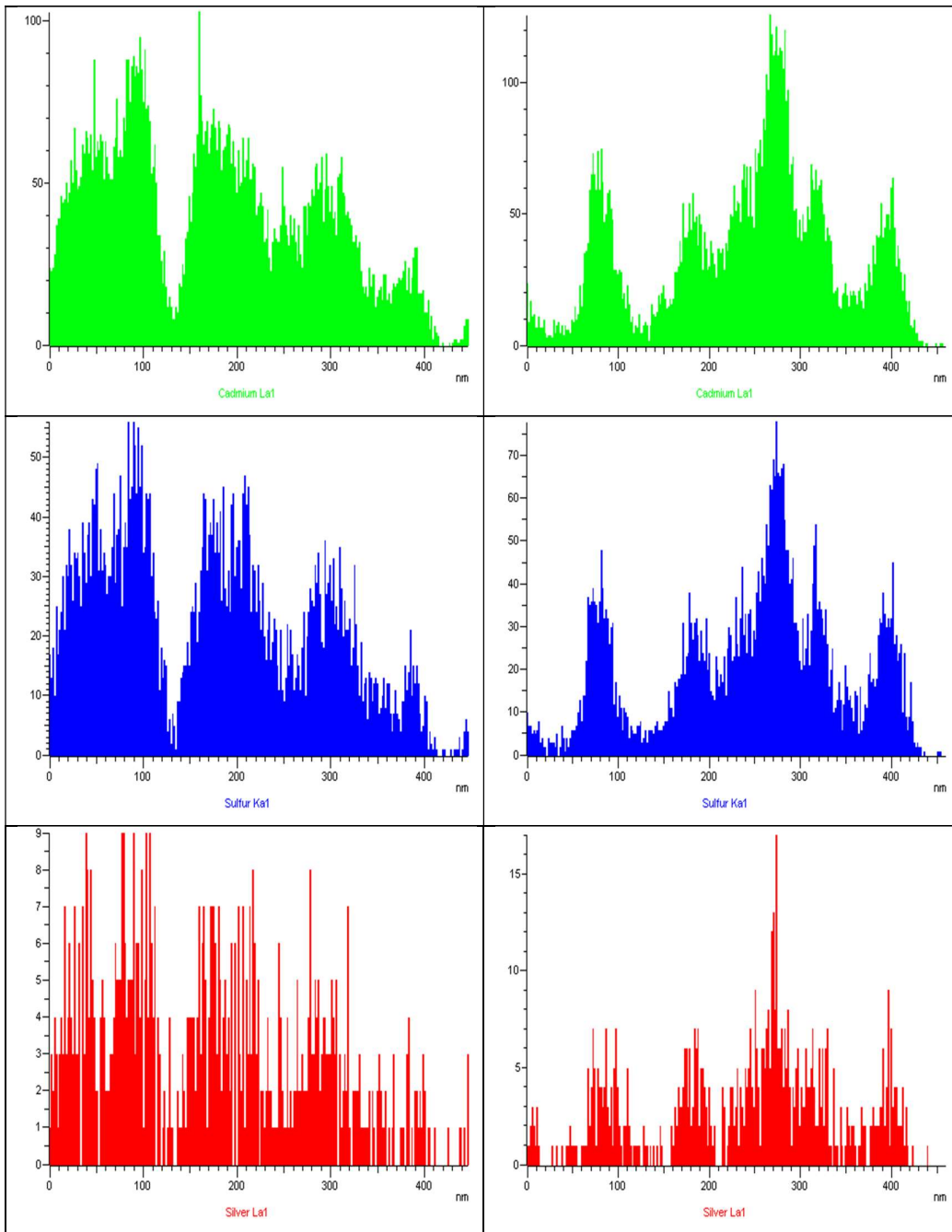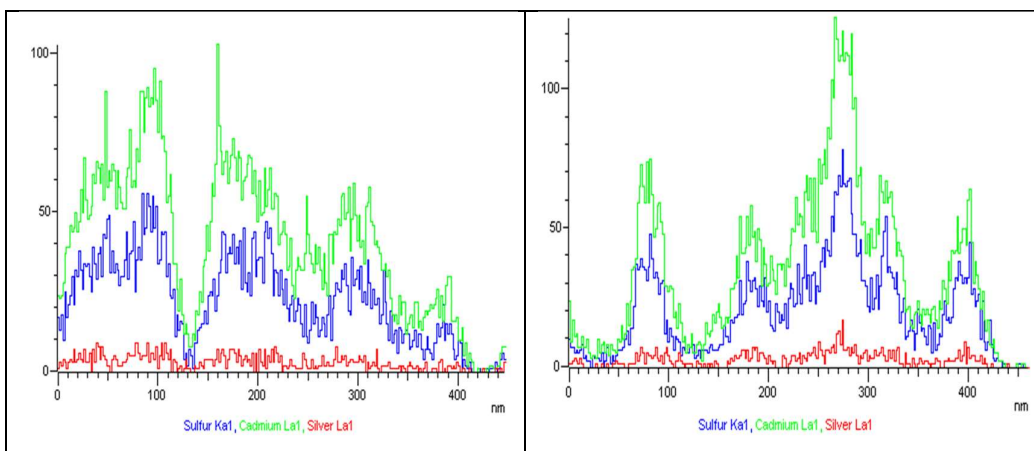
Figure 61: The atomic distribution of silver within two sample sites of aggregated cadmium sulfide nanoparticles using EDX line scanning through STEM analyses. The sample windows have been set to 450 nm (Sample Site 1) and 460 nm (Sample Site 2).

The scanning windows of Sample Site 1 (450 nm) and Sample Site 2 (460 nm) have depicted the presence of cadmium (green), sulfur (blue) and silver (red), all of which contained a uniform distribution of the respective elements over the analysis lengths (450−460 nm). Whilst the intensities of silver were significantly lower (due to the low weight loadings used during the sol-gel synthesis), the peak maxima matched well with those of cadmium and sulfur. This result suggested that silver was uniformly distributed on the cadmium sulfide.

The next objective of the cadmium sulfide study was to investigate the photo-physics behind the poor photocatalytic activity of silver encapsulated cadmium sulfide.

3.7.4. Understanding the limitations of silver encapsulated cadmium sulfide photocatalysis.

After identifying the distribution of silver nanoparticles on cadmium sulfide, the focus of the characterisation study was to further establish the photo-physical properties that were inhibiting cadmium sulfide from mediating alcohol oxidations by the use of powder diffuse reflectance spectroscopy, UV/Vis spectroscopy, electron microscopy, photoluminescence spectroscopy, and energy-dispersive X-ray spectroscopy (EDX).

3.7.4.1. Powder Diffuse Reflectance UV/Vis Spectroscopic Measurements and Microscopic Analyses of Uncalcined and Calcinated Cadmium Sulfide.

The cadmium sulfide samples (uncalcined and calcinated) were subjected to powder diffuse reflectance UV/Vis spectroscopic investigations in absorbance mode to further understand the optical absorption profiles (**Figure 62**).
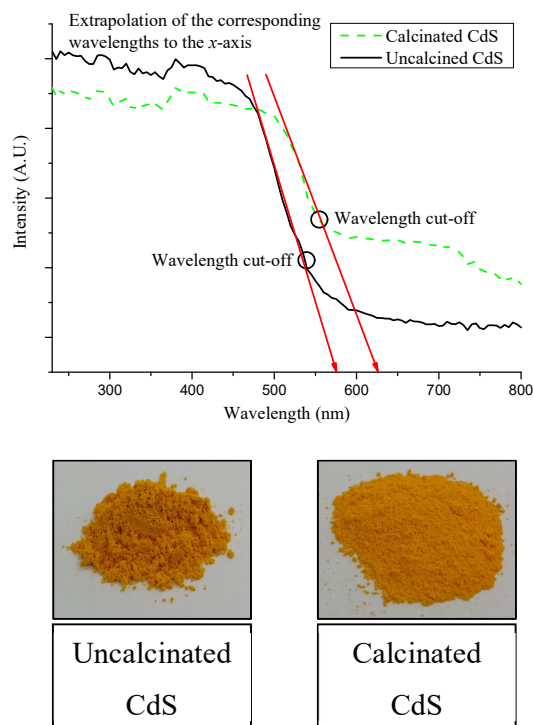
Figure 62: Powder diffuse reflectance UV/Vis spectra of calcinated (dotted green line) and uncalcined cadmium sulfide (solid black line). The red arrows indicate the cut-off wavelength with the *x*-axis, whereby an approximation of the band gap values could be obtained.

The calcination process enhanced the absorption capacity of cadmium sulfide (dotted green line, (**Figure 62**), compared to uncalcined cadmium sulfide (solid black line, **Figure 62**). However, a red shift cut-off absorbance wavelength (626 nm) for calcinated cadmium sulfide was noticed when compared to uncalcined cadmium sulfide (576 nm) (**Figure 62**). These two observations (enhanced absorption capacity and red shifted cut-off absorbance wavelength) have been recognised in the literature to emanate from the process of calcinating semiconductors at elevated temperatures that induce

crystalline growth, a decrease in the optical band gap value and hence a 'red shifted' absorption profile.[170],[171]

Despite the noted red shift for calcinated cadmium sulfide when compared to uncalcined cadmium sulfide (**Figure 62**), the proposed band gaps (calcinated = 1.98 eV [626 nm], uncalcined = 2.15 eV [576 nm]) did not agree with the literature value for cadmium sulfide (2.50−2.55 eV [486−496 nm][172]). The absorbance from silver nanoparticles was also excluded (despite the visible surface plasmon resonance of the silver nanoparticles being highly dependant on size and shape) as the measured UV/Vis absorption spectrum occurred at 412 nm (**Figure 63**), far below the red shifted wavelengths of 576−626 nm.[17],[21],[22]
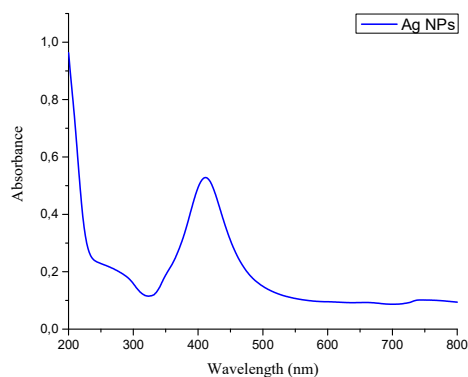
Figure 63: UV/Vis spectrum of colloidal nanoparticles suspected in de-ionised water.

The effect of calcinating cadmium sulfide inducing crystalline growth was subsequently explored using SEM and TEM microscopy (**Figure 64**).

	Uncalcined	Calcinated
SEM (200 nm)		
TEM (50 nm)		
TEM (50 nm)		
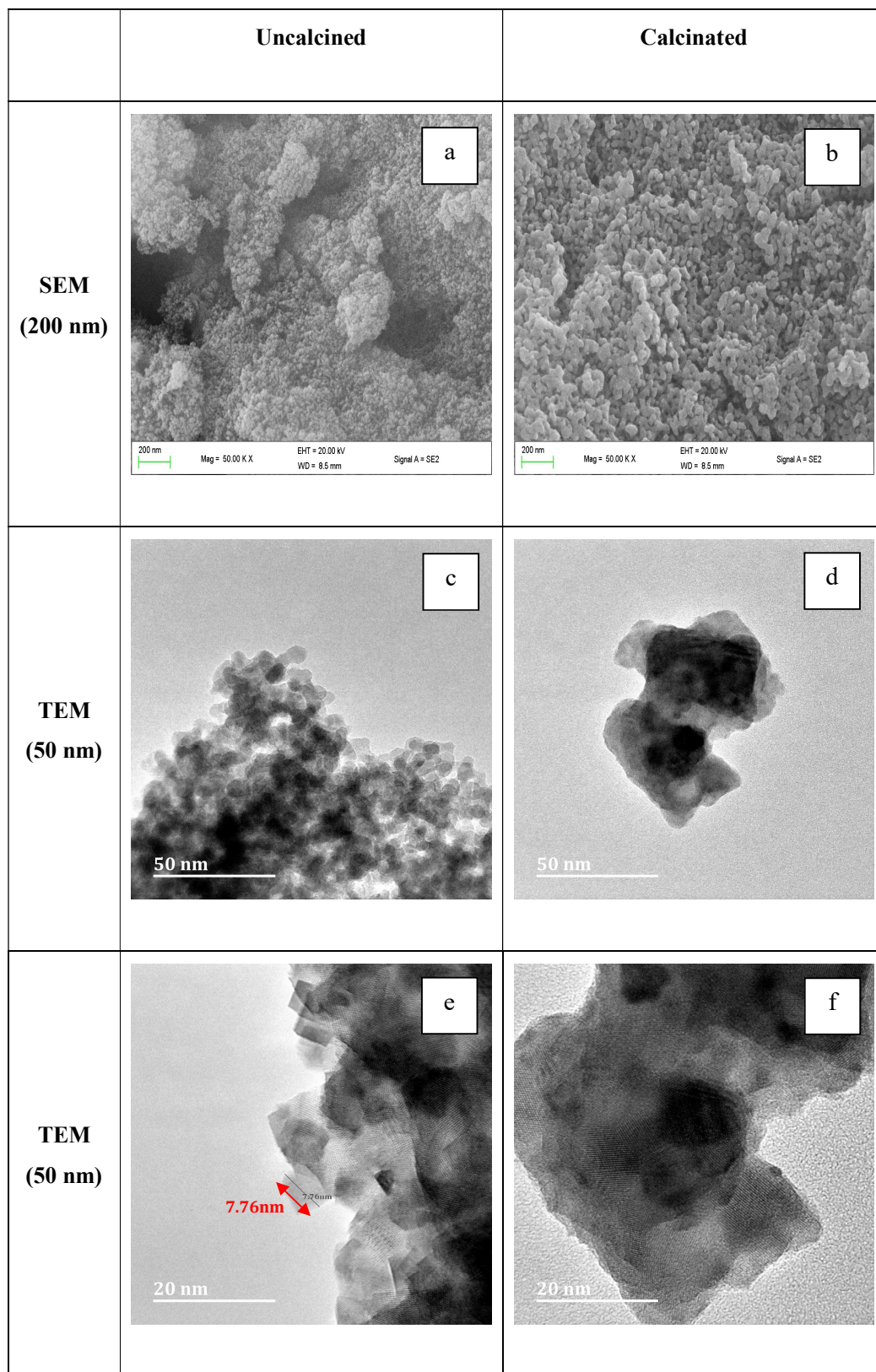
Figure 64: Electron micrographs depicting the size and morphology of uncalcined and calcinated silver functionalised cadmium sulfide nanoparticles.

The SEM and TEM micrographs presented in **Figure 64** have depicted that the calcination of cadmium sulfide induced crystalline growth of the semiconductor. Observe **Figure 64**, images a and b, which has depicted small ball-like aggregated structures of uncalcined cadmium sulfide with approximate particle sizes of 8 nm (**Figure 64**, image e). After the calcination process, the ball-like structures appeared to increase in size and form irregular spheres (**Figure 64**, image d). The calcinated cadmium sulfide irregular spheres were more than 50 nm (**Figure 64**, images d and f). This would support the observation in **Figure 62** of a red shifted wavelength for calcinated cadmium sulfide, due to larger particle sizes (*ca.* 74 nm *vs. ca.* 8 nm for uncalcined cadmium sulfide, **Figure 64**, images e and f), however *not* the reason for the position of the 626 nm cut-off wavelength itself.

To address why uncalcined and calcinated cadmium sulfide had cut-off wavelengths far above the excitonic band gap of cadmium sulfide (2.50−2.55 eV, 486−496 nm),[169] the supposition of exploring defect centres and potentially unknown materials in the cadmium sulfide semiconductors using photoluminescence spectroscopy, HRTEM and EDX was deemed appropriate.

3.7.4.2. Photoluminescence Spectroscopy, HRTEM and EDX Studies of Silver Functionalised Cadmium Sulfide

Photoluminescence spectroscopy was introduced to qualify the main emission energies from the cadmium sulfide samples (uncalcined and calcinated cadmium sulfide, **Figure 65**).
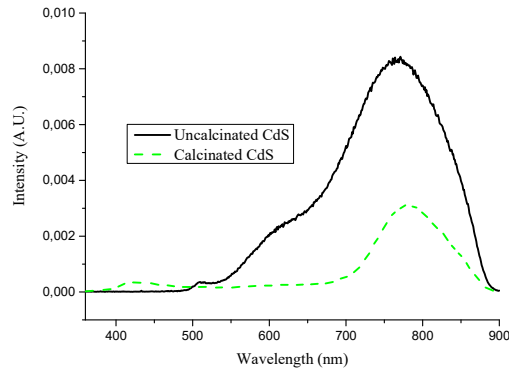
Figure 65: Photoluminescence spectra of calcinated and uncalcined cadmium sulfide. The lowered peak intensity of calcinated silver encapsulated cadmium sulfide (dotted green line) indicated improved charge separation compared to uncalcined silver encapsulated cadmium sulfide (solid black line).

After reviewing the photoluminescence spectra of uncalcined (solid black line) and calcinated cadmium sulfide (400 °C, dashed green line), the suspicion that defects were present within the cadmium sulfide materials was evident due to the dominant peaks residing at red shifted wavelengths (771−779 nm) from the excitonic emission (414−439 nm) wavelength of cadmium sulfide.

From the results presented in **Figure 65,** three pertinent observations were identified.

➤ A dominant peak at 771 nm with a shoulder peak between 594−638 nm was observed in uncalcined cadmium sulfide with a minor peak presence at 510 nm.

➤ Calcinated cadmium sulfide also had a central peak but slightly red shifted to 778 nm, and a smaller broad signal at 414−439 nm.

➤ Identifying the nature of the five identified peaks were expected to resolve the source of the red shifted wavelengths in the cadmium sulfide materials. However, cadmium sulfide has been reported in the literature to oxidise (cadmium sulfide to cadmium oxide) in an oxygen environment and under elevated temperatures.[173],[174]

114

Firstly, as expected, calcinating cadmium sulfide reduced the defect recombination process (at 771 nm) through crystal growth, which allowed for a degree of intrinsic sulfur-vacancy defects-sites to crystalise out of the lattice.[175] Literature has reported that heating semiconductors at elevated temperatures promote crystal growth and reduces defect-induced recombinations.[176] In addition, the evolution of minor excitonic emissions was present in the calcinated cadmium sulfide sample at 413−439 nm that were in agreement with the literature.[177] However, in opposing reports,[178] the same 413−439 nm emission peak has been accurately associated with isolated cadmium oxide.

The clarification of uncalcined cadmium sulfide was slightly more difficult. The 771 nm emission could also be ascribed to sulfur vacancy defects in accordance with the calcinated cadmium sulfide. However, the broad shoulder at 594−638 nm and the smaller peak at 510 nm needed further investigations. Cretu *et al.*[175] undertook an extensive study to evaluate the various intrinsic defects of cadmium sulfide ranging from 520−1030 nm. Within their research, they identified a 600−650 nm defect emission that matched well with the shoulder peak of uncalcined cadmium sulfide (594−638 nm), which was assigned by Cretu *et al.*[175] to originate from Cd interstitials. From the uncalcined cadmium sulfide, the 510 nm emission peak was still unresolved; either originating from excitonic emissions of cadmium sulfide [179] or cadmium oxide's oxygen vacancies.[180] As previously mentioned, cadmium sulfide is known to oxidise into cadmium oxide. Therefore, to investigate the possibility of the cadmium sulfide having undergone partial oxidation to cadmium oxide (before and after calcinating), the semiconductor was further examined using HRTEM to determine the *d*-lattice spacings of cadmium sulfide and a potential cadmium oxide component (**Figure 66**).
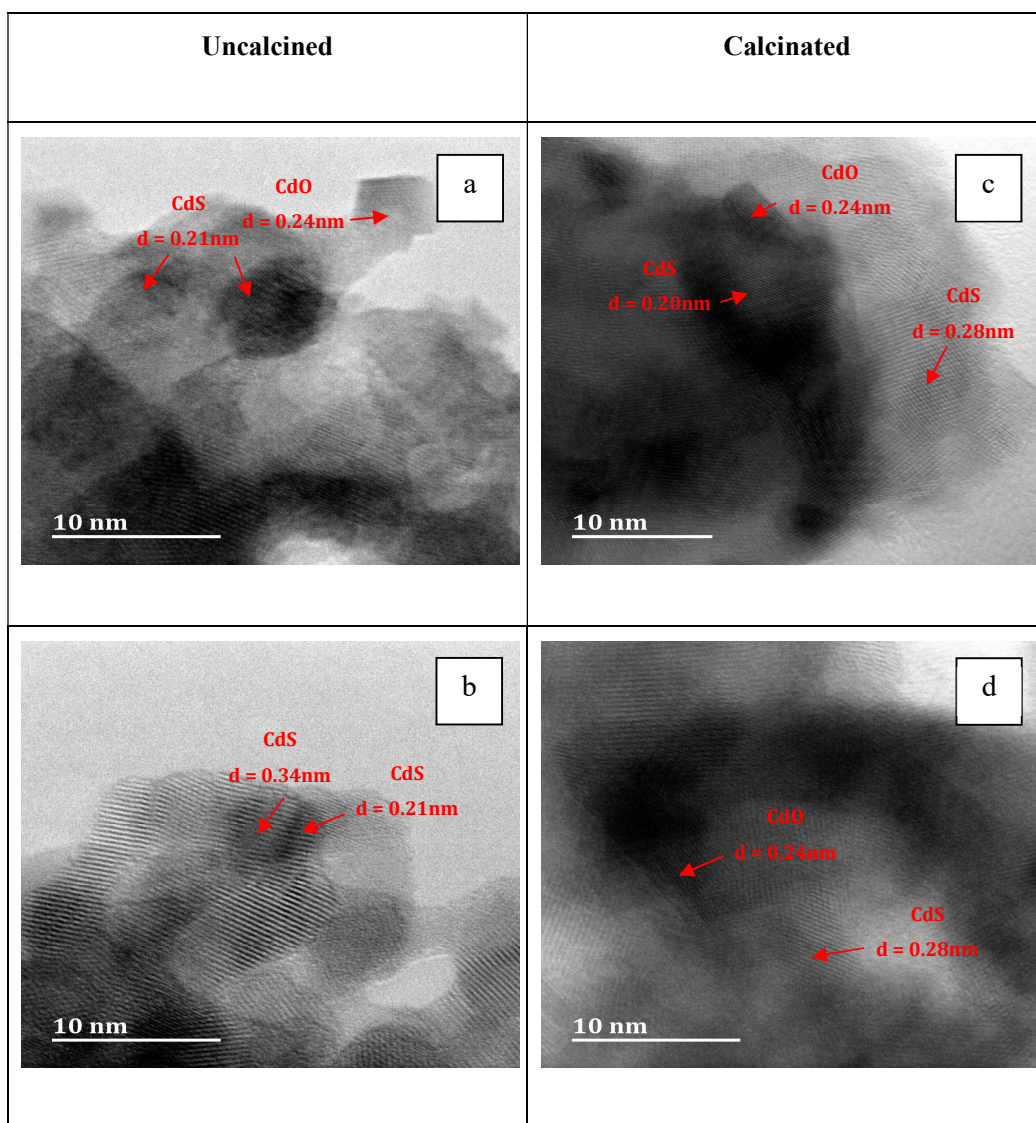
Figure 66: HRTEM imagery of calcinated cadmium sulfide with calculated lattice spacings. The reported values indicated that both cadmium sulfide and cadmium oxide were present in the calcinated silver functionalised cadmium sulfide semiconductor.

Cadmium oxide was indeed present in both uncalcined and calcinated cadmium sulfide samples, with *d*-lattice spacings that were shown to be in accordance with the literature.[181],[182],[183],[184],[185] In both instances, cadmium oxide's location was concentrated towards the periphery of the uncalcined and calcinated materials.

In conjunction to the HRTEM analyses of uncalcined and calcinated cadmium sulfide, energy-dispersive X-ray spectroscopic studies (EDX) of the semiconductors were

116

collected to obtain a qualitative measure of the weight percentages (wt%) of oxygen and sulfur in the uncalcined and calcinated cadmium sulfide materials over six sample sites. (**Table 6**).

Table 6: EDX analysis of uncalcined and calcinated cadmium sulfide over six sample sites. EDX was conducted to determine the wt% changes of sulfur and oxygen within CdS before and after the calcination period.

	Weight Percent					
Element	**Uncalcined**			**Calcinated**		
	Site 1	Site 2	Site 3	Site 4	Site 5	Site 6
C	13.57	9.58	15.80	20.28	7.97	10.72
O	**3.04**	**3.50**	**6.86**	**18.40**	**23.62**	**16.48**
S	**17.56**	**17.09**	**15.46**	**7.98**	**4.96**	**12.56**
Cd	65.52	69.50	61.57	53.24	63.44	59.86
Ag	0.00	0.14	0.08	0.10	0.00	0.38
Si	0.31	0.19	0.22	0.00	0.00	0.00
Totals	100	100	100	100	100	100

Amongst the EDX analyses, oxygen was present in both the uncalcined and calcinated samples with higher oxygen weight percentages observed in the calcinated material. Impurities (C, and Si) originated from the carbon tape used to mount the samples and an instrumental impurity, respectively.

After observing the EDX analyses of sulfur and oxygen in uncalcined and calcinated cadmium sulfide (**Table 6**), the 510 nm emission peak for uncalcined cadmium sulfide (**Figure 65**), could be assigned to cadmium oxide's oxygen vacancies, which was in agreement with the literature.[180] This conclusion was further supported after identifying that cadmium oxide was present in the uncalcined cadmium sulfide as determined by HRTEM lattice spacings and EDX analyses (**Figure 66**, **Table 6**).

The broad peak emission between 413−439 nm within calcinated cadmium sulfide could either be assigned to CdS or CdO excitonic emissions. However, based on the microscopic and EDX evidence, which revealed a higher weight percentage of oxygen in calcinated cadmium sulfide (**Table 6**), and from the reasoning that the same peak profile was absent in uncalcined cadmium sulfide (**Figure 65**), the conclusion from the collected evidence suggested that the broad emission peak belonged to cadmium oxide's excitonic emissions. This could be further substantiated after noticing that the 510 nm emission peak assigned to oxygen vacancies in uncalcined cadmium sulfide was absent. This observation would lend justification to conclude that after the calcination period, the oxygen vacancies within cadmium oxide crystallised out, leading to the growth of uniform cadmium oxide with only band edge emissions being observed in **Figure 65**.

3.7.5. Concluding Remarks to Silver Functionalised Cadmium Sulfide

During this study, a sol-gel approach was utilised to fabricate a potentially visible-light-activated silver functionalised cadmium sulfide semiconductor for alcohol oxidation studies. However, the material demonstrated poor photocatalytic properties in proof-of-concept studies whilst attempting to oxidise 3,4-dimethoxybenzyl alcohol. Instrumental information gathered from microscopic and spectroscopic analyses have lent support in identifying the reason for the material's poor photocatalytic potential:

➢ Powder diffuse reflectance UV/Vis spectroscopic studies identified excessive red shifted cut-off wavelengths for both uncalcined (626 nm) and calcinated (576 nm) cadmium sulfide, far beyond the intrinsic band gap value (486−496 nm).

➢ The results from the photoluminescence spectroscopy study concurred with the red shifted cut-off wavelengths, as numerous sulfur, cadmium and oxygen defects were detected. Sub-band gap defects dominated the optical emissions, while minimal band edge emissions were observed, thus leading to enhanced exciton recombinations at defect sites that quenched the oxidative potential of cadmium sulfide.

- In conjunction with EDX analyses and TEM lattice spacing calculations, an undesired cadmium oxide component was present in both uncalcined and calcinated cadmium sulfide.

Due to the low conversion of 3,4-dimethoxybenzyl alcohol and from the photo-physical observations for both uncalcined and calcinated silver functionalised cadmium sulfide noted above, further literature studies were reviewed to identify a viable visible-light-activated photocatalyst for alcohol oxidation studies.

In the two aforementioned studies, attempts toward identifying a visible-light activated semiconductor have been explored. The materials included Cu, Ni and Mn functioned titanium dioxide (TMT-Cu, TMT-Ni and TMT-Mn), and silver functionalised cadmium sulfide. As neither of the concepts demonstrated suitable photocatalytic properties to facilitate alcohol oxidations in proof-of-concept reactions, three new avenues to extend the study have been explored. These included a bi-metallic (Cu|Pd) alloy on silver functionalised cadmium sulfide, nitrogen functionalised titanium dioxide and constructing a $CdS|TiO_2$ heterojunction. The investigations led to the concluding development of a three-component system that demonstrated excellent potential for oxidising alcohols. Numerous microscopic, spectroscopic, and X-ray diffraction techniques were used concurrently to understand the nature and composition of the novel material, which governed its effective oxidative potential.

3.8. Strategies Towards Bi-Metallic and Nitrogen Functionalisation of Heterojunctioned Metal Chalcogenides

In this chapter, the focus has been directed towards the development of a three-component photocatalytic system. The research objectives have been noted below:

➢ An attempted strategy towards an alloyed system on the surface of cadmium sulfide.
➢ The evaluation of nitrogen functionalised titanium dioxide (prepared in accordance with the literature) in alcohol photo-oxidation studies.
➢ Coupling the alloy on nitrogen functionalised titanium dioxide and contrasting the photo-oxidative potential with and without silver functionalised cadmium sulfide towards a potentially viable heterojunctioned semiconductor system.

Each section has been discussed in further detail *vide infra* with the intention to accumulate the research study towards the desired outcome of identifying a viable photocatalytic material for photocatalysing alcohol oxidations. A comprehensive instrumental library was utilised to fully characterise and therefore understand the photo-physics of the three-component photocatalytic system.

3.8.1. Further Background Literature to the Functionalisation of Metal Chalcogenides

3.8.1.1. Loading Copper and Palladium onto Cadmium Sulfide

Throughout the research studies, metal functionalising agents were hypothesised to impart visible light photo-reactivity and alter the band gap structure of the semiconductors prepared in this thesis. However, the recent cadmium sulfide studies were unsuccessful, which necessitated a further review of the literature to work towards a viable photocatalytic material. Recent publications by Pan and co-workers,[33] Cheng and co-workers,[13] and Shiraishi and co-workers,[43] have indicated that metal

nanoparticles are capable of expediting photocatalytic reactions through electron donation into the orbital states of supporting semiconductors.

Pan and co-workers[33] discovered that a pre-irradiation cycle of titanium dioxide with benzyl alcohol afforded titanium dioxide with oxygen vacancies (**Figure 67**).
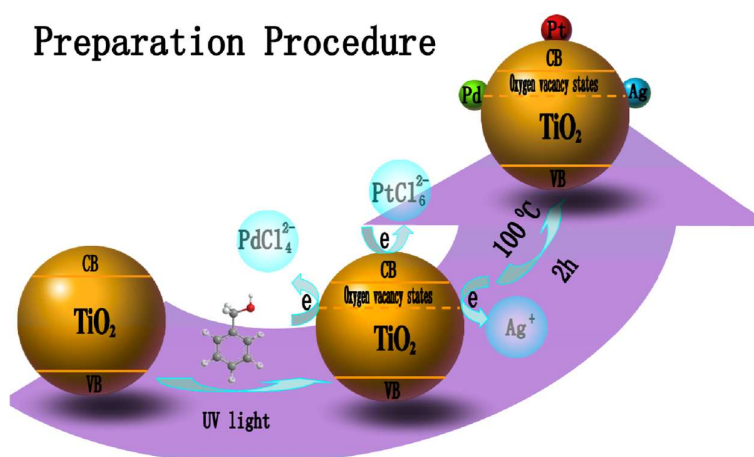
Figure 67: The diagram depicts the preparative procedure of creating oxygen vacancies on the surface of titanium dioxide under UV light irradiation for the subsequent reduction of Ag, Pt, and Pd salts onto the surface of titanium dioxide as metallic nanoparticles. Reprinted with permission from X. Pan, Y.-J. Xu, *The Journal of Physical Chemistry C* 2013, *117*, 17996−18005. Copyright (2013) American Chemical Society.

The authors[33] subsequently deposited three metals (silver, platinum and palladium) onto the surface of titanium dioxide through the photo-reduction of the available oxygen vacancy sites. Notable was the creation of metallic palladium nanoparticles (2 nm) on the surface of titanium dioxide. Amongst the three metal-functionalised titanium dioxide species with oxygen vacancies, palladium functionalised titanium dioxide (Pd-TiO$_2$-OV) yielded the highest oxidative conversion of benzyl alcohol (> 65 %). Pd-TiO$_2$-OV was speculated to deliver superior exciton separation efficiency over silver and platinum functionalised titanium dioxide and hence facilitate a greater alcohol oxidation conversion (Pd-TiO$_2$-OV [65 %], Ag-TiO$_2$-OV [10 %], Pd-TiO$_2$-OV [20 %]).

Shiraishi *et al.*[186] previously mentioned that platinum functionalised titanium dioxide significantly enhanced the apparent quantum yield of titanium dioxide to oxidise benzylic alcohols under visible light (7.1 % at 500 nm) compared to gold functionalised titanium dioxide (Au-TiO$_2$, 3.8 % at 500 nm). However, the electron transfer of photo-generated electrons from the platinum nanoparticles into the conduction band of titanium dioxide was determined as the rate-determining step in the overall photo-oxidation process due to the intrinsic metal-semiconductor Schottky Barrier height. Shiraishi *et al.*[43] later studied the effects of co-functionalising titanium dioxide with copper and platinum ions. Alloying copper and platinum lowered the intrinsic work function of platinum and hence reduced the metal (platinum)-semiconductor Schottky Barrier, which promoted a fast electron transfer from the alloy (Cu|Pt) to the semiconductor's conduction band (**Figure 68**).
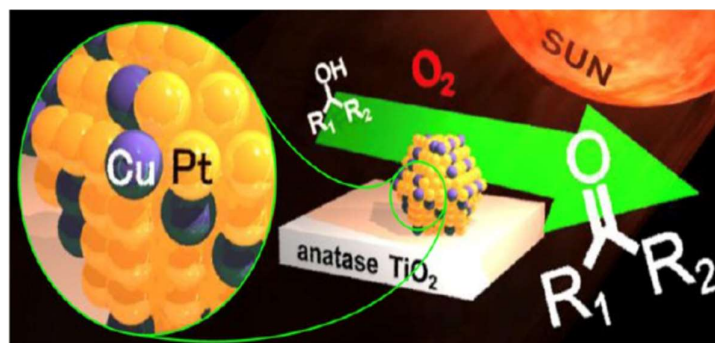
Figure 68: A pictorial representation of the catalytic function for a Cu|Pt alloy on the surface of titanium dioxide for alcohol oxidations in the presence of an electron scavenger (molecular oxygen) under visible light irradiation. Reprinted with permission from Y. Shiraishi, H. Sakamoto, Y. Sugano, S. Ichikawa, T. Hirai, *ACS Nano* 2013, *7*, 9287−9297. Copyright (2013) American Chemical Society.

The alloyed (Cu|Pt) system on the surface of titanium dioxide was reported to drastically enhance the visible light photo-efficiency of titanium dioxide to oxidise aromatic alcohols (apparent quantum yield of 17 % at 550 nm).

Therefore, based on the literature observations[13],[33],[43] a proposed concept of a copper|palladium alloy loaded onto the surface of silver functionalised cadmium sulfide has been summarised in the illustration below (**Scheme 3**).*
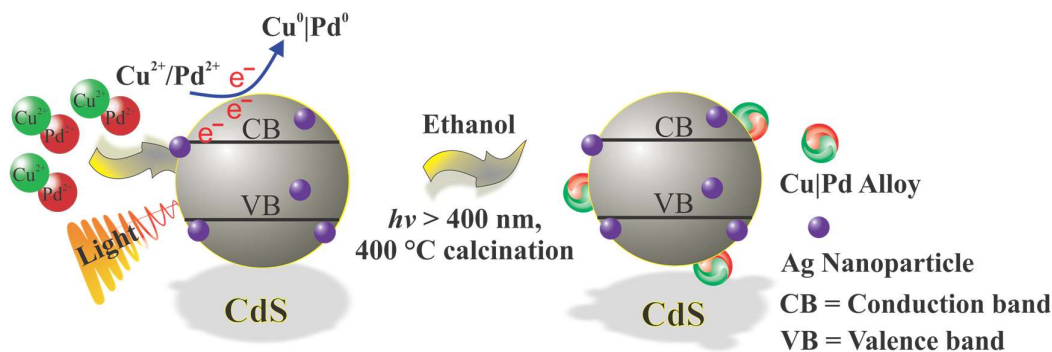
Scheme 3: Cu|Pd on silver functionalised CdS. Visible light (xenon) irradiation photo-excited cadmium sulfide and conduction band electrons reduced Cu^{2+}/Pd^{2+} to Cu|Pd.

Despite the undesired cadmium oxide phase in the cadmium sulfide, the effect of loading the bi-metallic (Cu|Pd) species onto silver functioned cadmium sulfide was expected to lower the work function of palladium that could potentially assist silver functionalised cadmium sulfide in operating more efficiently under visible light conditions. Palladium was chosen due to its reported photocatalytic synergy with semiconductors to effectively enhance visible light photoredox transformations.[25],[161],[187] Testing of the bi-metallic system (Cu|Pd) on silver functionalised cadmium sulfide was only envisaged after completing the coupling stage with the heterojunction counterpart, nitrogen functionalised titanium dioxide.

3.8.1.2. Functionalising Titanium dioxide with Nitrogen

Wang *et al.*[188] investigated the effect of nitrogen functionalised titanium dioxide towards the photodecomposition of methylene blue. Amongst the Fourier Transform Infrared spectroscopy, Raman spectroscopy, X-ray photoelectron spectroscopy and

---

* See the **Experimental Chapter 6** for the synthetic procedure to produce silver functionalised CdS.

powder X-ray diffraction analytical methods, the technique of powder diffuse reflectance UV/Vis spectroscopy revealed an intriguing observation (**Figure 69**).
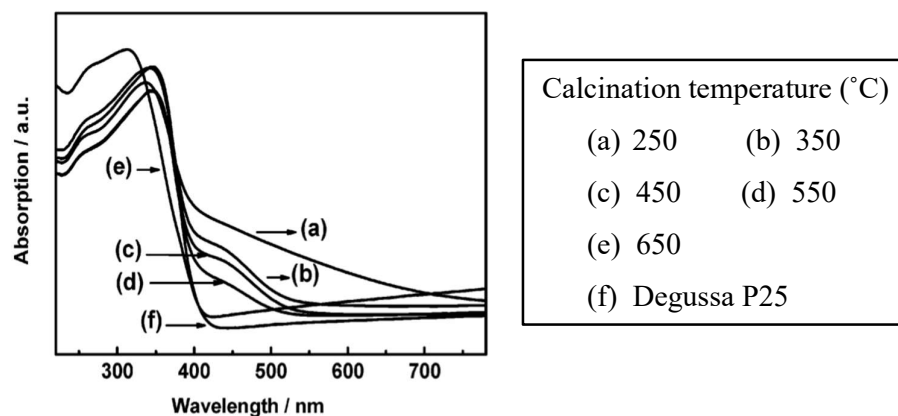
Figure 69: Powder diffuse reflectance UV/Vis spectra of nitrogen functionalised titanium dioxide. The spectra illustrate the potential of red shifting the optical band gap of nitrogen functionalised titanium dioxide after different calcination temperatures. Reprinted with permission from J. Wang, W. Zhu, Y. Zhang, S. Liu, The Journal of Physical Chemistry C 2007, 111, 1010−1014. Copyright (2007) American Chemical Society.

The red shifted wavelength of titanium dioxide has been depicted in **Figure 69**, which emanated from the ion exchange (substitution) of oxygen for nitrogen in the crystal lattice of titanium dioxide. The partial incorporation of nitrogen into titanium dioxide's lattice initiated orbital mixing between oxygen's 2p and nitrogen's 3p atomic orbitals. The outcome was a raised valence band edge that produced a visible-light sensitised titanium dioxide material. As observed in **Figure 69** from 250 ˚C (a) through to 650 ˚C (e), the calcination temperature of the nitrogen-doped titanium dioxide increased, and the red shifted 'visible light response' decreased as compared to the Degussa P25 reference (f). However, entry (b) (350 ˚C) presented a band profile that retained the intrinsic titanium dioxide absorption edge (at $\lambda < 400$ nm) and was suitable for benzylic alcohol oxidation studies. It also indicated an enhanced visible light response profile between 400−550 nm compared to non-functionalised titanium dioxide as depicted in **Figure 69**, entry (f). The significance of the article published by Wang and co workers[188] identified an approach to feasibly shift titanium dioxide's band gap into the visible spectrum that could be later coupled to cadmium sulfide in the heterojunction strategy.

3.8.1.3. Testing of Nitrogen Functionalised Titanium Dioxide

Stemming from the findings noted above, nitrogen functionalised titanium dioxide was prepared at 350 ˚C after following the literature procedure as outlined by Wang *et al*.[188]

As the nitrogen functionalised titanium dioxide had not been tested in this research before, its photo-oxidative potential was evaluated with a proof-of-concept alcohol oxidation study of 3,4-dimethoxybenzyl alcohol to 3,4-dimethoxybenzaldehyde (**Table 7**). If the synthesised nitrogen functionalised titanium dioxide was able to mediate the oxidation of 3,4-dimethoxybenzyl alcohol, then the material would be coupled in the heterojunction concept with the cadmium sulfide system (copper|palladium alloy loaded onto the surface of silver functionalised cadmium sulfide). The heterojunction procedure was expected to develop a novel photocatalytic material with the anticipated outcome of achieving high alcohol conversions.

Table 7: Oxidation of benzyl alcohol using nitrogen functionalised titanium dioxide.[a]

Entry	Catalyst	Aldehyde (%)[b]	Carboxylic acid (%)[b]
1	None	9	0
2	$N\text{-}TiO_2$ (10 mg)	31	0
3	$N\text{-}TiO_2$ (20 mg)	78	0

[a]Reaction conditions: 0.1 mmol 3,4-dimethoxybenzyl alcohol, 20 mg $N\text{-}TiO_2$, toluene solvent (2.5 mL), O_2 solvent bubbling (1.5 minutes) and a solar-simulated xenon irradiation source (5 hours). [b]Conversions determined using GC-MS peak areas.

A significant outcome was obtained from the nitrogen functionalised titanium dioxide; it was capable of oxidising 3,4-dimethoxybenzyl alcohol with good conversion (**Table 7**, entry 3). However, despite the high conversion of benzyl alcohol to benzaldehyde (**Table 7**, entry 3), the novelty of nitrogen functionalised titanium dioxide needed further refinement to develop a unique material capable of oxidising benzyl alcohol with a photocatalytic efficiency exceeding 78 %.

From the success of the nitrogen functionalised titanium dioxide affording a 78 % conversion of 3,4-dimethoxybenzaldehyde; the idea of extending the cadmium sulfide studies into the visible-light-activated nitrogen functionalised titanium dioxide would fashion a visible light semiconductor through the development of a cadmium sulfide-titanium dioxide heterojunction. The expected outcome of forming a heterojunction between cadmium sulfide and titanium dioxide would deliver a novel-visible light activated semiconductor.

3.8.1.4. Creating a Heterojunction between CdS and TiO$_2$

Whilst studying the literature[69] to compile the introduction to this dissertation, three known band gap heterojunction schemes were reported in the literature, straddling (Type 1), staggered (Type 2), and broken (Type 3), (**Chapter 1.2**, **Figure 25**:).

Semiconductor-semiconductor heterojunctions have the potential to significantly enhance the exciton separation effect between two band gap pairs through independent electron and positive hole migration (**Figure 70**).
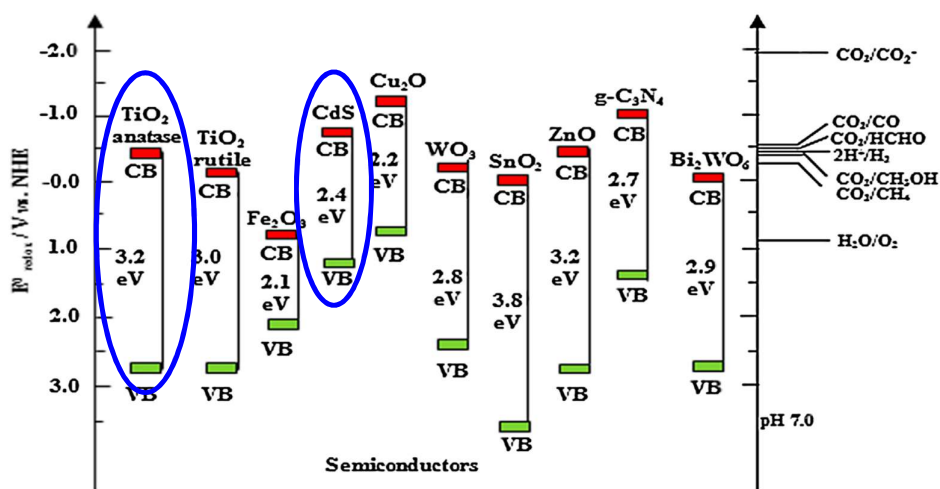
Figure 70: Band alignments of cadmium sulfide and titanium dioxide relative to the Normal Hydrogen Electrode (NHE). The figure parallels the respective potentials for the valence and conduction bands of cadmium sulfide and titanium dioxide, which create a favourable Z-scheme heterojunction pair.[189] Reprinted with permission from O. Ola and M. Maroto-Valer,

The possibility for improved positive hole migration from the valence band of titanium dioxide to the valence band of cadmium sulfide and electron transfer from the conduction band of cadmium sulfide to the conduction band of titanium dioxide has been illustrated in **Figure 71**.
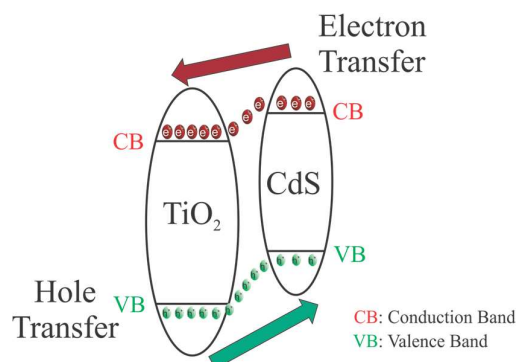
Figure 71: Exciton charge separation across the cadmium sulfide-titanium dioxide heterojunction. Electrons are transferred from the conduction band of CdS to the conduction band of TiO_2 and positive holes migrate from the valence band of TiO_2 into the valence band of CdS.

Based on the concept summarised in **Figure 71**, the alloying strategy (copper and palladium onto silver functionalised cadmium sulfide) and nitrogen functionalised titanium dioxide, a coupled heterojunction system between cadmium sulfide and titanium dioxide was investigated.

3.8.2. Coupling a Cu|Pd Alloy System and Nitrogen onto a CdS/TiO$_2$ Heterojunction

Until this point in the study, an approach for a copper|palladium alloy on silver functionalised cadmium sulfide was developed. The synthesised nitrogen functionalised titanium dioxide also afforded a 78 % conversion of 3,4-dimethoxybenzaldehyde. Therefore, the third section in this chapter was the

coupling of cadmium sulfide and titanium dioxide to develop the CdS-TiO$_2$ heterojunction system.

3.8.2.1. Synthesising and Evaluating the Photo-Oxidative Contribution from Cu, Pd, and N in CdS and TiO$_2$ Semiconductors with proof-of-concept studies

Before constructing the CdS|TiO$_2$ heterojunction, a research article published by Kuvarega et al.[25] delivered a pertinent evolution to the location of the components (Cu|Pd alloy) added to the heterojunction concept (**Figure 72**).
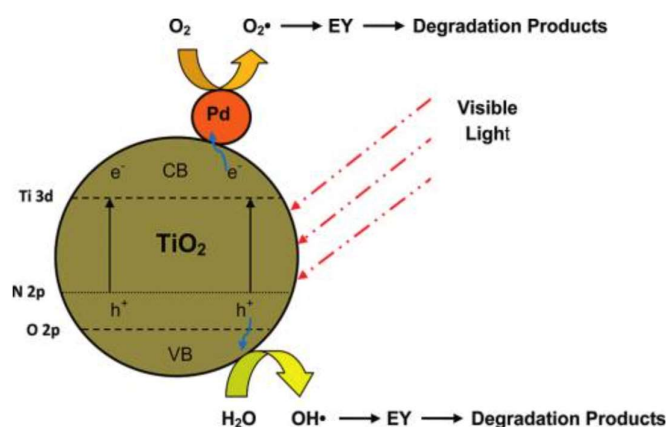
Figure 72: Nitrogen and palladium functionalised titanium dioxide. After visible light excitation, electrons migrate from the N$2p$ state into the conduction band of TiO$_2$. The electrons are trapped by metallic palladium that facilitates the photodegradation of eosin Y (EY) with superoxide radicals (O$_2^{\cdot-}$). Reprinted with permission from A. T. Kuvarega, R. W. M. Krause, B. B. Mamba, *J. Phys. Chem. C*, 2011, *115* (45), pp 22110–22120. Copyright (2011) American Chemical Society.

Kuvarega et al.[25] explored the possibility to photo-degrade eosin Y using titanium dioxide after its optical absorption profile was shifted into the visible spectrum through nitrogen and palladium doping. Nitrogen sensitised the band structure that consequently red shifted the absorption edge of titanium dioxide into the visible region through a narrower band gap. Palladium incorporation reportedly reduced the exciton recombination rate and increased the photo-activity of titanium dioxide under visible light.

Based on the literature information *vide supra*, nitrogen functionalised titanium dioxide was re-prepared with the addition of copper and palladium salts, thus producing Cu/Pd-N-TiO$_2$. Cu/Pd-N-TiO$_2$ was subsequently coupled to silver functionalise cadmium sulfide to fabricate the Ag-CdS on Cu/Pd-N-TiO$_2$ heterojunction (**Figure 73**).
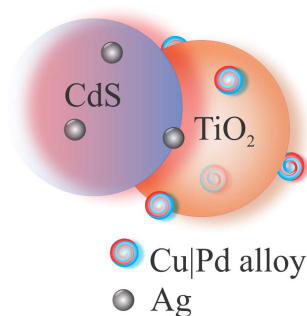
Figure 73: Conceptualised Ag-CdS on Cu/Pd-N-TiO$_2$, forming the complex heterojunctioned CdS-TiO$_2$ visible-light activated semiconductor.

On reflection, developing and modifying titanium dioxide's wide band gap with copper, palladium and nitrogen was anticipated to offer a superior photo-redox potential for the cadmium sulfide and titanium dioxide compounded semiconductor (Ag-CdS on Cu/Pd-N-TiO$_2$). Attenuating the wide band gap of titanium dioxide would shift the band edges into the visible region, whereas altering the narrow band gap of cadmium sulfide with copper and palladium would excessively red shift the band gap past any usable photo-redox potential.

The semiconductor heterojunction between cadmium sulfide and titanium dioxide was expected to overcome the low oxidation potential of cadmium sulfide's narrow band gap and assist titanium dioxide. The enhanced photo-reactivity of both metal chalcogen species was anticipated to arise through exciton charge separation (as depicted in **Figure 71**).

3.8.2.1.1. Synthetic Approach to the Preparation of Ag-CdS on Cu/Pd-N-TiO$_2$

Ag-CdS on Cu/Pd-N-TiO$_2$ was prepared according to the following procedure:

In a typical synthetic procedure, TTIP (10.55 mmol, 3.12 mL) was added drop-wise into de-ionised water (15 mL) followed by the addition of nitric acid (25 %, 4 mL). The mixture was stirred until the titanium hydroxide (Ti[OH]$_4$) precursor had dissolved from acid assistance (30 minutes). Cu(NO$_3$)$_2$·3H$_2$O (62.09 µmol, 15 mg in 2 mL absolute ethanol) and Pd(OAc)$_2$·4H$_2$O (30 mg in 2 mL absolute ethanol and 1 mL methanol) were prepared, added dropwise to the acidified aqueous titanium solution and proceeded with ten minutes stirring at room temperature. Aqueous ammonia (25 %) was subsequently added to lower the pH to *ca.* 9, which introduced the nitrogen component to the system. The solution colour turned light blue with a light blue precipitate forming upon addition of aqueous ammonia. After the neutralisation stage, the solution was filtered and the light blue Cu/Pd-N-TiO$_2$ precipitate was oven dried at 45 ˚C and calcinated at 350 ˚C for 2 hours. The resultant material, which was light brown in colour was ground to a fine powder for instrumental characterisations, which are discussed in further detail later.

After calcinating (350 ˚C for 2 hours) Cu/Pd-N-TiO$_2$, 45 mg of the as-synthesised material was left to stir in de-ionised water (10 mL) with the cadmium sulfide precursor, cadmium nitrate tetrahydrate (Cd[NO$_3$]$_2$·4H$_2$O, 0.12 mmol, 38.43 mg). Thereafter, aqueous (10 mL) sodium sulfide (Na$_2$S, 0.18 mmol, 14.05 mg) was left to slowly drip into the above stirring solution. The resultant dark brownish-yellow precipitate was centrifuged, washed with ethanol, de-ionised water, and then filtered. Once the solvents were removed and the material was oven dried at 60 ˚C for 5 hours, the powder was calcinated again at 350 ˚C for a further 2 hours to promote crystallisation of the cadmium sulfide onto the Cu/Pd-N-TiO$_2$. The powder remained dark brownish-yellow in colour.

From Step 1) above, half the nitrogen functionalised titanium dioxide with copper and palladium was kept aside from the heterojunction step with silver functionalised

cadmium sulfide (Step 2) as a comparative study. The purpose was to compare the oxidative effect of the heterojunctioned semiconductor system (Ag-CdS on Cu/Pd-N-TiO$_2$) against Cu/Pd-N-TiO$_2$. Due to the wide band gap of titanium dioxide, it was envisaged that the selected combination of copper, palladium and nitrogen functionalisation would red shift the optical absorption of titanium dioxide, therefore enhancing its photocatalytic ability in the visible spectrum for alcohol oxidations. The choice of keeping half the Cu/Pd-N-TiO$_2$ aside was shown to be an important consideration, as noted below.

3.8.2.1.2. The Photo-oxidative Success of Cu/Pd-N-TiO$_2$

To much delight, Cu/Pd-N-TiO$_2$ displayed viable visible-light-activated properties and was a capable semiconductor for photocatalysing a proof-of-concept alcohol oxidation **Table 8** (entry 5, $\geq$ 99 %). In order to confirm the success of Cu/Pd-N-TiO$_2$, various control reactions without the semiconductor, xenon irradiation, and in the absence of O$_2$ solvent bubbling were explored. The proof of concept results from the oxidation study of 3,4-dimethoxybenzyl alcohol have been reported below (**Table 8**).

Table 8: 3,4-Dimethoxybenzyl alcohol oxidation using Ag-CdS on Cu/Pd-N-TiO$_2$ and Cu/Pd-N-TiO$_2$.[a]

Entry	Catalyst	Aldehyde (%)[b]	Carboxylic acid (%)[b]
1	TiO$_2$	1	0
2	Uncalcinated Cu/Pd-N-TiO$_2$	3	0
3	N-TiO$_2$	78	0
4	Ag-CdS on calcinated Cu/Pd-N-TiO$_2$	22	0
5	Cu/Pd-N-TiO$_2$	$\geq$ 99	0
6[c]	No calcinated Ag-CdS or Cu/Pd-N-TiO$_2$	8	0
7[d]	Calcinated Cu/Pd-N-TiO$_2$	<1	0
8[e]	Calcinated Cu/Pd-N-TiO$_2$	83	0

9[f]	Calcinated Cu/Pd-N-TiO$_2$	1	0
10[g]	No calcinated Ag-CdS or Cu/Pd-N-TiO$_2$	1	0

[a]Reaction conditions: 0.1 mmol 3,4-dimethoxybenzyl alcohol, 20 mg photocatalyst, toluene solvent (2.5 mL), O$_2$ solvent saturation through bubbling (1.5 minutes) and solar-simulated xenon irradiation source (5 hours). [b]Conversions (%) determined using GC-MS peak areas. [c]Reaction performed without calcinated Ag-CdS or Cu/Pd-N-TiO$_2$. [d]Reaction performed in the absence of xenon irradiation–dark conditions. [e]Reaction performed in air without O$_2$ solvent saturation through bubbling. [f]Reaction performed in the absence of xenon irradiation-dark conditions and no O$_2$ solvent bubbling. [g]Reaction performed in the absence of calcinated Cu/Pd-N-TiO$_2$ and no xenon irradiation–dark conditions.

An unexpected result from **Table 8**, entry 4 was observed. Ag-CdS on Cu/Pd-N-TiO$_2$ was incapable of oxidising 3,4-dimethoxybenzyl alcohol more effectively than either N-TiO$_2$ (**Table 8**, entry 3, 78 %) or Cu/Pd-N-TiO$_2$ (**Table 8**, entry 5, $\geq$ 99 %). The semiconductor heterojunction induced a negative oxidative outcome, only yielding a 22 % conversion of 3,4-dimethoxybenzyl alcohol to 3,4-dimethoxybenzaldehyde. However, the result from **Table 8**, entry 5 was significantly more satisfactory, with the highest observed conversion in excess of 99 % (!). Cu/Pd-N-TiO$_2$ had demonstrated a near quantitative conversion of 3,4-dimethoxybenzyl alcohol to 3,4-dimethoxybenzaldehyde. The unique combination of coupling copper, palladium and nitrogen on titanium dioxide exemplified the significance of functionalising a suitable metal chalcogen with appropriate extrinsic doping agents for selected organic transformations (alcohol oxidations to aldehydes).

Various control reactions (**Table 8**, entries 6−10) demonstrated that without the combination of Cu/Pd-N-TiO$_2$ and xenon irradiation, poor conversions of 3,4-dimethoxybenzylaldehyde were obtained. **Table 8**, entry 8 did however, identify that molecular oxygen did not contribute significantly to the overall conversion of 3,4-dimethoxybenzylaldehyde, as an 83 % conversion was obtained in the absence of molecular oxygen. Mechanistic studies with electron-hole scavengers may be explored in future studies in order to identify the possible mode of oxidation in which

$Cu/Pd-N-TiO_2$ operates-either through direct hole oxidations or *via* an indirect route through conduction band electrons.

The proof-of-concept study for oxidising alcohols using a novel $(Cu/Pd-N-TiO_2)$ semiconductor was complete. Following the success of $Cu/Pd-N-TiO_2$, a brief outline of the photo-physical properties of Cu, Pd and N that imparted visible-light sensitivity into TiO_2 have been outlined below. A detailed instrumental characterisation of $Cu/Pd-N-TiO_2$ was subsequently undertaken to obtain a better insight as to the nature and composition of the three-component (Cu, Pd and N) system on TiO_2. After the characterisation studies of $Cu/Pd-N-TiO_2$, the photo-oxidative potential of $Cu/Pd-N-TiO_2$ has been evaluated in an array of cyclic alcohol oxidations.

3.8.2.1.3. The Visible Light Contributions Imparted by Cu, Pd and N to TiO_2

The concept of harnessing nitrogen functionalisation,[25] the photo-efficiency of palladium functionalised titanium dioxide,[33] and adapting the principle of copper and platinum to copper and palladium nanoparticles on titanium dioxide[43] presented a novel concept, which led to the development of a three-component functionalised titanium dioxide system $(Cu/Pd-N-TiO_2)$ in this research.

Nitrogen was chosen to reduce the band gap of titanium dioxide and red shift the optical absorption edge into the visible region. Nitrogen's insertion into the valence band of titanium dioxide would afford a mixed valence band state of oxygen $2p$ and nitrogen $2p$ orbitals and raise the intrinsic valence band to greater negative redox potentials.[190],[191]

Palladium would act as a light sensitiser, accepting visible light irradiation, while adsorbed on the surface of titanium dioxide. Simultaneously, titanium dioxide would also be absorbing visible light energy due to nitrogen doping that was chosen to attenuate the ultraviolet light activated band gap of titanium dioxide towards the visible region. However, palladium had a relatively large work function (5.55 eV),[192] which in turn determined the height of the metal-semiconductor Schottky Barrier. Copper

possessed a lower work function (4.65 eV) and therefore mixing copper and palladium would be expected to decrease the work function of palladium and reduce the overall Schottky Barrier height at the Cu|Pd-TiO$_2$ interface. The lowered Schottky Barrier height of Cu|Pd-TiO$_2$ would also be anticipated to reduce the exciton recombination centres of titanium dioxide and enhance the visible light photo-activity toward alcohol photo-oxidations.

3.9. Instrumental Insight into Copper/Palladium on Nitrogen Functionalised Titanium Dioxide, Cu/Pd-N-TiO$_2$

3.9.1. Characterising a Novel Semiconductor

The next chapter of the research was to understand the photo-physical properties of the three-component system (Cu, Pd and N) on titanium dioxide. Therefore, numerous instrumental techniques were employed, which have been discussed below to study the semiconductor further and included: electron microscopy, Brunauer-Emmett-Teller theory, energy-dispersive X-ray spectroscopy, inductively coupled plasma-mass spectrometry, powder diffuse reflectance UV/Vis spectroscopy, powder X-ray diffraction spectroscopy, Raman spectroscopy, photoluminescence spectroscopy, and X-ray photoelectron spectroscopy.

3.9.2. Brunauer-Emmett-Teller Theory and Electron Microscopy

Titanium dioxide nanoparticles are described as chemically robust, photo-catalytically reactive and relatively inexpensive for organic transformations and organic dyestuff degradation studies.[6],[193],[194] In essence, the nanoparticulate morphology of the metal oxide imparts a greater catalytic surface area compared to macroporous materials and hence improves photo-reactivity.[195] Therefore, a proposed instrumental study to determine how calcinated Cu/Pd-N-TiO$_2$ was capable of functioning as a visible light-sensitised semiconductor began with Brunauer-Emmett-Teller (B.E.T.) theory, scanning electron microscopy and transmission electron microscopy measurements.

B.E.T. theory was a useful technique to quantify surface areas, pore volumes, pore sizes, and average particle sizes of $Cu/Pd-N-TiO_2$, which was later compared to uncalcined $Cu/Pd-N-TiO_2$ and calcinated $N-TiO_2$ (**Table 9**).

Table 9: B.E.T. surface area measurements of calcinated $N-TiO_2$, uncalcined $Cu/Pd-N-TiO_2$ and calcinated $Cu/Pd-N-TiO_2$.[a]

B.E.T. Surface Area	Calcinated $N-TiO_2$	Uncalcined $Cu/Pd-N-TiO_2$	Calcinated $Cu/Pd-N-TiO_2$
B.E.T. Surface Area	132.9 m²/g	341.6 m²/g	119.9 m²/g
Pore Volume[b]	0.188 cm³/g	0.276 cm³/g	0.155 cm³/g
Pore Size[c]	56.73 Å	32.37 Å	51.59 Å

[a]The analysis of calcinated $N-TiO_2$, uncalcined $Cu/Pd-N-TiO_2$ and calcinated $Cu/Pd-N-TiO_2$ were studied by using 11 different pressure points for monitoring nitrogen physisorption, and a straight-line graph has been made available in the **Appendix**.
[b]Single point adsorption total pore volume of pores less than 1578.400 Å diameter at P/Po = 0.987590100

The B.E.T. surface area and pore volume of uncalcined $Cu/Pd-N-TiO_2$ (341.6 m²/g, 0.276 cm³/g, **Table 9**) were significantly higher than both calcinated $N-TiO_2$ (132.9 m²/g, 0.188cm³/g) and calcinated $Cu/Pd-N-TiO_2$ (119.9 m²/g, 0.155 cm³/g). The result was speculated to originate from the preparation of $Cu/Pd-N-TiO_2$ (before the calcination step) because the addition of aqueous ammonia to copper nitrate precipitated a cupramine ($Cu[NH_3]_4^{2+}$) complex. Hence, the recorded B.E.T. surface area and pore volume of uncalcined $Cu/Pd-N-TiO_2$ was a combination of uncalcined $Cu/Pd-N-TiO_2$ and the cupramine complex. After the calcination process (350 ˚C for two hours), the cupramine complex was thermally removed, which was later observed in the lower B.E.T. surface area and pore volume of calcinated $Cu/Pd-N-TiO_2$ (119.9 m²/g, 0.155 cm³/g). The noticeable reduction in surface area of calcinated $Cu/Pd-N-TiO_2$ in comparison to uncalcined $Cu/Pd-N-TiO_2$ could also be assigned to the particle aggregation of the material that was induced during the calcination (350 ˚C)

period. These findings were in agreement with published material by Chen *et al.*,[196] who described a lowering in the surface area of titanium dioxide nanoparticles after increasing the calcination temperature (250−700 ˚C in a nitrogen atmosphere). The pore sizes of calcinated N-TiO$_2$ (56.73 Å) and calcinated Cu/Pd-N-TiO$_2$ (51.59 Å) were also significantly larger than uncalcined Cu/Pd-N-TiO$_2$ (32.37 Å), and well within the International Union of Pure and Applied Chemistry's (IUPAC) rating for mesoporous materials (2−50 nm). Similar observations of mesoporous nanocrystalline titanium dioxide have been reported in the literature that correlated the lowering in the B.E.T. surface area and increase in both averaged nanoparticle size and pore size after calcinating the metal oxide. The observations were attributed to the crystallisation of the titanium dioxide's 'inorganic wall' and the collapse of the mesoporous structure.[197]

After completing the B.E.T. surface area study of calcinated N-TiO$_2$, uncalcined Cu/Pd-N-TiO$_2$ and calcinated Cu/Pd-N-TiO$_2$; scanning electron microscopy was utilised to identify the morphological structure of calcinated Cu/Pd-N-TiO$_2$ (**Figure 74**).

Uncalcined Cu/Pd-N-TiO$_2$	
Calcinated N-TiO$_2$	
Calcinated Cu/Pd-N-TiO$_2$	
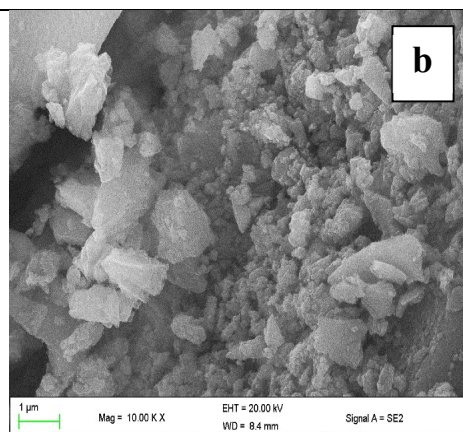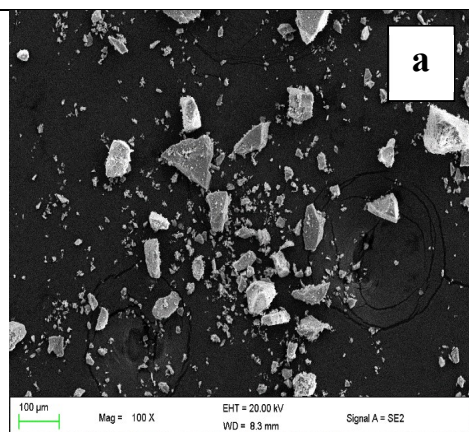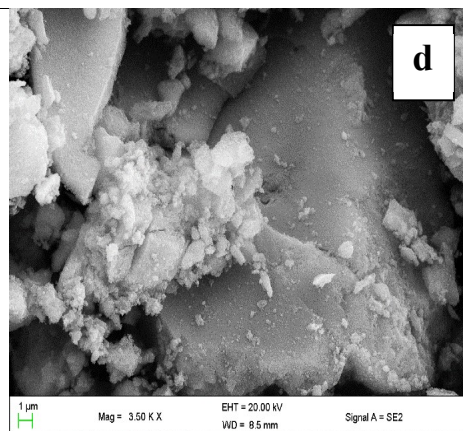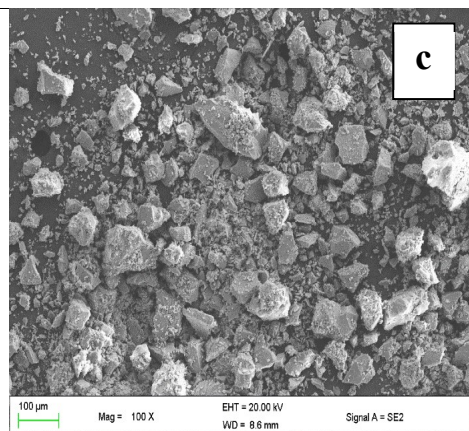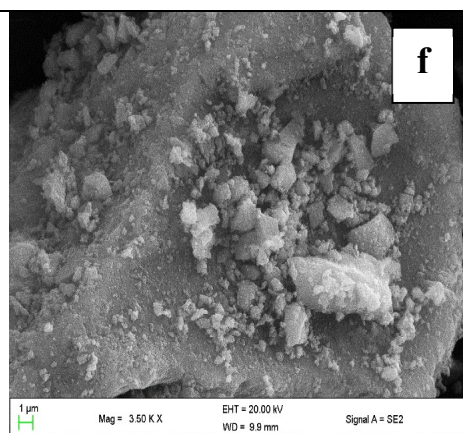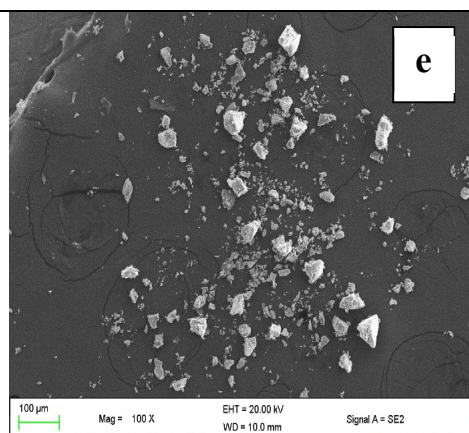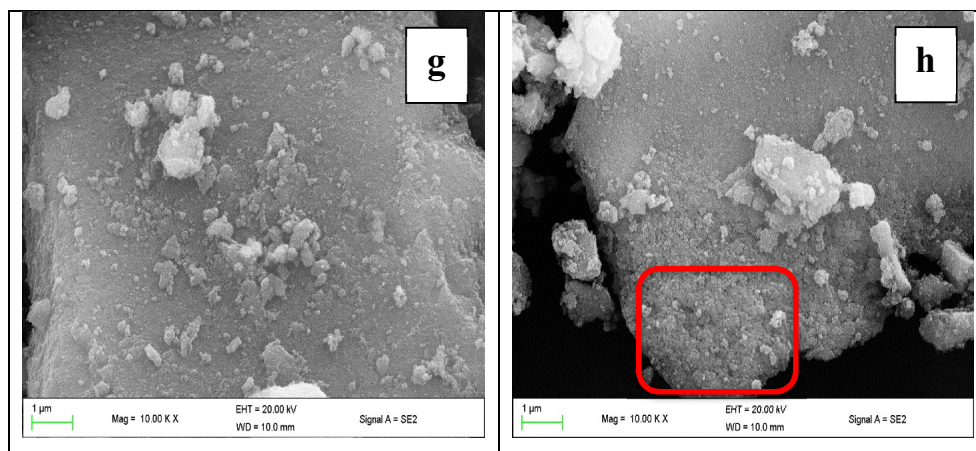
Figure 74: Electron micrographs of uncalcined Cu/Pd-N-TiO$_2$ (images a and b), calcinated N-TiO$_2$ (images c and d), and calcinated Cu/Pd-N-TiO$_2$ (images e, f, g, and h).

The scanning electron micrographs of uncalcined Cu/Pd-N-TiO$_2$, calcinated N-TiO$_2$, and calcinated Cu/Pd-N-TiO$_2$ at low 100× magnifications (**Figure 74** images a, c and e) depicted irregular micron-sized particulates in each of the three samples. The materials all consisted of various sub-micron (< 1 μm) and much larger (above 100 μm) asymmetrical structures. Further magnification of the three materials established that the sol-gel synthesis approach did not favour uniform morphological growth (**Figure 74** images b, d, f, g and h). However, the red-zoned edge of the polycrystalline structure in **Figure 74** image 'h' provided evidence to suggest that the micron-sized particulates were structured from much smaller spherical objects. After visual inspection of the electron micrographs shown in **Figure 74**, the average crystallite far exceeded the nanometer scale. However, literature has reported that other metal (tungsten) nanomaterials are also prone to aggregation, therefore limiting the application of scanning electron microscopy to identify the morphological state of the investigated material due to magnification limitations.[198]

Therefore, transmission electron micrographs of calcinated Cu/Pd-N-TiO$_2$ were collected (**Figure 75**). The calcinated Cu/Pd-N-TiO$_2$ was studied at higher magnifications to determine if the micron-sized calcinated Cu/Pd-N-TiO$_2$ particulates depicted in **Figure 74** were aggregated nanoparticles.
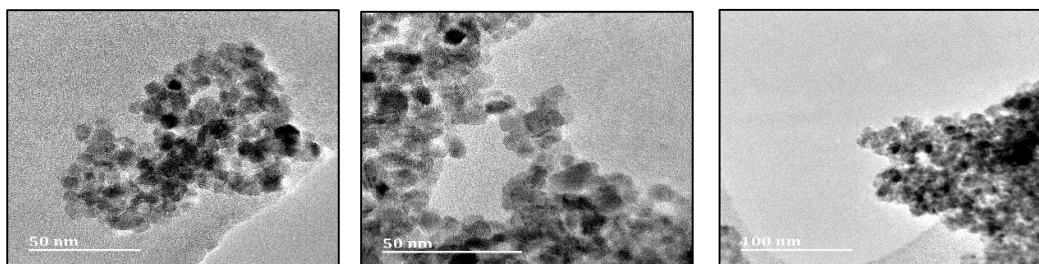
Figure 75: Transmission electron micrographs of aggregated calcinated Cu/Pd-N-TiO$_2$ nanoparticles. The micrographs depict clusters of *nano-seeds.* (50−100 nm scale bar).

While the scanning electron micrographs from **Figure 74,** postulated micron-sized particles, the transmission electron micrographs (**Figure 75**) had positively identified the morphological composition of calcinated Cu/Pd-N-TiO$_2$. Numerous clusters of *nano-seeds* were depicted in **Figure 75** with consistent diameters of less than 10 nm.

The aggregation of Cu/Pd-N-TiO$_2$ nano-seeds suggested that the synthetic procedure of Cu/Pd-N-TiO$_2$ could be improved in future studies. However, further microscopic investigations were required to ascertain whether the co-alloying principle of copper and palladium (Cu|Pd), which was based on the literature was successfully implanted onto the surface of titanium dioxide (**Figure 77**).[43],[25]

Energy-dispersive X-ray spectroscopy was initially employed to map the constituent metal (copper and palladium) elements in the proposed Cu/Pd-N-TiO$_2$ material (**Figure 76**).
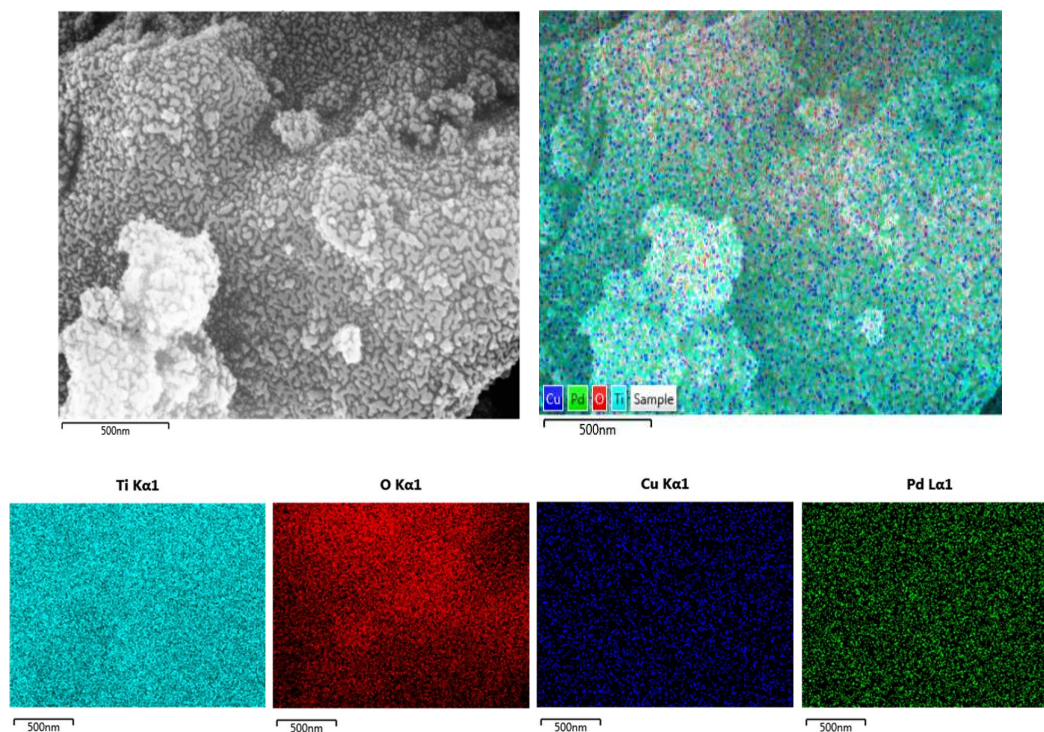
Figure 76: Elemental mapping of Ti, O, Cu, and Pd in the micron-sized Cu/Pd-N-TiO$_2$. Scale bar set at 500 nm.

The mapping analysis depicted that low concentrations of copper and palladium species were evenly distributed on Cu/Pd-N-TiO$_2$. However, the study was unable to identify if the desired Cu|Pd alloy had formed. To subsequently explore the potential of a Cu|Pd alloy, Cu/Pd-N-TiO$_2$ was further examined with HRTEM to detect potential lattice spacings for the Cu|Pd alloy pair (**Figure 77**).
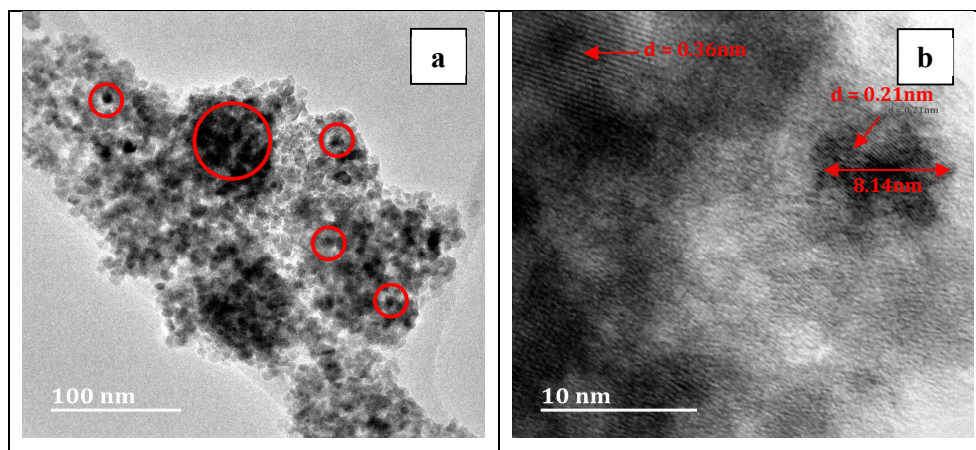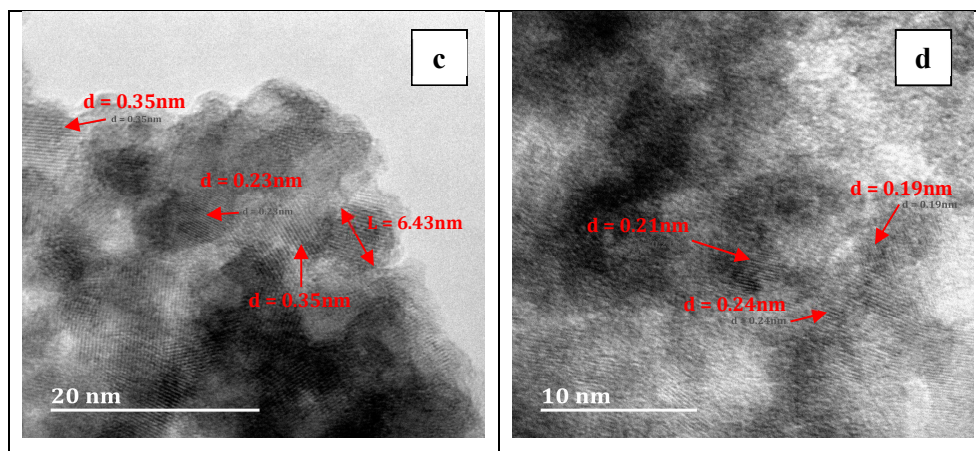
Figure 77: Lattice spacings of copper and palladium on Cu/Pd-N-TiO$_2$

The interpretation of **Figure 77** (image a) suggested that metal nanoparticles were present, yet randomly aggregated on Cu/Pd-N-TiO$_2$ (as evident by the circled dark spot regions, **Figure 77** image a). These however, could have just as likely originated from excess packing of TiO$_2$ nano-seeds. Several of the circled regions were in-fact identified as TiO$_2$ (*d*-lattice spacings: 0.35−0.36 nm).[199],[200] Although selected sites presented with *d*-lattice spacings that did not match those of TiO$_2$ as depicted in **Figure 77** (images b, c, and d), with lattice spacings of 0.19, 0.21, 0.23 and 0.24 nm. The literature has identified palladium (Pd^0) nanoparticles with *d*-lattice spacings of 0.19 nm and 0.21 nm,[201] PdO (0.26 nm),[202] copper nanoparticles (Cu^0 = 0.20 nm, CuO = 0.23 nm, and Cu$_2$O = 0.24 nm).[203],[204],[205] The expected Cu|Pd alloy has also been reported to consist of a unique lattice pair, 0.21 and either 0.29 or 0.30 nm that match the B2 phase of the Cu|Pd alloy.[206],[207] The absence of 0.29/0.30 nm lattice spacings in **Figure 77** despite the presence of 0.21 nm, suggested that the Cu|Pd alloy was not synthesised as expected, and the metal functionalisation of titanium dioxide only consisted of separate Pd^0, Cu$_2$O and or CuO nanoparticles. (further metal speciation analyses have been conducted later in this chapter with the application of X-ray photoelectron spectroscopy that has deduced the metallic oxidation state of palladium [Pd^0]).

3.9.3. Energy-Dispersive X-ray Spectroscopy

Calcinated $Cu/Pd-N-TiO_2$ was prepared using a sol-gel approach as outlined in **Chapter 3.8.2.1.1.** During the synthetic process, copper and palladium were incorporated into the titanium hydroxide matrix from metal salts dissolved in ethanol. However, to qualitatively confirm if copper and palladium ions were retained within the $Cu/Pd-N-TiO_2$ three component system after the workup procedure and subsequent calcination, energy-dispersive X-ray spectroscopy was used to detect the presence of both metals (**Figure 78**).

Element	Weight (%)
C Kα	3.33
N Kα	−3.95
O Kα	48.40
Ti Kα	51.86
Cu Kα	0.05
Pd Lα	0.30
Total	100.00
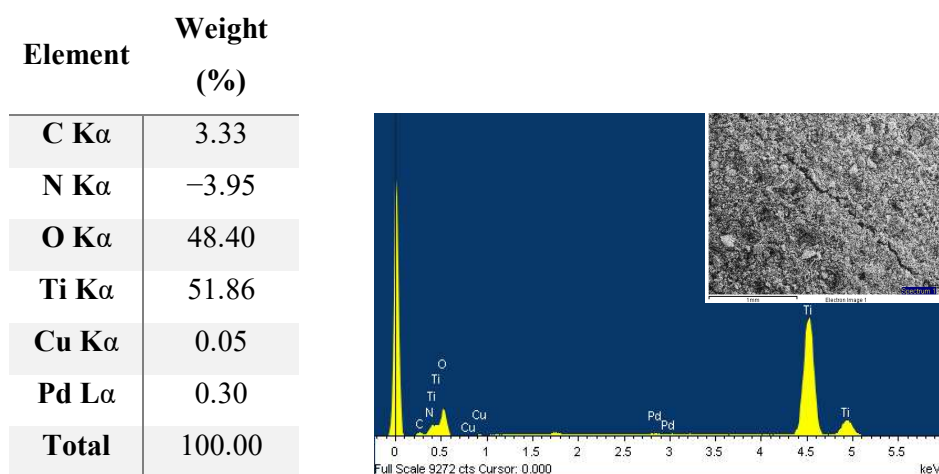
Figure 78: The energy-dispersive X-ray analysis of $Cu/Pd-N-TiO_2$ detailing the weight percentages of the various constituents in $Cu/Pd-N-TiO_2$ with the inclusion of Ti Kα.

Copper and palladium were present at low weight percentages (0.05 and 0.30 wt%, respectively), however, the tabulated data presented in **Figure 78** accumulated a negative weight percentage total for nitrogen (−3.95 wt%). However, after carefully examining X-ray energies of the periodic elements, nitrogen's Kα emission line resides at 0.392 KeV meanwhile titanium's Lα emission line is recorded at 0.452 KeV. Therefore, a peak overlap caused emission signature distortions and hence a negative nitrogen percentage. Therefore, the sample study was re-run without titanium's contribution to the percentage table (**Figure 79**).

Element	Weight (%)
C Kα	13.79
N Kα	17.80
O Kα	66.76
Cu Kα	0.33
Pd Lα	1.32
Total	100.00
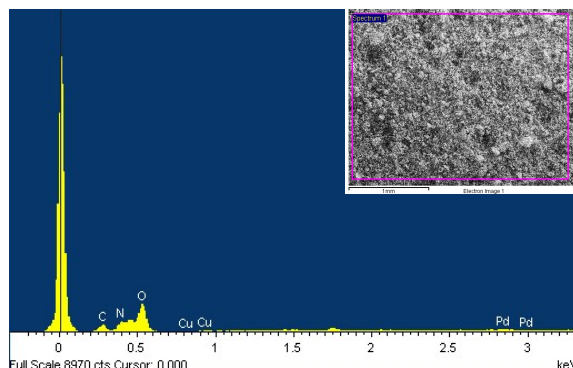
Figure 79: The energy-dispersive X-ray analysis of Cu/Pd-N-TiO$_2$ detailing the weight percentages of the various constituents in Cu/Pd-N-TiO$_2$ without the inclusion of Ti Kα.

After removing titanium's percentage (**Figure 79**), the adjusted figures recorded similar copper and palladium values, in addition to a positive nitrogen value. Additional studies were also conducted to determine the titanium percentage totals with nitrogen's exclusion and consistent weight percentages (49−52 wt% Ti) were recorded (See the **Appendix**). The data suggested that the weight percentages of copper and palladium in Cu/Pd-N-TiO$_2$ were 0.05–0.33 wt% and 0.30–1.32 wt%, respectively (**Figure 79** and **Figure 80**). It should be noted that EDX analyses are only qualitative, thus not determining the absolute weight percentages of the functionalising species (Cu, Pd, and N) in Cu/Pd-N-TiO$_2$. The quantification of Cu and Pd in Cu/Pd-N-TiO$_2$ has been determined by ICP-MS (**Table 10**).

Table 10: Copper and palladium loadings of Cu/Pd-N-TiO$_2$ as determined by ICP-MS.

Semiconductor (SC) material	Cu (mg/kg SC)	Pd (mg/kg SC)
Cu/Pd-N-TiO$_2$	407	1800

The ICP-MS analyses quantitatively confirmed the presence of copper and palladium in the three-component Cu/Pd-N-TiO$_2$. The weight loadings of copper and palladium were detected for Cu at 407 mg/kg SC (0.04 wt%) and Pd at 1800 mg/kg SC (0.18 wt%).

3.9.4. Powder diffuse reflectance UV/Vis spectroscopy

Copper oxide, palladium, and nitrogen functionalised titanium dioxide afforded a three-component semiconductor (Cu/Pd-N-TiO$_2$) that was activated using visible light (**Table 8**, entry 5). Therefore, after completing the microscopic and spectrometric analyses, Cu/Pd-N-TiO$_2$ was subjected to powder diffuse reflectance UV/Vis spectroscopy (operated in absorbance mode) to ascertain the degree of red shifted character in titanium dioxide after nitrogen's substitution for oxygen atoms and the surface loading of copper oxide and palladium (**Figure 80**).
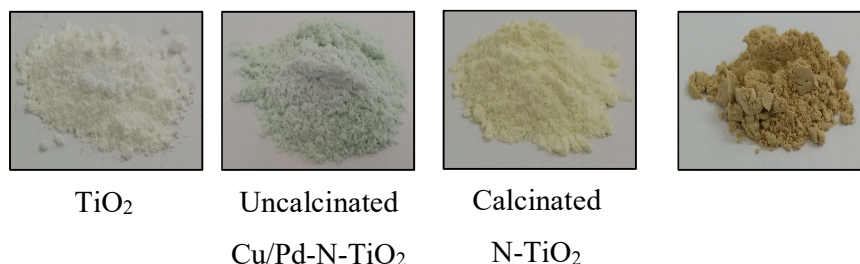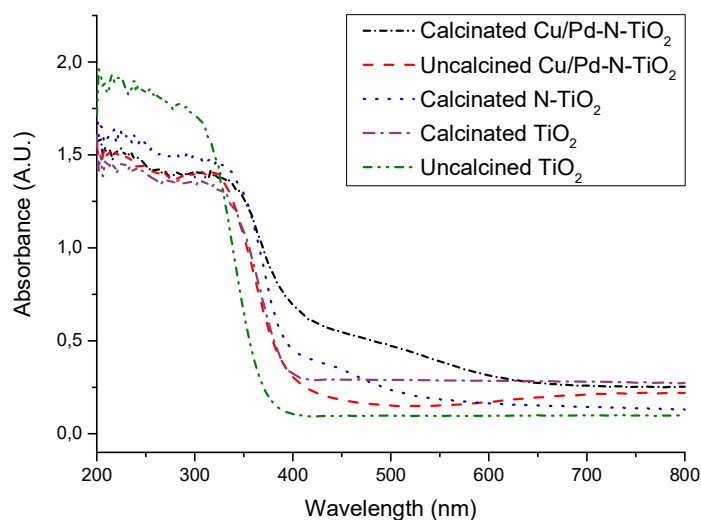
Figure 80: Powder diffuse reflectance UV/Vis spectra of Cu/Pd-N-TiO$_2$ derivatives.

Without the inclusion of copper oxide, palladium, and nitrogen, titanium dioxide (uncalcined and calcined, **Figure 80**) retained a defined wavelength cut-off without peak tailing at red shifted wavelengths ($\lambda > 400$ nm). The wavelength cut-off of both uncalcined and calcined titanium dioxide species had sharp cut-offs below 400 nm.

After nitrogen was incorporated into the calcinated titanium dioxide (N-TiO_2) structure, a red shifted adsorption shoulder was observed at 475 nm. Furthermore, after calcinating nitrogen functionalised titanium dioxide with copper oxide and palladium (Cu/Pd-N-TiO_2), the optical absorption profile drastically shifted into the visible region with enhanced absorbance values. However, uncalcined Cu/Pd-N-TiO_2 presented a poor red shifted character and low absorption profile compared to calcinated Cu/Pd-N-TiO_2, which was proposed to occur after calcinating Cu/Pd-N-TiO_2. The calcination procedure was expected to promote the anionic exchange (nitrogen for oxygen) and the crystallisation of the metal species (copper and palladium) on titanium dioxide. Cu/Pd-N-TiO_2 was calcinated at 350 ˚C to preserve the optimal nitrogen: visible light ratio. Wang *et al.*[188] reported that calcinating nitrogen functionalised titanium dioxide at temperatures above 350 ˚C promoted crystallisation of amorphous titanium dioxide at the expense of reducing the visible-light photo-activation of N-TiO_2 (due to the loss of lattice-bound nitrogen). Therefore 350 ˚C was chosen as an appropriate calcination temperature to balance the photo-efficiency of Cu/Pd-N-TiO_2 with the minimum temperature to ensure crystallisation of titanium dioxide into the anatase polymorph.

An important observation was observed in **Figure 80** after a broad absorbance peak (440 nm) for calcinated Cu/Pd-N-TiO_2 was observed to tail-off after 560 nm. In a palladium-doped titanium dioxide study, Grabowska *et al.*[187] noticed comparable findings during powder diffuse reflectance UV/Vis spectroscopy studies. Their[187] investigation concluded that the substantial overlap between *s*-, *p*- and, *d*-palladium bands (principal quantum numbers were not defined) induced a broad absorbance peak across most of the visible region (above 700 nm), which had arisen from a localised surface plasmonic resonance effect of the surface-loaded palladium nanoparticles. A similar observation was noticed in **Figure 80** (see calcinated Cu/Pd-N-TiO_2). However, as already noted, the peak tailed to lower absorbances after 560 nm. Despite the minimal copper loadings (0.04 wt% Cu, **Table 10**), the broad absorbance peak was suspected to arise from the mixture of palladium and copper oxide. Copper has also been shown to nominally shift the cut-off wavelength absorbance profile of titanium dioxide using sol-gel fabrication techniques.[208] Therefore, the combined effects of copper oxide, palladium, and nitrogen were proposed to functionalise the titanium dioxide host, which produced a unique powder UV/Vis absorbance profile.

3.9.5. Powder X-ray diffraction

The results from the powder diffuse reflectance UV/Vis spectroscopic data confirmed that calcinated Cu/Pd-N-TiO$_2$ had a strong visible light absorbing component compared to commercial titanium dioxide, calcinated N-TiO$_2$, and uncalcined Cu/Pd-N-TiO$_2$. However, it was unclear whether the copper and palladium species had altered the crystal structure of titanium dioxide's anatase polymorph (**Figure 81**).
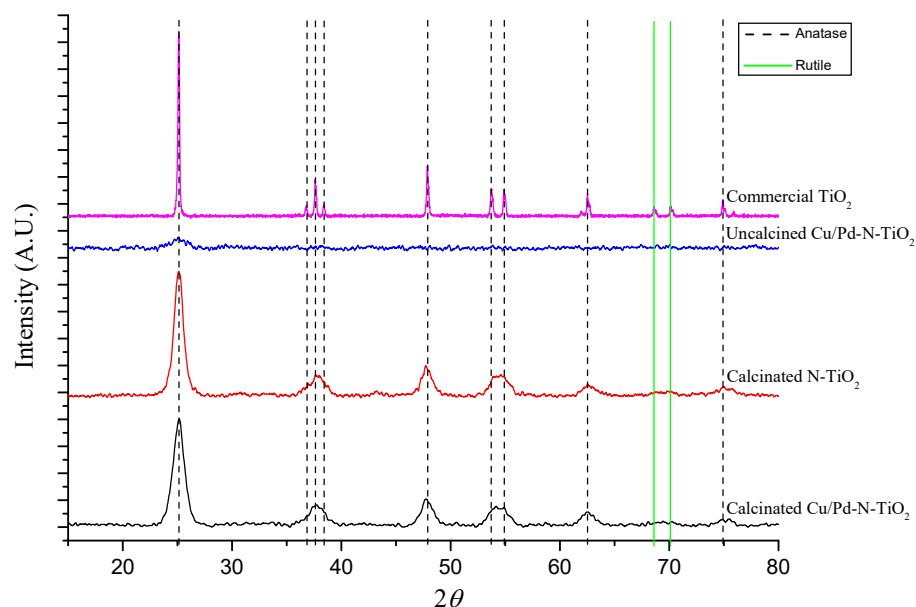
Figure 81: Powder X-ray diffractograms of titanium dioxide analogues.

After inspecting the powder X-ray diffractograms of **Figure 81**, commercial TiO$_2$ presented well-defined peaks between 2θ values of 25.1, 37.6, 47.9, 53.7, 54.9, 62.5, and 74.9 that indexed well with literature for anatase besides two rutile peaks at 2θ values of 68.6 and 70.1 (JCPDS card no. 21−1272).[209] **Figure 81** aptly demonstrated the need to calcinate Cu/Pd-N-TiO$_2$. Without the 350 ˚C/two-hour calcination period, uncalcined Cu/Pd-N-TiO$_2$ existed as an amorphous material. The photo-oxidative potential of uncalcined Cu/Pd-N-TiO$_2$ was evaluated during the optimisation studies (**Table 8**, entry 2). The results revealed that a 3 % conversion of 3,4-dimethoxybenzyl alcohol was obtained (**Table 8**), thus confirming the importance of calcinating and hence synthesising anatase in the Cu/Pd-N-TiO$_2$ photocatalytic system, which was in agreement with titanium dioxide (anatase) literature.[71]

A few additional observations were significant with respect to Cu/Pd-N-TiO$_2$. Compared to commercial titanium dioxide, the peak resolutions (**Figure 81**) of uncalcined Cu/Pd-N-TiO$_2$, calcinated N-TiO$_2$ and calcinated Cu/Pd-N-TiO$_2$ were broad. The literature has reported that peak shape is related to particle size.[210] No observable peaks for copper oxide or palladium were detected in **Figure 81** (which was expected, due to the low weight loadings, Cu [0.04 wt%] and Pd [0.18 wt%]). Therefore, the average particle size of Cu/Pd-N-TiO$_2$ was estimated using the Scherrer equation:

$$D_c = \frac{K\lambda}{\beta Cos\theta}$$

In the above expression, D_c is the average crystallite size, K is the Scherrer constant (0.89), λ is the cobalt X-ray wavelength (0.179 nm), β is the full width at half maximum (FWHM), and θ is the peak diffraction angle.

From **Figure 81**, the diffraction 2θ peaks at 25.12, 37.71, 47.83, 54.38, and 62.56 were used to compute the particulate sizes of calcinated Cu/Pd-N-TiO$_2$ as 7.07, 5.78, 7.96, 5.42, and 7.50 nm, respectively with an average crystallite size of 6.75 nm. This value (6.75 nm) was in good agreement with the measured particle size reported in **Figure 77** (image c) of 6.43 nm.

Similar X-ray diffraction reports of copper functionalised titanium dioxide noted that copper was undetected during the characterisation process. It was speculated that copper oxide was either absent from the titanium dioxide's surface, evenly included within titanium dioxide's lattice or was absent altogether. However, with respect to Cu/Pd-N-TiO$_2$ and the previously reported EDX and ICP-MS analyses in **Chapter 3.9.3**, copper was positively identified. Therefore, to attempt a further confirmation for the presence of copper and palladium species, Cu/Pd-N-TiO$_2$ was studied using Raman spectroscopy (**Chapter 3.9.6.**).

3.9.6. Raman spectroscopy

Due to the capacity of Raman spectroscopy to detect sensitive vibration mode changes in the crystal structure of solid-state materials, Cu/Pd-N-TiO$_2$ was subjected to investigation using this technique (**Figure 82**).

Commercial titanium dioxide presented three well-resolved vibrational modes, 391.3 cm^{-1} (B$_1$G), 511.5 cm^{-1} (A$_1$G), and 634.2 cm^{-1} (E$_g$, **Table 11**). In comparison to the as-prepared titanium dioxide analogues, uncalcined Cu/Pd-N-TiO$_2$, N-TiO$_2$ and calcinated Cu/Pd-N-TiO$_2$ presented with minor peak shifts (**Figure 82** and **Table** 11). Wang *et al.*[188] reported that doping titanium dioxide with nitrogen induced structural deviations to the metal oxide and hence variations in the vibrational peak shifts, of which minor shifts were observed in the three prepared Cu, Pd, and N functionalised titanium dioxide derivatives.
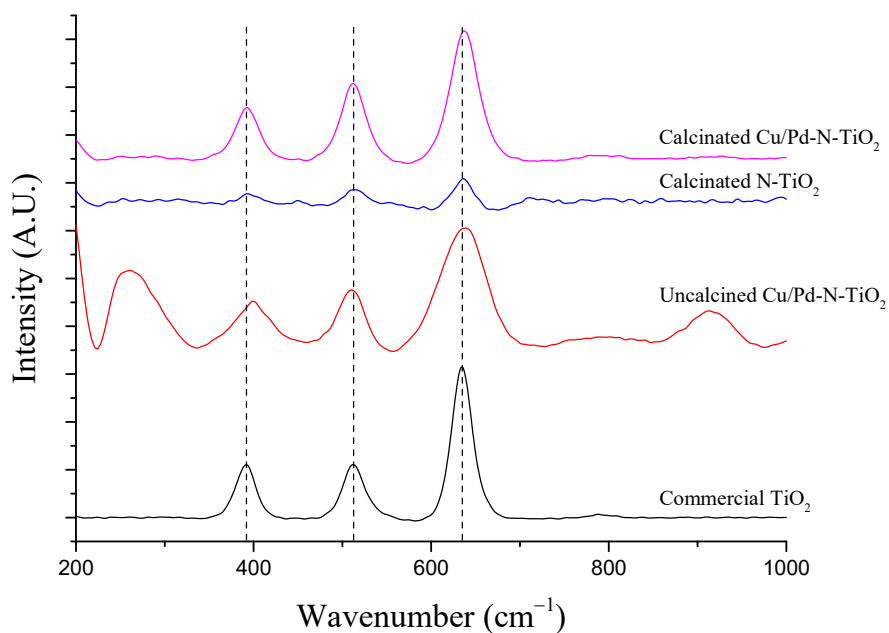
Figure 82: Stacked Raman spectra of the various (Cu, Pd, and N) functionalised titanium dioxide derivatives compared to commercial TiO$_2$.

Table 11: Vibrational peak shifts of N, Pd and Cu functionalised titanium dioxide derivatives.

Semiconductor	Wavenumber (cm^{-1})	Vibrational mode
Commercial	391.3	B_1G
TiO$_2$	511.5	A_1G
	634.2	E_g
Uncalcined	399.8	B_1G
Cu/Pd-N-TiO$_2$	510.1	A_1G
	637.7	E_g
Calcinated	392.5	B_1G
N-TiO$_2$	513.7	A_1G
	636.3	E_g
Calcinated	392.5	B_1G
Cu/Pd-N-TiO$_2$	511.5	A_1G
	637.7	E_g

Uncalcined Cu/Pd-N-TiO$_2$ presented two unknown peaks at 260.6 cm^{-1} and 912.3 cm^{-1}. These were unidentifiable peaks, which were suspected of being a result of metal (Cu/Pd) ligand complexes formed during the experimental procedure to synthesise Cu/Pd-N-TiO$_2$. Their absence in the calcinated Cu/Pd-N-TiO$_2$ suggested that the calcination temperature removed them during the heating process. The calcinated Cu/Pd-N-TiO$_2$ also presented no significant peak shifting, which was anticipated as the low weight percentage loadings of copper and palladium were minimal (Cu at 407 mg/kg SC (0.04 wt%) and Pd at 1800 mg/kg SC (0.18 wt%, **Table 10**)

Within the school, a new Renishaw® inVia Raman microscope was acquired and with the enhanced performance offered by this instrument, Cu/Pd-N-TiO$_2$ was further investigated to attempt the detection of the low weight loadings of copper oxide and palladium (**Figure 83**).
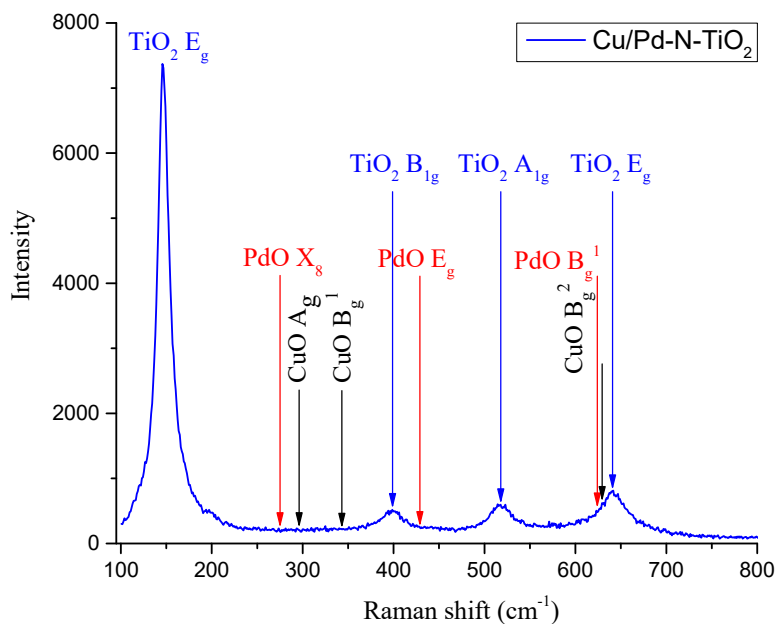
Figure 83: Raman spectrum obtained from the high-performance Renishaw® inVia Raman microscope.

There was no detectable evidence for neither copper nor palladium species on the surface of $Cu/Pd-N-TiO_2$ even when studied with the more advanced Renishaw® inVia Raman microscope, which was consistent with the prior Raman studies (**Figure 82** and **Table 11**). This was most likely due to the low weight percentage loadings of copper and palladium used to synthesise $Cu/Pd-N-TiO_2$ (**Table 10**). The expected Raman shifts of copper oxide and palladium oxide nanoparticles have been noted in **Figure 83**. Metallic palladium (Pd^0) has no Raman active modes and has not been indicated in **Figure 83**.[211]

The lack of any evidence to suggest ion-exchange or interstitial ion processes for either copper or palladium prompted the need to study $Cu/Pd-N-TiO_2$ further using photoluminescence spectroscopy.

3.9.7. Photoluminescence spectroscopy

Photoluminescence spectroscopy is a useful technique to study solid-state metal oxides as it provides an understanding of structural defects within the bulk and on the surface of a material under investigation. In an analogous approach to Raman spectroscopy that detects subtle changes in vibrational modes, which arise from lattice functionalisation of the *parent* target material (*i.e.* doping *titanium dioxide* with transitional metals), photoluminescence spectroscopy has the capacity to detect vacancy sites (*i.e.* defects), relative exciton lifetimes between HOMO-LUMO states (fluorescence) of different samples, indirect forbidden exciton transitions (phosphorescence) and self-trapped excitons located in defect sites (defect sites that may have arisen from lattice strain or miss-match after metal ion functionalisation).

Photoluminescence spectroscopy has proven to be a beneficial technique to qualify the degree of crystallinity in semiconductors and characterise the number of possible exciton quenching defects that may exist in or on the material. The single most significant intrinsic parameter of any semiconductor is the band gap, which has a defined energy (wavelength). However, possible defects that introduce sub-band gap states give rise to red shifted emission signatures after exciton quenching.

Related studies of gold functionalised titanium dioxide have demonstrated red shifted emission signatures (350 nm as far as 575 nm),[212] meanwhile copper and nitrogen co-functionalised titanium dioxide investigations have detected excitons trapped within impurity sites at emission wavelengths as high as 900 nm.[213] These red shifted emission signatures aid in identifying the number of structural deformities that may be present within the crystalline material. Identifying defects in semiconductors are important to detect potential undesirable recombination centre origins that act as carrier trapping components within the semiconductor.[214],[215]

The previously collected powder diffuse reflectance UV/Vis data for $Cu/Pd-N-TiO_2$ confirmed that $Cu/Pd-N-TiO_2$ possessed an improved visible light response compared to non-functionalised titanium dioxide. The improved visible light response was suspected to arise from the three-component (Cu, Pd and N) functionalising effect of titanium dioxide. Photoluminescence spectroscopic studies of $Cu/Pd-N-TiO_2$ were

subsequently explored to ascertain the improved visible light response compared to non-functionalised titanium dioxide. Cu/Pd-N-TiO$_2$ together with nitrogen functionalised titanium dioxide (N-TiO$_2$), copper-nitrogen functionalised titanium dioxide (Cu-N-TiO$_2$), palladium-nitrogen titanium dioxide (Pd-N-TiO$_2$) and non-functionalised titanium dioxide were prepared. The cumulative photoluminescence spectroscopy data were paralleled against Cu/Pd-N-TiO$_2$ to determine how copper oxide, palladium, and nitrogen had influenced the visible light response of titanium dioxide.

Non-functionalised titanium dioxide was initially studied to determine the nature of the exciton states in titanium dioxide without any impurities (**Figure 84**).
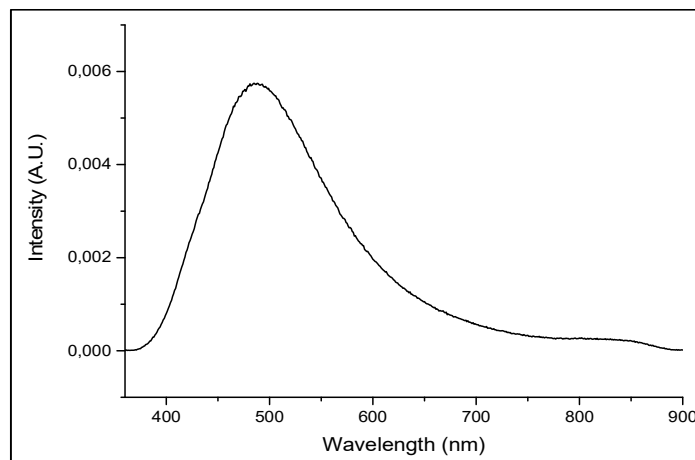
Figure 84: Photoluminescence spectrum of non-functionalised titanium dioxide.

Titanium dioxide without functionalising agents (copper oxide, palladium or nitrogen) depicted a uniform profile with an emission peak centralised at 480 nm. The intrinsic band gap emission energy (3.2 eV, 387 nm[4]) was minimal, which suggested that structural defects dominated the titanium dioxide's emission response as opposed to excitonic states. Liu *et al.*[216] discovered the same emission signature at 480 nm in titanium dioxide, which had been attributed to an electronic charge transfer process associated with TiO$_6^{8-}$ octahedral sites.

After collecting the photoluminescence spectrum of non-functionalised titanium dioxide (**Figure 84**), N-TiO$_2$, Cu-N-TiO$_2$, and Pd-N-TiO$_2$ spectra were also obtained (**Figure 85**).
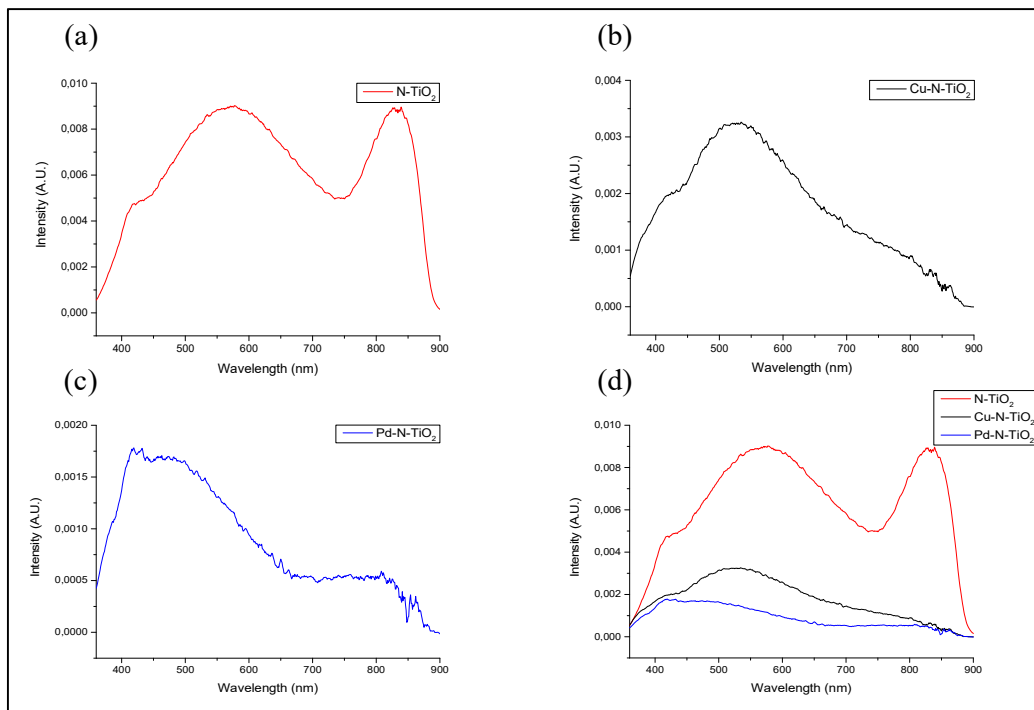
Figure 85: Photoluminescence spectra of N-TiO$_2$ (a), Cu-N-TiO$_2$ (b), Pd-N-TiO$_2$ (c), and combined (d).

Noticeable differences were apparent when the photoluminescence spectrum of non-functionalised titanium dioxide (**Figure 84**) was contrasted against the spectra of N-TiO$_2$, Cu-N-TiO$_2$, and Pd-N-TiO$_2$ (**Figure 85**). N-TiO$_2$ depicted emission peaks that had red shifted the optical band gap of titanium dioxide (3.2 eV, 389 nm)[4] and two discernible peaks were present at 579 nm and 839 nm. The intensities of these peaks were considerably higher than non-functionalised titanium dioxide (**Figure 84**), yet their presence had indicated that an apparent non-metal dopant had introduced a functionalised effect was imposed into the titanium dioxide's lattice.

Numerous reports are available in the literature to justify the nature of the 579 nm emission signature. Related carbon nanofibre-titanium dioxide studies have discussed similar yellow emission evidence, whereas peak tailings for Ag, Pt, and Pd

functionalised titanium dioxide were also observed experimentally.[33],[216] Elsewhere,[217] the literature has explained that the yellow luminescence of titanium dioxide has been closely associated with exciton fluorescence and was postulated to originate from electronic relaxations between the conduction band and mid-band gap states after nitrogen doping. However, researchers have also speculated that the longer emission wavelengths of titanium dioxide in photoluminescence spectral data could be linked to a considerable number of oxygen vacancies that induced defect centres within the TiO_6^{8-} octahedral structure.[218] After inspecting the results collected from **Figure 85** (image a) of N-TiO$_2$, the existence of the 579 nm and 839 nm were suspected to arise from nitrogen inclusions. In a study conducted by El Koura *et al.,*[213] various copper and nitrogen co-doped titanium dioxide films were studied *via* X-ray photoelectron spectroscopy and photoluminescence spectroscopy to determine the fundamental charge carrier dynamics behind the theory of splitting water. During El Koura and co-workers' research,[213] they identified that higher nitrogen concentrations introduced various forms of titanium-bound nitrogen. At low nitrogen concentrations, nitrogen substituted bonds were observed (as O-Ti-N). However, as the nitrogen concentration was increased, new Ti-N bonds were formed that excluded oxygen altogether. At reportedly 'high' nitrogen concentrations, a third nitrogen species was present; oxidised nitrogen (as NO) and interstitially bound nitrogen-titanium bonds (Ti-O-N-O and Ti-O-N). Shi *et al.*[219] reportedly observed 835 nm emission signatures from titanium dioxide. *Albeit* the calcination temperatures (600−900 °C) being higher than the operational temperature (350 °C) used to synthesise N-TiO$_2$ in **Figure 85** (image a), a near identical infrared emission response (835 nm) to N-TiO$_2$ (839 nm) was observed. Shi and co-workers [219] attributed the emission to an etaloning effect that arose from a back-illuminated charge coupled device principle.

The transitional metal (copper and palladium) functionalising of titanium dioxide in **Figure 85** (images b and c) demonstrated the enhanced emission reduction effect (in comparison to the intensities of non-functionalised TiO$_2$, **Figure 84**) of metal ion inclusion from broad peaks spanning 450−600 nm for Cu-N-TiO$_2$ and 400−550 nm for Pd-N-TiO$_2$, respectively. The identification and deconvolution of the broad 400−600 nm emission peaks have been noted in literature to occur from numerous potential defects, surface state defects, partially reduced titanium species, oxygen

vacancies, and self-trapped excitons, which are under consideration for future studies as an extension of this project.[220],[221],[222],[223]

It is worth noting that foreign inclusions (transition metals) into the host's lattice of a metal oxide are not directly detectable whilst studying the *parent* (titanium dioxide) material using photoluminescence spectroscopy. However, the effect of metal ion incorporation could be indirectly observed in the lowered peak intensities from **Figure 85** (images b and c). Metals are known to scavenge photogenerated electrons, especially palladium.[187] The inclusions of copper oxide and especially palladium were suspected of significantly reducing the exciton quenching effect on the surface of titanium dioxide as noticed by the lowered peak intensities at 515 nm and 407−497 nm in **Figure 85** (image d), respectively. Furthermore, palladium was hypothesised to reduce the recombination effect at the indirect band allowed transition (407 nm), which is in agreement with literature at this emission peak wavelength.[187] Once N-TiO$_2$, Cu-N-TiO$_2$, and Pd-N-TiO$_2$ were studied using photoluminescence spectroscopy (**Figure 85**); the visible light activity of Cu/Pd-N-TiO$_2$ was evaluated (**Figure 86**).
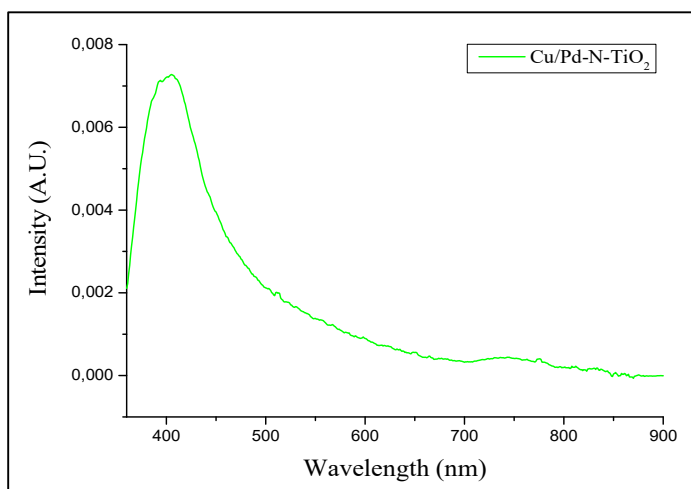
Figure 86: Photoluminescence emission spectrum of Cu/Pd-N-TiO$_2$.

The photoluminescence emission spectrum of the Cu/Pd-N-TiO$_2$ system (**Figure 86**) was clearly distinguishable from N-TiO$_2$, Cu-N-TiO$_2$, and Pd-N-TiO$_2$ (**Figure 85**) with a well-defined peak at 405 nm, which was in good agreement with the band gap exciton energy of titanium dioxide (398 nm).[187]

The emission spectrum of Cu/Pd-N-TiO$_2$ (**Figure 86**) presented significant differences from N-TiO$_2$, Cu-N-TiO$_2$, and Pd-N-TiO$_2$ (**Figure 85**) with respect to the possible structural defects over the wavelength range of 460−900 nm:

1) The emission trends of N-TiO$_2$, Cu-N-TiO$_2$, and Pd-N-TiO$_2$ had peak signatures centralised at wavelengths greater than 425 nm (**Figure 85**). However, an apparent blue shift for the major emission peak of Cu/Pd-N-TiO$_2$ (405 nm, **Figure 86**) was evident after the inclusion of the three-component principle (copper, palladium, and nitrogen).

2) Literature has reported that 420−480 nm emission signatures in titanium dioxide photoluminescence spectra arise from oxygen vacancies, which are self-trapped excitons and are isolated within TiO$_6$ octahedral planes.[187] This observation was noticeable for N-TiO$_2$, Cu-N-TiO$_2$, and Pd-N-TiO$_2$ in **Figure 85** (figures a, b, and c). The same observation was absent for Cu/Pd-N-TiO$_2$ in **Figure 86**.

3) The blue shifted emission maxima (405 nm) of Cu/Pd-N-TiO$_2$ and the absence of self-trapped excitons over the 420−480 nm emission region of **Figure 86** suggested that copper oxide and palladium stabilised the growth of uniform titanium dioxide crystals during the synthetic procedure (as confirmed by the collected powder X-ray diffractogram of Cu/Pd-N-TiO$_2$ (anatase) [**Chapter 3.9.5.**]). This was a significant finding as the method to synthesise titanium dioxide using a novel three-component system approach was theorised to reduce the frequency of defect sites that are known to easily form during synthetic procedures to manufacture titanium dioxide derivatives.

4) The choice of partnering copper and nitrogen has also been reported elsewhere to favourably shift the visible-light absorption capacity of titanium dioxide by only imparting a small shift in the conduction band potential.[216] A small shift would strain the titanium dioxide lattice and produce a potential defect emission, as was observed in **Figure 85** (image b). The combination of the three functionalising agents (copper, palladium and

nitrogen) may have contributed towards reducing this strain effect, however there is no evidence to support this supposition at this time.

5) While copper and nitrogen have been reported to sensitise titanium dioxide and shift its photocatalytic efficiency to operate in the visible region,[224] the oxidation state mismatch between cations (Ti^{4+}, Cu^{2+}, net positive [+2] charge) and furthermore anions (O^{2-} and N^{3-}, net negative [−1 charge]) produce energy strains within titanium dioxide that lead to crystal defects. However, in the Cu/Pd-N-TiO$_2$ system, the principle of charge balancing was suspected to occur after a Ti^{4+} ion was exchanged for a metal pair ($2Cu^+$ or $Cu^{2+}|Pd^{2+}$). **Figure 86** accounted for this supposition as the noticeable emission response (420−480 nm) was considerably lower, which indicated fewer oxygen vacancy defect sites.

6) The three-component system (copper, palladium, and nitrogen) which was used to functionalise titanium dioxide as Cu/Pd-N-TiO$_2$, conveyed a superior reduction in exciton recombination rates over the visible region (560−900 nm) when compared to all the previously prepared titanium dioxide analogues (TiO$_2$, N-TiO$_2$, Cu-N-TiO$_2$, and Pd-N-TiO$_2$).

Energy-dispersive X-ray spectroscopy, powder diffuse reflectance UV/Vis spectroscopy, and photoluminescence spectroscopy had previously assisted in detecting extrinsic functionalising agents (Cu, Pd, and N) on Cu/Pd-N-TiO$_2$. These techniques also validated the contribution from copper oxide, palladium, and nitrogen towards enhancing the visible light-absorbing properties of titanium dioxide. However, there was limited instrumental evidence to characterise the oxidation states for the elements (Cu, Pd, N, Ti, and O) within the complex photocatalyst (Cu/Pd-N-TiO$_2$). Collecting oxidation-state information for the relevant metals (Cu, Pd, and Ti) and non-metals (N, and O) using X-ray photoelectron spectroscopy (XPS) would clarify the nature of these species.

3.9.8. X-ray photoelectron spectroscopy

The XPS data for Cu/Pd-N-TiO$_2$ was collected at the National Nano Surface Characterization Facility, University of the Free State, South Africa. A monochromatic Al Kα X-ray beam (hv = 1486.6 eV) with a 100 µm diameter was used to study the binding energies of the respective elements (Cu, Pd, N, Ti, and O). Surface sputtering was applied with an Ar$^+$ ion beam (2KV, 2µA) and a neutraliser electron gun (low energy) to reduce surface contamination and lower surface charging.

However, the presentation of the data (**Figure 87**) and interpretation of the results (**Table 12**), which were based on the literature were performed by the candidate.

The high resolution XPS results of Cu/Pd-N-TiO$_2$ were contrasted against N-TiO$_2$, Cu-N-TiO$_2$, and Pd-N-TiO$_2$ to assess the binding energy responses of Ti^{4+} and O^{2-} after the inclusion of copper and palladium (**Figure 87**).

The extrinsic metal ions (Cu, and Pd) were expected to exist as either interstitially bound or surface loaded species (as metals or oxides) onto titanium dioxide. Nitrogen was postulated to have undergone a non-metal exchange substitution process with oxygen (N-Ti-O). Therefore, XPS was the last instrumental method used to study Cu/Pd-N-TiO$_2$ and hence, determine the nature of inclusion for the three extrinsic ions (Cu, Pd, and N) in the Cu/Pd-N-TiO$_2$ material.

High resolution spectra of Cu/Pd-N-TiO₂
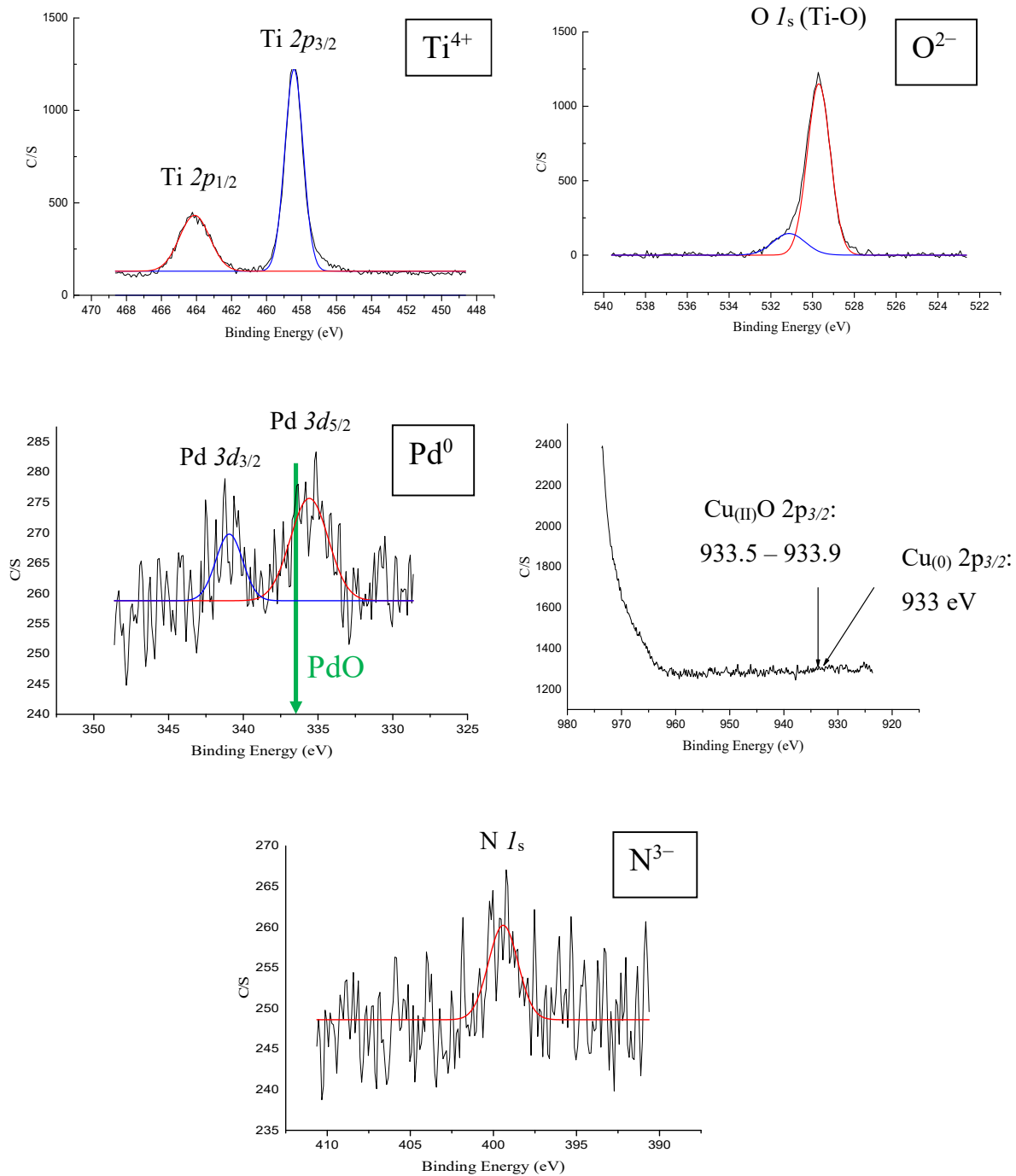
Figure 87: High-resolution peak binding energies of Cu, Pd, N, Ti, and O in Cu/Pd-N-TiO₂

From **Figure 87** of the high resolution XPS (HR XPS) spectra for $Cu/Pd-N-TiO_2$, the respective binding energies for Ti $2p_{3/2}$ and Ti $2p_{1/2}$, O $1s$, N $1s$, Pd $3d_{5/2}$ and Pd $3d_{3/2}$ were obtained (**Table 12**) using Origin Pro 9.1 with Gaussian peak fitting profiles. However, the baseline for nitrogen and palladium spectra were poorly defined due to high background noise. Despite the high background noise, the best fit profile was attempted for both elements, respectively. The remaining binding energies for $N-TiO_2$, $Cu-N-TiO_2$, $Pd-N-TiO_2$, and $Cu/Pd-N-TiO_2$ have been tabulated below.[*]

Table 12: Peak binding energies (eV) of the Cu, Pd, $N-TiO_2$ analogues.

TiO₂ analogue	N-TiO₂	Cu-N-TiO₂	Pd-N-TiO₂	Cu/Pd-N-TiO₂
Element				
[†]**Pd $3d_{5/2}$**	N/A	N/A	335.50	335.58
[†]**Pd $3d_{3/2}$**			341.39	340.94
[†]**N $1s$**	399.93	396.06	399.57	399.41
[†]**N $1s$**		398.94		
Ti $2p_{3/2}$	458.44	458.28	458.50	458.43
Ti $2p_{1/2}$	464.13	463.98	464.17	464.11
O $1s$	529.72	529.58	529.76	529.70
O $1s$	531.26	530.64	530.65	531.13

Unfortunately, no information was obtained with regards to the binding energies of copper in any of the titanium dioxide analogues ($N-TiO_2$, $Cu-N-TiO_2$, $Pd-N-TiO_2$, and

---

[*] Additional HR XPS spectra of $N-TiO_2$, $Cu-N-TiO_2$, and $Pd-N-TiO_2$ are available in the **Appendix** as a report that was compiled by the National Nano Surface Characterization Facility, University of the Free State, South Africa.

[†] Background noise too high to distinguish a reliable peak identification.

Cu/Pd-N-TiO$_2$). This was speculated from the low copper concentrations that were used to prepare the Cu-N-TiO$_2$ and Cu/Pd-N-TiO$_2$ materials.

Emanating from **Table 12** however, five important observations were established:

1) Well resolved peak pairs for Ti *2p$_{3/2}$* and Ti *2p$_{1/2}$* were detected with binding energies that correlated with the characteristic response for Ti(IV) ions in all four compounds (N-TiO$_2$, Cu-N-TiO$_2$, Pd-N-TiO$_2$, and Cu/Pd-N-TiO$_2$).[225] This result confirmed that reduced titanium (Ti[III]) was not produced during the sol-gel nor calcination processes.

2) According to the literature,[225] the binding energy of oxygen within metal oxide compounds ranges from 528.1 – 531.1 eV. Tabulated in **Table 12**, a peak at 529.69 eV (for Cu/Pd-N-TiO$_2$) was medially positioned within this range that could be favourably assigned to O-Ti-O bond of TiO$_2$ (charge of O^{2-}). However, a smaller and rather convoluted shoulder peak (531.13 eV) was also present. Literature has reported a similar observation at 531.1 eV that has been assigned to the Ti-N-O bonds in N-TiO$_2$.[226]

3) Two peaks for palladium (Pd *3d$_{5/2}$* and Pd *3d$_{3/2}$*) were detected amongst the two samples (Pd-N-TiO$_2$ and Cu/Pd-N-TiO$_2$) although with relatively high background interference, which could be attributed to the low palladium concentration within the materials. In order to distinguish the speciation of palladium on the titanium dioxide materials, the main Pd *3d$_{5/2}$* peak of palladium was identified as a suitable signal to differentiate between the possible metallic palladium or palladium oxide on the titanium dioxide. The core Pd *3d$_{5/2}$* peak assigned to metallic palladium at 335.58 eV (for Cu/Pd-N-TiO$_2$) with its corresponding Pd *3d$_{3/2}$* peak at 340.94 eV had a doublet separation of 5.36 eV that agreed favourably with the literature.[225],[227] A green arrow noting the referenced position of PdO *3d$_{5/2}$* has been added to **Figure 87**. According to the theory,[225] palladium and palladium oxide's *3d$_{5/2}$* peaks occur at 335.3 and 336.3 eV, respectively. These two signals were more well-defined than the Pd *3d$_{3/2}$* peak and were subsequently used to distinguish the speciation of palladium on the

Cu/Pd-N-TiO$_2$ ($3d_{5/2}$ = 335.58 eV) and Pd-N-TiO$_2$ ($3d_{5/2}$ = 335.50 eV) materials. The application of XPS spectroscopy identified the oxidation state of palladium in Cu/Pd-N-TiO$_2$ as Pd^0. The Pd $3d_{3/2}$ peak for Cu/Pd-N-TiO$_2$ (340.94 eV) was slightly lower than Pd-N-TiO$_2$ (341.39 eV) however as noted above, the broad Pd $3d_{3/2}$ meant than utilising the $3d_{5/2}$ would be more accurate in assigning the oxidative state of palladium. The XPS palladium analyses were in further agreement with the HRTEM lattice spacings of palladium that have been previously discussed in the chapter. The palladium precursor (Pd[OAc]$_2$) used to prepare Cu/Pd-N-TiO$_2$ has been reported to decompose to metallic palladium at elevated temperatures 200−300 °C.[228] Although, the metallic species (Pd^0) does not oxidise until temperatures of 413 °C.[229] This substantiated why PdO was not detected (in either HRTEM or XPS studies).

4) The X-ray photoelectron spectroscopic analysis of nitrogen in the functionalised titanium dioxide species (N-TiO$_2$, Cu-N-TiO$_2$, Pd-N-TiO$_2$, and Cu/Pd-N-TiO$_2$) also experienced high signal-to-noise ratios, which made the exact speciation impractical to define with absolute certainty. However, based on the relative positions of the N $1s$ peaks in **Table 12**, nitrogen could be cautiously assigned an oxidation state of −3 (N$^{3−}$). Between the four samples, Cu-N-TiO$_2$ presented an additional N $1s$ peak at 396.06 eV that accordingly to literature belongs to Ti-N linkages after nitrogen replaces oxygen atoms within the TiO$_2$ lattice.[213]

5) The XPS spectra of copper revealed no peaks that could be assigned to neither metallic copper, copper (I) oxide nor copper (II) oxide due to the low weight percentage loadings of Cu(NO$_3$)$_2$·3H$_2$O that were used to synthesise Cu-N-TiO$_2$ and Cu/Pd-N-TiO$_2$. However, for clarity, the expected peaks have been noted in **Figure 87**.

Stemming from the XPS spectroscopy results, titanium dioxide's crystal lattice was not altered through metal ion functionalising. However, based on the nitrogen binding energies from **Table 12**, it was plausible to conclude from the data that oxygen was

substituted for nitrogen atoms (O-Ti-N and Ti-N) during the synthesis of the titanium dioxide analogues.

A wide array of microscopy, spectroscopic, spectrometric, and X-ray diffraction techniques have been employed to obtain a thorough understanding of the nature and composition of the Cu/Pd-N-TiO$_2$ material. The instrumental evidence has led to conclude that the three functionalising agents (Cu, Pd and N) existed as copper oxide and metallic palladium that were surface loaded (copper oxide and palladium) and nitrogen which was bound (substitutional ion exchange) within the lattice structure of titanium dioxide. The three extrinsic agents induced a visible light component into titanium dioxide that attenuated the metal oxide away from the ultraviolet spectrum and into the visible light for mediating an alcohol oxidation. The success of the preliminary alcohol oxidation of 3,4-dimethoxybenzyl alcohol was extended to include an array of various cyclic alcohols.

3.10. Extending the Scope of Cu/Pd-N-TiO₂ in Alcohol Oxidation Reactions

After obtaining a detailed interpretation of the photo-physical properties that governed the visible light success of Cu/Pd-N-TiO₂, the scope and photo-oxidative potential of the semiconductor was extended to a broad cyclic alcohol oxidation study.

Table 13: Aromatic alcohol oxidation using Cu/Pd-N-TiO₂[a]
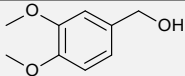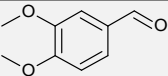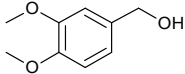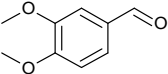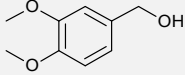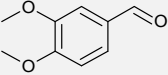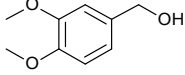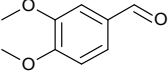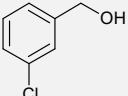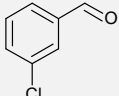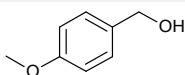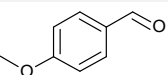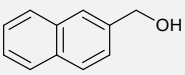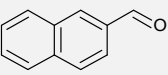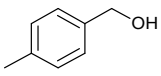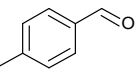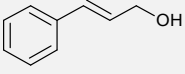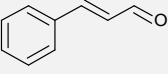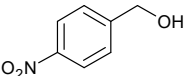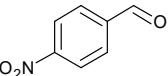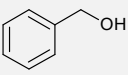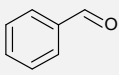
Entry	Alcohol	Aldehyde	Conv. (%)	Yield (%)	Sel. (%)
1[b]			> 99	(N/C)	(N/C)
2[b,c]			78	(N/C)	(N/C)
3[b,d]			3	(N/C)	(N/C)
4			≥ 99	96	96
5			41	38	92
6			≥ 99	96	96
7			88	83	95
8[e]			90	(N/D)	(N/D)
9			73	53	73
10			61	61	≥ 99
11			71	70	98

| 12 | | | 39 | 31 | 78 |
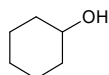
[a]Reaction conditions: 0.1 mmol 3,4-dimethoxybenzyl alcohol, 20 mg photocatalyst (0.25 mmol), toluene solvent (2.5 mL), O_2 solvent bubbling (1.5 minutes) and solar-simulated xenon irradiation source (5 hours); conversion, yield, and selectivity determined as reported in **Table 2** and **Table 3.** [b]Conversion determined using GC-MS peak areas. [c]Reaction performed with N-TiO$_2$. [d]Reaction performed with uncalcined Cu/Pd-N-TiO$_2$. N/C (not calculated) when using GC-MS peak areas. [e]N/D (Not determined), the corresponding aldehyde was not available to determine the relative response factor.

The high conversion of aromatic alcohols reported in **Table 13** had demonstrated that Cu/Pd-N-TiO$_2$ effectively oxidised electron donating (**Table 13**, entries 1, 6, 7) and phenolic substituted alkenes (**Table 13**, entry 9). Electron withdrawing aromatic alcohols (**Table 13**, entries 5, and 10) were slightly harder to oxidise with lower conversions of 41 % and 61 %, respectively. Literature has reported similar observations with electron withdrawing substituted aromatic alcohols, where the electron withdrawing nature of chlorine atoms inhibited the conversion.[230]

Numerous multi-component semiconductor systems have been reported in the literature, and in order to contrast Cu/Pd-N-TiO$_2$ with the current literature research, the results of this work (**Table 13**, entry 13) have been tabulated in **Table 14**.

Table 14: Comparison of the photo-oxidative potential of Cu/Pd-N-TiO$_2$ to the literature.

	Author	Catalyst	Alcohol	Conv. (%)	Comments
1	Yang et al.[230]	TiO$_2$-(PW$_{12}$-TW)$_8$		61	➤ 0.1 mmol alcohol ➤ BTF (solvent) ➤ O$_2$ atm2.5-hour reaction times ➤ 300 W xenon lamp ➤ 8 mg catalyst ➤ ≥ 99 % aldehyde selectivity
				41	
				45	
2	Askari et al.[231]	Co-TCPP@TiO$_2$/BiVO$_4$		80	➤ 0.1 mmol alcohol ➤ CH$_3$CN (solvent) ➤ Aerated atm

Table continued overleaf
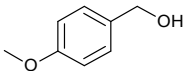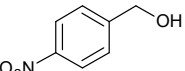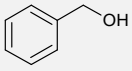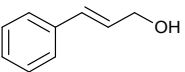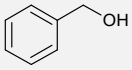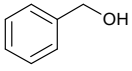
#	Author	Catalyst	Substrate	Yield	Notes
			4-methoxybenzyl alcohol	70	➢ 2-hour reactions ➢ 7 W LED
			4-nitrobenzyl alcohol	60	➢ 10 mg catalyst and TBHP (1.5 mmol) ➢ ≥ 99 % aldehyde selectivity
3	Lima et al.[232]	Ru/g-C_3N_4	benzyl alcohol	55	➢ 0.042 mmol alcohol ➢ H_2O (solvent) ➢ Ar atm ➢ 4-hour reactions ➢ UV LED ➢ 28 mg catalyst ➢ 72 % aldehyde selectivity
4	Raji et al.[105]	(001) faceted TiO_2	cinnamyl alcohol	99	➢ 0.5 mmol alcohol ➢ BTF (solvent) ➢ O_2 atm ➢ 24-hour reactions ➢ CFL lamp ➢ 15 mg catalyst ➢ Aldehyde selectivity N/S
5	Tomita et al.[233]	(Pd)-TiO_2	benzyl alcohol	41	➢ 1.3 mmol alcohol ➢ H_2O (solvent) ➢ Aerated atm ➢ 1-hour reactions ➢ 300 W xenon lamp ➢ 100 mg catalyst ➢ 11.5 % aldehyde selectivity
6	Marotta et al.[234]	TiO_2/Cu(II)	benzyl alcohol	82	➢ 0.00375 mmol alcohol ➢ H_2O (solvent) ➢ N_2 atm ➢ 3-hour reactions

Table continued overleaf
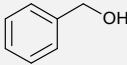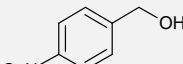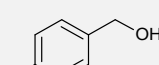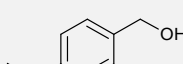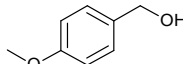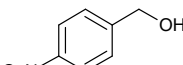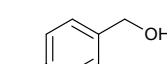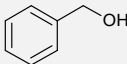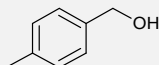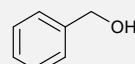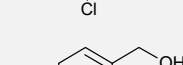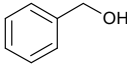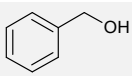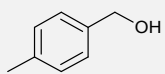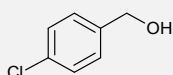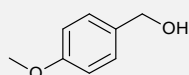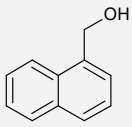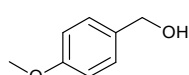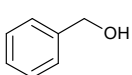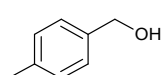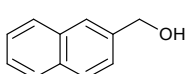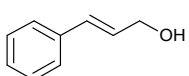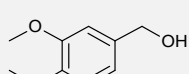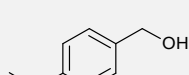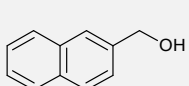
					➤ High pressure UV lamp
					➤ 200 mg TiO_2/L and 1.84 mM Cu(II)
					➤ > 90 % aldehyde selectivity
7	Verma et al.[235]	Pd@TiC		99	➤ 1 mmol alcohol
				96	➤ CH_3CN (solvent)
					➤ Aerated atm
					➤ 8-hour reactions
				95	➤ 20 W domestic bulb
					➤ 25 mg catalyst
				96	➤ 94−97 % aldehyde selectivity
8	Hosseini et al.[236]	TiO_2-P25-SO_3H		99	➤ 1.5 mmol alcohol
					➤ CH_3CN (solvent)
					➤ N_2 atm
				99	➤ 7-hour reactions
					➤ 3 W blue LED
				99	➤ 50 mg catalyst
					➤ Aldehyde selectivity N/S
9	Safaei et al.[237]	TiO_2/WO_3		59	➤ 0.1 mmol alcohol
				58	➤ CH_3CN (solvent)
					➤ Aerated atm
					➤ 1-hour reactions
				68	➤ 5 W LED
					➤ 8 mg catalyst
				56	➤ ≥ 99 % aldehyde selectivity
10	Li et al.[238]	TiO_2@Pd@ ZnO		42	➤ 20.9 mg/L alcohol
					➤ H_2O (solvent)
					➤ Aerated atm
					➤ 1-hour reactions
					➤ 300 W xenon lamp

#	Reference	Catalyst	Substrate	Yield (%)	Conditions
					➢ 8 mg catalyst
					➢ 44−85 % aldehyde selectivity
11	Chen et al.[239]	Pt$_2$-TiO$_2$	benzyl alcohol	99	➢ 0.1 mmol alcohol
			4-methylbenzyl alcohol	99	➢ BTF (solvent)
			4-chlorobenzyl alcohol	98	➢ O$_2$ atm
			4-methoxybenzyl alcohol	99	➢ 3−6-hour reactions
			1-naphthalenemethanol	81	➢ 300 W xenon lamp
					➢ 10 mg catalyst
					➢ 64 − ≥ 99 % aldehyde selectivity
12	Wang et al.[240]	Au@Pd@TiO$_2$	4-methoxybenzyl alcohol	91	➢ 0.5 mmol alcohol
			benzyl alcohol	88	➢ H$_2$O (solvent)
			4-methylbenzyl alcohol	> 99	➢ Aerated atm
			2-naphthalenemethanol	67	➢ 3−6-hour reactions
			cinnamyl alcohol	69	➢ Visible light (N/S)
					➢ 1.5 mol% Pd and 0.5 mmol K$_2$CO$_3$
					➢ 80 °C reaction temperature
					➢ 90 − ≥ 99 % aldehyde selectivity
13	**This Work**	**Cu/Pd-N-TiO$_2$**	**3,4-dimethoxybenzyl alcohol**	**≥ 99**	➢ **0.1 mmol alcohol**
			4-methoxybenzyl alcohol	**≥ 99**	➢ **Toluene (solvent)**
			2-naphthalenemethanol	**88**	➢ **O$_2$ atm**
					➢ **5-hour reactions**
					➢ **140 W xenon reactor**
					➢ **20 mg catalyst**
					➢ **73− ≥ 99 % selectivity**

In comparison to the literature (**Table 14**), the three-component (Cu, Pd and N) Cu/Pd-N-TiO$_2$ photocatalyst system favourably demonstrated to selectively oxidise benzylic alcohols with high conversions opposed to **Table 14**, entry 12 that yielded acid derivatives of the benzylic alcohol starting materials. By and large, Cu/Pd-N-TiO$_2$ also exhibited a superior 85 % (11 of 13 examples) overall improvement to convert benzylic alcohols at similar or higher concentrations compared to literature (**Table 14**, entries 1, 2, 3, 6, 9, and 10). However, related titanium dioxide (**Table 14**, entries 4, 8, and 12) and titanium carbide (**Table 14**, entry 7) semiconductors have exhibited comparable benzylic alcohol conversions but at higher initial substrate alcohol concentrations (0.5−1.5 mmol). The Cu/Pd-N-TiO$_2$ photocatalyst system also avoided the requirement for base assisted alcohol dehydrogenation agents (**Table 14**, entry 12, K$_2$CO$_3$, one mol equivalent), and secondary oxidants (**Table 14**, entry 2, TBHP at *15 mol equivalent excess*). Metal loadings (copper [0.04 wt%] and palladium [0.18 wt%]) of Cu/Pd-N-TiO$_2$ were also significantly lower than entry 6 (**Table 14**), where a 1.84 mM Cu(II) concentration was required to facilitate an 82 % conversion of 1.5 mM benzyl alcohol at pH = 2 and 200 mg TiO$_2$.

In comparison to similar literature compounds, this research had developed a novel three-component Cu/Pd-N-TiO$_2$ semiconductor that selectively oxidised benzylic alcohols with high selectivity to the benzaldehyde derivatives without detectable over-oxidised side-products. In numerous examples (**Table 14**, entries 1, 2, 3, 6, 9, and 10), Cu/Pd-N-TiO$_2$ achieved higher alcohol conversions at equal or higher starting alcohol concentrations without the need for acids, bases, or secondary oxidants (**Table 14**, entries 2, 6, 12). The use of visible light irradiation (solar simulated xenon irradiation source) and molecular oxygen supported the environmentally friendly application of Cu/Pd-N-TiO$_2$ to photo-oxidise benzylic alcohols. The findings from the benzylic alcohol oxidation study have been drafted as a publication and are available in the **Appendix**.

At this point in the project, the accumulation of information led to the development and application of a photocatalytically active three-component semiconductor (Cu/Pd-N-TiO$_2$). With the promising alcohol oxidation results tabulated in **Table 13**, the study was directed towards briefly exploring the remediation of two environmental water pollutants (methylene blue and eosin Y)

3.11. Organic Dyestuff Degradations using Cu/Pd-N-TiO$_2$

Proceeding from the positive photo-oxidation of alcohols reported in **Table 13**, the photo-activity of Cu/Pd-N-TiO$_2$ under visible light was further evaluated by attempting to photo-degrade organic dyestuffs in water. Organic dyestuffs (Congo red, methylene blue and brilliant green to mention a few) are typically used to colour textiles, agricultural purposes (flower pigmenting), and to tint paints. However, they have been identified as harmful organic pollutants that are highly persistent in the environment, are potential bio-accumulating toxins and as such have gained significant attention in the community to remediate.[241],[242] The World Health Organisation has published handbooks detailing the severity of aquatic pollutants and the consequential effects on the environment.[243],[244]

Therefore, in a similar manner to a study conducted by Kuvarega *et al.*,[25] who studied the photo-degradation of eosin Y at 15 ppm, the photo-oxidative potential of Cu/Pd-N-TiO$_2$ was evaluated by attempting to photo-degrade methylene blue and eosin Y (at 20 ppm concentrations). Reactions were performed with and without a semiconductor to evaluate the photo-oxidative potential of Cu/Pd-N-TiO$_2$.

Prior to the irradiation period, the test tubes (containing the organic dyestuffs) were equilibrated in the dark for thirty minutes. Following which, the test tubes were immediately irradiated using the simulated solar xenon irradiation source with pre-determined sampling times as noted below.

The photo-degradations of methylene blue and eosin Y were evaluated after collecting sample aliquots at 15-minute intervals for the first hour, and then subsequently every hour until hour five, with the last sample collected at the seventh hour (*i.e.* 15, 30, 45 minutes, 1, 2, 3, 4, 5, 7 hours respectively). Eosin Y photo-degraded at a faster rate than methylene blue and therefore aliquots of eosin Y samples were only collected until the third hour (*i.e.* 15, 30, 45 minutes, 1, 2, 3 hours respectively). Blank runs for each dyestuff (without Cu/Pd-N-TiO$_2$) were also studied to access the photo-oxidative effect of the simulated solar xenon irradiation source towards the degradation of methylene

blue and eosin Y (**Figure 88**). Lastly, control reactions with Cu/Pd-N-TiO$_2$ but without xenon irradiation were performed.
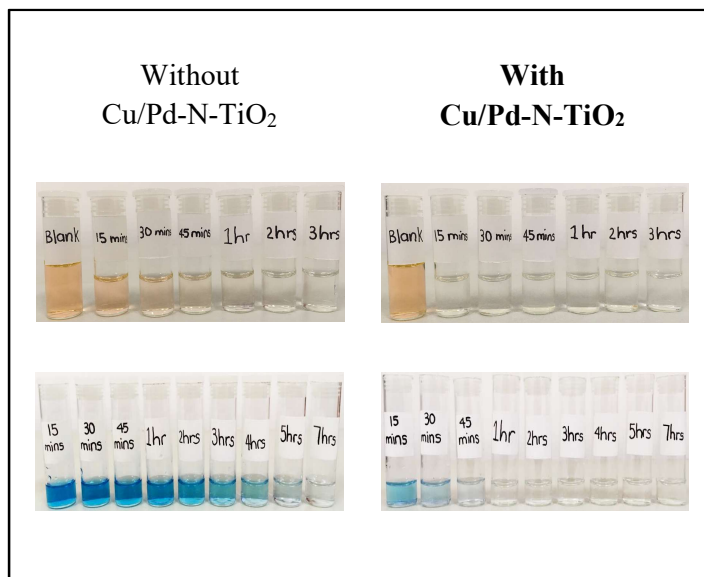
Figure 88: Methylene blue and eosin Y photo-degradation without (left) and with (right) Cu/Pd-N-TiO$_2$ in the presence of visible light irradiation.

From **Figure 88**, the solar simulated xenon irradiation source had partially facilitated the photo-oxidative degradation of methylene blue and eosin Y as observed by the colour change of both solutions over the seven- and three-hours periods, respectively. In comparison to the photo-degradation of methylene blue and eosin Y in the presence of Cu/Pd-N-TiO$_2$, a significant time reduction was evident. However, in the absence of xenon irradiation, less than 0.5 % methylene blue degradation was observed within one hour, which confirmed the requirement for Cu/Pd-N-TiO$_2$ and photocatalytic conditions (the UV/Vis absorbance profiles of methylene blue degradation in the absence of xenon irradiation are available in the **Appendix**).

Cu/Pd-N-TiO$_2$ had completely photo-degraded methylene blue and eosin Y after 60 minutes, as observed from the decrease in the optical absorbances at 664 nm (methylene blue) and 516 nm (eosin Y, **Figure 89**).
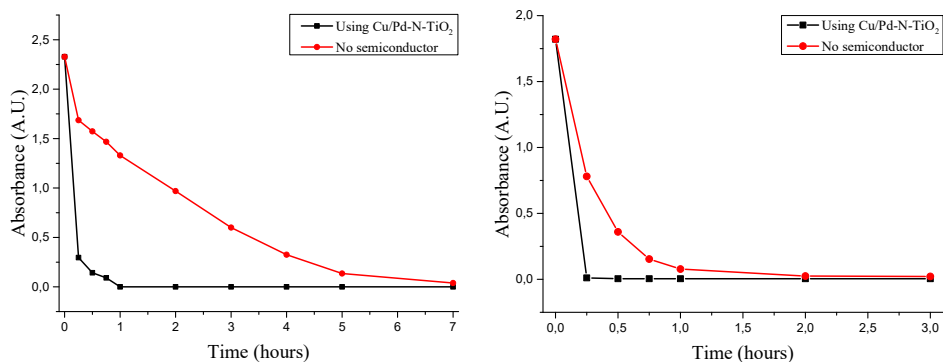
Figure 89: UV/Vis spectroscopic data of methylene blue and eosin Y degradation over seven and three hours, respectively.

Whilst Cu/Pd-N-TiO$_2$ had been demonstrated to effectively degrade methylene blue and eosin Y after 60 minutes (**Figure 89**), an important industrially relevant consideration was to assess the recycling potential of the semiconductor. In accordance with the literature on typical organic dye-stuff concentrations and catalyst loadings for photo-degradation studies,[245],[246] the recycling efficiency of Cu/Pd-N-TiO$_2$ was evaluated after photo-degrading six consecutive solutions (20 ppm) of eosin Y. Thirty milligrams of Cu/Pd-N-TiO$_2$ was subjected to six recycling reactions, while being washed with copious volumes of de-ionised water between runs. After completing the six-stage recycling study, Cu/Pd-N-TiO$_2$ demonstrated degradation efficiencies of eosin Y that exceeded 99 % in all cases.

In comparison to contemporary literature for the photo-degradation of methylene blue and eosin Y (heterojunctioned Fe$_3$O$_4$/TiO$_2$, metal [Fe^{3+}] functionalised TiO$_2$, TiO$_2$/MgZnAl layered double hydroxide and Cu-coated ZnO microrods), Cu/Pd-N-TiO$_2$ completely photo-mineralised the two organic dyestuffs in shorter reaction times and at higher starting concentrations of methylene blue and eosin Y.[*]

In this chapter, Cu/Pd-N-TiO$_2$ was demonstrated to successfully facilitate the conversion of nine cyclic alcohols to the corresponding aldehydes. The three-component (Cu, Pd, and N) system on titanium dioxide enhanced the visible light

---

[*] A comparison of Cu/Pd-N-TiO$_2$ with contemporary semiconductors to photo-degrade methylene blue and eosin Y is available in the **Appendix**.

sensitivity of titanium dioxide and selectivity controlled the conversions of nine cyclic alcohols without any detection of the over-oxidised benzoic acid derivatives.

A brief preliminary study into remediating environmental pollutants in water has also demonstrated promising results for the Cu/Pd-N-TiO$_2$ system in future studies to photo-mineralise more complex industrial wastewater contaminants.

4. Conclusion

Two functionalisation strategies which originated from this research have indicated enhanced visible-light photocatalytic responses of two wide band gap semiconductors (zinc oxide and titanium dioxide).

A saturated silver-sodium electrolyte was developed that significantly lowered the concentration of silver nitrate (18 to 1 equivalent), which was required to stabilise the physi-adsorbed alizarin red organic dye on the surface of zinc oxide. The photo-oxidative potential of the alizarin red/Ag-Na/ZnO/TEMPO photocatalytic system was re-accessed and was shown to oxidise seven aromatic alcohols (59 to $\geq$ 99%) and furthermore eight traditionally unreactive aliphatic alcohols ranging from 10 to 88 %.

The photocatalytic system (alizarin red/Ag-Na/ZnO/TEMPO) required additional characterisation to theorise how the photoelectronic migration was occurring between the highest occupied molecular orbital of alizarin red and zinc oxide before the electrons were quenched by ionic silver. Instrumental insight gathered from photoluminescence spectroscopy detected a defect emission at 507 nm that was subsequently shown to reduce in intensity after alizarin red was adsorbed onto the surface of zinc oxide. An approximate five-fold reduction in the emission intensity matched favourably with powder diffuse reflectance studies, which indicated that the alizarin red organic dye was quenching the availability for electrons (from the valence band of zinc oxide) to relax into the defect of zinc oxide and further absorbing the emitted corresponding energy. These findings were supported by a computation study using Gaussian, which calculated that the electronic migration of electron density proceeded from alizarin red to reside over the alizarin red-zinc oxide coordination site after visible light activation.

The study was expanded with the aim of identifying additional novel metal-functionalised titanium dioxide systems that were solely activated using visible light. Three titanium dioxide derivatives (TMT-Cu, TMT-Ni, and TMT-Mn) of the expected A_3TiO_5 type formula were synthesised, however, were found to be unsuccessful at oxidising benzyl alcohol. Subsequent powder X-ray diffraction studies

using phase mapping analyses confirmed that the desired A_3TiO_5 were not obtained but rather mixtures of CuO, TiO_2 (rutile) and Mn_2O_3, TiO_2 (rutile), respectively. TMT-Ni presented no crystallographic phase and was concluded as an amorphous material. Various possibilities of a visible light activated semiconductor followed from the A_3TiO_5 concept. Iron oxide (Fe_2O_3) and vanadium pentoxide (V_2O_5) in a heterojunction system and V_2O_5 mounted on silica gel beads were briefly investigated yet with limited success in converting alcohols into aldehydes. A visible light activated band gap material, silver functionalised cadmium sulfide was also synthesised; however, neither demonstrated viable photocatalytic properties. The semiconductor was extensively studied with numerous instrumental techniques to identify the low conversion of alcohols that were observed. The synthetic method that was used to produce silver functionalised cadmium sulfide induced the growth of undesired cadmium oxide, as determined from the CdO lattice spacings that were detected from high-resolution transmission electron microscopic analyses. Photoluminescence spectroscopy detected numerous sulfur, cadmium and oxygen defects that further inhibited the material from functioning as an effective oxidant.

Despite the interrelated study of numerous non-viable photocatalysts, the concept of introducing metal species into cadmium sulfide led to the development of a novel three-component (Cu, Pd, and N) system on titanium dioxide ($Cu/Pd-N-TiO_2$) that favourably photocatalysed the oxidation of 3,4-dimethoxybenzyl alcohol to 3,4-dimethoxybenzaldehyde. This novel material was fully characterised using a wide array of instrumental techniques. These included amongst others; SEM and TEM microscopy, Raman spectroscopy, ICP-MS, Photoluminescence spectroscopy, and X-ray photoelectron spectroscopy. This allowed for the full understanding of the nature and composition of the semiconductor. As noted above, the detailed characterisation of the novel system highlighted a number of unique properties of the $Cu/Pd-N-TiO_2$ material.

Powder diffuse reflectance studies confirmed a significant red shift in the optical band gap after incorporating the three-component system (Cu, Pd, and N) on titanium dioxide. SEM and TEM studies depicted that small nano-seed (approximate size of 6.75 nm, as calculated from the Scherrer equation) clusters of $Cu/Pd-N-TiO_2$ were highly aggregated with copper oxide and Pd^0 nanoparticles being evenly distributed on

Cu/Pd-N-TiO$_2$. Calculated *d*-lattice spacings from high-resolution transmission electron micrographs identified the presence of copper oxide and metallic palladium species rather than a Cu|Pd alloy. X-ray photoelectron spectroscopy further validated the oxidation state of palladium due to the detection of Pd *3d$_{5/2}$* and Pd *3d$_{3/2}$* binding energies that favourably matched metallic palladium (335.58 eV and 340.94 eV, respectively).

Photoluminescence spectroscopic investigations lent support to conclude that the selected combination of copper and palladium had assisted in a 'charge balancing' principle whilst synthesising Cu/Pd-N-TiO$_2$, as a noticeable reduction in the oxygen vacancy defect emission (420−480 nm) was observed.

The intensive characterisation study of Cu/Pd-N-TiO$_2$ led to a better understanding of the photophysical processes that governed the photo-reactivity of Cu/Pd-N-TiO$_2$. Subsequently, the photo-reactivity of the material was demonstrated to mediate an array of nine cyclic alcohol oxidations in moderate to excellent conversions ranging from 41 to ≥ 99 %. A further study was successfully conducted which has reported that the photo-oxidative potential of Cu/Pd-N-TiO$_2$ could be extended to typical environmental pollutants such as methylene blue and eosin Y. In summary, a serendipitous novel three component system (Cu/Pd-N-TiO$_2$) has demonstrated a promising potential as an organic oxidant in this research and in future studies, which to the best of our knowledge, has not been reported elsewhere in the literature to date.

5. Future Studies

Whilst Cu/Pd-N-TiO$_2$ has demonstrated to selectively oxidise aromatic alcohols to aldehydes, and degrade organic dyestuffs (methylene blue and eosin Y) using a solar simulated xenon irradiation source, additional research avenues require further in-depth investigations. These include:

➢ The photo-oxidation potential of Cu/Pd-N-TiO$_2$ will be further evaluated by attempting to oxidise complex and traditionally unreactive alcohols. Natural products such as D-pyroglutaminol and aliphatic alcohol systems will be investigated to fully access the photo-oxidation potential of Cu/Pd-N-TiO$_2$.

➢ Cu/Pd-N-TiO$_2$ was mild enough to limit the oxidation of aromatic alcohols to benzaldehyde derivatives (and not carboxylic acids) yet achieve a complete optical photo-degradation of highly conjugated organic dyestuff molecules (methylene blue and eosin Y). With the application of mass spectrometry, Cu/Pd-N-TiO$_2$ will be utilised in industrial wastewater remediation analyses. The expected outcomes will be the photo-mineralisation of numerous commercial effluents that are currently polluting water sources and identification of plausible mechanistic degradation pathways of the conjugated organic pollutants.

➢ Investigate alternative photocatalytically driven processes (water splitting, nitroaromatic reductions, and or the degradation of endocrine disruptors [*n*-chloro phenols]), which will expand the possible applications of Cu/Pd-N-TiO$_2$ and potentially find an industrial scale opportunity.

➢ The design and synthesis of new three-component systems (Cu|Fe, Zn|Fe) on the surface of N-TiO$_2$ and or N-ZnO.

➢ Further characterise Cu/Pd-N-TiO$_2$ using more advanced spectroscopic techniques, amongst which include ultraviolet photoelectron spectroscopy, and

time resolved photoluminescence spectroscopy. These techniques will develop a greater understanding to calculate band edge positioning and identify the relative exciton recombination times of Cu/Pd-N-TiO$_2$ compared to commercial titanium dioxide species.

Lastly, contemporary research is currently establishing the biological effects of nanoparticle materials in biological tissue cells. Therefore, Cu/Pd-N-TiO$_2$ nanomaterials will be exposed to embryonic zebra fish to assess if any cytotoxicity-induced deformations will occur during the exposure period.

6. Experimental

6.1 Instrumental equipment

6.1.1. Nuclear magnetic resonance spectroscopy

NMR spectroscopic data was obtained on a Bruker Avance III 400 MHz spectrometer. The instrument was fitted with a 5 mm BBO-Z probe. The operating temperature was set at 30 ˚C. Deuterated chloroform was used as the referencing solvent in all ^{1}H NMR spectra and set at δ_H = 7.26 ppm.

6.1.2. Gas chromatography-mass spectrometry (GC-MS)

All the reactions studied using GC-MS were conducted on a Shimadzu QP2010SE.

The GC columns used in the study were:
1) InertCap 5MS/Sil
2) Zebron ZB-5ms+

Both columns had the same specifications: 0.25 mm I.D. × 30 m, df = 0.25 μm.

The GC program on the Shimadzu QP2010SE gas chromatograph-mass spectrometer was set accordingly:

➢ Column temperature: 40 °C (1-minute hold) - 12 °C/minute - 200 °C
➢ Carrier gas: He at 1.32 mL/min
➢ Detection: MS
➢ Sample volume: 3 μL
Internal standard volume: 3 μL

6.1.3. B.E.T. Theory

The B.E.T. study was conducted on a Micromeretics Tristar II instrument and the data was processed using Tristar software.

6.1.4. Electron microscopy

All scanning electron micrographs were collected using a Zeiss Ultra Plus FEGSEM (field emission gun scanning electron microscope). The data was processed using Zeiss SmartSEM UIF V05.04.02.00 and AzTec for EDX analyses. Samples were mounted on carbon adhesion tape that was bound to metal stub holders. Both high and variable pressure vacuum analyses were utilised to obtain the respective magnifications. At high pressure, the samples were gold coated to avoid charging. All transmission electron micrographs were collected on a JEOL 2100 high resolution transmission electron microscope for HRTEM and STEM analyses. The images were taken using Gatan Digital Micrograph V2.10.1282.0 software. The energy-dispersive X-ray spectroscopic studies were performed on an Oxford X-Max 80mm^2 SDD (Silicon drift detector) analyser using Oxford Instruments Inca V4.15 software.

6.1.5. Raman spectroscopy

Two instruments were used in this study and have been listed below:

1) Advantage 532 (Serial Number: 500-022). The software used was NuSpec.
2) Renishaw$_®$ inVia Raman microscope. The software used was Renishaw's WiRE (Windows-based Raman Environment).

6.1.6. UV/Vis spectroscopy

The optical absorbance measurements of methylene blue and eosin Y were studied in solution on a PG Instruments Limited T80 UV/VIS spectrophotometer. Data was processed with UVWin5 analytical software (V5.1.1.1).

6.1.7. Powder diffuse reflectance UV/Vis spectroscopy

Powdered semiconductor samples were studied on a Shimadzu UV-2600 UV/Vis spectrophotometer that was equipped with a Shimadzu ISR-2600/ISR-2600Plus integrating sphere attachment.

6.1.8. Powder X-ray diffraction

The samples were prepared for X-ray diffraction analysis using the back-loading preparation method.

A PANalytical Empyrean Diffractometer equipped with a X'Celerator detector and Co-Kα radiation was used for all the analyses. The generator was set at 40 kV (voltage) and 40 mA (current).Phase identifications and Rietveld analyses were performed using the HighScore Plus software, version 3.0d.

6.1.9. Photoluminescence spectroscopy

Emission spectra were collected from 360-900 nm. A continuous He-Cd laser produced a 325 nm excitation wavelength and was used in all experiments. A restriction to the laser pulse (120 *Hz*) was applied. The signals from a Horiba iHR320 monochromator were collected from a photomultiplier tube that was coupled to a lock-in amplifier. The samples were mounted as thin powder films.

6.1.10. X-ray photoelectron spectroscopy

System: PHI 5000 scanning ESCA microprobe.

Mounting method: The samples were mounted as thin powder films.

A 100 µm diameter monochromatic Al K_α X-ray beam ($hv = 1486.6$ eV) was generated by a 25 W, 15 KV electron beam and was used to analyse the different binding energy peaks. Carbon was used as the binding energy reference and the corresponding data

was shifted towards 284.5 eV (C*1s*). The fitting software used was OriginPro 9.1. A Gaussian function was used to perform the XPS curve fitting with either a manual (for high background noise samples) or Shirley-type background subtraction.

Surface sputtering was performed using an Ar^+ ion gun (2 KV, 2 µA), and a low-energy neutraliser electron gun. This process minimised surface charging and removed surface contamination on the powdered samples during storage.

6.2. Sodium-silver electrolyte solution for stabilising alizarin red

Table 15 listed below, has tabulated the ionic strength calculations of silver nitrate and sodium nitrate relative to the amount of starting alcohol used in the optimisation reactions for alizarin red-sensitised zinc oxide to mediate alcohol oxidations. The previous ionic strength solution (silver nitrate, 1.2 M) proposed by Jeena and Robinson[59] has been standardised with the current research's refinement study to identify the masses of silver nitrate and sodium nitrate that was needed to achieve an ionic electrolyte of near-equal concentration.

Table 15: The determination of the optimal silver-sodium electrolyte concentration to stabilise alizarin red-sensitised zinc oxide in water. The ionic equivalents were prepared relative to the chosen alcohol scale (mmol).

Alcohol scale (mmol)	Ionic equivalents	Ionic Concentration(s)	Ref.
	Previous research		
0.1 mmol	**18 equiv. $AgNO_3$**	**1.2 M (306 mg in 1.5 mL water)**	Jeena[92]
	This research		
0.2 mmol	15 equiv. $NaNO_3$	6.0 M (255 mg in 0.5 mL water)	
0.2 mmol	10 equiv. $NaNO_3$	4.0 M (170 mg in 0.5 mL water)	
0.2 mmol	5 equiv. $NaNO_3$	2.0 M (85 mg in 0.5 mL water)	
0.2 mmol	3 equiv. $NaNO_3$ + 1 equiv. $AgNO_3$	**1.2 M $NaNO_3$ + 0.4 M $AgNO_3$ (51 mg [$NaNO_3$] + 34 mg [$AgNO_3$] in 0.5 mL water) (Total ionic strength = 1.24 M)**	**This Work**
0.2 mmol	1equiv. $NaNO_3$	0.4 M (17 mg in 0.5 mL water)	

6.3. Alcohol quantification using gas chromatography-mass spectrometry

6.3.1. 4-Octylphenol calibration curve

The accurate quantification of oxidised products from the use of either alizarin red/ZnO/Ag/TEMPO or Cu/Pd-N-TiO$_2$ required an internal standard during the chromatographic process. For this purpose, 4-octylphenol was introduced into the study (Tables 2, 3 and 8). An internal standard using gas chromatography was chosen as the appropriate quantitative method as many starting material/product(s) made it impractical to perform a full external calibration curve for each reaction. In addition, the low reaction scale (0.1−0.2 mmol) made it experimentally impossible to purify the product in sufficient quantity.

A calibration curve (20−140 ppm) was constructed using 4-octylphenol (**Figure 90**).

$$Y = (166446.01250)X + (115744.28571)$$
$$R = 0.997$$
$$R2 = 0.995$$
$$\%RSD = 6.67$$
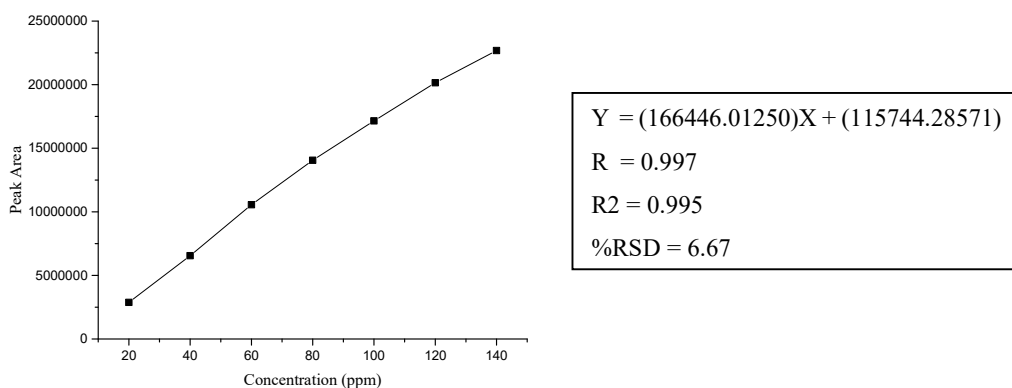
Figure 90: 20−140 ppm calibration curve of 4-octylphenol that was used to quantitate the conversion of alcohols to aldehydes.

During the work up stage after each reaction, a product concentration of approximately 80 ppm was prepared. The concentration (*ca.* 80 ppm) was chosen to fall within the internal standard's calibration set (20−140 ppm), which would further improve the accuracy of the respective (alcohol and internal standard) response factors.

6.3.2. Quantitative formulations to detect the remaining alcohol after the reaction process.

The conversion of alcohols into aldehydes was quantitatively measured using gas chromatography-mass spectrometry (GC-MS) on a Shimdazu QP2010SE equipped with a Zebron ZB-5MSplus column. Gas chromatography was the chosen quantitative technique to determine the oxidised product due to the low reaction scale (0.1−0.2 mmol).

Therefore, an internal standard (4-octylphenol) was calibrated against each alcohol tested after which, relative response factors were calculated and used as references to determine the amount of unreacted alcohol that remained after each photocatalytic reaction, and hence the alcohol conversion. The internal standard was also calibrated against the corresponding aldehyde for the accurate quantification of the aldehyde's yield and selectivity.

The response factor of the selected alcohol was based upon the relationship between peak area and the concentration of the alcohol. The same equation applied to the corresponding aldehyde, as noted in **Equation 2**:

$$RF = \frac{PA_A}{[A]}$$

Equation 2

Where: * RF = Response factor

* PA$_A$ = Peak area of the alcohol or aldehyde

* [A] = Alcohol or aldehyde concentration

Furthermore, in order to establish the association between the alcohol (and aldehyde) with the internal standard, which would later serve to quantify the remaining alcohol in the reaction test (or the amount of aldehyde formed), a response factor of the alcohol

(and the corresponding aldehyde) relative to the internal standard needed consideration (**Equation 3**).

From the expression,

$$RRF = \frac{RF_A}{RF_{IS}}$$

Equation 3

Where: * RRF = Relative response factor

          * RA$_A$ = Response factor of the alcohol or aldehyde

          * RF$_{IS}$ = Response factor of the internal standard or aldehyde

Consider for example **Figure 91**:
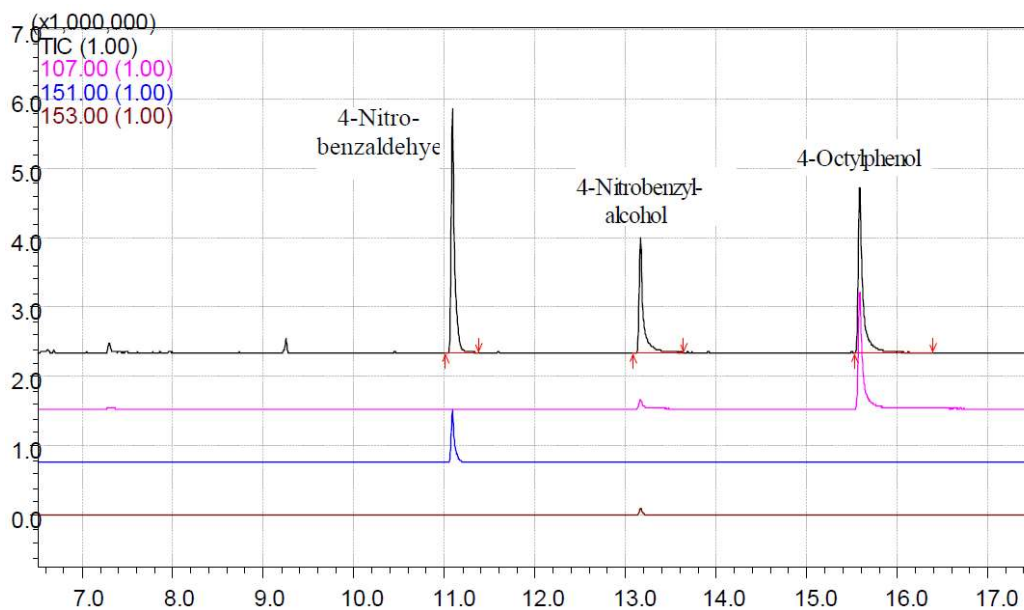
Figure 91: The chromatogram representing the oxidation of 4-nitrobenzyl alcohol to 4-nitrobenzaldehyde and the presence of the internal standard (4-octylphenol) to quantitate the reaction progress.

Note: A Slight incompatibility existed between the polarity of starting alcohols and/or solvent with the column stationary phase, which was observed from the minor peak tailing in selected chromatograms.

The peak areas of 4-nitrobenzyl alcohol, 4-nitrobenzaldehyde and 4-octylphenol were integrated to obtain their respective values (4-nitrobenzyl alcohol [5272312], 4-nitrobenzaldehyde [8754300] and 4-octylphenol [5361877]) in **Figure 91**.

From independent response factor chromatograms, the response factors for 4-nitrobenzyl alcohol (131809.09) and 4-nitrobenzaldehyde (139243.91) were calculated. From these response factors, the relative response factors to the internal standard were subsequently determined (4-nitrobenzyl alcohol [0.78] and 4-nitrobenzaldehyde [0.82]). The relative response factor values of the alcohols and aldehydes used in the photo-oxidation studies have been tabulated below (**Table 16**).

Table 16: Relative response factors for the alcohols and aldehydes used in the photo-oxidation studies

	Relative Response Factors (RRF)	
Alcohols	**Alcohol (OH) RRF (OH)**	**Aldehyde (CHO) RRF(CHO)[b]**
3,4-Dimethoxybenzyl alcohol	1,11	1,03
4-Methoxybenzyl alcohol	1,12	1,08
4-Nitrobenzyl alcohol	0,78	0,82
2-Naphthalene methanol	1,62	1,46
Cinnamyl alcohol	1,23	1,28
3-Clorobenzyl alcohol	0,99	1,07
Benzyl alcohol	1,14	1,01
Cyclohexanol	0,77	0,58
4-Methylbenzyl alcohol	0,88	Not available

Table continued overleaf

Furfuryl alcohol	0,41	0,40
Benzoin	0,96	1,03
2-Hydroxyphenethyl alcohol	0,85	Not available
1-Hexanol	0,51	0,09
1-Heptanol	0,74	0,44
trans-2-Hexen-1-ol	0,53	0,03
2-Decanol	0,57	Not available
2,2-Dimethyl-1,3-propanediol	0,41	Not available

[b]Not available, the corresponding aldehyde was not available to determine the relative response factor.

Once the quantitative parameters were collected (relative response factors for both 4-nitrobenzyl alcohol and 4-nitrobenzaldehyde), the sample (**Figure 91**) could be quantitatively analysed.

The concentration of the remaining 4-nitrobenzyl alcohol after the reaction was calculated from knowing the response factor of 4-nitrobenzyl alcohol and 4-octyl phenol after combining **Equation 2** and **Equation 3**:

$$[A] = PA_A \times \frac{[IS]}{PA_{IS}} \times \frac{1}{RRF_A} \qquad \text{\textbf{Equation 4}}$$

For example: The oxidation of 4-nitrobenzyl alcohol to 4-nitrobenzaldehyde (**Figure 92**).
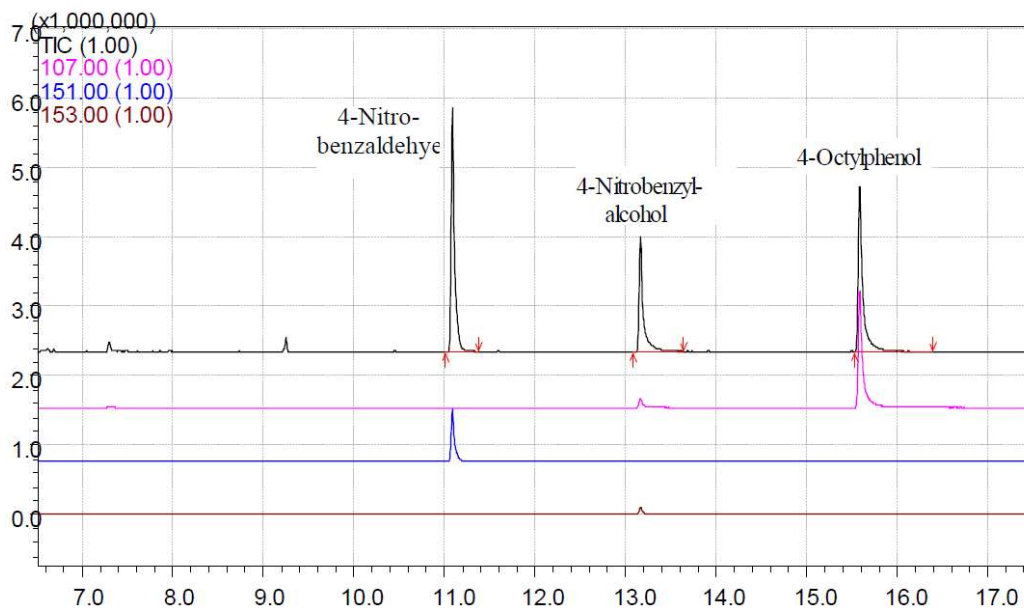
Figure 92: The chromatogram representing the oxidation of 4-nitrobenzyl alcohol to 4-nitrobenzaldehyde using $Cu/Pd-N-TiO_2$.

Calculations:

$$[OH] = PA_{OH} \times \frac{[IS]}{PA_{IS}} \times \frac{1}{RRF_{OH}}$$

$$= PA_{OH} \times \frac{[IS]}{PA_{IS}} \times \frac{1}{\dfrac{RF_{OH}}{RF_{IS}}}$$

$$= 5272312 \times \frac{31.52}{5361877} \times \frac{1}{\dfrac{131809.09}{170019.28}}$$

$$= 39.98 \text{ ppm} \pm 6.67\ \%$$

The concentration (39.98 ppm) of 4-nitrobenzyl alcohol noted above was the remaining alcohol in the reaction solution after the five-hour reaction period. The same calculation (**Equation 4**) was used to determine the corresponding 4-nitrobenzaldehyde concentration after the five-hour reaction period (62.86 ppm).

Note: Prior to analysing the reaction contents (**Equation 4**), the crude mixture was too concentrated for a direct injection into the GC-MS. An approximate analyte concentration of 80 ppm was prepared as it was within the calibration curve's concentration range (20−140 ppm). The sample dilution (to achieve an *ca.* 80 ppm analyte solution) was prepared accordingly:

Sample dilution factor:

Assuming 0 % conversion of 0.1 mmol 4-nitrobenzyl alcohol in 2.5 mL toluene (reaction solvent), the alcohol concentration would be calculated as follows:

   0.1 mmol of 4-methylbenzyl alcohol = 15.31 mg

   15.31 mg in 2.50 mL = 6124.00 ppm

To achieve an alcohol concentration of *ca.* 80 ppm, a 59.38× dilution was introduced (25.26 µL of the reaction analyte in 1474.47 µL of solvent). The total volume prepared for GC-MS analysis = 1.5 mL.

At 0 % conversion, the concentration of 4-nitrobenzyl alcohol was:

   = 6124.00/59.38

   = 103.13 ppm

The conversion of 4-nitrobenzyl alcohol was then determined as follows:

$$C = \frac{[OH]^0 - [OH]^t}{[OH]^0} \times 100$$ where $[OH]^0$ = alcohol concentration at the start of the reaction, *i.e.* 0% conversion and $[OH]^t$ = alcohol concentration remaining at the end of the reaction period 't'.

$$C = \frac{103.13 - 3 \ .98}{103.13} \times 100$$

$$= 61 \ \%$$

The yield of 4-nitrobenzylaldehyde was then determined as follows:

$$Y = \frac{[CHO]^t}{[OH]^0} \times 100$$ where $[CHO]^t$ = aldehyde concentration at the end of the reaction period 't' and $[OH]^0$ = the alcohol concentration at the start of the reaction period.

$$Y = \frac{62.86}{103.13} \times 100$$

$$= 61 \ \%$$

The selectivity for 4-nitrobenzaldehyde was then determined as follows:

$$S = \frac{[CHO]^t}{[OH]^0 - [OH]^t} \times 100$$ where $[CHO]^t$ = aldehyde concentration at the end of the reaction period 't', $[OH]^O$ = alcohol concentration at the start of the reaction, *i.e.* 0% conversion and $[OH]^t$ = alcohol concentration remaining at the end of the reaction period 't'.

$$S = \frac{62.86}{103.13 - 3 \ .98} \times 100$$

$$= \geq 99 \ \%$$

6.4. Synthesis of alizarin red-sensitised zinc oxide

Zinc oxide powder (975 mg, Hugh Source [International] LTD, 99.5 % minimum) and alizarin red (25 mg) were mechanically mixed in a 50 mL beaker. De-ionised water was added dropwise until a homogeneous thick purple paste was obtained. The resulting mixture was left to stir overnight until dry, after which it was ground to a fine purple powder for further use.

6.5. Typical photocatalysed reaction using the alizarin red/ ZnO/Ag-Na/TEMPO

In a borosilicate test tube (7.5 mL), $NaNO_3$ (51 mg, 0.6 mmol), $AgNO_3$ (34 mg, 0.2 mmol) were dissolved in de-ionised water (0.5 mL). TEMPO (15 mg, 0.096 mmol), alizarin red-sensitised zinc oxide power (20 mg) and the appropriate alcohol (0.2 mmol) were subsequently added. The test tube (containing a clear solution with a suspension of purple alizarin red-sensitised zinc oxide) was sealed with a rubber septum and parafilm. The contents of the test tube were irradiated using an OSRAM® VIALOX 70W (65600 lumens, emission spectrum reported below [**Figure 93**]) incandescent lamp for 7 hours with continuous stirring. After the irradiation period, the purple colour of the alizarin red-sensitised zinc oxide changed to dark grey, suggesting the organic dye had decomposed. The organics from the reaction were extracted using chloroform (3 × 1 mL). From the crude organic reaction mixture, 9 μL was extracted and diluted in 1491 μL of acetonitrile (*ca.* 80 ppm solution). The reaction products were quantitatively analysed using gas chromatography-mass spectrometry on a Shimadzu QP2010SE equipped with a Zebron ZB-5MSplus column.
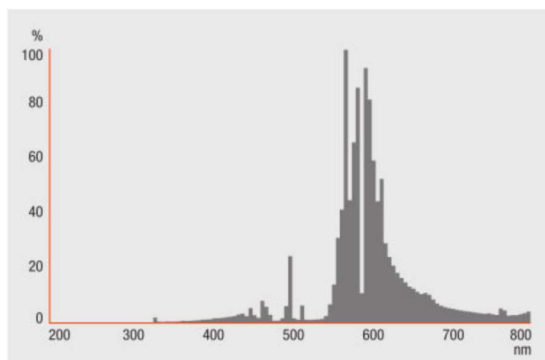
Figure 93: Emission spectrum of OSRAM® VIALOX 70W.^{Sourced from product brochure.}

6.5.1. Attempted Synthesis of Cu_3TiO_5, Ni_3TiO_5 and Mn_3TiO_5

The attempted syntheses of Cu_3TiO_5, Ni_3TiO_5 and Mn_3TiO_5 have been outlined below. However, the synthetic procedures followed did not successfully lead to the development of the desired A_3TiO_5 materials (where A = Cu, Ni, or Mn) but rather mixtures of CuO and TiO_2, amorphous Ni-TiO_2, and lastly Mn_2O_3 and TiO_2, respectively.

6.5.1.1. Cu_3TiO_5

Cu_3TiO_5 was synthesised from titanium tetraisopropoxide (TTIP, 2.59 mmol, 765.93 µL) and copper (II) nitrate trihydrate ($Cu[NO_3]_2 \cdot 3H_2O$, 2.63 mmol, 634.61 mg) in absolute ethanol (20 mL). The solution was stirred for 1 hour, filtered and calcinated at 800˚C for 4 hours, 15 minutes. The resultant black powder was finely ground for further use.

$$\text{Ti in TTIP} = 47.87 \text{ g. mol}^{-1} \text{ in } 284.22 \text{ g. mol}^{-1} \text{ (17 %)}$$
$$\text{Cu in Cu(NO}_3)_2 \cdot 3H_2O = 63.55 \text{ g. mol}^{-1} \text{ in } 241.60 \text{ g. mol}^{-1} \text{ (26 %)}$$

$$Cu_3TiO_5 = 191.42 \text{ g. mol}^{-1} \text{ (Cu [wt%]} = 33\%, \text{ Ti [wt%]} = 25 \text{ %)}$$

500 mg Cu₃TiO₅ preparative scale

Cu_3 (wt% on 33 % above) = 165 mg

Ti   (wt% on 25 % above) = 125 mg

Therefore $165 \text{ mg} \times \dfrac{100}{26} = 634.61 \text{ mg Cu(NO}_3)_2 \cdot 3H_2O$ required and,

$$125 \text{ mg} \times \frac{100}{17} = 735.29 \text{ mg TTIP}$$

$$\text{volume}_{(TTIP)} = \frac{\text{mass}}{\text{density}}$$

$$= \frac{735.29}{0.96} \qquad \text{Density}_{(TTIP)}: 0.96 \text{ g.mL}^{-1}$$

$$= 765.93 \text{ μL}$$

6.5.1.2. Ni₃TiO₅

Ni_3TiO_5 was synthesised from titanium tetraisopropoxide (TTIP, 4.60 mmol, 1.31 mL) and nickel (II) acetate tetrahydrate ($Ni[OAc]_2 \cdot 4H_2O$, 10 mmol, 2.48g) in absolute ethanol (20 mL). The solution was stirred for 1 hour, filtered and calcinated at 800°C for 4 hours, 15 minutes. The resultant light green powder was finely ground for further use.

$$\text{Ti in TTIP} = 47.87 \text{ g. mol}^{-1} \text{ in } 284.22 \text{ g. mol}^{-1} \text{ (17 \%)}$$
$$\text{Ni in Ni(OAc)}_2 \cdot 4H_2O = 248.84 \text{ g. mol}^{-1} \text{ (24 \%)}$$

Preparative scale based on 10 mmol of Ni(OAc)₂·4H₂O

3 : 1 molar ratio Ni (2.4 mmol): Ti (0.8 mmol) in Ni₃TiO₅, therefore;

$Ni(OAc)_2 \cdot 4H_2O$: 10 mmol = 2.48g (2.4 mmol Ni)

TTIP: 4.60 mmol = 1.26 g (0.8 mmol Ti)

Volume$_{(TTIP)}$ 1.26 g TTIP = 1.31 mL (4.60 mmol) Mr_{TTIP} = 284.22 g.mol^{-1}, density = 0.96 g.mL^{-1}

6.5.1.3. Mn_3TiO_5

Mn_3TiO_5 was synthesised from titanium tetraisopropoxide (TTIP, 0.70 mmol, 200 mg) and manganese (II) chloride tetrahydrate ($MnCl_2 \cdot 4H_2O$, 3.03 mmol, 600 mg) in absolute ethanol (20 mL). The solution was stirred for 1hour, filtered and calcinated at 800˚C for 4 hours, 15 minutes. The resultant black powder was finely ground for further use.

Mn (3) : Ti (1) in Mn_3TiO_5

$MnCl_2 \cdot 4H_2O$: 600 mg

TTIP: 208.33 µL = 200 mg

Volume($_{TTIP}$) 200 mg TTIP = 208.33 µL, Mr_{TTIP} = 284.22 g.mol^{-1}, density = 0.96 g.mL^{-1}

6.6. Synthesis of cadmium sulfide derivatives

6.6.1. Colloidal silver nanoparticles

The synthesis of silver nanoparticles was adapted from Zhang *et al.*[57] 50 ml of aqueous silver nitrate (0.3 mM, 0.01 mmol, 2.55 mg) was heated to its boiling point in a round bottom flask and 1% tri-sodium citrate aqueous solution (2.5 mL) was slowly added drop-wise with constant stirring. The mixture was then left to reflux for a further 4 hours. After refluxing, a pale-yellow colloidal suspension was left to cool to room temperature.

6.6.2. Silver functionalised cadmium sulfide

[STEP A]: Cadmium nitrate tetrahydrate ($Cd(NO_3)_2 \cdot 4 H_2O$, 1 mmol, 236.4 mg) and urea (10 mmol, 600.6 mg) were added to de-ionised water (25 mL). A portion (15 mL) of the colloidal silver nanoparticle solution (from 6.6.1

above) was subsequently added with an additional stirring period (10 minutes).

[STEP B]: Sodium sulfide (Na_2S, 1.2 mmol, 93.65 mg) in de-ionised water (15 mL) was slowly added dropwise to STEP A solution over 10 minutes.

The resultant mixture was stirrer for a further 30 minutes, refluxed for 24 hours and left to cool to room temperature. After centrifuging the yellow suspension to remove the supernatant liquid, washing with de-ionised water and absolute ethanol, the silver functionalised cadmium sulfide was oven dried (333 K) and then calcinated at 673 K for 2 hours.

6.7. TiO$_2$ derivatives

6.7.1. Nitrogen functionalised titanium dioxide

Nitrogen functionalised titanium dioxide (N-TiO$_2$) was prepared according to a literature method reported by Wang *et al.*[161] In a typical synthetic procedure, TTIP (10.55 mmol, 3.12 mL) was added drop-wise into de-ionised water (15 mL) followed by the addition of nitric acid (25 %, 4 mL). The mixture was continuously stirred until the titanium hydroxide (Ti[OH]$_4$) precursor had dissolved from acid assistance (30 minutes). Nitrogen was introduced after aqueous ammonia (25 %) was added to obtain a solution of pH *ca.* 9. Once the nitrogen source was added, the heterogeneous aqueous mixture was filtered, and the white precipitate was washed several times with de-ionised water. The nitrogen functionalised titanium dioxide was oven dried at 45 ˚C and calcinated at 350 ˚C for 2 hours, which afforded a yellow powder that was finely ground for further use.

6.7.2. Cu/Pd-N-TiO$_2$

In a typical synthetic procedure, TTIP (10.55 mmol, 3.12 mL) was added drop-wise into de-ionised water (15 mL) followed by the addition of nitric acid (25 %, 4 mL). The

mixture was stirred until the titanium hydroxide (Ti[OH]$_4$) precursor had dissolved from acid assistance (30 minutes). Cu(NO$_3$)$_2$·3H$_2$O (62.09 µmol, 15 mg in 2 mL absolute ethanol) and Pd(OAc)$_2$·4H$_2$O (30 mg in 2 mL absolute ethanol and 1 mL methanol) were prepared, added dropwise to the acidified aqueous titanium solution and proceeded with ten minutes stirring at room temperature. Aqueous ammonia (25 %) was subsequently added to lower the pH to *ca.* 9, which introduced the nitrogen component to the system. The solution colour turned light blue with a light blue precipitate forming upon addition of aqueous ammonia. After the neutralisation stage, the solution was filtered and the light blue Cu/Pd-N-TiO$_2$ precipitate was oven dried at 45 ˚C and calcinated at 350 ˚C for 2 hours. The resultant material, which was light brown in colour was ground to a fine powder for instrumental characterisations.

6.8. Methylene blue and eosin Y preparation

Methylene blue and eosin Y were prepared at 80 ppm stock solutions (20 mg in 250 ml volumetric flasks and topped up to mark with de-ionised water). For each photo-degradation reaction, 5 mL of 80 ppm stock solution were dissolved in 15 mL de-ionised water to prepare 20 mL of 20 ppm organic dyestuff solution for analysis.

6.9. Chemical list

The following chemicals were used in this study:

- Acetonitrile: Burdick and & Jackson: CAS 75-05-8, ≥ 99.9 %
- Acetonitrile: ALDRICH: E CHROMASOLV®, > 99.9 %34888
- Alizarin red S: BDH Indicators, C.I. 58005
- Cadmium nitrate AR: Associated Chemical Enterprises, 08TT00500
- 3-Chlorobenzyl alcohol: ALDRICH, C27107, 98 %
- Chloroform – D1, Merck, MagniSolv™, 1.02450.0500, 99.8%
- Cinnamyl alcohol: Merck, 70313190
- Copper (II) nitrate trihydrate: ALDRICH, 61197
- Cyclohexanol: Merck, Art. 2891
- 2-Decanol: ALDRICH, 118311, 98 %
- 3,4-Dimethoxybenzyl alcohol: Merck, 2263629
- 2,2-Dimethyl-1,3-propanediol, 41510: Fluka Chemika, 41510, > 98 %
- Eosin Y: Janssen Chimica, indicator grade
- Furfuryl alcohol: UNILAB, SAARCHEM, 250 525
- Heptan-1-ol: BDH Laboratory Reagents, 28474
- Hexan-1-ol: UNILAB, 286 85 00
- 2-Hydroxyphenethyl alcohol: ALDRICH, 188247, 99 %
- Manganese (II) chloride tetrahydrate: ALDRICH, M3634
- 4-Methoxybenzyl alcohol: ALDRICH, 13,690-5, 98 %
- 4-Methylbenzyl alcohol: ALDRICH, 127809, 98 %
- Methylene blue: SAARCHEM, 416 46 00, 98.5 %
- 2-Naphthalenemethanol: ALDRICH, 187313, 98 %
- Nitric acid (55 %): Merck, Saarchem, 446 50 40 LC
- 4-Nitrobenzyl alcohol: ALDRICH, N1,282-1, 99 %
- 4-Octylphenol: ALDRICH, 99 %, 384445
- Palladium (II) acetate (47 % Pd): Merck, 8.18056.0001
- 1-Phenyl-ethanol: ALDRICH: P1,380-0, 98 %
- Sodium nitrate GR: Merck, Art. 6537, > 99 %
- Titanium tetraisopropoxide: ALDRICH, 87560, ≥ 97 %
- TLC silca gel 60 F_{254}: Merck, 1.05554.0001
- trans-2-Hexen-1-ol: Merck, Art. 818674
- Tri-sodium citrate: SAARCHEM, 582 2500
- Zinc oxide: Hugh Source (International) LTD, > 99.5 %

7. References

[1]   A. Yoshikawa, H. Matsunami, Y. Nanishi, in *Wide Bandgap Semiconductors: Fundamental Properties and Modern Photonic and Electronic Devices* (Eds.: K. Takahashi, A. Yoshikawa, A. Sandhu), Springer, Berlin, Heidelberg, **2007**, pp. 1-24.

[2]   J. Schneider, M. Matsuoka, M. Takeuchi, J. Zhang, Y. Horiuchi, M. Anpo, D. W. Bahnemann, *Chemical Reviews* **2014**, *114*, 9919-9986.

[3]   M. Dahl, Y. Liu, Y. Yin, *Chemical Reviews* **2014**, *114*, 9853-9889.

[4]   C. Dette, M. A. Pérez-Osorio, C. S. Kley, P. Punke, C. E. Patrick, P. Jacobson, F. Giustino, S. J. Jung, K. Kern, *Nano Letters* **2014**, *14*, 6533-6538.

[5]   W. Maziarz, A. Kusior, A. Trenczek-Zajac, *Beilstein J. Nanotechnol.* **2016**, *7*, 1718-1726.

[6]   S. Higashimoto, N. Kitao, N. Yoshida, T. Sakura, M. Azuma, H. Ohue, Y. Sakata, *Journal of Catalysis* **2009**, *266*, 279-285.

[7]   T. Yui, A. Kan, C. Saitoh, K. Koike, T. Ibusuki, O. Ishitani, *ACS Applied Materials & Interfaces* **2011**, *3*, 2594-2600.

[8]   D. Ljubas, G. Smoljanić, H. Juretić, *Journal of Environmental Management* **2015**, *161*, 83-91.

[9]   M. Zhang, C. Chen, W. Ma, J. Zhao, *Angewandte Chemie International Edition* **2008**, *47*, 9730-9733.

[10]   L. Yang, Z. Liu, *Energy Conversion and Management* **2007**, *48*, 882-889.

[11]   M. Nishikawa, S. Yuto, T. Nakajima, T. Tsuchiya, N. Saito, *Catalysis Letters* **2017**, *147*, 292-300.

[12]   B. Trujillo-Navarrete, M. del Pilar Haro-Vázquez, R. M. Félix-Navarro, F. Paraguay-Delgado, H. Alvarez-Huerta, S. Pérez-Sicairos, E. A. Reynoso-Soto, *Journal of Rare Earths* **2017**, *35*, 259-270.

[13]   H. Cheng, K. Fuku, Y. Kuwahara, K. Mori, H. Yamashita, *Journal of Materials Chemistry A* **2015**, *3*, 5244-5258.

[14]   A. G. Milekhin, L. L. Sveshnikova, T. A. Duda, N. A. Yeryukov, E. E. Rodyakina, A. K. Gutakovskii, S. A. Batsanov, A. V. Latyshev, D. R. T. Zahn, *Physica E: Low-dimensional Systems and Nanostructures* **2016**, *75*, 210-222.

[15]   L. Gomathi Devi, R. Kavitha, *Applied Surface Science* **2016**, *360, Part B*, 601-622.

[16]   C. Han, Q. Quan, H. M. Chen, Y. Sun, Y.-J. Xu, *Small* **2017**, 1602947.

[17]   J. J. Mock, M. Barbic, D. R. Smith, D. A. Schultz, S. Schultz, *The Journal of Chemical Physics* **2002**, *116*, 6755-6759.

[18]   T. Atay, J.-H. Song, A. V. Nurmikko, *Nano Letters* **2004**, *4*, 1627-1631.

[19]   K. Kolwas, A. Derkachova, M. Shopa, *Journal of Quantitative Spectroscopy and Radiative Transfer* **2009**, *110*, 1490-1501.

[20]   W. Hou, S. B. Cronin, *Advanced Functional Materials* **2013**, *23*, 1612-1619.

[21]   K. Kim, A. Husakou, J. Herrmann, *Optics Express* **2010**, *18*, 7488-7496.

[22]   X. Ma, X. Wu, Y. Wang, Y. Dai, *Physical Chemistry Chemical Physics* **2017**, *19*, 18750-18756.

[23]   X. Cheng, X. Yu, Z. Xing, J. Wan, *Energy Procedia* **2012**, *16*, 598-605.

[24]   S. A. Ansari, M. M. Khan, M. O. Ansari, M. H. Cho, *New Journal of Chemistry* **2016**, *40*, 3000-3009.

[25]   A. T. Kuvarega, R. W. M. Krause, B. B. Mamba, *The Journal of Physical Chemistry C* **2011**, *115*, 22110-22120.

[26]   W. Mekprasart, W. Pecharapa, *Energy Procedia* **2011**, *9*, 509-514.

[27]   B. Choudhury, A. Choudhury, *Journal of Applied Physics* **2013**, *114*, 203906.

[28]   A. A. Murashkina, P. D. Murzin, A. V. Rudakova, V. K. Ryabchuk, A. V. Emeline, D. W. Bahnemann, *The Journal of Physical Chemistry C* **2015**, *119*, 24695-24703.

[29]   W. Zhou, Y. Guan, D. Wang, X. Zhang, D. Liu, H. Jiang, J. Wang, X. Liu, H. Liu, S. Chen, *Chemistry, an Asian journal* **2014**, *9*, 1648-1654.

[30]   D. Nassoko, Y.-F. Li, J.-L. Li, X. Li, Y. Yu, *International Journal of Photoenergy* **2012**, *2012*, 10.

[31]   K. V. Baiju, P. Periyat, W. Wunderlich, P. Krishna Pillai, P. Mukundan, K. G. K. Warrier, *Journal of Sol-Gel Science and Technology* **2007**, *43*, 283-290.

[32]   C. Fan, C. Chen, J. Wang, X. Fu, Z. Ren, G. Qian, Z. Wang, *Scientific Reports* **2015**, *5*, 11712.

[33]   X. Pan, Y.-J. Xu, *The Journal of Physical Chemistry C* **2013**, *117*, 17996-18005.

[34]   A. Hamdi, D. P. Ferreira, A. M. Ferraria, Concei, #xe7, #xe3, D. S. o, L. F. Vieira Ferreira, A. P. Carapeto, S. Boufi, S. Bouattour, A. M. Botelho do Rego, *Journal of Nanomaterials* **2016**, *2016*, 11.

[35] Z. Yu, F. Qu, X. Wu, *Dalton Transactions* **2014**, *43*, 4847-4853.

[36] S. Yurdakal, V. Augugliaro, *RSC Advances* **2012**, *2*, 8375-8380.

[37] L. Zhu, Q. Lu, L. Lv, Y. Wang, Y. Hu, Z. Deng, Z. Lou, Y. Hou, F. Teng, *RSC Advances* **2017**, *7*, 20084-20092.

[38] Y. Liao, W. Que, Q. Jia, Y. He, J. Zhang, P. Zhong, *Journal of Materials Chemistry* **2012**, *22*, 7937-7944.

[39] D. Reyes-Coronado, G. Rodríguez-Gattorno, M. E. Espinosa-Pesqueira, C. Cab, R. d. Coss, G. Oskam, *Nanotechnology* **2008**, *19*, 145605.

[40] P. Bindu, S. Thomas, *Journal of Theoretical and Applied Physics* **2014**, *8*, 123-134.

[41] S. Verma, S. L. Jain, *Inorganic Chemistry Frontiers* **2014**, *1*, 534-539.

[42] X. Chen, Z. Zheng, X. Ke, E. Jaatinen, T. Xie, D. Wang, C. Guo, J. Zhao, H. Zhu, *Green Chemistry* **2010**, *12*, 414-419.

[43] Y. Shiraishi, H. Sakamoto, Y. Sugano, S. Ichikawa, T. Hirai, *ACS Nano* **2013**, *7*, 9287-9297.

[44] M. Cherevatskaya, B. König, *Russian Chemical Reviews* **2014**, *83*, 183.

[45] J. Bardeen, *Physical Review* **1947**, *71*, 717.

[46] V. Heine, *Physical Review* **1965**, *138*, A1689.

[47] R. T. Tung, *Applied Physics Reviews* **2014**, *1*, 011304.

[48] G.-S. Kim, S.-W. Kim, S.-H. Kim, J. Park, Y. Seo, B. J. Cho, C. Shin, J. H. Shim, H.-Y. Yu, *ACS Applied Materials & Interfaces* **2016**, *8*, 35419-35425.

[49] D. E. Eastman, *Physical Review B* **1970**, *2*, 1-2.

[50] I. Pašti, S. Mentus, *Materials Chemistry and Physics* **2009**, *116*, 94-101.

[51] H. Zhuang, Y. Zhang, Z. Chu, J. Long, X. An, H. Zhang, H. Lin, Z. Zhang, X. Wang, *Physical Chemistry Chemical Physics* **2016**, *18*, 9636-9644.

[52] K. Obata, K. Kishishita, A. Okemoto, K. Taniya, Y. Ichihashi, S. Nishiyama, *Applied Catalysis B: Environmental* **2014**, *160-161*, 200-203.

[53] J. Vargas Hernández, S. Coste, A. García Murillo, F. Carrillo-Romo, A. Kassiba, *Effects of metal doping (Cu, Ag, Eu) on the electronic and optical behavior of nanostructured TiO 2, Vol. 710*, **2017**.

[54] H. Sakamoto, J. Imai, Y. Shiraishi, S. Tanaka, S. Ichikawa, T. Hirai, *ACS Catalysis* **2017**, *7*, 5194-5201.

[55] B. Chen, X. Li, R. Zheng, R. Chen, X. Sun, *Journal of Materials Chemistry A* **2017**, *5*, 13382-13391.

[56]   N. Zhang, X. Fu, Y.-J. Xu, *Journal of Materials Chemistry* **2011**, *21*, 8152-8158.

[57]   C. D. Wagner, W. M. Riggs, L. E. Davis, J. F. Moulder, *Handbook of X-ray Photoelectron Spectroscopy*, Perkin Elmer, Eden Prairie, **1979**.

[58]   S. Balachandran, S. G. Praveen, R. Velmurugan, M. Swaminathan, *RSC Advances* **2014**, *4*, 4353-4362.

[59]   V. Jeena, R. S. Robinson, *Chemical Communications* **2012**, *48*, 299-301.

[60]   V. Jeena, R. S. Robinson, *Dalton Transactions* **2012**, *41*, 3134-3137.

[61]   P. Kar, S. Verma, A. Sen, A. Das, B. Ganguly, H. N. Ghosh, *Inorganic Chemistry* **2010**, *49*, 4167-4174.

[62]   J. Low, J. Yu, M. Jaroniec, S. Wageh, A. A. Al-Ghamdi, *Advanced Materials Research* **2017**, *29*, 1601694.

[63]   I. Aslam, C. Cao, M. Tanveer, M. H. Farooq, W. S. Khan, M. Tahir, F. Idrees, S. Khalid, *RSC Advances* **2015**, *5*, 6019-6026.

[64]   C. Shifu, J. Lei, T. Wenming, F. Xianliang, *Dalton Transactions* **2013**, *42*, 10759-10768.

[65]   Y. Zang, L. Li, Y. Zuo, H. Lin, G. Li, X. Guan, *RSC Advances* **2013**, *3*, 13646-13650.

[66]   J.-C. Wang, L. Zhang, W.-X. Fang, J. Ren, Y.-Y. Li, H.-C. Yao, J.-S. Wang, Z.-J. Li, *ACS Applied Materials & Interfaces* **2015**, *7*, 8631-8639.

[67]   X.-F. Gao, W.-T. Sun, Z.-D. Hu, G. Ai, Y.-L. Zhang, S. Feng, F. Li, L.-M. Peng, *The Journal of Physical Chemistry C* **2009**, *113*, 20481-20485.

[68]   S. Liu, N. Zhang, Z.-R. Tang, Y.-J. Xu, *ACS Applied Materials & Interfaces* **2012**, *4*, 6378-6385.

[69]   S. M. Aze, K. K. Ng, in *Physics of Semiconductor Devices* (Eds.: S. Sze, K. K. Ng), Wiley, **2006**.

[70]   L. Jingxiang, J. Chuanjia, C. Bei, W. Swelm, A. G. A. A., Y. Jiaguo, *Small Methods* **2017**, *1*, 1700080.

[71]   T. Luttrell, S. Halpegamage, J. Tao, A. Kramer, E. Sutter, M. Batzill, *Scientific Reports* **2014**, *4*, 4043.

[72]   D. O. Scanlon, C. W. Dunnill, J. Buckeridge, S. A. Shevlin, A. J. Logsdail, S. M. Woodley, C. R. A. Catlow, M. J. Powell, R. G. Palgrave, I. P. Parkin, G. W. Watson, T. W. Keal, P. Sherwood, A. Walsh, A. A. Sokol, *Nat Mater* **2013**, *12*, 798-801.

[73] S. Yngvesson, in *Microwave Semiconductor Devices* (Ed.: S. Yngvesson), Springer US, Boston, MA, **1991**, pp. 1-22.

[74] A. O. Ibhadon, P. Fitzpatrick, *Catalysts* **2013**, *3*, 189-218.

[75] A. Hamrouni, N. Moussa, A. Di Paola, L. Palmisano, A. Houas, F. Parrino, *Journal of Photochemistry and Photobiology A: Chemistry* **2015**, *309*, 47-54.

[76] Z. Yang, X. Xu, X. Liang, C. Lei, Y. Cui, W. Wu, Y. Yang, Z. Zhang, Z. Lei, *Applied Catalysis B: Environmental* **2017**, *205*, 42-54.

[77] J. S. Jang, S. J. Hong, J. Y. Kim, J. S. Lee, *Chemical Physics Letters* **2009**, *475*, 78-81.

[78] Z. Yang, X. Xu, X. Liang, C. Lei, Y. Wei, P. He, B. Lv, H. Ma, Z. Lei, *Applied Catalysis B: Environmental* **2016**, *198*, 112-123.

[79] R. Fagan, D. E. McCormack, S. J. Hinder, S. C. Pillai, *Materials* **2016**, *9*, 286.

[80] S. Anandan, M. Miyauchi, *Chemical Communications* **2012**, *48*, 4323-4325.

[81] J. Yu, S. Wang, J. Low, W. Xiao, *Physical Chemistry Chemical Physics* **2013**, *15*, 16883-16890.

[82] Y. Liu, G. Ji, M. A. Dastageer, L. Zhu, J. Wang, B. Zhang, X. Chang, M. A. Gondal, *RSC Advances* **2014**, *4*, 56961-56969.

[83] L. Nie, Y. Zheng, J. Yu, *Dalton Transactions* **2014**, *43*, 12935-12942.

[84] Y. Zhong, J. Yuan, J. Wen, X. Li, Y. Xu, W. Liu, S. Zhang, Y. Fang, *Dalton Transactions* **2015**, *44*, 18260-18269.

[85] Y. Su, P. Chen, F. Wang, Q. Zhang, T. Chen, Y. Wang, K. Yao, W. Lv, G. Liu, *RSC Advances* **2017**, *7*, 34096-34103.

[86] H. Wang, H. Ye, B. Zhang, F. Zhao, B. Zeng, *Journal of Materials Chemistry A* **2017**, *5*, 10599-10608.

[87] J. Fu, S. Cao, J. Yu, *Journal of Materiomics* **2015**, *1*, 124-133.

[88] H. Li, W. Tu, Y. Zhou, Z. Zou, *Advanced Science* **2016**, *3*, 1500389-n/a.

[89] M. Miyauchi, Y. Nukui, D. Atarashi, E. Sakai, *ACS Applied Materials & Interfaces* **2013**, *5*, 9770-9776.

[90] L. Kvítek, R. Prucek, A. Panáček, R. Novotný, J. Hrbáč, R. Zbořil, *Journal of Materials Chemistry* **2005**, *15*, 1099-1105.

[91] P. Fageria, S. Gangopadhyay, S. Pande, *RSC Advances* **2014**, *4*, 24962-24972.

[92] C. Zheng, G. He, X. Xiao, M. Lu, H. Zhong, X. Zuo, J. Nan, *Applied Catalysis B: Environmental* **2017**, *205*, 201-210.

[93] K. Rome, A. McIntyre, *Chromatography Today* **2012**, *52*.

[94]   G. Guiochon, C. L. Guillemin, in *Journal of Chromatography Library, Vol. 42* (Eds.: G. Guiochon, C. L. Guillemin), Elsevier, **1988**, pp. 629-659.

[95]   J. M. Hoover, B. L. Ryland, S. S. Stahl, *ACS Catalysis* **2013**, *3*, 2599-2605.

[96]   S. Zavahir, Q. Xiao, S. Sarina, J. Zhao, S. Bottle, M. Wellard, J. Jia, L. Jing, Y. Huang, J. P. Blinco, H. Wu, H.-Y. Zhu, *ACS Catalysis* **2016**, *6*, 3580-3588.

[97]   E. J. Corey, G. W. J. Fleet, *Tetrahedron Letters* **1973**, *14*, 4499-4501.

[98]   B. Delina, N. Ronny, *Advanced Synthesis & Catalysis* **2010**, *352*, 293-298.

[99]   T.-J. L. Cheng-Kun Lin, *Tetrahedron* **2010**, *66*, 9688-9693.

[100]   B. Guan, D. Xing, G. Cai, X. Wan, N. Yu, Z. Fang, L. Yang, Z. Shi, *Journal of the American Chemical Society* **2005**, *127*, 18004-18005.

[101]   M. Hunsen, *Tetrahedron Letters* **2005**, *46*, 1651-1653.

[102]   Q. Xiao, Z. Liu, A. Bo, S. Zavahir, S. Sarina, S. Bottle, J. D. Riches, H. Zhu, *Journal of the American Chemical Society* **2015**, *137*, 1956-1966.

[103]   T. Lu, Z. Du, J. Liu, H. Ma, J. Xu, *Green Chemistry* **2013**, *15*, 2215-2221.

[104]   L. Li, R. Matsuda, I. Tanaka, H. Sato, P. Kanoo, H. J. Jeon, M. L. Foo, A. Wakamiya, Y. Murata, S. Kitagawa, *Journal of the American Chemical Society* **2014**, *136*, 7543-7546.

[105]   V. Raji, B. A. Kalam, S. Tapan, P. Provas, G. Bishwajit, G. S. Chandra, P. A. Baran, *Chemistry – An Asian Journal* **2016**, *11*, 3084-3089.

[106]   N. S. Han, H. S. Shim, J. H. Seo, S. Y. Kim, S. M. Park, J. K. Song, *Journal of Applied Physics* **2010**, *107*, 084306.

[107]   D. Montenegro, V. Hortelano, O. Martínez, M. C. Martínez-Tomas, V. Sallet, V. Muñoz, J. Jiménez, *MRS Proceedings* **2013**, *1538*, 317-322.

[108]   R. K. Saroj, S. Dhar, *Materials Research Express* **2014**, *1*, 045904.

[109]   T. Kondela, J. Greguš, M. Zahoran, T. Roch, *IOP Conference Series: Materials Science and Engineering* **2010**, *15*, 012041.

[110]   D. N. Montenegro, V. Hortelano, O. Martínez, M. C. Martínez-Tomas, V. Sallet, V. Muñoz-Sanjosé, J. Jiménez, *Journal of Physics D: Applied Physics* **2013**, *46*, 235302.

[111]   Y. Kumar, M. Herrera, F. Singh, K. U. Kumar, S. Kumar, D. Kanjilal, S. F. Olive-MŽndez, V. Agarwal, *Physics Procedia* **2012**, *29*, 12-17.

[112]   A. D. Becke, *The Journal of Chemical Physics* **1993**, *98*, 5648-5652.

[113]   C. Lee, W. Yang, R. G. Parr, *Physical Review B* **1988**, *37*, 785-789.

[114] S. H. Vosko, L. Wilk, M. Nusair, *Canadian Journal of Physics* **1980**, *58*, 1200-1211.

[115] P. J. Stephens, F. J. Devlin, C. F. Chabalowski, M. J. Frisch, *The Journal of Physical Chemistry* **1994**, *98*, 11623-11627.

[116] A. D. McLean, G. S. Chandler, *The Journal of Chemical Physics* **1980**, *72*, 5639-5648.

[117] R. Krishnan, J. S. Binkley, R. Seeger, J. A. Pople, *The Journal of Chemical Physics* **1980**, *72*, 650-654.

[118] S. Kegnæs, J. Mielby, U. V. Mentzel, C. H. Christensenc, A. Riisager, *Green Chemistry* **2010**, *12*, 1437-1441.

[119] H. Kazuhito, I. Hiroshi, F. Akira, *Japanese Journal of Applied Physics* **2005**, *44*, 8269.

[120] M. Crişan, M. Răileanu, N. Drăgan, D. Crişan, A. Ianculescu, I. Niţoi, P. Oancea, S. Şomăcescu, N. Stănică, B. Vasile, C. Stan, *Applied Catalysis A: General* **2015**, *504*, 130-142.

[121] R. d. S. Santos, G. A. Faria, C. Giles, C. A. P. Leite, H. d. S. Barbosa, M. A. Z. Arruda, C. Longo, *ACS Applied Materials & Interfaces* **2012**, *4*, 5555-5561.

[122] M. Safari, R. Talebi, M. H. Rostami, M. Nikazar, M. Dadvar, *Journal of Environmental Health Science and Engineering* **2014**, *12*, 19-19.

[123] Q. R. Deng, X. H. Xia, M. L. Guo, Y. Gao, G. Shao, *Materials Letters* **2011**, *65*, 2051-2054.

[124] L. Zhang, L. Zhu, L. Hu, Y. Li, H. Song, Z. Ye, *RSC Advances* **2016**, *6*, 57403-57408.

[125] R. Chauhan, A. Kumar, R. P. Chaudhary, *Spectrochimica Acta Part A: Molecular and Biomolecular Spectroscopy* **2012**, *98*, 256-264.

[126] B. Gao, T. Wang, X. Fan, H. Gong, H. Guo, W. Xia, Y. Feng, X. Huang, J. He, *Inorganic Chemistry Frontiers* **2017**, *4*, 898-906.

[127] D. Jing, Y. Zhang, L. Guo, *Chemical Physics Letters* **2005**, *415*, 74-78.

[128] H. K. Dong, S. L. Kyung, K. Yoon‑Suk, C. Yong‑Chae, K. Sun‑Jae, *Journal of the American Ceramic Society* **2006**, *89*, 515-518.

[129] L. S. Yoong, F. K. Chong, B. K. Dutta, *Energy* **2009**, *34*, 1652-1661.

[130] P. Pongwan, K. Wetchakun, S. Phanichphant, N. Wetchakun, *Research on Chemical Intermediates* **2016**, *42*, 2815-2830.

[131] H. M. Yadav, S. V. Otari, V. B. Koli, S. S. Mali, C. K. Hong, S. H. Pawar, S. D. Delekar, *Journal of Photochemistry and Photobiology A: Chemistry* **2014**, *280*, 32-38.

[132] Y. Zhao, C. Li, X. Liu, F. Gu, H. L. Du, L. Shi, *Applied Catalysis B: Environmental* **2008**, *79*, 208-215.

[133] Y. Yu, J. Wang, W. Li, W. Zheng, Y. Cao, *CrystEngComm* **2015**, *17*, 5074-5080.

[134] C. Wattanawikkam, W. Pecharapa, *Integrated Ferroelectrics* **2015**, *165*, 167-175.

[135] Y. Wang, R. Zhang, J. Li, L. Li, S. Lin, *Nanoscale Research Letters* **2014**, *9*, 46.

[136] H. Pätow, L. Riekert, *Berichte der Bunsengesellschaft für Physikalische Chemie* **1979**, *83*, 807-811.

[137] M. A. Farrokhzad, T. I. Khan, *Oxidation of Metals* **2014**, *81*, 267-285.

[138] H. Jin, X. Zhao, X. Su, C. Zhu, C. Cao, L. Guo, *International Journal of Hydrogen Energy* **2017**, *42*, 4943-4950.

[139] P. Kanhere, Z. Chen, *Molecules* **2014**, *19*, 19995-20022.

[140] I. Oja, A. Mere, M. Krunks, C. H. Solterbeck, M. Es-Souni, *Solid State Phenomena* **2004**, *99-100*, 259-264.

[141] M. O. Abou-Helal, W. T. Seeber, *Applied Surface Science* **2002**, *195*, 53-62.

[142] I. H. Chowdhury, S. Kundu, M. K. Naskar, *Journal of Physics and Chemistry of Solids* **2018**, *121*, 367-374.

[143] P. Kajitvichyanukul, J. Ananpattarachai, S. Pongpom, *Science and Technology of Advanced Materials* **2005**, *6*, 352-358.

[144] J. Dharma, A. Pisal, *Simple Method of Measuring the Band Gap Energy Value of TiO2 in the Powder Form using a UV/Vis/NIR Spectrometer*, PerkinElmer, Inc., **2009-2012**.

[145] M. J. Torralvo, J. Sanz, I. Sobrados, J. Soria, C. Garlisi, G. Palmisano, S. Çetinkaya, S. Yurdakal, V. Augugliaro, *Applied Catalysis B: Environmental* **2018**, *221*, 140-151.

[146] D. M. Tobaldi, A. Tucci, A. S. Škapin, L. Esposito, *Journal of the European Ceramic Society* **2010**, *30*, 2481-2490.

[147] N. J. Calos, J. S. Forrester, G. B. Schaffer, *Journal of Solid State Chemistry* **1996**, *122*, 273-280.

[148] N. E. Brese, M. O'Keeffe, B. L. Ramakrishna, R. B. Von Dreele, *Journal of Solid State Chemistry* **1990**, *89*, 184-190.

[149] P. Niggli, *Zeitschrift fuer Kristallographie, Kristallgeometrie, Kristallphysik, Kristallchemie* **1922**, *57*, 253-299.

[150] Z. G. Pinsker, M. F. Bundule, V. I. Khitrova, *Golden Book of Phase Transitions, Vol. 1*, **2002**.

[151] W. Hase, *Golden Book of Phase Transitions, Vol. 1*, **2002**.

[152] Q. Xiao, L. Ouyang, *Chemical Engineering Journal* **2009**, *148*, 248-253.

[153] M. Iwasaki, M. Hara, H. Kawada, H. Tada, S. Ito, *Journal of Colloid and Interface Science* **2000**, *224*, 202-204.

[154] K. A. Michalow, D. Logvinovich, A. Weidenkaff, M. Amberg, G. Fortunato, A. Heel, T. Graule, M. Rekas, *Catalysis Today* **2009**, *144*, 7-12.

[155] A. Kubacka, G. Colón, M. Fernández-García, *Catalysis Today* **2009**, *143*, 286-292.

[156] V. Štengl, S. Bakardjieva, N. Murafa, *Materials Chemistry and Physics* **2009**, *114*, 217-226.

[157] H. Yan, X. Wang, M. Yao, X. Yao, *Progress in Natural Science: Materials International* **2013**, *23*, 402-407.

[158] M. J. Pavan., F. Helena, S. Gal, S. A. I, L. N. Gabriel, M. Taleb, *ChemCatChem* **2018**, *10*, 2541-2545.

[159] J. Tian, X. Hu, N. Wei, Y. Zhou, X. Xu, H. Cui, H. Liu, *Solar Energy Materials and Solar Cells* **2016**, *151*, 7-13.

[160] L. Gu, J. Wang, Z. Zou, X. Han, *Journal of Hazardous Materials* **2014**, *268*, 216-223.

[161] C. D. Elvidge, D. M. Keith, B. T. Tuttle, K. E. Baugh, *Sensors* **2010**, *10*, 3961.

[162] A. Presciutti, F. Asdrubali, A. Marrocchi, A. Broggi, G. Pizzoli, A. Damiani, *Sustainability* **2014**, *6*, 6830.

[163] X. Ning, S. Meng, X. Fu, X. Ye, S. Chen, *Green Chemistry* **2016**, *18*, 3628-3639.

[164] N. Zhang, Y. Zhang, X. Pan, X. Fu, S. Liu, Y.-J. Xu, *The Journal of Physical Chemistry C* **2011**, *115*, 23501-23511.

[165] Z.-R. Tang, X. Yin, Y. Zhang, Y.-J. Xu, *Inorganic Chemistry* **2013**, *52*, 11758-11766.

[166] X. Dai, M. Xie, S. Meng, X. Fu, S. Chen, *Applied Catalysis B: Environmental* **2014**, *158-159*, 382-390.

[167] Z. Chai, T.-T. Zeng, Q. Li, L.-Q. Lu, W.-J. Xiao, D. Xu, *Journal of the American Chemical Society* **2016**, *138*, 10128-10131.

[168] K. J. Green, R. Rudham, *Journal of the Chemical Society, Faraday Transactions* **1992**, *88*, 3599-3603.

[169] U. Rössler, R. Blachnik, J. Chu, R. R. Galazka, J. Geurts, J. Gutowski, B. Hönerlage, D. Hofmann, J. Kossut, R. Levy, *II-VI and I-VII Compounds; Semimagnetic Compounds: Supplement to Vols. III/17b, 22a (Print Version) Revised and Updated Edition of Vols. III/17b, 22a (CD-ROM)*, Springer Berlin Heidelberg, **1999**.

[170] K. Varunkumar, R. Hussain, G. Hegde, A. S. Ethiraj, *Materials Science in Semiconductor Processing* **2017**, *66*, 149-156.

[171] J. Wei, J. C. Zhang, *IOP Conference Series: Materials Science and Engineering* **2017**, *167*, 012037.

[172] H. Landolt, R. Börnstein, in *II-VI and I-VII Compounds; Semimagnetic Compounds* (Eds.: O. Madelung, U. Rössler, M. Schulz), Springer Berlin Heidelberg, Berlin, Heidelberg, **1999**, pp. 1-9.

[173] R. I. Dimitrov, N. Moldovanska, I. K. Bonev, *Thermochimica Acta* **2002**, *385*, 41-49.

[174] C.-H. Li, C.-W. Hsu, S.-Y. Lu, *Journal of Colloid and Interface Science* **2018**, *521*, 216-225.

[175] O. Cretu, C. Zhang, D. Golberg, *Applied Physics Letters* **2017**, *110*, 111904.

[176] J. Yan, G. Wu, N. Guan, L. Li, Z. Li, X. Cao, *Physical Chemistry Chemical Physics* **2013**, *15*, 10978-10988.

[177] J. W. M. Chon, M. Gu, C. Bullen, P. Mulvaney, *Applied Physics Letters* **2004**, *84*, 4472-4474.

[178] S. Kumar, A. K. Ojha, B. Walkenfort, *Journal of Photochemistry and Photobiology B: Biology* **2016**, *159*, 111-119.

[179] V. Smyntyna, B. Semenenko, V. Skobeeva, N. Malushin, *Beilstein Journal of Nanotechnology* **2014**, *5*, 355-359.

[180] B. Goswami, A. Choudhury, *Journal of Experimental Nanoscience* **2015**, *10*, 900-910.

[181] A. Khan, Z.-u. Rehman, A. Khan, H. Ambareen, H. Ullah, S. M. Abbas, Y. Khan, R. Khan, *Inorganic Chemistry Communications* **2017**, *79*, 99-103.

[182] M. Behboudnia, B. Khanbabaee, *Colloids and Surfaces A: Physicochemical and Engineering Aspects* **2006**, *290*, 229-232.

[183] Y.-C. Liang, T.-W. Lung, *Nanoscale research letters* **2016**, *11*, 264-264.

[184] D. Wang, X. Li, L.-L. Zheng, L.-M. Qin, S. Li, P. Ye, Y. Li, J.-P. Zou, *Nanoscale* **2018**, *10*, 19509-19516.

[185] W. Yang, W. Wu, W. Chen, J. Zhao, X. Hu, *Catalysis Science & Technology* **2018**, *8*, 5280-5287.

[186] Y. Shiraishi, D. Tsukamoto, Y. Sugano, A. Shiro, S. Ichikawa, S. Tanaka, T. Hirai, *ACS Catalysis* **2012**, *2*, 1984-1992.

[187] E. Grabowska, M. Marchelek, T. Klimczuk, G. Trykowski, A. Zaleska-Medynska, *Journal of Molecular Catalysis A: Chemical* **2016**, *423*, 191-206.

[188] J. Wang, W. Zhu, Y. Zhang, S. Liu, *The Journal of Physical Chemistry C* **2007**, *111*, 1010-1014.

[189] O. Ola, M. M. Maroto-Valer, *Journal of Photochemistry and Photobiology C: Photochemistry Reviews* **2015**, *24*, 16-42.

[190] D. A. Agyeman, K. Song, S. H. Kang, M. R. Jo, E. Cho, Y.-M. Kang, *Journal of Materials Chemistry A* **2015**, *3*, 22557-22563.

[191] R. G. Palgrave, D. J. Payne, R. G. Egdell, *Journal of Materials Chemistry* **2009**, *19*, 8418-8425.

[192] J. Hölzl, F. K. Schulte, in *Solid Surface Physics* (Eds.: J. Hölzl, F. K. Schulte, H. Wagner), Springer Berlin Heidelberg, Berlin, Heidelberg, **1979**, pp. 1-150.

[193] L.-l. Zheng, X.-y. Xiao, Y. Li, W.-p. Zhang, *Transactions of Nonferrous Metals Society of China* **2017**, *27*, 1117-1126.

[194] Y. Shiraishi, Y. Sugano, S. Tanaka, T. Hirai, *Angewandte Chemie* **2010**, *122*, 1700-1704.

[195] D. L. Liao, B. Q. Liao, *Journal of Photochemistry and Photobiology A: Chemistry* **2007**, *187*, 363-369.

[196] Y.-F. Chen, C.-Y. Lee, M.-Y. Yeng, H.-T. Chiu, *Journal of Crystal Growth* **2003**, *247*, 363-370.

[197] Y.-C. Lee, Y. S. Chang, L. G. Teoh, Y. L. Huang, Y. C. J. J. o. S.-G. S. Shen, Technology, *Journal of Sol-Gel Science and Technology* **2010**, *56*, 33-38.

[198] H. Li, T. Lin, H. Shao, C. Wu, Z. Guo, J. Luo, *Rare Metals* **2008**, *27*, 197-200.

[199] Y. Yu, W. Wen, X.-Y. Qian, J.-B. Liu, J.-M. Wu, *Scientific Reports* **2017**, *7*, 41253.

[200] J. O. Olowoyo, M. Kumar, T. Dash, S. Saran, S. Bhandari, U. Kumar, *International Journal of Hydrogen Energy* **2018**, *43*, 19468-19480.

[201] Y. Guo, J. Qian, A. Iqbal, L. Zhang, W. Liu, W. Qin, *International Journal of Hydrogen Energy* **2017**, *42*, 15167-15177.

[202] L. Li, N. Zhang, X. Huang, Y. Liu, Y. Li, G. Zhang, L. Song, H. He, *ACS Catalysis* **2018**, *8*, 3222-3231.

[203] I. Mondal, U. Pal, *Physical Chemistry Chemical Physics* **2016**, *18*, 4780-4788.

[204] G. Cheng, A. R. J. A. Hight Walker, B. Chemistry, *Analytical and Bioanalytical Chemistry* **2010**, *396*, 1057-1069.

[205] Y. Yang, D. Xu, Q. Wu, P. Diao, *Scientific Reports* **2016**, *6*, 35158.

[206] C. Wang, D. P. Chen, X. Sang, R. R. Unocic, S. E. Skrabalak, *ACS Nano* **2016**, *10*, 6345-6353.

[207] H. Ye, Y. Li, J. Chen, J. Sheng, X.-Z. Fu, R. Sun, C.-P. J. J. o. M. S. Wong, *Journal of Materials Science* **2018**, *53*, 15871-15881.

[208] X. H. Liu, D. Meng, H. Y. Wang, Y. Deng, B. Deng, J. H. Tian, *Advanced Materials Research* **2012**, *550-553*, 340-346.

[209] Y. Wang, L. Li, X. Huang, Q. Li, G. Li, *RSC Advances* **2015**, *5*, 34302-34313.

[210] E. Westsson, S. Picken, G. Koper, *Chemical Communications* **2019**, *55*, 1338-1341.

[211] E. Ismail, M. Khenfouch, M. Dhlamini, S. Dube, M. Maaza, *Journal of Alloys and Compounds* **2017**, *695*, 3632-3638.

[212] Y. H. Tseng, I. G. Chang, Y. Tai, K. W. Wu, *Journal of nanoscience and nanotechnology* **2012**, *12*, 416-422.

[213] Z. El Koura, M. Cazzanelli, N. Bazzanella, N. Patel, R. Fernandes, G. E. Arnaoutakis, A. Gakamsky, A. Dick, A. Quaranta, A. Miotello, *The Journal of Physical Chemistry C* **2016**, *120*, 12042-12050.

[214] V. Jagadeesh babu, S. Vempati, Y. Ertas, T. Uyar, *RSC Advances* **2015**, *5*, 66367-66375.

[215] X. Yu, Y. Wang, Y. K. Kim, *Physical Chemistry Chemical Physics* **2017**, *19*, 24049-24058.

[216] J. Liu, J. Li, A. Sedhain, J. Lin, H. Jiang, *The Journal of Physical Chemistry C* **2008**, *112*, 17127-17132.

[217] T. Okumura, Y. Kinoshita, H. Uchiyama, H. Imai, *Materials Chemistry and Physics* **2008**, *111*, 486-490.

[218] Y. Zhu, C. Ding, G. Ma, Z. Du, *Journal of Solid State Chemistry* **1998**, *139*, 124-127.

[219] J. Shi, J. Chen, Z. Feng, T. Chen, Y. Lian, X. Wang, C. Li, *The Journal of Physical Chemistry C* **2007**, *111*, 693-699.

[220] K. Iijima, M. Goto, S. Enomoto, H. Kunugita, K. Ema, M. Tsukamoto, N. Ichikawa, H. Sakama, *Journal of Luminescence* **2008**, *128*, 911-913.

[221] K. Wakabayashi, Y. Yamaguchi, T. Sekiya, S. Kurita, *Journal of Luminescence* **2005**, *112*, 50-53.

[222] R. Sato, T. Kawai, K. Kifune, *Journal of Non-Crystalline Solids* **2010**, *356*, 1300-1304.

[223] M. Memesa, S. Lenz, S. G. J. Emmerling, S. Nett, J. Perlich, P. Müller-Buschbaum, J. S. J. C. Gutmann, P. Science, *Colloid and Polymer Science* **2011**, *289*, 943-953.

[224] R. Jaiswal, J. Bharambe, N. Patel, A. Dashora, D. C. Kothari, A. Miotello, *Applied Catalysis B: Environmental* **2015**, *168-169*, 333-341.

[225] J. F. Moulder, W. F. Stickle, P. E. Sobol, K. D. Bomben, *Handbook of X Ray Photoelectron Spectroscopy: A Reference Book of Standard Spectra for Identification and Interpretation of Xps Data* Physical Electronics, **1995**.

[226] L. Zhang, P. Y. Tan, C. K. Lim, X. Guo, M. S. Tse, O. K. Tan, V. W. C. Chang, *Journal of Environmental Chemical Engineering* **2016**, *4*, 357-364.

[227] A. M. Venezia, A. Rossi, D. Duca, A. Martorana, G. Deganello, *Applied Catalysis A: General* **1995**, *125*, 113-128.

[228] P. K. Gallagher, M. E. Gross, *Journal of Thermal Analysis and Calorimetry - J THERM ANAL CALORIM* **1986**, *31*, 1231-1241.

[229] J. Rymarczyk, E. Czerwosz, R. Diduszko, M. Kozlowski, *Materials Science-Poland* **2017**, *35*, 594-600.

[230] X. Yang, H. Zhao, J. Feng, Y. Chen, S. Gao, R. Cao, *Journal of Catalysis* **2017**, *351*, 59-66.

[231] P. Askari, S. Mohebbi, *New Journal of Chemistry* **2018**, *42*, 1715-1724.

[232] M. J. Lima, P. B. Tavares, A. M. T. Silva, C. G. Silva, J. L. Faria, *Catalysis Today* **2017**, *287*, 70-77.

[233] O. Tomita, T. Otsubo, M. Higashi, B. Ohtani, R. Abe, *ACS Catalysis* **2016**, *6*, 1134-1144.

[234] R. Marotta, I. Di Somma, D. Spasiano, R. Andreozzi, V. Caprio, *Chemical Engineering Journal* **2011**, *172*, 243-249.

[235] S. Verma, R. B. Nasir Baig, M. N. Nadagouda, R. S. Varma, *Tetrahedron* **2017**, *73*, 5577-5580.

[236] S. Hosseini, A. Amoozadeh, *Journal of Photochemistry and Photobiology A: Chemistry* **2018**, *364*, 516-523.

[237] E. Safaei, S. Mohebbi, M. Irani, *Journal of Sol-Gel Science and Technology* **2018**, *87*, 170-182.

[238] S. Li, J. Cai, X. Wu, F. Zheng, *Applied Surface Science* **2018**, *443*, 603-612.

[239] Y. Chen, Y. Wang, W. Li, Q. Yang, Q. Hou, L. Wei, L. Liu, F. Huang, M. Ju, *Applied Catalysis B: Environmental* **2017**, *210*, 352-367.

[240] X. Wang, D. Baiyila, X. Li, *RSC Advances* **2016**, *6*, 107233-107238.

[241] Y. Xie, C. He, L. Liu, L. Mao, K. Wang, Q. Huang, M. Liu, Q. Wan, F. Deng, H. Huang, X. Zhang, Y. Wei, *RSC Advances* **2015**, *5*, 82503-82512.

[242] U. Shanker, M. Rani, V. J. E. C. L. Jassal, **2017**, *15*, 623-642.

[243] W. H. Organization, U. N. E. Programme, *Water pollution control*
A guide to the use of water quality management principles, **1997**.

[244] M. Kabuto, G. L. Peralta, S. Ikeda, Y. Honda, , World Health Organization
United Nations Development Programme **2001**.

[245] G. Zhao, J. Zou, C. Li, J. Yu, X. Jiang, Y. Zheng, W. Hu, F. Jiao, *Journal of Materials Science: Materials in Electronics* **2018**, *29*, 7002-7014.

[246] I. Medina-Ramírez, J. L. Liu, A. Hernández-Ramírez, C. Romo-Bernal, G. Pedroza-Herrera, J. Jáuregui-Rincón, M. A. Gracia-Pinilla, *Journal of Materials Science* **2014**, *49*, 5309-5323.